Electron swarm properties under the influence of a very strong attachment in SF_6 and CF_3I obtained by Monte Carlo rescaling procedures

You may also be interested in:

Boltzmann equation and Monte Carlo studies of electron transport in resistive plate chambers
D Bošnjakovi, Z Lj Petrovi, R D White et al.

Non-conservative electron transport in CF4
S Dujko, R D White, K F Ness et al.

Positron transport in water vapour
A Bankovi, S Dujko, R D White et al.

High-order fluid model for streamer discharges: I. Derivation of model and transport data
S Dujko, A H Markosyan, R D White et al.

A multi-term solution of the nonconservative Boltzmann equation
S Dujko, R D White, Z Lj Petrovi et al.

Monte Carlo studies of electron transport in CF4
S Dujko, Z M Raspopovi and Z Lj Petrovi

Fluid modeling of resistive plate chambers: impact of transport data on development of streamers and induced signals
D Bošnjakovi, Z Lj Petrovi and S Dujko

Electron swarm properties under the influence of a very strong attachment in SF_6 and CF_3I obtained by Monte Carlo rescaling procedures

J Mirić[1], D Bošnjaković[1], I Simonović[1], Z Lj Petrović[1,2] and S Dujko[1]

[1] Institute of Physics, University of Belgrade, PO Box 68, 11080 Belgrade, Serbia
[2] Serbian Academy of Sciences and Arts, Knez Mihailova 35, 11001 Belgrade, Serbia

E-mail: sasa.dujko@ipb.ac.rs

Abstract

Electron attachment often imposes practical difficulties in Monte Carlo simulations, particularly under conditions of extensive losses of seed electrons. In this paper, we discuss two rescaling procedures for Monte Carlo simulations of electron transport in strongly attaching gases: (1) discrete rescaling, and (2) continuous rescaling. The two procedures are implemented in our Monte Carlo code with an aim of analyzing electron transport processes and attachment induced phenomena in sulfur-hexafluoride (SF_6) and trifluoroiodomethane (CF_3I). Though calculations have been performed over the entire range of reduced electric fields E/n_0 (where n_0 is the gas number density) where experimental data are available, the emphasis is placed on the analysis below critical (electric gas breakdown) fields and under conditions when transport properties are greatly affected by electron attachment. The present calculations of electron transport data for SF_6 and CF_3I at low E/n_0 take into account the full extent of the influence of electron attachment and spatially selective electron losses along the profile of electron swarm and attempts to produce data that may be used to model this range of conditions. The results of Monte Carlo simulations are compared to those predicted by the publicly available two term Boltzmann solver BOLSIG+. A multitude of kinetic phenomena in electron transport has been observed and discussed using physical arguments. In particular, we discuss two important phenomena: (1) the reduction of the mean energy with increasing E/n_0 for electrons in SF_6 and (2) the occurrence of negative differential conductivity (NDC) in the bulk drift velocity only for electrons in both SF_6 and CF_3I. The electron energy distribution function, spatial variations of the rate coefficient for electron attachment and average energy as well as spatial profile of the swarm are calculated and used to understand these phenomena.

Keywords: Monte Carlo, electron transport, electron attachment, SF_6, CF_3I

(Some figures may appear in colour only in the online journal)

1. Introduction

Electron transport in strongly attaching gases has long been of interest, with applications in many areas of fundamental physics and technology. Electron attaching gases support key processes for plasma etching and cleaning in semiconductor fabrication [1, 2], high-voltage gas insulation [3] and particle detectors in high energy physics [4–6]. The importance of studies of electron attachment has also been recognized in other fields, including planetary atmospheres, excimer lasers, plasma medicine and lighting applications, as well as in life science for understanding radiation damage in biological matter.

The fundamental importance of electron attachment processes has led to many experimental and theoretical swarm studies. For some gases the cross sections for attachment may be very large resulting in a rapid disappearance of free electrons that greatly complicates the measurements of transport coefficients [1, 7–9]. The pioneering studies date back to the 1970s, and the well-known swarm method of deriving cross section for electron attachment developed by Christophorou and his co-workers [10]. According to this method, trace amounts of an electron attaching gas are mixed into the buffer gases, typically nitrogen to scan the lower mean energies and argon to scan the higher mean energies. This technique results in the removal of electrons without disturbing the electron energy distribution function. In such mixtures the losses depend only on the very small amount of the added gas and we may measure the density reduced electron attachment rate coefficient. Electron attachment cross sections can be determined by deconvoluting the mixture data, since the electron energy distribution function is a known function of E/n_0 as calculated for the pure buffer gas. Examples of this procedure are cross sections for electron attachment in SF_6 and SF_6-related molecules [11–15] as well as cross sections and rate coefficients for a range of fluorocarbons [1, 12, 16–18] and other relevant gases for applications [1, 19–22]. In addition to non-equilibrium data, there is a separate category of experiments, including flowing afterglow, the Cavalleri diffusion experiment [9, 23, 24], and others that provide attachment rates for thermal equilibrium (i.e. without an applied electric field). These may be taken at different temperatures, but the range of energies covered by this technique is very narrow. These two techniques have been used to evaluate the cross sections for SF_6 and CF_3I, always under the assumption that the effect of attachment is merely on the number of particles and not on any other swarm properties.

A thorough understanding of the influence of attachment on the drift and diffusion of the electrons provides information which could be used in analysis of kinetic phenomena in complex electronegative gases and related plasmas. The attachment cooling and heating [25, 26], negative absolute electron flux mobility [27, 60] and anomalous phase shifts of drift velocity in AC electric fields [28] are some examples of these phenomena in strongly attaching gases, which may not be trivially predicted on the basis of individual collision events and external fields. Negative differential conductivity (NDC) induced by 3-body attachment for lower E/n_0 and higher pressures in molecular oxygen and its mixture with other gases is another example of phenomena induced by strong electron attachment [29]. The duality in transport coefficients, e.g. the existence of two fundamentally different families of transport coefficients, the bulk and flux, is caused by the explicit effects of electron impact ionization and electron attachment [7, 30–32]. The differences between two sets of data vary from a few percents to a few orders of magnitude and hence a special care is needed in the implementation of data in fluid models of plasma discharges [7, 31, 33–35]. On one hand, most plasma modeling is based on flux quantities while experiments aimed at yielding cross section data provide mostly but not uniquely the bulk transport data. This differentiation between flux and bulk transport properties is not merely a whimsy of theorists, but it is essential in obtaining and applying the basic swarm data. In addition, the production of negative ions has a large effect on the transport and spatial distribution of other charged particle species as well as on the structure of the sheath and occurrence of relaxation oscillations in charged particle densities [36–41].

There are three main approaches to the theoretical description of electron transport in gases: the kinetic Boltzmann equation, the stochastic particle simulation by the Monte Carlo method and semi-quantitative momentum transfer theory. Restrictions on the accuracy of momentum transfer theory for studies of electron transport in attaching gases, particularly under non-hydrodynamic conditions, have already been discussed and illustrated [31, 42, 43]. Boltzmann equation analyses for SF_6 and its mixtures with other gases (see for example [11, 44–50]) have been performed several times in the past. Two important studies devoted to the calculation of electron swarm parameters based on a Boltzmann equation have also been performed for CF_3I [51, 52]. Theories for solving the Boltzmann equation were usually restricted to low-order truncations in the Legendre expansions of the velocity dependence assuming quasi-isotropy in velocity space. The explicit effects of electron attachment were also neglected and electron transport was studied usually in terms of the flux data only. These theories had also restricted domains of validity on the applied E/n_0 in spite of their coverage of a considerably broader range. One thing that strikes the reader surveying the literature on electron transport in SF_6 is the systematic lack of reliable data for electron transport coefficients for E/n_0 less than 50 Td. Contemporary moment methods for solving Boltzmann's equation [31, 53] are also faced with a lot of systematic difficulties, particularly under conditions of the predominant removal of the lower energy electrons which results in an increase in the mean energy, i.e. attachment heating. Under these conditions the bulk of the distribution function is shifted towards a higher energy which in turn results in the high energy tail falling off much slower than a Maxwellian. This is exactly what may happen in the analysis of electron transport in strongly attaching gases such as SF_6 or CF_3I for lower E/n_0. The moment method for solving Boltzmann's equation under these circumstances usually requires the prohibitive number of basis functions for resolving the speed/energy dependency of the distribution function and/or unrealistically large computation time. As a consequence, the standard numerical schemes employed within the framework of moment methods usually fail.

The present investigation is thus mainly concerned with the Monte Carlo simulations of electron transport in strongly attaching gases. Monte Carlo simulations have also been employed for the analysis of electron transport in the mixtures of SF_6 [46, 54–57] and CF_3I [58] with other gases usually with an aim of evaluating the insulation strength and critical electric fields. However, electron attachment in strongly electronegative gases often imposes practical difficulties in Monte Carlo simulations. This is especially noticeable at lower E/n_0, where electron attachment is one of the dominant processes which may lead to the extensive vanishing of the seed electrons and

consequently to the decrease of the statistical accuracy of the output results. In extreme cases, the entire electron swarm might be consumed by attachment way before the equilibrated (steady-state regime) is achieved. An obvious solution would be to use a very large number of initial electrons, but this often leads to a dramatic increase of computation time and/or required memory/computing resources which are beyond practical limits. Given the computation restrictions of the time, the workers were forced to develop methods to combat the computational difficulties induced by the extensive vanishing of the seed electrons. Two general methods were developed: (1) addition of new electrons by uniform scaling of the electron swarm at certain time instants under hydrodynamic conditions [26, 59] or at certain positions under steady-state Townsend conditions [60], when number of electrons reaches a pre-defined threshold, and (2) implementation of an additional fictitious ionization channel/process with a constant collision frequency (providing that the corresponding ionization rate is chosen to be approximately equal to the attachment rate) [54]. On the other hand, similar rescaling may be applied for the increasing number of electrons as has been tested at the larger E/n_0 by Li *et al* [61]. Further distinction and specification between methods developed by Nolan *et al* [26] and Dyatko *et al* [60] on one hand and Raspopović *et al* [59] on the other, will be discussed in later sections. These methods have not been compared to each other in a comprehensive and rigorous manner. This raises a number of questions. How accurate, these methods are? Which is the more efficient? Which is easier for implementation? What is their relationship to each other? Which one is more flexible? In this paper, we will try to address some of these issues. In particular, the present paper serves to summarize the salient features of these methods in a way which we hope will be of benefit to all present and future developers of Monte Carlo codes. Finally, it is also important to note that in the present paper we extend the method initially developed by Yousfi *et al* [54], by introducing time-dependent collision frequency for the fictitious ionization process.

This paper is organized as follows: in section 2, we briefly review the basic elements of our Monte Carlo code, before detailing the rescaling procedures employed to combat the computational difficulties initiated by the rapid disappearance of electrons. In the same section, we illustrate the issue of electron losses by considering the evolution of the number of electrons for a range of E/n_0 in SF_6 and CF_3I. In section 3, we evaluate the performance of rescaling procedures by simulating electron transport in SF_6 and CF_3I over a wide range of E/n_0. We will also highlight the substantial difference between the bulk and flux transport coefficients in SF_6 and CF_3I. Special attention will be paid to the occurrence of negative differential conductivity (NDC) in the profile of the bulk drift velocity. For electrons in SF_6 another phenomenon arises: for certain reduced electric fields we find regions where the swarm mean energy decreases with increasing E/n_0. In the last segment of the section 3, we discuss two important issues: (1) how to use the rescaling procedures in Monte Carlo codes, and (2) rescaling procedures as a tool in the modeling of non-hydrodynamic effects in swarm experiments. In section 4, we present our conclusions and recommendations.
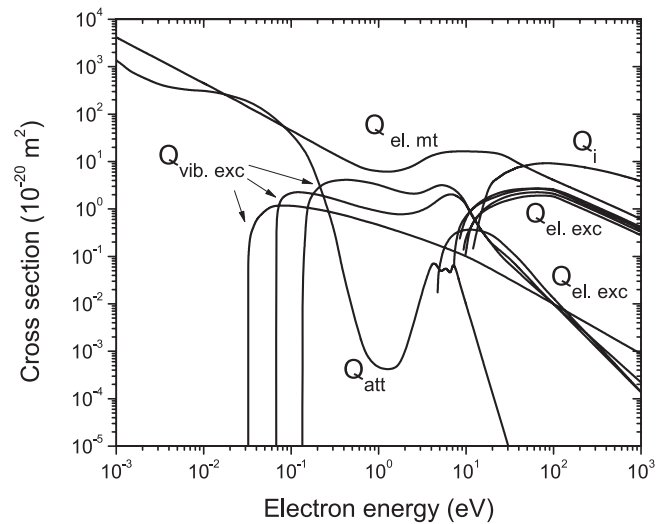

Figure 1. Electron impact cross-sections for CF_3I used in this study [62]: $Q_{el. mt}$ momentum transfer in elastic collisions, $Q_{vib. exc}$ vibrational excitation, $Q_{el. exc}$ electronic excitation, Q_{att} dissociative attachment and Q_i electron-impact ionization.

2. Input data and computational methods

2.1. Cross sections for electron scattering and simulation conditions

We begin this section with a brief description of cross sections for electron scattering in SF_6 and CF_3I. For the SF_6 cross sections we use the set developed by Itoh *et al* [47]. This set was initially based on published measurements of cross sections for individual collision processes. Using the standard swarm procedure, the initial set was modified to improve agreement between the calculated swarm parameters and the experimental values. The set includes one vibrational channel, one electronic excitation channel, as well as elastic, ionization and five different attachment channels.

This study considers electron transport in CF_3I using the cross section set developed in our laboratory [62]. This set of cross sections is shown in figure 1. It should be noted that this set is similar but not identical to that developed by Kimura and Nakamura [63]. We have used the measured data under pulsed Townsend conditions for pure CF_3I and its mixtures with Ar and CO_2 in a standard swarm procedure with the aim of improving the accuracy and completeness of a set of cross sections. It consists of the elastic momentum transfer cross section, three cross sections for vibrational and five cross sections for electronic excitations as well as one cross section for electron-impact ionization with a threshold of 10.4 eV and one cross section for dissociative attachment. For more details the reader is referred to our future paper [64].

For both SF_6 and CF_3I all electron scattering are assumed isotropic and hence the elastic cross section is the same as the elastic momentum transfer cross section. Simulations have been performed for E/n_0 ranging from 1 to 1000 Td. The pressure and temperature of the background gas are 1 Torr and 300 K, respectively. It should be mentioned that special care in our Monte Carlo code has been paid to proper treatment of the thermal motion of the host gas molecules and their influence
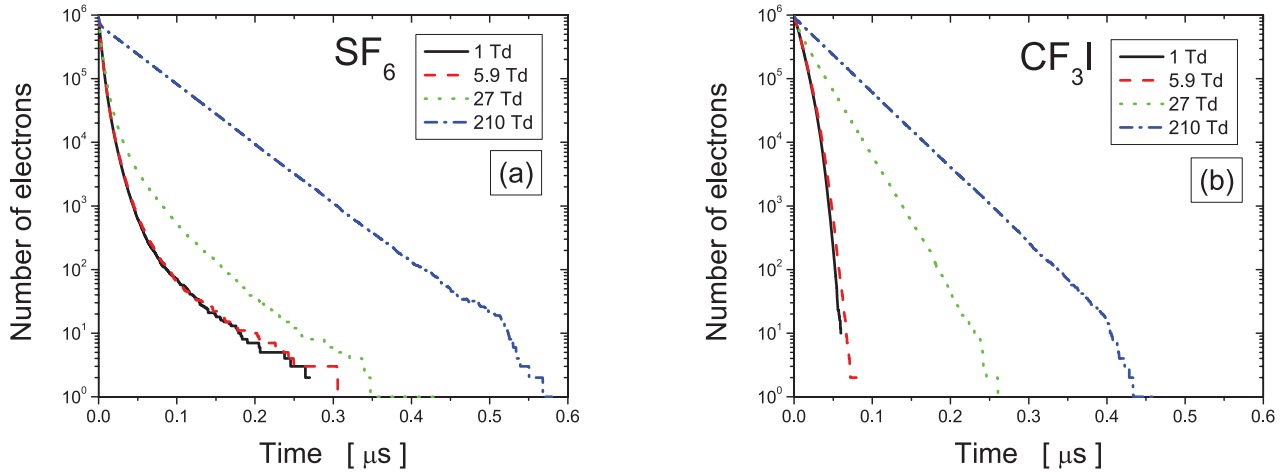
Figure 2. Electron number density decay for four different reduced electric fields as indicated on the graph. Calculations are performed for SF_6 (a) and CF_3I (b).

on electrons, which is very important at low electric fields, when the mean electron energy is comparable to the thermal energy of the host gas [65]. After ionization, the available energy is partitioned between two electrons in such a way that all fractions of the distribution are equally probable.

2.2. Monte Carlo method

The Monte Carlo simulation technique used in the present work is described at length in our previous publications [32, 53, 59, 66, 67]. In brief, we follow the spatiotemporal evolution of each electron through time steps which are fractions of the mean collision time. In association with random numbers, these finite time steps are used to solve the integral equation for the collision probability in order to determine the time of the next collision. The number of time steps is determined in such a way as to optimize the performance of the Monte Carlo code without reducing the accuracy of the final results. When the moment of the next collision is established, the additional sequences of random numbers are used, first to determine the nature of a collision, taking into account the relative probabilities of the various collision types, and second to determine the change in the direction of the electron velocity. All dynamic properties of each electron such as position, velocity, and energy are updated between and after the collisions. Sampling of electron dynamic properties is not correlated to the time of the next collision and is performed in a way that ensemble averages can be taken in both the velocity and configuration space. Explicit formulas for the bulk and flux transport properties have been given in our previous publications [59, 66]. To evaluate the accuracy of the Monte Carlo code, Boltzmann analyses were performed in parallel with the Monte Carlo calculations using the multi term method described in detail by Dujko *et al* [53]. In addition, we use the BOLSIG+, a publicly available Boltzmann solver based on a two term theory [68]. The most recent version of this code might be used to study the electron transport in terms of both the flux and bulk data which is very useful for some aspects of plasma modeling [7]. At the same time, the comparison between our results and those computed by BOLSIG+ which is presented in this paper, should

be viewed as the first benchmark for the bulk BOLSIG+ data. Our Monte Carlo code and multi term codes for solving the Boltzmann equation have been subject of a detailed testing for a wide range of model and real gases [31, 53, 59, 67].

In figure 2 we illustrate the losses of electrons during the evolution of the swarm towards the steady-state. The initial number of electrons is set to 1×10^6 and calculations are performed for a range of reduced electric fields E/n_0 as indicated on the graphs. For both SF_6 and CF_3I, we observe that at small E/n_0, i.e. at low mean energies, the number of electrons decreases much faster. This is a clear sign that collision frequency for electron attachment increases with decreasing E/n_0. Electrons in CF_3I are lost continuously and consequently the number of electrons in the swarm decreases exponentially with time. The same trend may be observed for electrons in SF_6 at 210 Td. For the remaining E/n_0 the number of electrons is reduced with time even faster. Comparing SF_6 and CF_3I, it is evident that the electrons are more efficiently consumed by electron attachment in SF_6 in the early stage of the simulation. Conversely, in the last stage of simulation the electrons are more consumed by electron attachment in CF_3I than in SF_6. In any case, the electron swarms in both cases are entirely consumed by attachment way before the steady-state regime and hence the simulations are stopped. In other words, the number density drops down by six orders of magnitude over the course of several hundred nanoseconds in both gases. To facilitate the numerical simulation, it is clear that some kind of rescaling of the number density is necessary to compensate for the electrons consumed by electron attachment. This procedure should not in any way disrupt the spatial gradients in the distribution function. On the other hand, releasing electrons with some fixed arbitrary initial condition would require that they equilibrate with the electric field during which time again majority of such additional electrons would be lost.

2.3. Rescaling procedures

To counteract the effect of attachment in an optimal fashion while keeping the statistical accuracy, the following rescaling procedures were proposed and applied so far:

(1) Uniform generation of new electrons with initial properties taken from the remaining electrons thus taking advantage of the equilibration that has been achieved so far [59]. To make this procedure effective i.e. to avoid losing population in some smaller pockets of the ensemble the population should be allowed to oscillate between N_1 and N_0, where $N_1 > N_0$ but their difference is relatively small. Here N_0 is minimum allowed number of electrons while N_1 is maximum number of electrons in the simulation after rescaling.

(2) Uniform scaling of an electron swarm by a factor of 2 or 3 at certain instants of time [26] or distance [60] depending on the simulation conditions where the probability of scaling for each electron is set to unity.

(3) Introduction of an additional fictitious ionization process with a constant ionization frequency (that is close to the rate for attachment), which artificially increases the number of simulated electrons [54, 61]. Uniform rescaling of the swarm is done by randomly choosing the electrons which are to be 'duplicated'. The newborn electron has the same initial dynamic properties, coordinates, velocity, and energy as the original. Following the creation of a new electron their further histories diverge according to the independently selected random numbers.

Comparing the procedures (1) and (2), it is clear that there are no essential differences between them. The only difference lies in the fact that in the procedure (2) duplicating is performed for all the electrons in the simulation while according the procedure (1), the probability of duplication is determined by the current ratio of the number of electrons to the desired number of electrons in the simulation, which is specified in advance. On the other hand, fictitious ionization collision generates a new electron which is given the same position, velocity and energy as the primary electron that is not necessarily the electron lost in attachment. In this paper, we shall refer to the procedure (1) as *discrete rescaling*, since the procedure is applied at discrete time instants. The procedure (2) shall be termed as *swarm duplication* and finally we shall refer to the procedure (3) as the *continuous rescaling* since the rescaling is done during the entire simulation. An important requirement is that the rescaling must not perturb/change/disturb the normalized electron distribution function and its evolution. Li *et al* [61] showed that the continuous rescaling procedure meets this requirement. In case of discrete rescaling as applied to the symmetrical yet different problem of excessive ionization, it was argued that one cannot be absolutely confident that the rescaled distribution is a good representation of the original [69], except when steady state is achieved [70].

In what follows, we discuss the continuous rescaling. Following the previous works [54, 61], the Boltzmann equation for the distribution function $f(\mathbf{r}, \mathbf{c}, t)$ without rescaling and $f^\star(\mathbf{r}, \mathbf{c}, t)$ with rescaling are given by:

$$(\partial_t + \mathbf{c} \cdot \nabla_\mathbf{r} + \mathbf{a} \cdot \nabla_\mathbf{c}) f(\mathbf{r}, \mathbf{c}, t) = -J(f), \tag{1}$$

and

$$(\partial_t + \mathbf{c} \cdot \nabla_\mathbf{r} + \mathbf{a} \cdot \nabla_\mathbf{c}) f^\star(\mathbf{r}, \mathbf{c}, t) = -J(f^\star) + \nu_{\mathrm{fi}}(t) f^\star, \tag{2}$$

where $\mathbf{a}$ is the acceleration due to the external fields, $J(f)$ is the collision operator for electron-neutral collisions and ν_{fi} is time-dependent fictitious ionization rate. If the collision operator is linear (i.e. if electron–electron collisions are negligible) and if the initial distributions (at time $t = 0$) are the same, it can be easily shown that the following relationship holds

$$f^\star(\mathbf{r}, \mathbf{c}, t) = f(\mathbf{r}, \mathbf{c}, t) \exp\left(\int_0^t \nu_{\mathrm{fi}}(\tau) \mathrm{d}\tau \right). \tag{3}$$

Substituting equation (3) into equation (2) and using the linearity of the collision operator yields the following equation

$$J(f^\star) = \exp\left(\int_0^t \nu_{\mathrm{fi}}(\tau) \mathrm{d}\tau \right) J(f). \tag{4}$$

Note that in contrast to Li *et al* [61] the collision frequency for the fictitious ionization is now a time-dependent function. In terms of numerical implementation, the only difference between our continuous rescaling procedure and the one described in [54, 61] is that we do not need to provide the fictitious ionization rate which is estimated by trial and error, in advance (*a priori*). Instead, our fictitious ionization rate is initially chosen to be equal to the calculated attachment rate at the beginning of the simulation. Afterwards, it is recalculated at fixed time instants in order to match the newly developed attachment rates. As a result, the number of electrons during the simulation usually does not differ from the initial one by more than 10%. It should be noted that the fictitious ionization process must not in any way be linked to the process of real ionization. It was introduced only as a way to scale the distribution function, or in other words, as a way of duplicating the electrons.

3. Results and discussion

In this section the rescaling procedures and associated Monte Carlo code outlined in the previous section are applied to investigate transport properties and attachment induced phenomena for electrons in SF_6 and CF_3I. Electron transport in these two strongly attaching gases provides a good test of different rescaling procedures, particularly for lower E/n_0 where electron attachment is the dominant non-conservative process. In addition to comparisons between different rescaling procedures, the emphasis of this section is the observation and physical interpretation of the attachment induced phenomena in the E/n_0-profiles of mean energy, drift velocity and diffusion coefficients. In particular, we investigate the differences between the bulk and flux transport coefficients. We do not compare our results with experimentally measured data as it would distract the reader's attention to the problems associated with the quality of the sets of the cross sections for electron scattering. There are no new experimental measurements of transport coefficients for electrons in SF_6, particularly for E/n_0 less than 50 Td and thus we have deliberately chosen not to display the comparison. On the other hand, one cannot expect the multi term results to be useful here as the conditions with excessive attachment would make convergence difficult in the low E/n_0 region, where comparison would be of
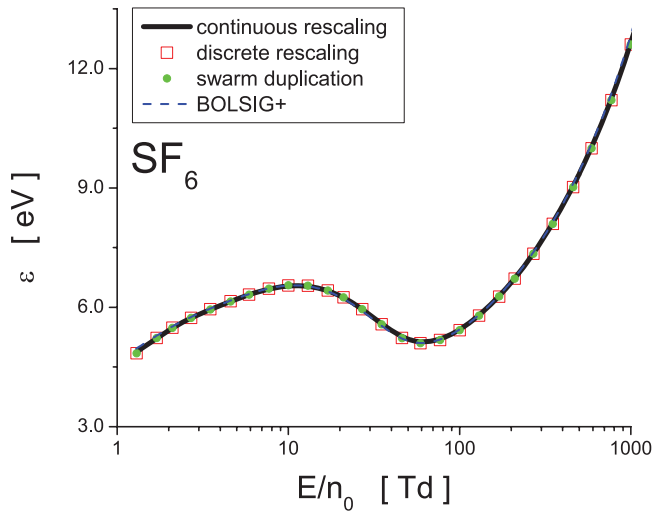
Figure 3. Variation of the mean energy with E/n_0 for electrons in SF_6. Monte Carlo results using three different techniques for electron number density compensation (rescaling) are compared with the BOLSIG+ results.

Figure 4. Electron energy distribution functions for E/n_0 of 10, 27, 59 and 210 Td. Cross sections for elastic momentum transfer (Qmt), electronic excitation (Qexc) and ionization (Qion) as well as for attachments that lead to the formation of SF_6^- (Qatt1) and SF_5^- (Qatt2) ions, are also included.

interest. Thus, for clarity the multi term results are omitted. Both experimental and theoretical work on electron swarms in SF_6 prior to 1990 is summarized in the papers of Phelps and van Brunt [11], Gallagher *et al* [71] and Morrow [72]. Recent results can be found in the book by Raju [22] and the review article of Christophorou and Olthoff [12]. The swarm analysis and further improvements of the cross sections for electron scattering in CF_3I is a subject of our future work [64].

3.1. Transport properties for electrons in SF_6 and CF_3I

3.1.1. Mean energy. In figure 3 we show the variation of the mean energy with E/n_0 for electrons in SF_6. The agreement between different rescaling procedures is excellent. This suggests that all rescaling procedures are equally valid for calculation of the mean energy (provided that rescaling is performed carefully). In addition, the BOLSIG+ results agree very well with those calculated by a Monte Carlo simulation technique. For lower E/n_0, the mean energy initially increases with E/n_0, reaching a peak at about 10 Td, and then surprisingly it starts to decrease with E/n_0. The minimum of mean energy occurs at approximately 60 Td. For higher E/n_0 the mean energy monotonically increases with E/n_0. The reduction in the mean energy with increasing E/n_0 has been reported for electrons in Ar [73] and O_2 [74] but in the presence of very strong magnetic fields. In the present work, however, the mean energy is reduced in absence of magnetic field which certainly represents one of the most striking and anomalous effects observed in this study. Moreover, this behavior is contrary to previous experiences in swarm physics as one would expect the mean swarm energy to increase with increasing E/n_0. This is discussed in detail below.

In order to understand the anomalous behavior of the mean energy of electrons in SF_6, in figure 4 we display the electron energy distribution functions for E/n_0 at 10, 27, 59 and 210 Td. Cross sections for some of the more relevant collision processes are also included, as indicated in the graph.
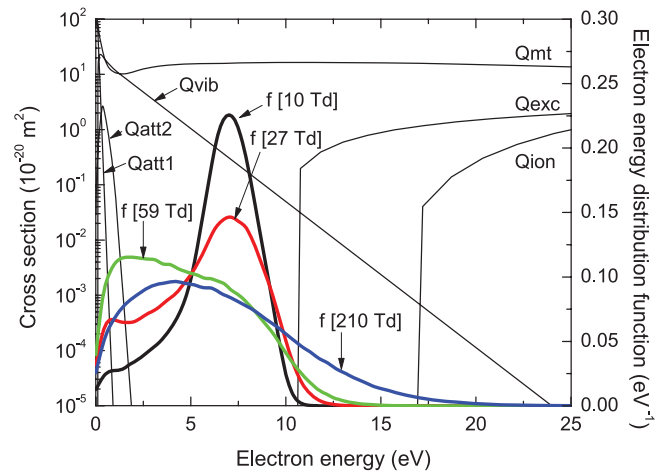
For clarity, the attachment cross sections for the formation of SF_4^-, F_2^- and F^- are omitted in the figure. For E/n_0 of 10 and 27 Td we observe the clear signs of 'hole burning' in the electron energy distribution function (EEDF). This phenomenon has been extensively discussed for electrons in O_2 [75, 76], O_2 mixtures [29, 77] and under conditions leading to the phenomenon of absolute negative electron mobility [27, 60] as well as for electrons in the gas mixtures of $C_2H_2F_4$, iso-C_4H_{10} and SF_6 used in resistive plate chambers in various high energy physics experiments at CERN [6]. For electrons in SF_6, the collision frequency for electron attachment decreases with energy and hence the slower electrons at the trailing edge of the swarm are preferentially attached. As a consequence, the electrons are 'bunched' in the high-energy part of the distribution function which in turn moves the bulk of the distribution function to higher energies. This is the well-known phenomenon of attachment heating which has already been discussed in the literature for model [25, 26] and real gases [6, 29]. In the limit of the lowest E/n_0 we see that due to attachment heating the mean energy attains the unusually high value of almost 5 eV. For a majority of molecular gases, however, the mean energy is significantly reduced for lower E/n_0 due to presence of rotational, vibrational and electronic excitations which have threshold energies over a wide range. As E/n_0 further increases the mean energy is also increased as electrons are accelerated through a larger potential. However, in case of SF_6, for E/n_0 increasing beyond 10 Td the mean energy is reduced. This atypical situation follows from the combined effects of attachment heating and inelastic cooling. From figure 4 we see that for E/n_0 of 27 and 59 Td the electrons from the tail of the corresponding distribution functions have enough energy to undergo the electronic excitation. Whenever an electron undergoes electronic excitations (or ionization) it loses the threshold energy of 9.8 eV (or 15.8 eV in case of ionization) and emerges from the collision with a reduced energy. This in turn diminishes the phenomenon of 'hole burning' in the distribution function by repopulating
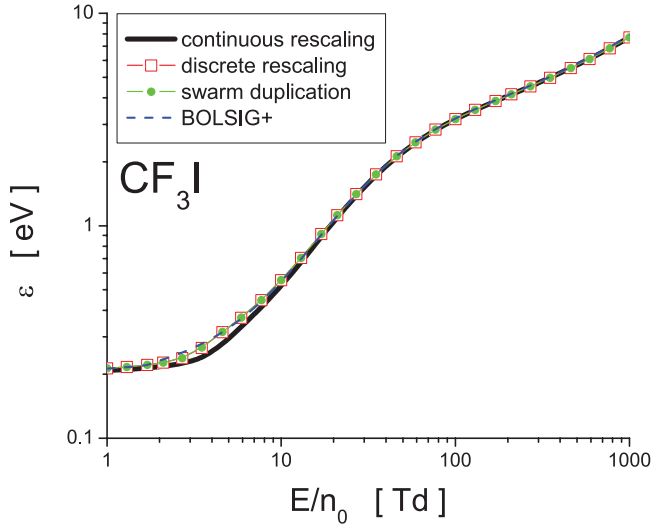
Figure 5. Variation of the mean energy with E/n_0 for electrons in CF_3I. Monte Carlo results using three different techniques for electron compensation are compared with the BOLSIG+ results.

Figure 6. Variation of the drift velocity with E/n_0 for electrons in SF_6. Monte Carlo results using three different techniques for electron number density compensation are compared with the BOLSIG+ results.

the distribution function at the lower energy. The combined effects of attachment heating and inelastic cooling and subsequent redistribution of low-energy electrons are more significant for the energy balance than the energy gain from electric field and losses in other collisions. The vibrational excitation with the threshold of 0.098 eV is of less importance having in mind the actual values of the mean energy. For E/n_0 higher than 60 Td, the dominant part in the energy balance is the energy gain from the electric field while attachment heating and induced phenomena are significantly suppressed. Thus, for E/n_0 higher than 60 Td the mean energy monotonically increases with increasing E/n_0.

The variation of the mean energy with E/n_0 for electrons in CF_3I is shown in figure 5. The agreement between different rescaling procedures is very good. Small deviations between discrete rescaling and swarm duplication from one side and continuous rescaling from the other side are present between approximately 3 and 20 Td. BOLSIG+ slightly overestimates the mean energy only in the limit of the lowest E/n_0. In contrast to mean energy of the electrons in SF_6, the mean energy of the electrons in CF_3I monotonically increases with E/n_0 without signs of anomalous behavior. If we take a careful look, then we can isolate three distinct regions of electron transport in CF_3I as E/n_0 increases. First, there is an initial region where the mean energy raises relatively slowly due to large energy loss of the electrons in low-threshold vibrational excitations. In this region the mean energy of the electrons is well above the thermal energy due to extensive attachment heating. The mean energy is raised much sharper between approximately 5 and 50 Td, indicating that electrons become able to overcome low-threshold vibrational excitations. The following region of slower rise follows from the explicit cooling of other inelastic processes, including electronic excitations and ionization, as these processes are now turned on. In conclusion, the nature of cross sections for electron scattering in CF_3I and their energy dependence as well as their mutual relations do not favor the development of the anomalous behavior of the swarm mean energy.
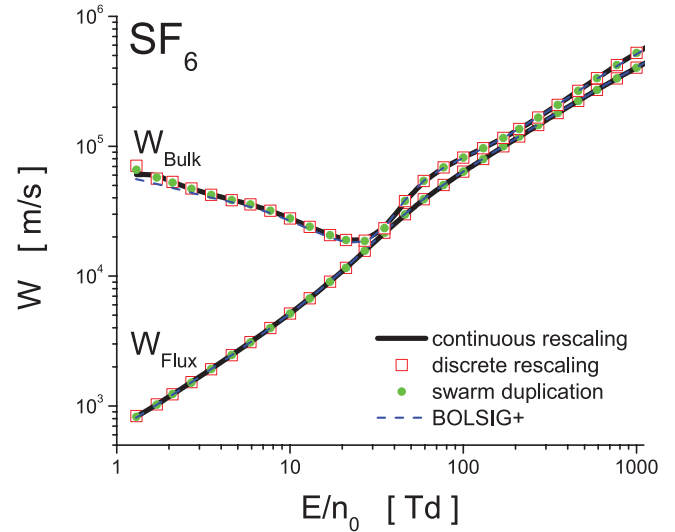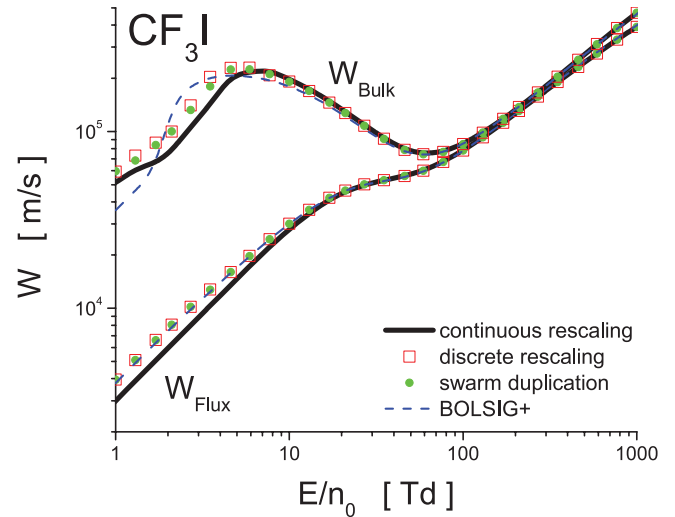

Figure 7. Variation of the drift velocity with E/n_0 for electrons in CF_3I. Monte Carlo results using three different techniques for electron number density compensation are compared with the BOLSIG+ results.

3.1.2. Drift velocity. In figures 6 and 7 we show variation of the bulk and flux drift velocity with E/n_0 for electrons in SF_6 and CF_3I, respectively. For electrons in SF_6 the agreement between different rescaling procedures for electron compensation is excellent for both the bulk and flux drift velocity over the entire E/n_0 range considered in this work. The BOLSIG+ bulk results slightly underestimate the corresponding bulk Monte Carlo results in the limit of the lowest E/n_0. For electrons in CF_3I, the agreement among different rescaling procedures for electron compensation is also good except for lower E/n_0 where the continuous rescaling gives somewhat lower results than other techniques.

For both SF_6 and CF_3I, we see that the bulk dominates the flux drift velocity over the entire E/n_0 range considered in this work. For lower E/n_0 this is a consequence of a very intense
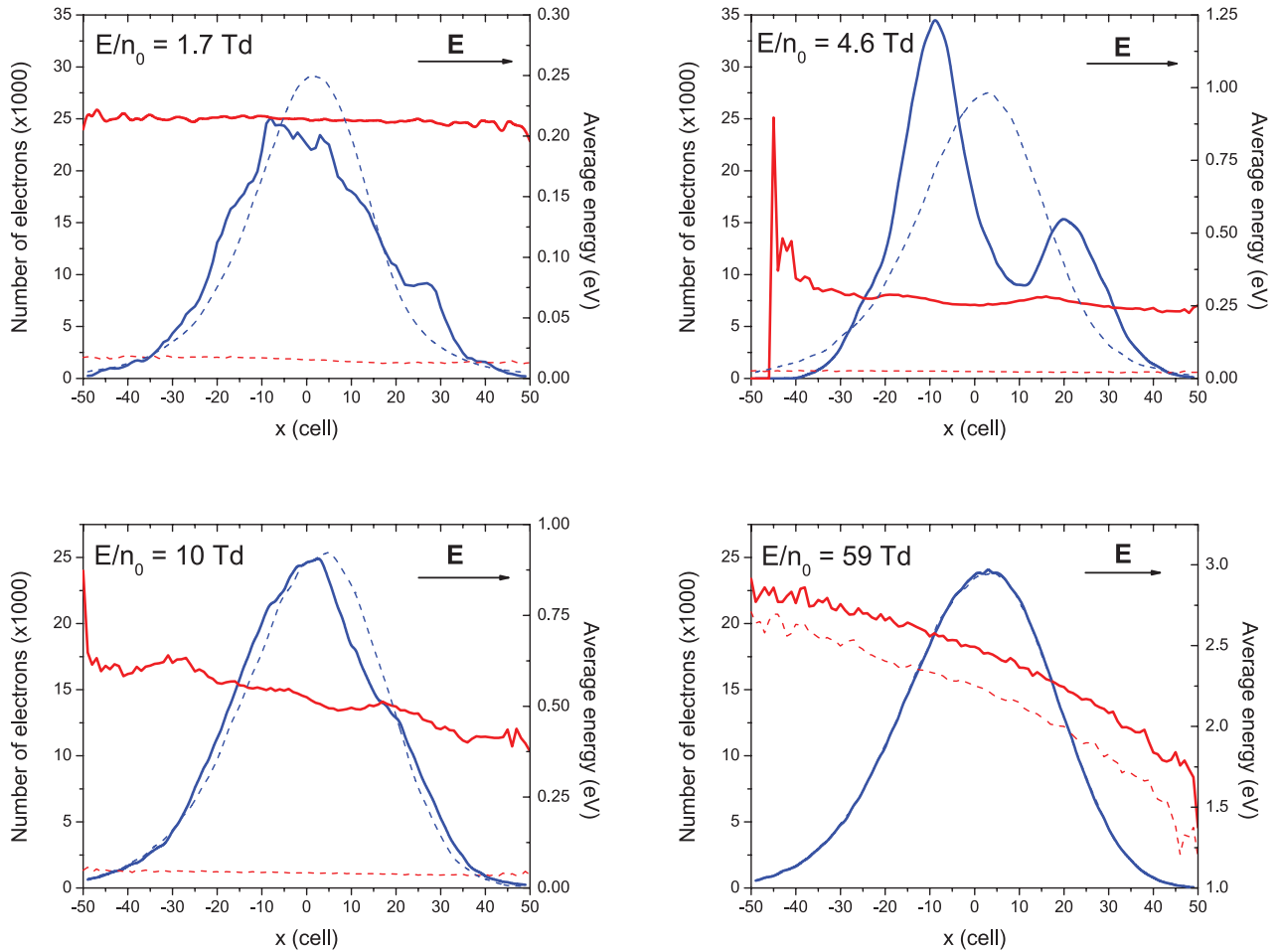
Figure 8. Spatial profile of electrons (blue curves) and spatially resolved averaged energy (red curves) at four different E/n_0 in CF_3I. Full lines denote the results when electron attachment is treated as a non-conservative process, while the dashed lines represent our results when electron attachment is treated as a conservative inelastic process with zero energy loss.

attachment heating while for higher E/n_0 this follows from the explicit effects of ionization. As mentioned above, when transport processes are greatly affected by attachment heating the slower electrons at the back of the swarm are consumed at a faster rate than those at the front of the swarm. Thus, in the case of drift, the electron attachment acts to push the centre of mass forward, increasing the bulk drift velocity above its flux component. For higher E/n_0 when ionization takes place, the ionization rate is higher for faster electrons at the front of the swarm than for slower electrons at the back of the swarm. As a result, electrons are preferentially created at the front of the swarm which results in a shift in the centre of mass. Of course, this physical picture is valid if collision frequency for ionization is an increasing function of electron energy. This is true for electrons in both SF_6 and CF_3I. The explicit effects of electron attachment are much stronger than those induced by ionization. When ionization is dominant non-conservative process, the differences between two sets of data are within 30% for both gases. When attachment dominates ionization, however, then the discrepancy between two sets of data might be almost two orders of magnitude, as for electrons in SF_6 in the limit of the lowest E/n_0.

The flux drift velocity is a monotonically increasing function of E/n_0 while the bulk component behaves in a qualitatively

different fashion. A prominent feature of electron drift in SF_6 and CF_3I is the presence of a very strong NDC in the profile of the bulk drift velocity. On the other hand, a decrease in the flux drift velocity with increasing E/n_0 has not been observed. Such behavior is similar of the recently observed NDC effect for positrons in molecular gases [78, 79] where Positronium (Ps) formation plays the role of electron attachment.

In order to provide physical arguments for an explanation of NDC in the bulk drift velocity, in figure 8 we show the spatial profile and spatially resolved average energy of electrons in CF_3I. Calculations are performed for four different values of E/n_0 as indicated in the graph. The direction of the applied electric field is also shown. Two fundamentally different scenarios are discussed: (1) the electron attachment is treated as a conservative inelastic process with zero energy loss, and (2) the electron attachment is treated regularly, as a true non-conservative process. The first scenario is made with the aim of illustrating that NDC is not primarily caused by the shape of cross section for attachment but rather by the synergism of explicit and the implicit effects of the number changing nature of the process on electron transport. Sampling of spatially resolved data in our Monte Carlo simulations is performed using the continuous rescaling. The continuous rescaling produces smoother curves and in most cases it is more reliable

as compared to the discrete rescaling and swarm duplication. The results of the first scenario are presented by dashed lines while the second scenario where electron attachment is treated as a true non-conservative process, is represented by full lines.

When electron attachment is treated as a conservative inelastic process, the spatial profile of electrons has a well defined Gaussian profile with a small bias induced by the effect of electric field. The non-symmetrical feature of spatial profile is further enhanced with increasing E/n_0. While for lower E/n_0 the spatial variation of the average energy is relatively low, for higher E/n_0, e.g. for E/n_0 of 59 Td the slope of the average energy is quite high, indicating that the electron swarm energy distribution is normally spatially anisotropic. It is important to note that there are no imprinted oscillations in the spatial profile of the electrons or in the profile of the average energy which is a clear sign that the collisional energy loss is governed essentially by 'continuous' energy loss processes [32].

When electron attachment is treated as a true non-conservative process, the spatial profile and the average energy of electrons are drastically changed. For all considered reduced electric fields spatially resolved average energy is greater as compared to the case when electron attachment is treated as a conservative inelastic process. For E/n_0 of 1.7 and 4.6 Td the spatial profiles of electrons depart from a typical Gaussian shape. For 1.7 Td there is very little spatial variation in the average energy along the swarm. When E/n_0 = 4.6 Td, however, the spatial profile is skewed, asymmetric and shifted to the left. This shift corresponds approximately to the difference between bulk drift velocities in the two scenarios. We observe that the trailing edge of the swarm is dramatically cut off while the average energy remains essentially unaltered. At the leading edge of the swarm, however, we observe a sharp jump in the average energy which is followed by a sharp drop-off. In addition, the height of spatial profile is significantly increased in comparison to the Gaussian profile of the swarm when electron attachment is treated as a conservative inelastic process. For higher E/n_0 the signs of explicit effects of electron attachment are still present but are significantly reduced. For E/n_0 = 10 Td the spatial dependence of the average energy is almost linear with a small jump at the leading edge of the swarm. Comparing trailing edges of the swarms at 4.6 and 10 Td we see that for higher electric field the spatial profile of electrons is by far less cut off. This suggests that for increasing E/n_0 there are fewer and fewer electrons that are consumed by electron attachment. Finally, for E/n_0 = 59 Td the spatial profile of electrons is exactly the same as the profile obtained under conditions when electron attachment is treated as a conservative inelastic process.

The spatially resolved attachment rates are displayed in figure 9 and are calculated under the same conditions as for the spatial profile of the electrons and spatially averaged energy. We see that the attachment rate peaks at the trailing edge of the swarm where the average energy of the electrons is lower. Attachment loss of these lower energy electrons causes a forward shift to the swarm centre of mass, with a corresponding increase in the bulk drift velocity. For increasing E/n_0, the spatially resolved attachment rate coefficients are reduced and linearly decrease from the trailing edge towards the leading
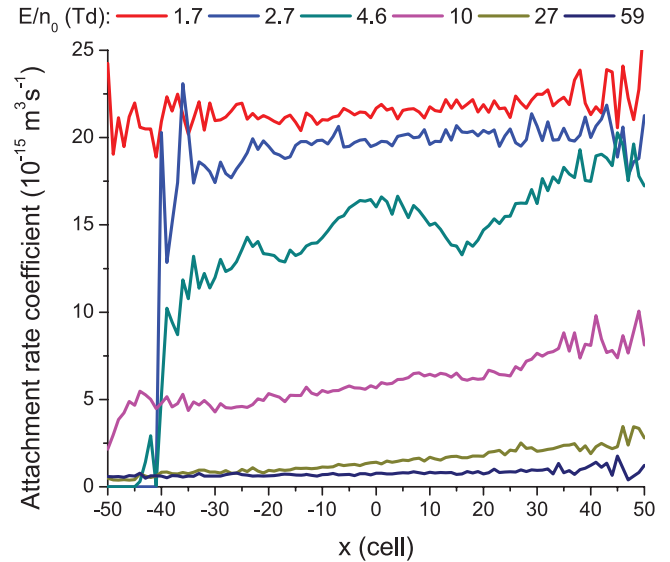

Figure 9. Spatially resolved attachment rate coefficient for a range of E/n_0 as indicated on the graph. Calculations are performed for electrons in CF_3I.

part of the swarm. At the same time the electrons at the leading edge of the swarm have enough energy to undergo ionization. This suggests much less explicit influence of electron attachment on the electron swarm behavior. As a consequence, NDC is removed from the profile of the bulk drift velocity.

In addition to the explicit effects of electron attachment there are implicit effects due to energy specific loss of electrons, which changes the swarm energy distribution as a whole, and thus indirectly changes the swarm flux. Generally speaking, it is not possible to separate the explicit from implicit effects, except by analysis with and without the electron attachment. Using these facts as motivational factors, in figure 10 we show the electron energy distribution functions for the same four values of E/n_0 considered above. The electron energy distribution functions are calculated when electron attachment is treated as a true non-conservative process (full line) and under conditions when electron attachment is assumed to be a conservative inelastic process (dashed line). As for electrons in SF_6, we observe a 'hole burning' effect in the energy distribution function which is certainly one of the most illustrative examples of the implicit effects. Likewise, we see that the high energy tail of the distribution function falls off very slowly even slower than for Maxwellian. Under these circumstances, when the actual distribution function significantly deviates from a Maxwellian, the numerical schemes for solving the Boltzmann equation in the framework of moment methods usually fail. Indeed, for E/n_0 less than approximately 20 Td we have found a sudden deterioration in the convergence of the transport coefficients which was most pronounced for the bulk properties. Furthermore, we see that the 'hole burning' effect is not present when electron attachment is treated as a conservative inelastic process. The lower energy part of the distribution function is well populated while high energy part falls off rapidly. For increasing E/n_0 and when electron attachment is treated as a true non-conservative process, the effect of hole burning is reduced markedly while
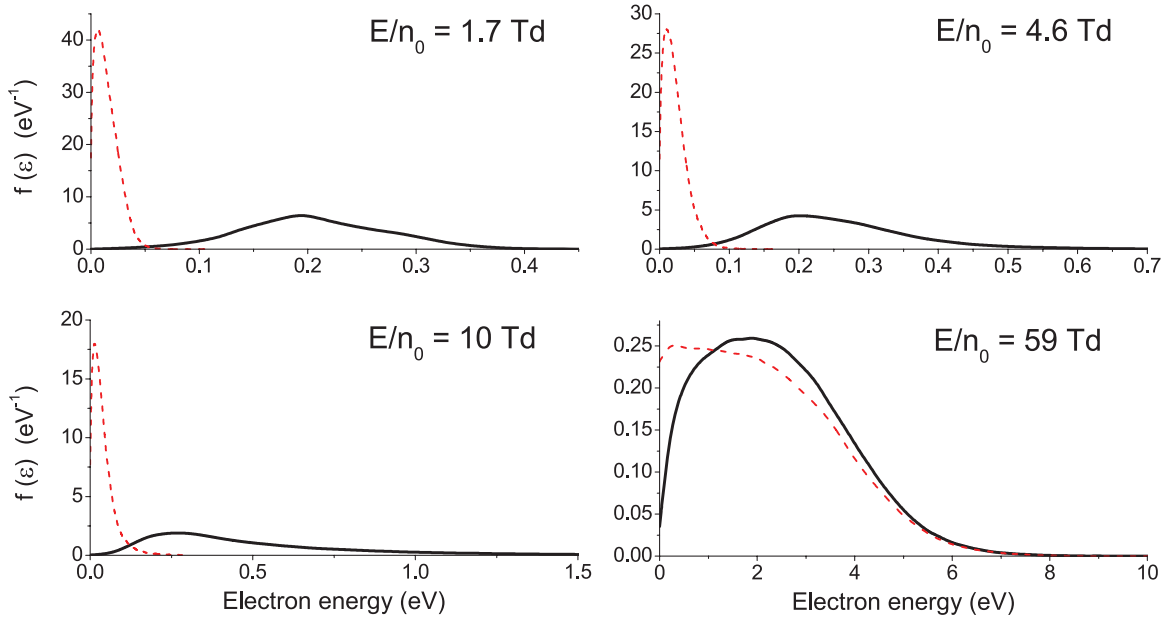
Figure 10. Energy distribution functions for four different E/n_0 for electrons in CF_3I. Black lines denote the results when electron attachment is treated as non-conservative process while dashed red lines represent our results when electron attachment is treated as a conservative inelastic process.

the high energy part of the distribution function coincides with the corresponding one when electron attachment is treated as a conservative inelastic process.

Before embarking on a discussion of our results for diffusion coefficients, one particular point deserves more mention. NDC phenomenon in the bulk drift velocity has not been experimentally verified, neither for SF_6 nor for CF_3I. On the other hand, as we have already seen, the two entirely different theoretical techniques for calculating the drift velocity predict the existence of the phenomenon. Thus, it would be very useful to extend the recent measurements of the drift velocity in both SF_6 and CF_3I to lower E/n_0 with the aim of confirming the existence of NDC. On the other hand, such measurements are most likely very difficult, even impossible due to rapid losses of electron density in experiment.

3.1.3. Diffusion coefficients. Variations of the longitudinal and transverse diffusion coefficients with E/n_0 for electrons in SF_6 are displayed in figures 11 and 12, respectively. From the E/n_0-profiles of the longitudinal and transverse flux diffusion coefficients, we observe that different rescaling procedures for Monte Carlo simulations agree very well. For the bulk components, the agreement is also very good for intermediate and higher E/n_0 and only in the limit of the lowest E/n_0 the agreement is deteriorated. Over the range of E/n_0 considered we see that there is an excellent agreement between continuous and discrete rescaling.

Comparing Monte Carlo and BOLSIG+ results, the deviations are clearly evident. They might be attributed to the inaccuracy of the two term approximation of the Boltzmann equation which is always considerably higher for diffusion than for the drift velocity. For higher E/n_0, inelastic collisions are significant and the distribution function deviates substantially from isotropy in velocity space. In these circumstances,
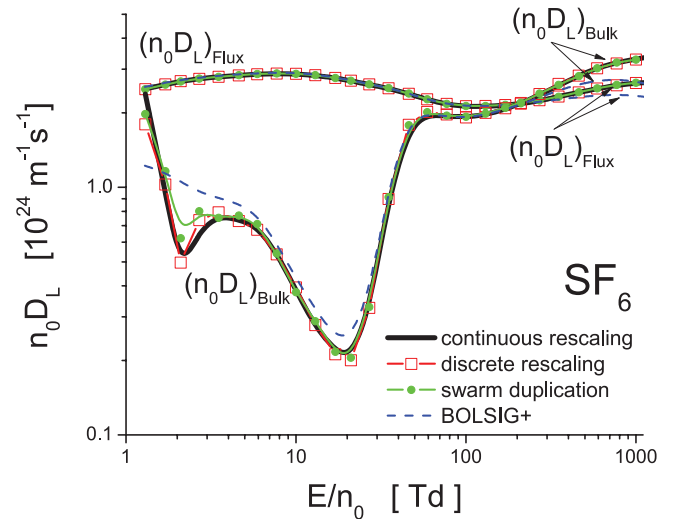
Figure 11. Variation of the longitudinal diffusion coefficient with E/n_0 for electrons in SF_6. Monte Carlo results using three different techniques for electron number density compensation are compared with the BOLSIG+ results.

the two term approximation of the Boltzmann equation fails and multi-term Boltzmann equation analysis is required. For lower E/n_0, however, the role of inelastic collisions is of less significance, but still discrepancies between the BOLSIG+ and Monte Carlo results are clearly evident, particularly for the longitudinal diffusion coefficient. This suggests that further analyses of the impact of electron attachment on the distribution function in velocity space of electrons in SF_6 would be very useful.

From the profiles of the longitudinal diffusion coefficient at lower and intermediate values of E/n_0 we observe the following interesting points. In contrast to drift velocity (and transverse diffusion coefficient shown in figure 12) we see
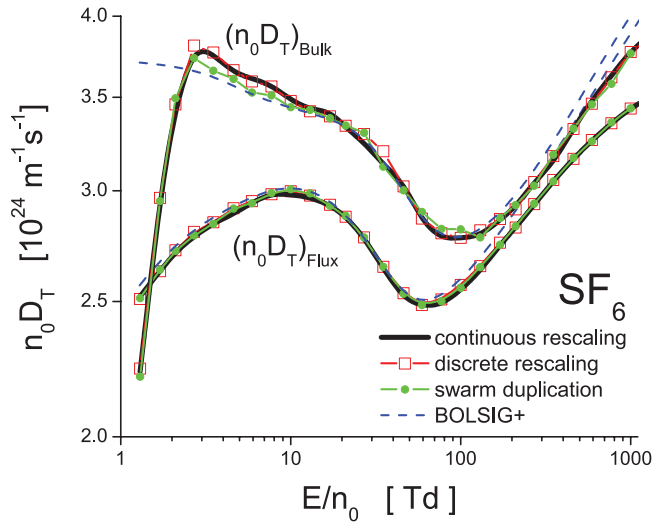
Figure 12. Variation of the transverse diffusion coefficient with E/n_0 for electrons in SF_6. Monte Carlo results using three different techniques for electron number density compensation are compared with the BOLSIG+ results.

Figure 13. Variation of the longitudinal diffusion coefficient with E/n_0 for electrons in CF_3I. Monte Carlo results using three different techniques for electron number density compensation are compared with the BOLSIG+ results.

that the bulk diffusion coefficient is smaller than the corresponding flux component. This indicates that the decrease in electron numbers due to attachment weakens diffusion along the field direction. As already discussed, attachment loss of electrons from the trailing edge of the swarm causes a forward shift to the swarm centre of mass, with the corresponding increases in the bulk drift velocity and mean energy. The same effects result in an enhancement of the flux longitudinal diffusion. It should be noted that when attachment heating takes place, the opposite situation (bulk is higher than flux) has also been reported [25]. This is a clear sign that the energy dependence of the cross sections for electron attachment is of primary importance for the analysis of these phenomena. For higher E/n_0, however, where the contribution of ionization becomes important, we observe that the diffusion is enhanced along the field direction, e.g. the bulk dominates the flux. This is always the case if the collision frequency for ionization is an increasing function of the electron energy, independently of the gaseous medium considered.

From the profiles of the transverse diffusion coefficient the bulk values are greater than the corresponding flux values over the range of E/n_0 considered in this work. Only in the limit of the lowest E/n_0 the opposite situation holds: the flux is greater than the bulk. In contrast to the longitudinal diffusion, spreading along the transverse directions is entirely determined by the thermal motion of the electrons. The flux of the Brownian motion through a transverse plane is proportional to the speed of the electrons passing through the same plane. Therefore, the higher energy electrons contribute the most to the transversal expansion, so attachment heating enhances transverse bulk diffusion coefficient.

Figures 13 and 14 show the variations of the longitudinal and transverse diffusion coefficients with E/n_0 for electrons in CF_3I, respectively. From the E/n_0-profiles of the bulk diffusion coefficients we observe an excellent agreement between different rescaling procedures for $E/n_0 > 10$ Td. The same applies for the flux component of the longitudinal diffusion.
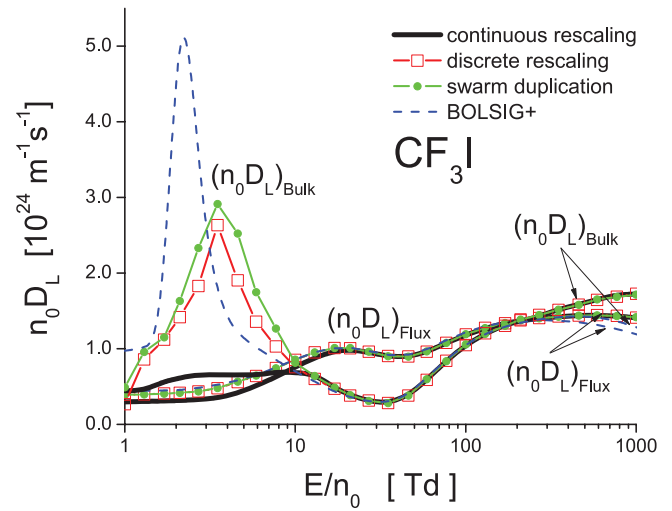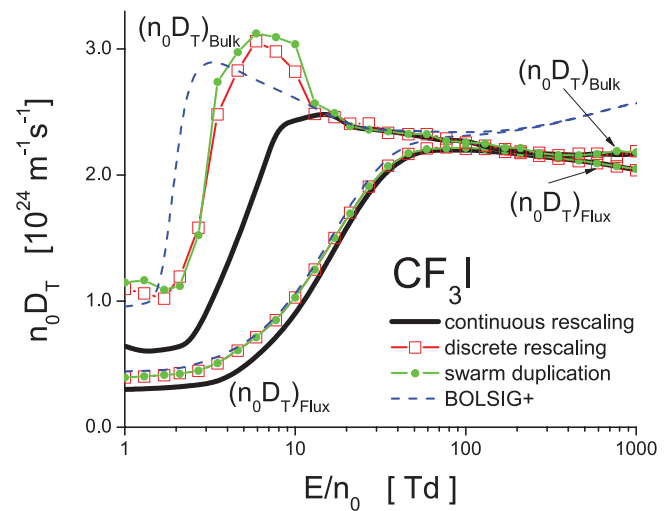

Figure 14. Variation of the transverse diffusion coefficient with E/n_0 for electrons in CF_3I. Monte Carlo results using three different techniques for electron number density compensation are compared with the BOLSIG+ results.

For $E/n_0 < 10$ Td the agreement is poor for bulk components, particularly between the continuous rescaling from one side and discrete rescaling and/or swarm duplication from the other side. The agreement is better for the flux components.

Comparing Monte Carlo and BOLSIG + results, we see that the maximum error in the two term approximation, for both diffusion coefficients occurs at lower and higher E/n_0. In contrast to SF_6, CF_3I has rapidly increasing cross sections for vibrational excitations in the same energy region where the cross section of momentum transfer in elastic collisions decreases with the electron energy. Under these conditions, the energy transfer is increased and collisions no longer have the effect of randomizing the direction of electron motion. As a consequence, the distribution function deviates significantly from isotropy in velocity space and two term approximation of the Boltzmann equation fails.

When considering the differences between the bulk and flux values of diffusion coefficients the situation is much more complex comparing to SF_6. From the E/n_0-profiles of the longitudinal diffusion coefficient one can immediately see that for lower and higher E/n_0, the bulk is greater than the corresponding flux values while at intermediate E/n_0 the opposite situation holds: the flux is greater than the bulk. The behavior of the transverse diffusion coefficient is less complex, as over the entire of E/n_0 the bulk is greater that the corresponding flux values.

As we have demonstrated, in contrast to drift velocity the behavior and differences between the bulk and flux diffusion coefficients is somewhat harder to interpret. This follows from the complexity of factors which contribute to or influence the diffusion coefficients. The two most important factors are the following: (a) the thermal anisotropy effect resulting from different random electron motion in different directions; and (b) the anisotropy induced by the electric field resulting from the spatial variation of the average energy and local average velocities throughout the swarm which act so as to either inhibit or enhance diffusion. Additional factors include the effects of collisions, energy-dependent total collision frequency, and presence of non-conservative collisions. Couplings of these individual factors are always present and hence sometimes it is hard to elucidate even the basic trends in the behavior of diffusion coefficients. In particular, to understand the effects of electron attachment on diffusion coefficients and associated differences between bulk and flux components, the variation in the diffusive energy tensor associated with the second-order spatial variation in the average energy with E/n_0 should be studied. This remains the program of our future work.

3.1.4. Rate coefficients. In figure 15 we show the variation of steady-state Townsend ionization and attachment coefficients with E/n_0 for electrons in SF_6. The agreement between different rescaling procedures and BOLSIG+ code is very good. It is important to note that the agreement is very good, even in the limit of the lowest E/n_0 considered in this work where the electron energy distribution function is greatly affected by electron attachment. The curves show expected increase in α/n_0 and expected decrease in η/n_0, with increasing E/n_0. The value obtained for critical electric field is 361 Td which is in excellent agreement with experimental measurements of Aschwanden [80].

In figure 16 we show variation of the steady-state Townsend ionization and attachment coefficients with E/n_0 for electrons in CF_3I. The agreement between different rescaling procedure and BOLSIG+ code is excellent for ionization coefficient. From the E/n_0-profile of attachment coefficient, we see that the continuous rescaling slightly overestimates the remaining scenarios of computation. The critical electric field for CF_3I is higher than for SF_6. This fact has been recently used as a motivational factor for a new wave of studies related to the insulation characteristics of pure CF_3I and its mixture with other gases, in the light of the present search for suitable alternatives to SF_6. The value obtained for critical electric field in our calculations is 440 Td which is in close agreement with experimental measurements under steady-state [63, 81]
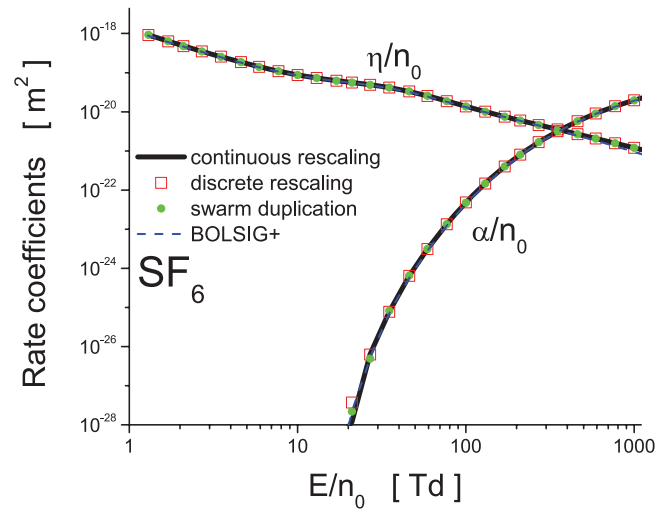

Figure 15. Variation of the rate coefficients with E/n_0 for electrons in SF_6. Monte Carlo results using three different techniques for electron number density compensation are compared with the BOLSIG+ results.
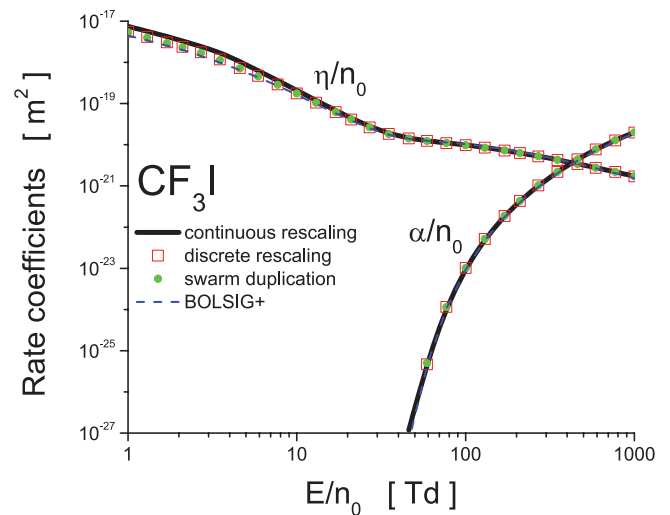

Figure 16. Variation of the rate coefficients with E/n_0 for electrons in CF_3I. Monte Carlo results using three different techniques for electron number density compensation are compared with the BOLSIG+ results.

and pulsed-Townsend [82] conditions, as well as with recent calculations performed by Kawaguchi *et al* [58] and Deng and Xiao [52].

3.2. Recommendations for implementation

In this section, we discuss the main features of the rescaling procedures and we give recommendations on how to use them in future Monte Carlo codes. Based on our experience achieved by simulating the electron transport in SF_6, CF_3I and other attaching gases, we have observed that if correctly implemented the procedures generally agree very well. The agreement between different rescaling procedures is always better for the flux than for the bulk properties. We found a poor agreement for the bulk diffusion coefficients, particularly for the lower E/n_0 while for mean energy, drift velocity and

rate coefficients the agreement is reasonably good. For lower E/n_0 when the distribution function is extremely affected by electron attachment, the agreement between swarm duplication and discrete rescaling is also good. This is not surprising as these two techniques are essentially the same.

In terms of implementation, the Monte Carlo codes can be relatively easily upgraded with the procedures for swarm duplication and/or discrete rescaling. Special attention during the implementation of these procedures should be given to the choice of the length of time steps after which the cloning of the electrons is done. If the length of this time step appears to be too long as compared to the time constant which corresponds to the attachment collision frequency, then the distribution function could be disturbed due to a low statistical accuracy. In other words, depleting certain pockets of the EEDF means that those cannot be recovered at all. On the other hand, if the length of the time steps is too small, the speed of simulation could be significantly reduced. The implementation of the continuous rescaling procedure is somewhat more complicated.

Which procedure is, the most flexible? It is difficult to answer this question because the answer depends on the criteria of flexibility. If the criterion for flexibility is associated with the need for *a priori* estimates which are necessary for setting the simulation, then the technique of continuous rescaling is certainly the most flexible. Once implemented, and thoroughly tested this procedure allows the analysis of electron transport in strongly attaching gases regardless of the energy dependence of the cross section for electron attachment. On the other hand, for the analysis of electron transport in weakly attaching gases, the discrete rescaling is very convenient because it is easier for implementation into the codes and less demanding in terms of the CPU time.

In terms of reliability and accuracy, the comparison of the results obtained for various transport properties using the rescaling procedures for Monte Carlo simulations and the Boltzmann equation codes shows that the rescaling procedures described herein are highly reliable. It should be noted that only the multi term codes for solving the Boltzmann equation may offer the final answer. Restrictions of the TTA for solving the Boltzmann equation were demonstrated many times in the past [7, 31], especially when it comes to the calculations of diffusion coefficients. Testing and benchmarking against other Boltzmann solvers are currently ongoing.

3.3. Experiments in strongly attaching gases: difficulties induced by non-hydrodynamic effects

It must be noted at this point that most processes scale with pressure, so the independence on pressure would be maintained and so would be the equilibration of EEDFs affected by excessive attachment. Most of the processes fall into that category. These processes are best visualized in an infinite uniform environment. Standard swarm experiments are built in such a way that boundaries are not felt over appreciable volume and thus, they mimic hydrodynamic conditions very well. However, going to high E/n_0 requires operating at lower pressures and there the boundaries may be felt over a larger

portion of the volume. In general, whenever boundaries of any kind are introduced selective losses resulting in very different mean free paths of different groups of particles may lead to selective losses. The resulting holes in the distribution may be filled in by collisions, so when considerable selective losses are introduced results may become the pressure dependent (even when the cross section is not dependent on the pressure). The same is true for temporal limitations. For example, if the frequency of collisions is small, so that the mean free time is comparable to the time required to accelerate to energies where cross sections decrease with the electron energy, the runaway effects may be developed. Similar effects may be created due to temporal variations of the field that do not allow full equilibration. The pressure dependence of the results will develop under such conditions (and so would the dependence on the size of the vessel). The development of a non-hydrodynamic theory for solving the Boiltzmann equation is difficult and the best solution is a Monte Carlo simulation technique. For that reason, rescaling procedures are essential in modeling of the non-hydrodynamic (non-local) development of charged particle ensembles.

Experiments in gases with a very large attachment (typically at low energies) may be difficult to carry out due to a large loss of electrons. The fact that experiments in diluted gas mixtures of such gases may be feasible, means that cross sections may be obtained. Yet, one should be aware of two main problems. Even in such mixtures and depending on the size of the experiment, attachment may be high enough to induce depletion of the distribution function thus making results pressure dependent or abundance dependent. If one wants to extend the calculations to pure attaching gas for smaller vessels and pressures, one needs to be aware that only techniques that take full non-hydrodynamic description of the swarm development, are required. Similar effects have been observed in gases always associated with strong attachment such as oxygen [76] and water vapor [83]. In any case, the critical effects that include NDC for bulk drift velocity as a result of excessive loss of electrons in attachment can be observed in gases like SF_6 and CF_3I based on hydrodynamic expansion and even based on the two term theory provided that theory takes into account the explicit and implicit non-conservative effects of the attachment.

4. Conclusion

In this paper, we have presented the development, implementation and benchmarking of the rescaling procedures for Monte Carlo simulations of electron transport in strongly attaching gases. The capabilities of the rescaling procedures have been described by systematic investigation of the influence of electron attachment on transport coefficients of electrons in SF_6 and CF_3I. Among many important points, the key results arising from this paper are:

(1) We have presented two distinctively different methods for compensation of electrons in Monte Carlo simulations of electron transport in strongly attaching gases, e.g. the discrete and the continuous procedures. In order to avoid the

somewhat arbitrary choice of the fictitious ionization rate, we have extended the continuous rescaling procedure, initially developed by Li *et al* [61], by introducing a time-dependent collision frequency for the fictitious ionization process.

(2) One of the initial motivating factors for this work was to provide accurate data for transport properties of electrons in SF_6 and CF_3I which are required as input in fluid models of plasma discharges. In this work, for the first time, we have calculated the mean energy, drift velocity and diffusion coefficients as well as rate coefficients for lower E/n_0 for electrons in SF_6 and CF_3I.

(3) We have demonstrated the differences which can exist between the bulk and flux transport coefficients and the origin of these differences. Our study has shown that the flux and bulk transport properties can vary substantially from one another, particularly in the presence of intensive attachment heating. Thus, one of the key messages of this work is that theories which approximate the bulk transport coefficients by the flux are problematic and generally wrong.

(4) We have demonstrated and interpreted physically the phenomenon of the anomalous behavior of the mean energy of electrons in SF_6, in which the mean energy is reduced for increasing E/n_0. The phenomenon was associated with the interplay between attachment heating an inelastic cooling. The same phenomenon has not been observed for electrons in CF_3I indicating that the role of the cross sections is vital.

(5) We have explained and identified a region of NDC in the bulk drift velocity, originating from the explicit influence of electron attachment. The phenomenon has been explained using the concept of spatially-resolved transport properties along the swarm.

(6) The publicly available two term Boltzmann solver, BOLSIG+, has been shown to be accurate for calculations of mean energy, drift velocity and rate coefficients for electrons in SF_6 and CF_3I. On the other hand, significant differences between our Monte Carlo and BOLSIG+ results for diffusion coefficients have been observed, particularly for electrons in CF_3I in the limit of the lowest E/n_0 considered in this work.

Various rescaling procedures for Monte Carlo simulations described in this work have recently been applied to modeling of electron transport in strongly attaching gases under the influence of time-dependent electric and magnetic fields. It will be challenging to investigate the synergism of magnetic fields and electron attachment in radio-frequency plasmas. Likewise, the remaining step to be taken, is to apply the rescaling procedures presented in this work to investigate the influence of positronium formation on the positron transport properties. This remains the focus of our future investigation. Finally, we hope that this paper will stimulate further discussion on methods of correct representation of the effects induced by electron attachment on transport properties of electrons in strongly attaching gases.

References

[1] Christophorou L G and Olthoff J K 2004 *Fundamental Electron Interactions with Plasma Processing Gases* (New York: Springer)
[2] Makabe T and Petrović Z Lj 2014 *Plasma Electronics: Applications in Microelectronic Device Fabrication* (New York: CRC Press)
[3] Christophorou L G and Pinnaduwage L A 1990 *IEEE Trans. Electr. Insul.* **25** 55
[4] Rolandi L, Riegler W and Blum W 2008 *Particle Detection with Drift Chambers* (Berlin: Springer)
[5] Sauli F 2014 *Gaseous Radiation Detectors* (Cambridge: Cambridge University Press)
[6] Bošnjaković D, Petrović Z Lj, White R D and Dujko S 2014 *J. Phys. D: Appl. Phys.* **47** 435203
[7] Petrović Z Lj, Dujko S, Marić D, Malović G, Nikitović Ž, Šašić O, Jovanović J, Stojanović V and Radmilović-Radjenović M 2009 *J. Phys. D: Appl. Phys.* **42** 194002
[8] Petrović Z Lj, Šuvakov M, Nikitović Ž, Dujko S, Šašić O, Jovanović J, Malović G and Stojanović V 2007 *Plasma Sources Sci. Technol.* **16** S1
[9] Huxley L G H and Crompton R W 1974 *The Drift and Diffusion of Electrons in Gases* (New York: Wiley)
[10] Christophorou L G, McCorkle D L and Anderson V E 1971 *J. Phys. B: At. Mol. Phys.* **4** 1163
[11] Phelps A V and van Brunt R J 1988 *J. Appl. Phys.* **64** 4269
[12] Christophorou L G and Olthoff J K 2000 *J. Phys. Chem. Ref. Data* **29** 267
[13] Jarvis G K, Kennedy R A and Mayhew C A 2001 *Int. J. Mass Spectrom.* **205** 253
[14] Dahl D A and Franck C M 2013 *J. Phys. D: Appl. Phys.* **46** 445202
[15] Rabie M, Haefliger P, Chachereau A and Franck C M 2015 *J. Phys. D: Appl. Phys.* **48** 075201
[16] Hunter S R and Christophorou L G 1984 *J. Chem. Phys.* **80** 6150
[17] Novak J P and Frechette M F 1988 *J. Appl. Phys.* **63** 2570
[18] Hunter S R, Carter J G and Christophorou L G 1988 *Phys. Rev.* A **38** 58
[19] Petrović Z Lj, Wang W C and Lee L C 1988 *J. Appl. Phys.* **64** 1625
[20] Petrović Z Lj, Wang W C, Suto M, Han J C and Lee L C 1990 *J. Appl. Phys.* **67** 675
[21] Raju G G 2006 *Gaseous Electronics: Theory and Practice* (New York: CRC Press)
[22] Raju G G 2012 *Gaseous Electronics: Tables, Atoms, and Molecules* (New York: CRC Press)
[23] Cavalleri G 1969 *Phys. Rev.* **179** 186
[24] Petrović Z Lj and Crompton R W 1985 *J. Phys. B: At. Mol. Phys.* **17** 2777
[25] Ness K F and Robson R E 1986 *Phys. Rev.* A **34** 2185
[26] Nolan A M, Brennan M J, Ness K F and Wedding A B 1997 *J. Phys. D: Appl. Phys.* **30** 2865
[27] Dujko S, Raspopović Z M, Petrović Z Lj and Makabe T 2003 *IEEE Trans. Plasma Sci.* **31** 711
[28] White R D, Robson R E and Ness K F 1999 *Phys. Rev.* E **60** 7457
[29] Dujko S, Ebert U, White R D and Petrović Z Lj 2011 *Japan J. Appl. Phys.* **50** 08JC01
[30] Robson R E 1991 *Aust. J. Phys.* **44** 685

[31] White R D, Robson R E, Dujko S, Nicoletopoulos P and Li B 2009 *J. Phys. D: Appl. Phys.* **42** 194001

[32] Dujko S, White R D, Raspopović Z M and Petrović Z Lj 2012 *Nucl. Instrum. Methods Phys. Res.* B **279** 84

[33] Robson R E, White R D and Petrović Z Lj 2005 *Rev. Mod. Phys.* **77** 1303

[34] Dujko S, Markosyan A H, White R D and Ebert U 2013 *J. Phys. D: Appl. Phys.* **46** 475202

[35] Markosyan A H, Dujko S and Ebert U 2013 *J. Phys. D: Appl. Phys.* **46** 475203

[36] Bletzinger P 1990 *J. Appl. Phys.* **67** 130

[37] Stoffels E, Stoffelsd W, Venderm D, Haverlaag M, Kroesen G M W and de Hoog F J 1995 *Contrib. Plasma Phys.* **35** 331

[38] Chabert P and Sheridan T E 2000 *J. Phys. D: Appl. Phys.* **33** 1854

[39] Kono A 2002 *Appl. Surf. Sci.* **192** 115

[40] Zhao S X, Gao F, Wang Y N and Bogaerts A 2012 *Plasma Sources Sci. Technol.* **21** 025008

[41] Chabert P, Lichtenberg A J, Lieberman M A and Marakhtanov A M 2003 *J. Appl. Phys.* **94** 831

[42] Robson R E 1986 *J. Chem. Phys.* **85** 4486

[43] Vrhovac S B and Petrović Z Lj 1996 *Phys. Rev.* E **53** 4012

[44] Yousfi M, Segur P and Vassiliadis T 1985 *J. Phys. D: Appl. Phys.* **18** 359

[45] Itoh H, Miurat Y, Ikuta N, Nakao Y and Tagashira H 1988 *J. Phys. D: Appl. Phys.* **21** 922

[46] Itoh H, Kawaguchi M, Satoh K, Miura Y, Nakano Y and Tagashira H 1990 *J. Phys. D: Appl. Phys.* **23** 299

[47] Itoh H, Matsumura T, Satoh K, Date H, Nakano Y and Tagashira H 1993 *J. Phys. D: Appl. Phys.* **26** 1975

[48] Frechette M F and Novak J P 1987 *J. Phys. D: Appl. Phys.* **20** 438

[49] Pinheiro M J and Loureiro J 2002 *J. Phys. D: Appl. Phys.* **35** 3077

[50] Tezcan S S, Akcayol M A, Ozerdem O C and Dincer M S 2010 *IEEE Trans. Plasma Sci.* **38** 2332

[51] Li X, Zhao H, Wu J and Jia S 2013 *J. Phys. D: Appl. Phys.* **46** 345203

[52] Deng Y and Xiao D 2014 *Japan J. Appl. Phys.* **53** 096201

[53] Dujko S, White R D, Petrović Z Lj and Robson R E 2010 *Phys. Rev.* E **81** 046403

[54] Yousfi M, Hennad A and Alkaa A 1994 *Phys. Rev.* E **49** 3264

[55] Dincer M S and Gaju G R 1983 *J. Appl. Phys.* **54** 6311

[56] Dincer M S, Ozerdem O C and Bektas S 2007 *IEEE Trans. Plasma Sci.* **35** 1210

[57] Satoh K, Itoh H, Nakano Y and Tagashira H 1988 *J. Phys. D: Appl. Phys.* **21** 931

[58] Kawaguchi S, Satoh K and Itoh H 2014 *Eur. Phys. J.* D **68** 100

[59] Rapopović Z M, Sakadžić S, Bzenić S and Petrović Z Lj 1999 *IEEE Trans. Plasma Sci.* **27** 1241

[60] Dyatko N A and Napartovich A P 1999 *J. Phys. D: Appl. Phys.* **32** 3169

[61] Li Y M, Pitchford L C and Moratz T J 1989 *Appl. Phys. Lett.* **54** 1403

[62] Mirić J, Šašić O, Dujko S and Petrović Z Lj 2014 *Proc. 27th Summer School and Int. Symp. on the Physics of Ionized Gases (Belgrade) (*Belgrade: Institute of Physics) p 122

[63] Kimura M and Nakamura Y 2010 *J. Phys. D: Appl. Phys.* **43** 145202

[64] Mirić J, de Urquijo J, Bošnjaković D, Petrović Z Lj and Dujko S 2016 *Plasma Sources Sci. Technol.* submitted

[65] Ristivojević Z and Petrović Z Lj 2012 *Plasma Sources Sci. Technol.* **21** 035001

[66] Dujko S, White R D and Petrović Z Lj 2008 *J. Phys. D: Appl. Phys.* **41** 245205

[67] Petrović Z Lj, Raspopović Z, Dujko S and Makabe T 2002 *Appl. Surf. Sci.* **192** 1

[68] Hagelaar G J M and Pitchford L C 2005 *Plasma Sources Sci. Technol.* **14** 722

[69] Kline L and Siambis J 1972 *Phys. Rev.* A **5** 794

[70] Kunhardt E and Tzeng Y 1986 *J. Comput. Phys.* **67** 279

[71] Gallagher J W, Beaty E C, Dutton J and Pitchford L C 1983 *J. Phys. Chem. Ref. Data* **12** 109

[72] Morrow R 1986 *IEEE Trans. Plasma Sci.* **PS-14** 234

[73] Ness K F and Makabe T 2000 *Phys. Rev.* E **62** 4083

[74] White R D, Robson R E, Ness K F and Makabe T 2005 *J. Phys. D: Appl. Phys.* **38** 997

[75] Skullerud H R 1983 *Aust. J. Phys.* **36** 845

[76] McMahon D R A and Crompton R W 1983 *J. Chem. Phys.* **78** 603

[77] Hegerberg R and Crompton R W 1983 *Aust. J. Phys.* **36** 831

[78] Banković A, Dujko S, White R D, Marler J P, Buckman S J, Marjanović S, Malović G, Garcia G and Petrović Z Lj 2012 *New J. Phys.* **14** 035003

[79] Banković A, Dujko S, White R D, Buckman S J and Petrović Z Lj 2012 *Nucl. Instrum. Methods* B **279** 92

[80] Aschwanden Th 1984 *Gaseous Dielectrics* IV ed L G Christophorou and M O Pace (New York: Pergamon) p 24

[81] Hasegawa H, Date H, Shimozuma M and Itoh H 2009 *Appl. Phys. Lett.* **95** 101504

[82] de Urquijo J, Juarez A M, Basurto E and Hernandez-Avila J L 2007 *J. Phys. D: Appl. Phys.* **40** 2205

[83] Robson R E, White R D and Ness K F 2011 *J. Chem. Phys.* **134** 064319

PAPER

Transport of electrons and propagation of the negative ionisation fronts in indium vapour

To cite this article: S Dujko *et al* 2021 *Plasma Sources Sci. Technol.* **30** 115019

View the article online for updates and enhancements.

Transport of electrons and propagation of the negative ionisation fronts in indium vapour

S Dujko[1,*] ⓘ, J Atić[1] ⓘ, D Bošnjaković[1] ⓘ, R D White[2] ⓘ, P Stokes[2] ⓘ,
K R Hamilton[3] ⓘ, O Zatsarinny[3,10] ⓘ, K Bartschat[3] ⓘ, M S Rabasović[1],
D Šević[1] ⓘ, B P Marinković[1] ⓘ, D V Fursa[4] ⓘ, I Bray[4] ⓘ, R P McEachran[5],
F Blanco[6] ⓘ, G García[7], D B Jones[8,11] ⓘ, L Campbell[8] ⓘ and
M J Brunger[8,9] ⓘ

[1] Institute of Physics Belgrade, University of Belgrade, Pregrevica 118, 11080 Belgrade, Serbia
[2] College of Science and Engineering, James Cook University, Townsville, Queensland 4810, Australia
[3] Department of Physics and Astronomy, Drake University, Des Moines, IA 50311, United States of America
[4] Curtin Institute for Computation and Department of Physics and Astronomy, Perth 6102, WA, Australia
[5] Laser Physics Centre, RSP, Australian National University, Canberra, ACT 0200, Australia
[6] Departamento de Estructura de La Materia, Física Térmica y Electrónica e IPARCOS, Universidad Complutense de Madrid, Avenida Complutense, E-28040 Madrid, Spain
[7] Instituto de Física Fundamental, CSIC, Serrano 113-bis, E-28006 Madrid, Spain
[8] College of Science and Engineering, Flinders University, GPO Box 2100, Adelaide, SA 5001, Australia
[9] Department of Actuarial Science and Applied Statistics, Faculty of Business and Management, UCSI University, Kuala Lumpur 56000, Malaysia

E-mail: sasha@ipb.ac.rs

CrossMark

Abstract

We study the transport of electrons and propagation of the negative ionisation fronts in indium vapour. Electron swarm transport properties are calculated using a Monte Carlo simulation technique over a wide range of reduced electric fields E/N (where E is the electric field and N is the gas number density) and indium vapour temperatures in hydrodynamic conditions, and under non-hydrodynamic conditions in an idealised steady-state Townsend (SST) setup. As many indium atoms are in the first $(5s^2 5p)^2 P_{3/2}$ metastable state at vapour temperatures of a few thousand Kelvin, the initial Monte Carlo code was extended and generalized to consider the spatial relaxation and the transport of electrons in an idealised SST experiment, in the presence of thermal motion of the host-gas atoms and superelastic collisions. We observe a significant sensitivity of the spatial relaxation of the electrons on the indium vapour temperature and the initial conditions used to release electrons from the cathode into the space between the electrodes. The calculated electron transport coefficients are used as input for the classical fluid model, to investigate the inception and propagation of negative ionisation fronts in indium vapour at various E/N and vapour temperatures. We calculate the electron density, electric field, and velocity of ionisation fronts as a function of E/N and indium vapour

---

[*] Author to whom any correspondence should be addressed.
[11] Present address: Flinders Microscopy and Microanalysis, College of Science and Engineering, Flinders University, GPO Box 2100, Adelaide, SA 5001, Australia.
[10] Dr Oleg Zatsarinny passed away during the preparation of this manuscript.

temperature. The presence of indium atoms in the first $(5s^2 5p)^2 P_{3/2}$ metastable state significantly affects the characteristics of the negative ionisation fronts. The transition from an avalanche into a negative ionisation front occurs faster with increasing indium vapour temperature, due to enhanced ionisation and more efficient production of electrons at higher vapour temperatures. For lower values of E/N, the electron density behind the streamer front, where the electric field is screened, does not decay as one might expect for atomic gases, but it could be increased due to the accumulation of low-energy electrons that are capable of initiating ionisation in the streamer interior.

(Some figures may appear in colour only in the online journal)

1. Introduction

Studies of electron swarm transport processes in metal vapours go back many years, for example to the Franck–Hertz experiment and the genesis of quantum physics [1]. Yet much remains to be understood from a fundamental point of view [2–5]. Early studies of electron transport in metal vapours were limited to the vapours of mercury, caesium, and other alkali metals, due to the many technical difficulties associated with the control of high temperatures in swarm experiments. In addition to decades of studying the transport of electrons in mercury vapour [6–11], swarm studies were performed in the vapours of sodium, potassium, and caesium [12] while the experimental results of breakdown voltages and $V–I$ characteristics were measured for sodium, potassium, cadmium, and zinc [13]. The primary driving force behind these early studies was the modelling and optimization of light sources containing mercury [8, 14, 15], sodium [16, 17], and zinc [18, 19]. Other applications include the modelling of a gas laser [20], the magnetohydrodynamics of arcs [21], and a post-arc breakdown plasma [22].

Recently, a new wave of studies on electron scattering in metal vapours has triggered the modelling and analysis of electron transport and different types of plasma discharges in those vapours. The *B*-spline *R*-matrix (close-coupling) with pseudo-states method was employed to calculate the cross sections for electron collisions with caesium atoms [23, 24], and those calculated cross sections were then used to model an excimer-pumped alkali laser with caesium as one of the constituent species [24]. The cross sections for the scattering of electrons from zinc [25] and magnesium [26] vapours were recently calculated, using both non-relativistic and relativistic optical-potential methods. The computed cross-sections were subsequently used as input to solve the Boltzmann equation to calculate the electron swarm transport coefficients. The publicly available two-term Boltzmann equation solver BOLSIG+ [27], as well as the Monte Carlo code METHES [28], were recently used to investigate the electron transport and breakdown in a copper vapour post-arc plasma [22]. The relativistic complex optical potential method has also been used to study electron–beryllium scattering [29].

As part of our ongoing investigations of electron scattering and transport in metal vapours, we report in this paper on our study of electron transport and propagation of negative ionisation fronts in indium vapour. Indium (In) is a soft, grey metallic element with an atomic number of 49. It belongs to the group-III elements of the periodic table and has two stable isotopes, ^{115}In and ^{113}In, with abundances of 95.7% and 4.3%, respectively. With an electronic configuration $4d^{10}5s^2 5p$ indium is the first in a series of the $5p$ elements in the periodic table, and most commonly donates the three outermost electrons to become In^{3+} [30]. In certain cases, however, the $5s$-electron pair is not donated, resulting in In$^+$ [31]. Because of its low melting point of 429.75 K, indium has been recognized as a material with great potential for many technological applications. For example, as an indium tin oxide it is used to produce transparent electrodes in liquid-crystal displays [32], and it is also employed as a light filter in low-pressure sodium lamps. Furthermore, indium has numerous semi-conductor-related applications, including the use of InAs and InSb for low-temperature transistors and InP for high-temperature transistors [33]. Furthermore, InGaN and InGaP are found in both light-emitting diodes and laser diodes [34].

Even though the above-mentioned applications of indium are of great importance in fundamental science and modern technology, the basic motivating factors in the study of electron scattering and transport in indium vapour relate to the modelling of plasma discharges. Since the use of toxic mercury in low-pressure and high-pressure light sources is highly limited in both the European Union and many other countries, there is a strong incentive nowadays to find a less toxic material as an alternative to mercury. For low-pressure discharge lamps, one option would be to use mixtures of halogen–indium compounds with argon [35–37]. The collisional-radiative models of such systems require the knowledge of electron swarm transport coefficients, including rate coefficients for various collisional processes such as ionisation and electron-impact excitation. It is clear that further optimization and understanding of indium-based light sources crucially depends on an accurate knowledge of the cross sections for electron–indium scattering, the relevant transport coefficients,

and in appreciating the physical processes involved in indium vapour discharges.

While electron scattering in indium vapour has been thoroughly discussed in our recent publications [38, 39], in the present paper we focus on electron transport processes and the propagation of negative ionisation fronts. To that end, electron swarm transport coefficients are calculated using a Monte Carlo simulation technique under hydrodynamic conditions, and also for non-hydrodynamic conditions in an idealised steady-state Townsend (SST) setup, over a wide range of reduced electric fields (E/N) and indium vapour temperatures. In particular, the initial Monte Carlo code, which was specifically developed to study the spatial relaxation of electrons in an idealised SST experiment [40–42], was extended and generalized for the present work to investigate the effects of gas temperature in the presence of electron-impact ionisation of indium atoms in the ground state and the lowest-lying metastable state. We comprehensively studied the influence of the indium metastable state $(5s^2 5p)^2P_{3/2}$ at temperatures of several thousand Kelvin on the electron transport and the spatial relaxation of the electrons. To the best of our knowledge, we present the first systematic investigation for the spatial relaxation of electrons in hot metal vapours, where thermal motion of the background atoms and their influence on the electrons are rigorously considered by implementing electron collisions with the indium atoms in the metastable state $(5s^2 5p)^2P_{3/2}$, including the effects of superelastic collisions.

The second major objective of the present study is to simulate negative ionisation fronts in indium vapour. Due to the high accelerating voltages in high-pressure light sources, the transition from an electron avalanche into a streamer is a rapid process, which has been studied both experimentally and by means of numerical simulations [43, 44]. It has been shown that streamer-like ionising channels can originate from both the anode and the cathode, and that they can propagate through the gas volume as well as along the inner wall of the discharge lamp. In particular, the first phase of the streamer-breakdown is characterized by a constricted streamer process between the electrode tips [43]. In combination with mercury, indium vapour may serve in high-intensity discharge lamps as a radiation-emitting substance due to its high-vapour pressure and because its emitted radiation covers the UV and visible ranges of the spectrum. Therefore, it is clear that studies of the development of an electron avalanche and its transition into a streamer in indium vapour may support investigations to find the optimal discharge conditions and increase the plasma efficiency. In order to simulate the inception and propagation of negative ionisation fronts in indium vapour, we here apply the classical fluid model, which is based on the drift–diffusion approximation, the local field approximation, and Poisson's equation. This model is implemented numerically in 1D and 1.5D configurations. Our calculated electron swarm transport coefficients, including the ionisation coefficient, drift velocity, and longitudinal diffusion coefficient, are used as input data in this model. However, it should be noted that in the present work we are not attempting to model the inception of the cathode-directed streamers, due to the accumulation of positive space charge near the cathode, nor do we attempt to consider the effects of the breakdown voltage on the parameters of the equivalent circuit. Both remain the subject of future studies. Instead, we isolate and investigate the dynamics of the negative ionisation fronts only, and in particular we study the effects of varying the indium vapour temperature on the formation and development of those negative ionisation fronts under the action of an externally applied electric field.

The remainder of this paper is organized as follows. In section 2 we briefly present a set of cross sections for electron scattering in indium vapour, including those for excitation from the ground state $(5s^2 5p)^2P_{1/2}$ and the first excited metastable state $(5s^2 5p)^2P_{3/2}$. In section 3.1 we present the methods of our calculations, including the basic elements of our Monte Carlo approach for simulating the electron swarm transport properties under hydrodynamic and SST conditions. In section 3.2 we present the basic elements of the classical 1.5D fluid model, which is used for studying the development of an electron avalanche, and its transition into a negative ionisation front in indium vapour. The results of this work are then given in section 4. Specifically, in section 4.2 we show the variation of the electron swarm transport coefficients with E/N and indium vapour temperature, while in section 4.3 we present the results of our study under non-hydrodynamic conditions in an idealised SST setup. Results describing the development of an electron avalanche and its transition into a negative ionisation front are presented in section 4.4. Finally, we summarize our conclusions in section 5 and also provide an outlook regarding possible future studies of electron transport and streamer discharges in indium vapour.

2. Cross sections for electron scattering in indium vapour

2.1. Elastic momentum transfer, electronic excitations and total ionisation

In this work, we utilize the cross sections for electron scattering in indium vapour, which have recently been generated and discussed in detail in our previous publications [38, 39] and to which we refer the interested reader. Here we simply note that the elastic momentum transfer cross section, for energies from 0.001 eV to 10 000 eV, and for scattering from the ground $(5s^2 5p)^2P_{1/2}$ level, is tabulated in reference [39]. Uncertainty estimates of $\sim \pm 20\%$ for electron energies less than 3 eV and $\sim \pm 15\%$ for energies above 3 eV were quoted [39]. The elastic momentum transfer cross section for scattering from the lowest-lying $(5s^2 5p)^2P_{3/2}$ metastable state is also tabulated in reference [39].

Cross sections for discrete inelastic transitions from the $^2P_{1/2}$ ground state and the close-lying metastable $^2P_{3/2}$ level were calculated using a relativistic *B*-spline *R*-matrix (DBSR) method by Hamilton *et al* [39]. In particular, 21 discrete inelastic cross sections for excitation from the ground state and 21 discrete inelastic cross sections for excitation from the lowest metastable state were provided [39]. Among many interesting points, near-threshold structures in the majority of the discrete inelastic cross sections were reported [39].

The total ionisation cross section for indium atoms initially in the electronic ground state was determined for energies from threshold to 10 000 eV in [39]. The quoted uncertainty on those data was $\sim \pm 20\%$ [39]. The total ionisation cross section for indium atoms in the first $(5s^2 5p)^2 P_{3/2}$ metastable state (0.274 eV), was estimated by simply moving its threshold from that of the ground state (5.786 eV) downward by 0.274 eV.

2.2. Superelastic collisions

One of the objectives of the present work is to study the effects of the indium vapour temperatures on electron transport and the propagation of negative ionisation fronts. To do this, we need to take into account superelastic collisions in our Monte Carlo simulations and/or the solutions of the Boltzmann equation. As pointed out in our previous work [39], the thermal energy at $T = 1260$ K is $\frac{3}{2} kT \approx 0.163$ eV, i.e. near the threshold energy of the first $(5s^2 5p)^2 P_{3/2}$ metastable state. It is therefore important to consider the influence of superelastic collisions on electron transport at indium vapour temperatures of a few thousand Kelvin.

Cross sections for superelastic collisions can be evaluated by applying the principle of microscopic reversibility and detailed balance in a thermal equilibrium. According to this fundamental principle, the cross section for superelastic collision σ_s may be calculated from the cross section σ_j for the discrete inelastic transition to the state j, with the threshold energy ϵ_j and statistical weight g_j, as

$$\sigma_s (\epsilon) = \frac{g_0}{g_j} \frac{\epsilon + \epsilon_j}{\epsilon} \sigma_j \left(\epsilon + \epsilon_j \right), \quad (1)$$

where g_0 is the statistical weight of the ground state.

In figure 1 we show the fractional populations of indium atoms in the ground $(5s^2 5p)^2 P_{1/2}$ state, the first excited $(5s^2 5p)^2 P_{3/2}$ metastable state, and the sum of all the upper excited states, as a function of the indium vapour temperature. At $T = 1260$ K, we observe that 86% of indium atoms are in the ground $(5s^2 5p)^2 P_{1/2}$ state while the remaining 14% are in the first $(5s^2 5p)^2 P_{3/2}$ metastable state. Similarly, but now at $T = 3260$ K, 57% of the indium atoms are in the ground $(5s^2 5p)^2 P_{1/2}$ state while the remaining 43% of indium atoms are in the metastable state. The fractional populations of the third and higher excited levels are only larger than 1% at $T = 7260$ K and higher temperatures. Thus, we limit our calculations to an upper limit of $T = 5260$ K.

The cross sections for electron scattering in indium vapour from the ground state $(5s^2 5p)^2 P_{1/2}$ level and the close-by metastable $(5s^2 5p)^2 P_{3/2}$ level are displayed in figures 2 and 3, respectively. The total cross section for superelastic collisions is multiplied with the corresponding fractional populations of the first excited metastable state at 1260 K, 3260 K and 5260 K, and these quantities are also included in figures 2 and 3, respectively. Note that the cross sections for elastic momentum transfer, inelastic discrete transitions and ionisation should be multiplied with the corresponding weighting factors to account for the appropriate fractional populations
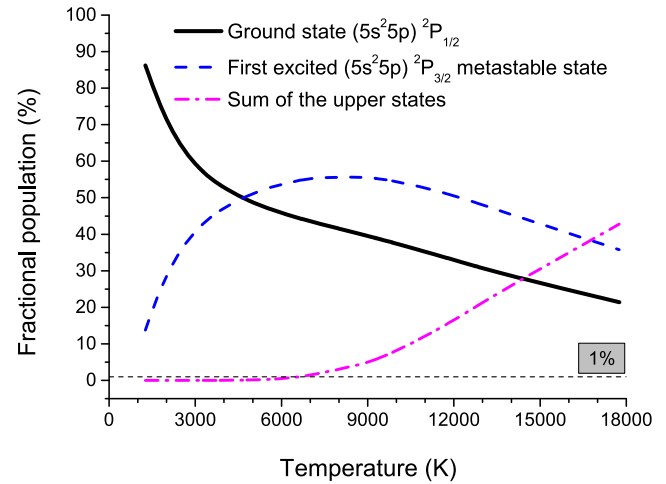
Figure 1. Fractional populations of indium atoms in the $(5s^2 5p)^2 P_{1/2}$ ground state, the first excited $(5s^2 5p)^2 P_{3/2}$ metastable state, and the sum of all higher excited states, as a function of the indium vapour temperature.

of the ground state $(5s^2 5p)^2 P_{1/2}$ and the metastable state $(5s^2 5p)^2 P_{3/2}$ at the temperature being considered.

3. Methods of calculations

3.1. Monte Carlo simulations

In Monte Carlo simulations, we follow the spatial and temporal evolution of a large number of electrons moving under the action of an external electric field in a spatially homogenous indium vapour. Under swarm conditions, the electron density is sufficiently low, so that only electron collisions with indium atoms are taken into account. Electrons gain energy from the externally applied electric field and in superelastic collisions with excited indium atoms. This energy input is released through binary collisions between the electrons and the atoms. Thermal motion of the background indium atoms and their influence on the electrons are taken into account. We implemented an algorithm for calculating the collision frequency in the case when thermal motion of the background indium atoms with a Maxwellian velocity distribution cannot be neglected [45]. We assume isotropic scattering in the electronic excitation and ionisation collisions. The anisotropic nature of elastic collisions is implicitly included through the use of the elastic momentum transfer cross section. The energy available for division after an ionising collision is given by the difference between the incident electron energy and the indium ionisation energy, here modelled as a constant value of 5.786 eV for indium atoms in the ground state and a value of 5.512 eV for indium atoms in the first excited metastable state. To allocate the available energy to the two-post collision electrons, a random fraction of the available energy is awarded to one electron, with the remaining energy being awarded to the second electron. In other words, the available energy is distributed assuming a uniform distribution indicating that all fractions of the available energy post-collision are equally probable.
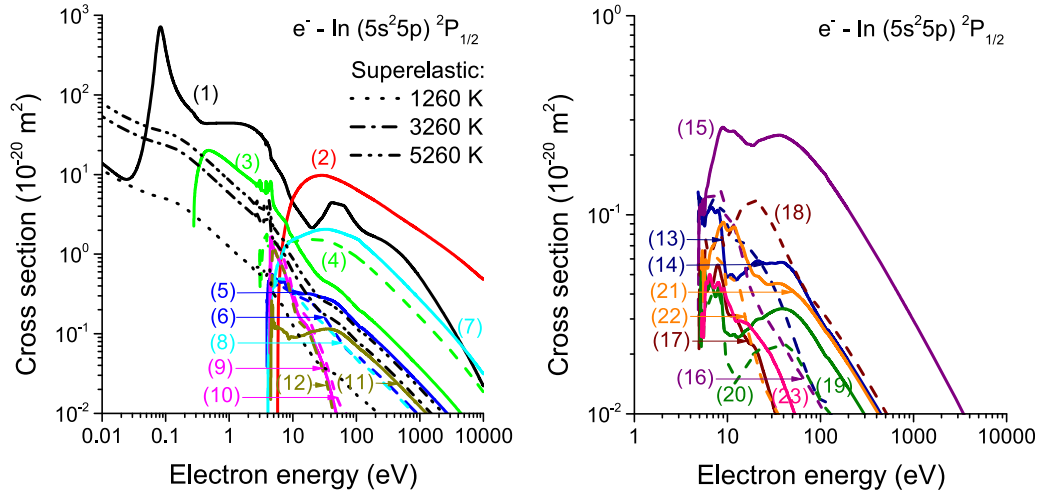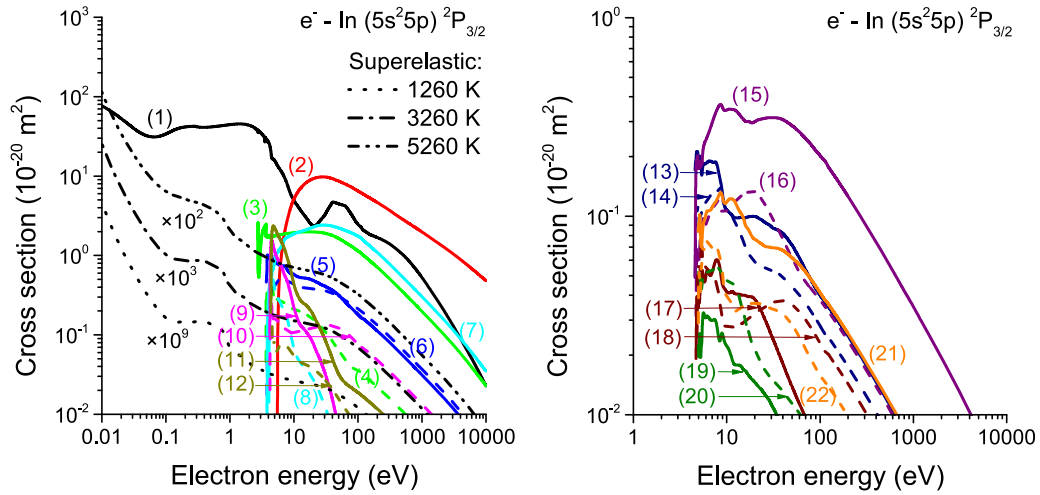
Figure 2. Integral cross sections for electron scattering in indium vapour for atoms in the ground state $(5s^2 5p)^2 P_{1/2}$. The left panel shows the elastic momentum transfer (1), total ionization (2), and quantities that are obtained by multiplying the total cross section for superelastic collisions with the corresponding fractional populations of the first excited metastable state at indium vapour temperatures of 1260 K, 3260 K, and 5260 K. The left panel also includes the following discrete inelastic transitions: $(5s^2 5p)^2 P_{3/2}$ (3), $(5s^2 6s)^2 S_{1/2}$ (4), $(5s^2 6p)^2 P_{1/2}$ (5), $(5s^2 6p)^2 P_{3/2}$ (6), $(5s^2 5d)^2 D_{3/2}$ (7), $(5s^2 5d)^2 D_{5/2}$ (8), $(5s^2 4p)^2 P_{1/2}$ (9), $(5s^2 4p)^2 P_{3/2}$ (10), $(5s^2 7s)^2 S_{1/2}$ (11) and $(5s^2 4p)^2 P_{5/2}$ (12). The right panel includes the following discrete inelastic transitions: $(5s^2 7s)^2 P_{1/2}$ (13), $(5s^2 7s)^2 P_{3/2}$ (14), $(5p^2 6d)^2 D_{3/2}$ (15), $(5p^2 6d)^2 D_{5/2}$ (16), $(5p^2 4f)^2 F_{7/2}$ (17), $(5p^2 4f)^2 F_{5/2}$ (18), $(5p^2 8s)^2 S_{1/2}$ (19), $(5p^2 8s)^2 P_{1/2}$ (20), $(5s^2 7d)^2 D_{3/2}$ (21), $(5s^2 7d)^2 D_{5/2}$ (22) and $(5s^2 8p)^2 P_{3/2}$ (23).

Figure 3. Integral cross sections for electron scattering in indium vapour for atoms in the metastable state $(5s^2 5p)^2 P_{3/2}$. The left panel shows the elastic momentum transfer (1), total ionization (2), and quantities that are obtained by multiplying the total cross section for superelastic collisions with the corresponding fractional populations of the first excited metastable state at indium vapour temperatures of 1260 K, 3260 K, and 5260 K. The quantities obtained as the product of the total cross section for superelastic collisions and the corresponding fractional populations of the first excited metastable state were subsequently multiplied by factors of 10^9, 10^3, and 10^2, at indium vapour temperatures of 1260, 3260 and 5260, respectively. The left panel also includes the following discrete inelastic transitions: $(5s^2 6s)^2 S_{1/2}$ (3), $(5s^2 6p)^2 P_{1/2}$ (4), $(5s^2 6p)^2 P_{3/2}$ (5), $(5s^2 5d)^2 D_{3/2}$ (6), $(5s^2 5d)^2 D_{5/2}$ (7), $(5s^2 4p)^2 P_{1/2}$ (8), $(5s^2 4p)^2 P_{3/2}$ (9), $(5s^2 7s)^2 S_{1/2}$ (10), $(5s^2 4p)^2 P_{5/2}$ (11) and $(5s^2 7s)^2 P_{1/2}$ (12). The right panel includes the following discrete inelastic transitions: $(5s^2 7s)^2 P_{3/2}$ (13), $(5p^2 6d)^2 D_{3/2}$ (14), $(5p^2 6d)^2 D_{5/2}$ (15), $(5p^2 4f)^2 F_{7/2}$ (16), $(5p^2 4f)^2 F_{5/2}$ (17), $(5p^2 8s)^2 S_{1/2}$ (18), $(5p^2 8s)^2 P_{1/2}$ (19), $(5s^2 7d)^2 D_{3/2}$ (20), $(5s^2 7d)^2 D_{5/2}$ (21) and $(5s^2 8p)^2 P_{3/2}$ (22).

We then track a large number of electrons between collisions using finite length time steps. The time step is determined as a fraction of the mean collision time, which is calculated from the total collision frequency. Finite time steps are used to solve the integral equation for the collision probability, in order to determine the exact time of the next collision [46, 47]. If the length of these time steps is too large, then the time of the next collision can be inaccurately computed, which in turn affects the accuracy of the calculation of the electron trajectories. On the other hand, too small time steps lead to an enormous increase of computing time, which is equally unacceptable. For this investigation, the time step was

fixed at one hundredth of the mean time between collisions, regardless of the electron energy. This allows for a precise determination of the time of the next collision and the trajectory of the electrons.

The equation for the collision probability is solved by numerical integration using the above-mentioned time steps. When the moment of the next collision is determined, the next step is to define the nature of the collision. For this purpose, the relative probabilities for each collision process are calculated at the given electron energy. All electron scattering processes are assumed to be isotropic regardless of their specific nature and energy. Therefore, the change in direction of the electron velocity is expressed by a uniformly distributed scattering angle within the interval $[0, \pi]$ and by the azimuthal angle that is uniformly distributed within the interval $[0, 2\pi]$. The change in the electron energy, after elastic and inelastic collisions, is calculated using the laws of elementary collision dynamics. For more details the reader is referred to [40, 47].

3.1.1. Sampling of the bulk and flux transport coefficients.
Under hydrodynamic conditions, the electron swarm transport coefficients are calculated after the relaxation of the swarm to the stationary state. The measurable and universal transport coefficients are the bulk transport coefficients [48]. They are calculated in our Monte Carlo simulations from the rate of change of the appropriate averages of the positions of the electrons, in configuration space [40, 47]. The number-changing reaction rate, which for indium vapour is reduced to the ionisation frequency, is defined by

$$\nu_{\text{ION}} = \frac{\text{d}}{\text{d}t}\left(\ln N_{\text{e}}\right), \tag{2}$$

the bulk drift velocity by

$$\boldsymbol{W} = \frac{\text{d}}{\text{d}t}\langle\boldsymbol{r}\rangle, \tag{3}$$

and the bulk diffusion tensor by

$$\boldsymbol{D} = \frac{1}{2}\frac{\text{d}}{\text{d}t}\langle\boldsymbol{r}^{\star}\boldsymbol{r}^{\star}\rangle. \tag{4}$$

Here N_{e} is the total number of electrons at any time t, $\langle\boldsymbol{r}\rangle$ is the coordinate of the swarm's centre of mass, and $\boldsymbol{r}^{\star} = \boldsymbol{r} - \langle\boldsymbol{r}\rangle$. The coordinate of the swarm's centre of mass is given by

$$\langle\boldsymbol{r}\rangle = \frac{1}{N_{\text{e}}}\sum_{k=0}^{N_{\text{e}}}\boldsymbol{r}_{k}, \tag{5}$$

where $\boldsymbol{r}_{k}$, $(k = 1, 2, \ldots, N_{\text{e}})$ are the coordinates of all electrons.

The flux transport coefficients are required for some aspects of plasma modelling and elsewhere [49]. The flux drift velocity is given by

$$\boldsymbol{W}^{\star} = \left\langle\frac{\text{d}\boldsymbol{r}}{\text{d}t}\right\rangle = \langle\boldsymbol{v}\rangle, \tag{6}$$

and the flux diffusion tensor by

$$\boldsymbol{D}^{\star} = \frac{1}{2}\left\langle\frac{\text{d}}{\text{d}t}\left(\boldsymbol{r}^{\star}\boldsymbol{r}^{\star}\right)\right\rangle. \tag{7}$$

The flux drift velocity is in fact the average velocity of the electrons. It is given by

$$\langle\boldsymbol{v}\rangle = \frac{1}{N_{\text{e}}}\sum_{k=0}^{N_{\text{e}}}\boldsymbol{v}_{k}, \tag{8}$$

where

$$\boldsymbol{v}_{k} = \frac{\text{d}\boldsymbol{r}_{k}}{\text{d}t}. \tag{9}$$

Although, at first glance, the expressions (3) and (6) look the same, they are fundamentally different in the presence of non-conservative collisions. Using expressions (5) and (9), the equality of the bulk drift velocity and the flux drift velocity is reduced to

$$\frac{1}{N_{\text{e}}}\frac{\text{d}}{\text{d}t}\sum_{k=0}^{N_{\text{e}}}\boldsymbol{r}_{k} = \frac{1}{N_{\text{e}}}\sum_{k=0}^{N_{\text{e}}}\frac{\text{d}}{\text{d}t}\boldsymbol{r}_{k}. \tag{10}$$

In the absence of non-conservative collisions (e.g. ionisation), the total number of the electrons N_{e} remains the same during the simulation, and hence the time derivative commutes with the sum. However, in the presence of non-conservative collisions, the total number of electrons N_{e} is neither a constant nor a continuous function of time and thus the equality (10) no longer holds. In other words, in the presence of non-conservative collisions, the bulk and the flux transport coefficients are not the same. This is no moot point, as the differences between the two families of transport coefficients are often significant, ranging from a few percent to a few orders of magnitude [50].

For electrons in indium vapour, the differences between the bulk and flux transport coefficients are induced by the explicit contribution of ionisation processes. Ionisation is most likely to occur at the leading edge of the swarm, where the higher-energy electrons are located. Thus, in the case of drift, ionisation always acts in such a manner as to push the centre of mass of the swarm forward, which in turn increases the bulk drift velocity. Therefore, for electrons in indium vapour, we may expect that the bulk drift velocity is always larger in magnitude than the flux drift velocity. Similarly, the increase in electron numbers, due to ionisation in the indium vapour, enhances diffusion in both the longitudinal and transverse directions. These observations will be discussed and illustrated later by showing the E/N-profiles of the drift velocity and diffusion coefficients (see section 4.2).

3.1.2. Sampling of spatially-resolved transport data. Under non-hydrodynamic SST conditions, the electrons are released from the cathode into the space between the electrodes. In contrast to our initial Monte Carlo code, where the electrons were released one by one from the cathode [40–42], in this work all electrons are released from the cathode at the same time. In this way, it is possible to use swarm rescaling procedures under SST conditions, which is of great importance for the simulation of electrons at high values of E/N, where a large number of secondary electrons is formed by ionisation processes. Similarly, the code designed in this way permits the

simulation of transport in strongly-attaching molecular gases under SST conditions [50]. The back-diffusion of electrons is not considered, and the electrons are followed until reaching the anode. Note that both electrodes are regarded as perfectly absorbing. Due to the presence of the electrodes, both the implicit and explicit gradients of the electron density exist. Consequently, the hydrodynamic approximation is not valid under SST conditions and the concept of transport coefficients makes no sense, even after reaching the equilibration of the swarm. The spatially-resolved transport data are thus calculated using the so-called box-sampling technique [40, 41]:

$$
\langle \xi \rangle_j = \left(\frac{1}{\Delta z} \int_{z_j - \Delta z/2}^{z_j + \Delta z/2} f_{\mathrm{SST}}(z, v)\, \mathrm{d}\mathbf{r}\, \mathrm{d}\mathbf{v} \right)^{-1} \frac{1}{\Delta z}
$$

$$
\times \int_{z_j - \Delta z/2}^{z_j + \Delta z/2} \xi f_{\mathrm{SST}}(z, v)\, \mathrm{d}\mathbf{r}\, \mathrm{d}\mathbf{v}
$$

$$
\approx \left(\sum_{k=1}^{N_e} \Delta t_k^j \right)^{-1} \sum_{k=1}^{N_e} \xi_k^j \Delta t_k^j. \tag{11}
$$

Here $f_{\mathrm{SST}}(z, v)$ is the steady-state distribution function, ξ_j^k is the value of the quantity to be sampled when the kth electron is contained in the jth box, Δt_k^j is the residence time of the electron in that box, and N_e is the number of electrons that appear there.

The spatially-resolved rate coefficients are calculated by determining the number of collisions of type m in the jth spatial box located at z_j [40, 51]:

$$
R^m(z_j) = \frac{N_j^m}{\Delta z\, N_e(z_j)}, \tag{12}
$$

where N_j^m denotes the number of collisions m, Δz is the width of box, and $N_e(z_j)$ is the total number of resident electrons. The expression (12) was tested in nitrogen and other gases, by comparing the calculated ionisation coefficient with the experimental results obtained from the slope of the electron emission, as well as with the results obtained by integrating the distribution function and the corresponding cross section for ionisation [51]. The agreement between these independent techniques was excellent, indicating the accuracy and validity of the methodology used for sampling the spatially-resolved rate coefficients.

3.2. Classical fluid model

The inception and propagation of negative ionisation fronts were studied using a classical fluid model. The classical model involves the first two velocity moments of the Boltzmann equation, i.e. the equation of continuity and the momentum balance equation. The classical drift–diffusion approximation is obtained by assuming a steady state of the momentum balance equation and that the energy of the field-directed motion is much larger than the thermal contribution. For the full and strict derivation of this model the reader is referred to [52]. The generalized one-dimensional continuity equation for the

electron number density is

$$
\frac{\partial n_e}{\partial t} = \frac{\partial}{\partial x} \left(W\, \mathrm{sgn}\,(E)\, n_e + D_{\mathrm{L}} \frac{\partial n_e}{\partial x} \right) + \nu_{\mathrm{ION}} n_e, \tag{13}
$$

where W and D_{L} are the electron drift velocity and longitudinal diffusion coefficient, respectively, E is oriented along the x-axis, while ν_{ION} is the ionisation coefficient. The drift and diffusion of positive ions are neglected here on the basis of the time scales of interest in the present work. Likewise, the discharge model is not coupled to the gas dynamics, even though the indium vapour may be additionally heated by the discharge [53, 54].

The model is realized in a 1.5-dimensional (1.5D) setup, according to which the streamer radius R_0 is fixed. Thus, the total electric field in the system is evaluated as the sum of the uniform external electric field and the electric field due to space charge:

$$
E(x, t) = E_0 + \frac{e}{2\varepsilon_0} \int_0^d (n_p - n_e) \left(\mathrm{sgn}\,(x - x') \right.
$$

$$
\left. - \frac{x - x'}{\sqrt{(x - x')^2 + R_0^2}} \right) \mathrm{d}x', \tag{14}
$$

where E_0 and ε_0 are the external (applied) electric field and vacuum permittivity, respectively, and d is the length of the system.

The above fluid equations are closed, assuming the local field approximation. According to this approximation, the input data, including W, D_{L}, and ν_{ION}, are assumed to be functions of the local instantaneous electric field. Equations (13) and (14) are solved numerically, imposing the homogeneous Dirichlet boundary conditions for the electron density n_e as

$$
n_e(x = 0, t) = 0, \qquad n_e(x = d, t) = 0, \tag{15}
$$

and initial conditions

$$
n_e(x, t = 0) = \frac{N_{e0}}{\pi R_0^2 \sigma_0 \sqrt{2\pi}} \exp\left(-\frac{1}{2} \frac{(x - x_0)^2}{\sigma_0^2} \right). \tag{16}
$$

Here N_{e0} is the initial number of electrons with a Gaussian distribution centred at x_0 and a standard deviation σ_0. In the numerical implementation of our fluid model, the spatial discretization is performed by employing the second-order central finite-difference method, while the fourth order Runge–Kutta method is used for the integration in time. For more details, the reader is referred to [52, 55].

4. Results and discussion

4.1. Preliminaries

In Monte Carlo simulations, in which electron transport under hydrodynamic conditions is studied, we cover a range of reduced electric fields E/N between 0.01 Td and 10 000 Td. The pressure of the background gas of indium atoms is fixed at 1 Torr, and our calculations are performed for the indium
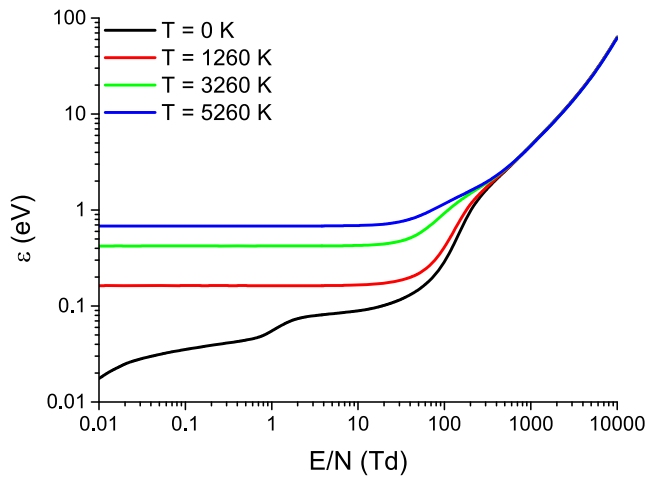
Figure 4. Variation of the mean energy ε of the electron swarm as a function of E/N for various indium vapour temperatures.

vapour temperatures of 1260, 3260, and 5260 K. The cold-gas approximation, according to which the background indium atoms are at rest ($T = 0$ K), is also analysed. The number of electrons in our Monte Carlo simulations, under hydrodynamic conditions was varied between 2.5×10^5 for lower values of E/N to 1×10^6 at higher values of E/N. Under SST conditions, however, the number of electrons is varied between 1×10^5 and 5×10^5, depending on the distance between the electrodes and the applied reduced electric field E/N. In section 4.2 we present the electron swarm transport coefficients as a function of the reduced electric field E/N and indium vapour temperatures, T, while in section 4.3 we present the electron swarm transport properties and spatial relaxation profiles as a function of E/N and T. In the latter case the electrons are released from the cathode under two different sets of initial conditions: (i) the Maxwell–Boltzmann velocity distribution with starting mean energies of 0.1 eV, 1 eV, and 10 eV, and (ii) the beam initial velocity distribution with the same starting mean energies. Finally, in section 4.4 the development of an electron avalanche and its transition into a negative ionisation front is considered.

4.2. Electron transport under hydrodynamic conditions

As noted above, in this section we present results showing the variation of electron swarm transport properties with E/N and indium vapour temperature, T. Figure 4 illustrates the variation of the mean energy with E/N for various temperatures. In the $T = 0$ K profile, we observe that ε is a monotonically increasing function of E/N. The rate of increase of the mean energy varies with E/N, reflecting the energy dependence of the cross sections for electron scattering. For $T = 1260$ K, $T = 3260$ K, and $T = 5260$ K, the profiles of the mean energy also exhibit some generic features. At lower values of E/N, we observe initial plateaus in the profiles, indicating that the electrons are in near thermal equilibrium with the indium vapour. In this range of lower values of E/N, which extends up to approximately 10 Td, the distribution of electrons is of thermal-Maxwellian form, and the mean energy

depends distinctively on the indium vapour temperature. This low E/N regime can be characterized as a vapour-dominated regime, where the electrons are essentially thermalized. As E/N rises, the electrons gain more energy from the electric field and are no longer thermalized. As a result, the velocity distribution deviates from a thermal-Maxwellian, but to a large extent the temperature of the indium vapour still controls the behaviour of the electrons. This is the so-called intermediate regime, which extends from approximately 10 Td to 400 Td. For E/N larger than approximately 400 Td, the mean energies are considerably higher than the corresponding thermal energies. We observe that the influence of indium vapour temperature on the mean energy is minimal in this regime. In what follows, we will refer to this region of electron transport as the field-dominated regime.

Figure 5 shows the variation of the bulk drift velocity with E/N for various T. At first glance, for lower values of E/N, we observe that the drift velocity for $T = 0$ K varies very slowly with increasing E/N. However, looking more closely, we in fact observe that the drift velocity exhibits a region of negative differential conductivity (NDC), i.e. over a range of E/N values the drift velocity decreases as the driving electric field increases [56]. NDC takes place here between approximately 0.03 Td and 0.3 Td, where there is a noticeable transition in the dominant energy loss mechanism from inelastic to elastic processes. In the transition regime, due to numerous elastic collisions, the enhanced randomization of the directed motion decreases the drift velocity even though the mean energy increases. As E/N increases further, NDC is suppressed due to numerous elastic and inelastic collisions. Consequently, for E/N larger than approximately 0.3 Td and at $T = 0$ K, the drift velocity is a monotonically increasing function of E/N. From the E/N-profiles of the bulk drift velocity for $T = 1260$ K, $T = 3260$ K, and $T = 5260$ K, we observe no such NDC and that the drift velocities are increasing functions of E/N. In the vapour-dominated and intermediate regimes, the drift velocity generally decreases with increasing vapour temperature. In this low E/N regime, the drift velocities for $T = 1260$ K is essentially linear, which is a signature of constant mobility. In the field-dominated regime, the impact of the vapour temperature on the drift velocity is minimal.

In figures 6 and 7, respectively, we show the variation of the bulk longitudinal ND_L and bulk transverse ND_T diffusion coefficients with E/N, for various vapour temperatures. In the vapour-dominated and intermediate regimes, at fixed E/N, we observe that ND_L increases with T. On the other hand, in the field-dominated regime, both ND_L and ND_T show no sensitivity with respect to the vapour temperature. We observe a deep minimum in the E/N-profile of ND_L for $T = 0$ K at around 0.45 Td, which can be attributed to the rapid increase of the elastic momentum transfer cross section in the limit of the lowest values of electron energies. For E/N larger than approximately 0.45 Td, ND_L is a generally increasing function of E/N. Similarly, we observe a distinct minimum in the E/N-profile of ND_T for $T = 0$ K at about 30 Td. The fall in ND_T occurs less rapidly in comparison with that of ND_L, but it extends over a wider range of E/N. As for ND_L, the decline in ND_T at $T = 0$ K reflects the rapidly increasing cross section for
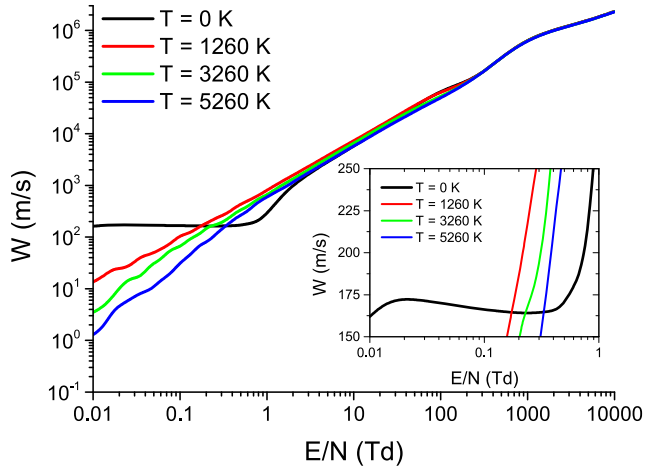
Figure 5. Variation of the bulk drift velocity of the electron swarm as a function of E/N for various indium vapour temperatures.
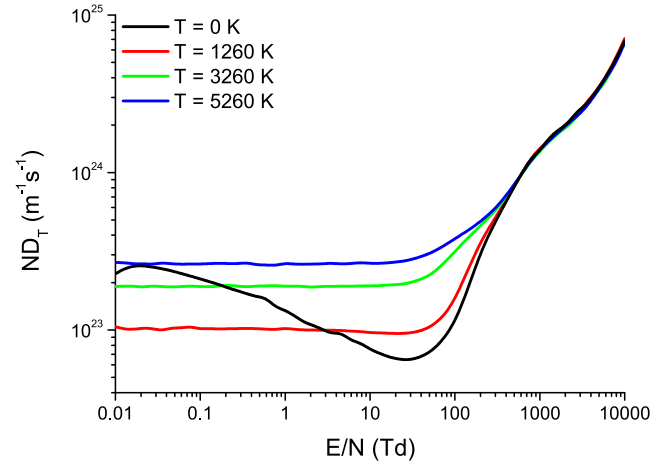

Figure 7. Variation of the bulk transverse diffusion coefficient of the electron swarm as a function of E/N for various indium vapour temperatures.
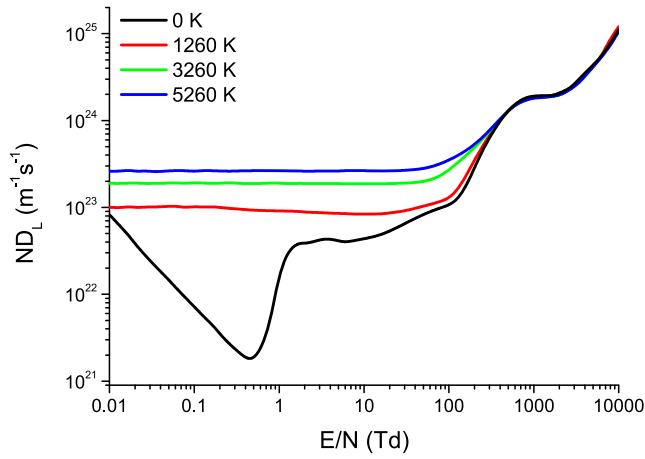

Figure 6. Variation of the bulk longitudinal diffusion coefficient of the electron swarm as a function of E/N for various indium vapour temperatures.
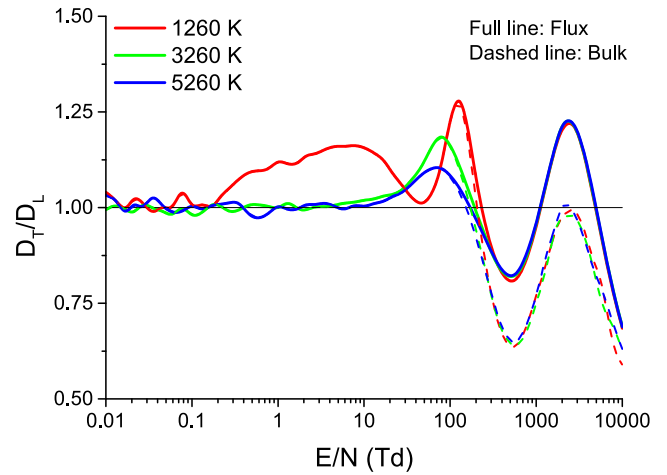

Figure 8. Variation of the ratio of ND_T to ND_L of the electron swarm as a function of E/N for various indium vapour temperatures.

momentum transfer in elastic collisions and the cross section for excitation of the $(5s^2 5p)^2 P_{3/2}$ metastable state. In the vapour-dominated regime, from the E/N-profiles of both ND_L and ND_T for $T = 1260$ K, $T = 3260$ K, and $T = 5260$ K, we observe that the diffusion coefficients have essentially thermal values. These values of the diffusion coefficients are increasing functions of the vapour temperature. As expected, the thermal values of ND_L and ND_T are nearly identical, indicating that the velocity distribution of the electrons is approximately thermal-Maxwellian. As E/N increases further, the intermediate regime is characterized by non-thermal values of the diffusion coefficients, which are still temperature dependent. The temperature dependence of the diffusion coefficients is, however, minimal upon reaching the field-dominated regime.

The anisotropy of the diffusion tensor, i.e. $D_L \neq D_T$, exists over the entire range of E/N for $T = 0$ K. Figure 8 exhibits the ratio of ND_T to ND_L, as a function of E/N, for $T = 1260$ K, $T = 3260$ K, and $T = 5260$ K. As indicated on the graph, both the flux and bulk data are shown. Generally speaking, the anisotropy of the diffusion for electrons in

indium vapour, over the range of vapour temperatures considered in the present work, is relatively low, with the differences between ND_T and ND_L not exceeding approximately 30%. In the limit of the lowest values of E/N, as already emphasized, the diffusion is nearly isotropic. Small fluctuations of the ratio between ND_T and ND_L around unity follow from the statistical uncertainties of the dynamical properties sampled in our Monte Carlo simulations, which are required for the calculation of the diffusion coefficients. As E/N increases further, we observe that the anisotropy of the diffusion tensor is reduced for increasing vapour temperature in the intermediate regime. For higher values of E/N, the sensitivity of the ratio of ND_T to ND_L, with respect to the indium vapour temperature, is minimal in the field-dominated regime. It is also interesting to note that for E/N larger than approximately 200 Td, the bulk values of ND_L are larger than the bulk values of ND_T. This is not the case for the corresponding flux values of the diffusion coefficients.
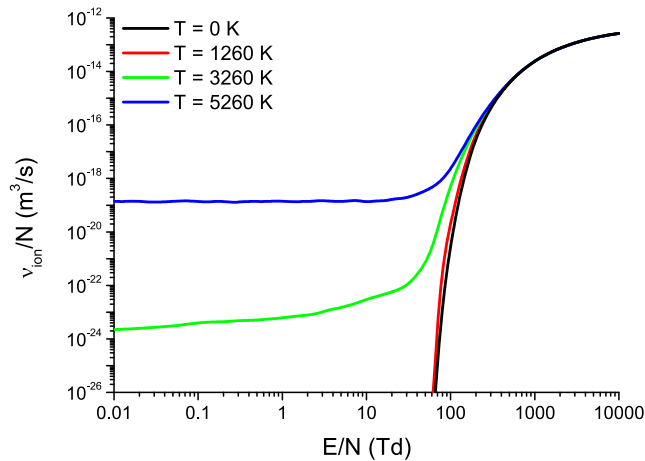
Figure 9. Variation of the ionisation rate of the electron swarm as a function of E/N for various indium vapour temperatures.

In figure 9 we plot the variation of the ionisation rate coefficient as a function of E/N for various vapour temperatures. The ionization rate coefficient corresponds to the density reduced ionization frequency, where the ionization frequency is given by equation (2). As expected, the ionisation rate increases with E/N for all temperatures. The E/N-profiles of ν_{ion}/N, are similar for $T = 0$ K and $T = 1260$ K and resemble the typical behaviour of the ionisation rate in other gases. This follows from the fact that, as in most cases, the E/N-profiles of ν_{ion}/N are essentially featureless, as ionisation only becomes considerable for higher values of E/N when sufficient electrons have enough energy to cause ionisation. However, for higher indium vapour temperatures, e.g. for $T = 3260$ K and $T = 5260$ K, the electrons have enough energy to cause ionisation even in the vapour-dominated regime, i.e. in the limit of the lowest E/N considered in the present work. While at $T = 5260$ K the ionisation rate essentially remains unaltered, at $T = 3260$ K the ionisation rate increases with E/N. Then, as E/N is increased further, the ionisation rates for both $T = 3260$ K and $T = 5260$ K increase rapidly, reaching the field-dominated regime, where the vapour temperature does not affect this property.

Figure 10 displays the variation in the rate coefficients for transfer of momentum in elastic collisions, summed excitation, summed de-excitation, and ionisation as a function of E/N for various vapour temperatures. At $T = 0$ K, the elastic momentum transfer rate increases with E/N up to about 1 Td. Then, as E/N further increases, it starts to decrease slowly in magnitude. For $T = 1260$ K, $T = 3260$ K, and $T = 5260$ K, however, the elastic momentum transfer rate essentially remains constant, before decreasing in the limit of the highest E/N considered in the present work. The summed excitation rate coefficient for $T = 0$ K is a rapidly increasing function of E/N, until ionisation processes start to play a significant role at around 200 Td. For $T = 1260$ K, $T = 3260$ K, and $T = 5260$ K, the summed excitation and de-excitation rates are identical for lower values of E/N, e.g. in the vapour-dominated regime. This follows from detailed balancing and the fact that the electrons are in thermal equilibrium with the

indium vapour. These rate coefficients begin to depart from each other at approximately 20 Td for $T = 1260$ K, 30 Td for 3260 K, and 40 Td for 5260 K, with an increase in excitation events and a decrease in de-excitation events. Comparing the ionisation rates with the rate coefficients for all the other processes considered, we observe that ionisation dominates in the limit of the highest E/N considered in the present study.

In order to illustrate the explicit effects of ionisation collisions on the drift and diffusion of electrons in indium vapour, we show in figure 11 the variation of the percentage difference between the bulk and flux values of the drift velocity (a), and the bulk and flux values of the longitudinal diffusion coefficient (b), as a function of E/N for various vapour temperatures. Figure 11 indicates that the influence of ionisation on the drift and diffusion is not apparent until approximately 200 Td. Even though ionisation is considerable for $T = 3260$ K and $T = 5260$ K in the vapour-dominated regime, the differences between the bulk and flux values of the drift velocity and longitudinal diffusion coefficient are minimal. This could be explained by considering the E/N-dependence of the rate coefficients for the other processes shown in figure 10. There we observe that competitive processes, including electronic excitations and de-excitations, are much more frequent than ionisation processes. As a consequence, the explicit contribution of ionisation to the measurable transport coefficients, e.g. the bulk drift velocity and the bulk diffusion coefficients, are reduced. As E/N increases further, the percentage difference between the bulk and flux values increases, reaching a maximum of around 45% and 80% for the drift velocity and the longitudinal diffusion coefficient, respectively. This indicates that the increase in electron numbers due to ionisation enhances both the drift and diffusion of the electrons in indium vapour. For the highest E/N considered here, the differences between the bulk and flux values are again reduced. Generally speaking, the influence of the vapour temperature on the differences between the bulk and flux values is minimal, reflecting the weak dependence of the drift velocity and longitudinal diffusion coefficient on the temperature in the field-dominated regime. In order to better understand the dual nature of the transport coefficients, and the associated differences between the bulk and flux values of the transport coefficients, the reader is referred to our previous publications [40, 47, 50].

4.3. Electron transport under SST conditions

In this section we present results showing the spatial relaxation of electrons and the variation of electron swarm transport properties with E/N and vapour temperature T under non-hydrodynamic conditions in an idealised SST experiment. Figure 12 shows the exponential growth of the electron number, in the region between the electrodes, as a function of E/N and the temperature. The electrons are released from the cathode into the space between the electrodes, assuming a Maxwell–Boltzmann velocity distribution, with the starting mean energy $\epsilon_0 = 1$ eV. The growth rate in the electron number increases with increasing E/N, indicating that ionisation processes become increasingly important with increasing E/N.
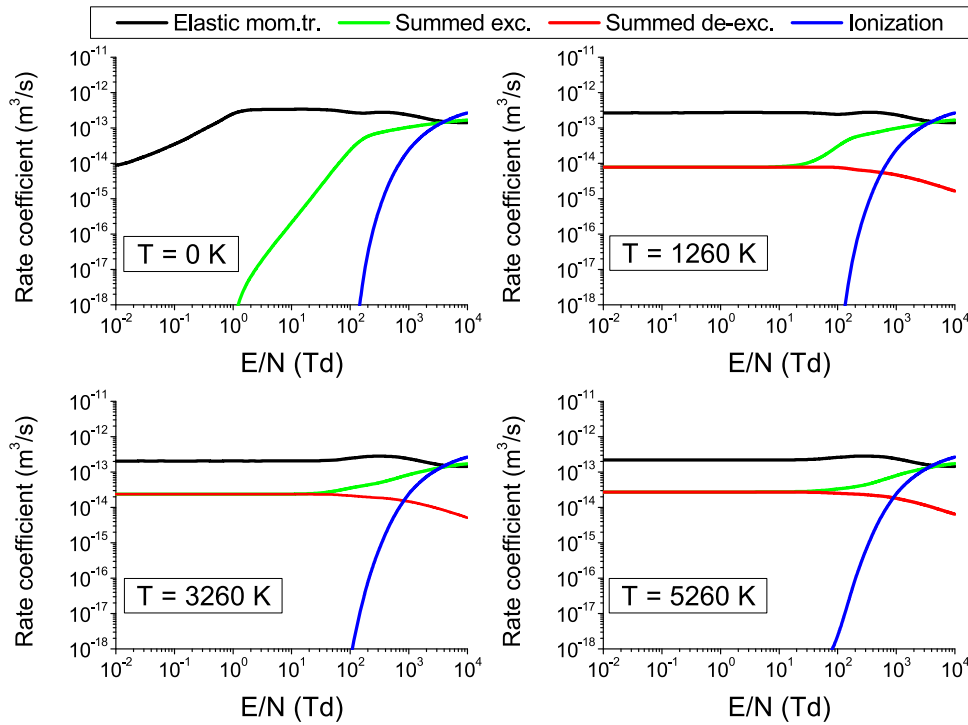
Figure 10. Variation of the rate coefficients for transfer of momentum in elastic collisions, summed excitation, summed de-excitation, and ionisation of the electron swarm, as a function of E/N, for various indium vapour temperatures.
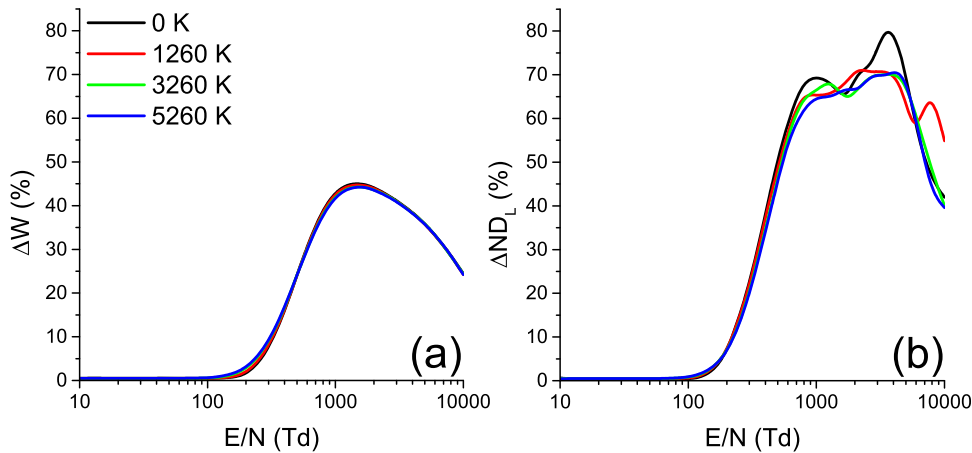

Figure 11. Variation of the percentage difference between the bulk and flux values of the drift velocity (a) and longitudinal diffusion coefficient (b) of the electron swarm, as a function of E/N, for various indium vapour temperatures.

Even though the results are presented on a log–log scale, we observe that the rate of increase in the number of electrons for a fixed E/N increases with the vapour temperature. This is a cumulative effect of the initial spatial relaxation and the following arguments may be used to account for its occurrence. At a fixed reduced electric field, in the initial phase of spatial relaxation, thermal effects play a key role in the multiplication of electrons in ionisation processes. This means that the higher the indium vapour temperature, the more electrons are produced at the beginning of the spatial relaxation. After relaxation, when a steady-state is achieved, these thermal effects are considerably reduced. This is indicative of the field-dominated regime, where swarm behaviour is entirely controlled by the electric field. In this regime, the ionization coefficient is not a function of the indium vapour temperature, which can be clearly seen in figure 9.

Figures 13 and 14 display relaxation profiles of the mean energy and the average velocity for a range of applied reduced electric fields E/N, as indicated on each graph. In both plots the electrons are released from the cathode assuming an initial beam velocity distribution, with a starting mean energy of 1 eV, in indium vapour at $T = 1260$ K. The behaviour of the transport properties is not considered in close vicinity of the anode. The relaxation profiles of the mean energy and the average velocity in indium vapour are consistent with earlier investigations on this topic for other gases [2, 5, 41, 42, 57–59]. First,
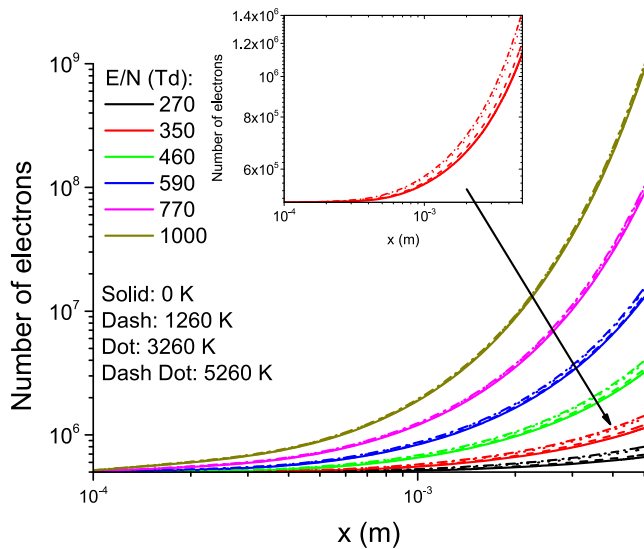
Figure 12. Exponential growth of the number of electrons in an idealized SST experiment as a function of E/N for various indium vapour temperatures.

we observe a limited range of E/N, where the mean energy and average velocity exhibit oscillatory behaviour as they relax towards the stationary state far downstream from the cathode. The spatial relaxation characteristics, including the period and amplitude of the oscillations, and the spatial relaxation length, are distinctively dependent on the applied E/N.

When electrons undergo elastic collisions in indium vapour, the energy transfer is a continuous process occurring in relatively small portions of energy. In inelastic collisions, however, the energy transfer is a discrete process with several orders of magnitude larger portions of energy. In the presence of elastic collisions only, the spatial profiles of the transport quantities would be exclusively monotonic and without oscillations along the relaxation profiles. On the other hand, in the presence of inelastic collisions only, due to the discrete electron energy losses, the spatial profiles would be periodic, with a period inversely proportional to the electric field strength, and an energy threshold that is a composite of several closely-lying inelastic processes that control the relaxation process. For electrons in indium vapour under the conditions considered in the present work, except the zero-temperature case, the electrons undergo both elastic and inelastic collisions with the presence of the elastic collisions always tending to dampen the oscillatory behaviour of the transport properties and broaden the peaks from the profiles. The key quantity in this complex interplay between the elastic and inelastic collisional energy loss processes is the mean energy of the swarm. In the presence of both elastic and inelastic collisions, when the mean swarm energy is much smaller or much larger than the lowest energy threshold of the inelastic processes, the collisional energy loss is controlled by the continuous energy loss processes and, therefore, the spatial relaxation profiles are monotonic or quasi-monotonic on their way to a spatially homogeneous form. Conversely, if the collisional energy loss is primarily controlled by the discrete energy loss processes, then the spatial profiles are periodically decaying.

The occurrence of oscillatory relaxation is particularly stimulated when the threshold energies of the various inelastic processes are concentrated in a relatively narrow energy region. For electrons in indium vapour, the threshold energies span the energy region between approximately 0.3 eV and 6 eV [38, 39]. With the exception of the $T = 0$ K case, for $E/N \leqslant 1$ Td the sensitivity of the relaxation profiles of the mean energy and the average velocity to E/N is minimal. This follows from the fact that the electrons are disturbed only in close vicinity of the cathode, while at longer distances they are essentially in quasi-thermal equilibrium with the indium atoms. As E/N further increases, the oscillatory feature is enhanced, as more and more electrons undergo inelastic collisions. However, the relaxation becomes dramatically slower and the amplitude and period of oscillations are reduced. In particular, when the mean energy is increased to a level that energy losses by inelastic collisions become continuous, the oscillatory feature is reduced. The spatial profiles are then monotonic and the transport properties relax to the spatially uniform states without oscillations.

Figure 15 displays relaxation profiles of the mean energy for a range of applied reduced electric fields E/N and indium vapour temperatures T, as indicated on the graphs. For a fixed value of E/N and for increasing indium vapour temperature T, we observe that significant changes in the spatial relaxation profiles of the mean energy occur. The relaxation proceeds much quicker and, if oscillations are present in the spatial profile, they are quickly dampened. Even though the spatial relaxation of the transport properties is distinctively dependent on E/N, the oscillatory feature is clearly evident for the lower vapour temperatures. As an illustrative example, for $E/N = 4.6$ Td and $T = 0$ K, we observe a sawtooth profile of the mean energy, where the amplitude of oscillations reduces slowly with the distance from the cathode (x). As the temperature T is further increased to 1260 K and 3260 K, the oscillations are first damped and thereafter entirely removed from the spatial profile by $T = 5260$ K. Generally speaking, the spatial relaxation of the mean energy and the other transport properties is monotonic over the entire range of E/N considered in the present work for the indium vapour temperature of 5260 K. For $T = 3260$ K, the relaxation profiles show reduced irregular oscillations, which are quickly dampened with increasing distance from the cathode. Comparing the spatial profiles at $T = 0$ K and $T = 1260$ K over a wide range of E/N (not shown here), we have observed that a window of reduced electric fields, for which the mean energy and transport properties exhibit oscillatory behaviour, is shifted to lower values of E/N. This occurs because of the increase in the mean energy as the indium vapour temperature T rises, enhancing the energy losses due to inelastic collisions, which in turn makes the discrete energy losses more continuous.

Figure 16 displays relaxation profiles of the mean energy for $E/N = 13$ Td and an indium vapour temperature $T = 1260$ K, assuming two different sets of initial conditions, including the beam initial velocity distribution with mean energies of 0.1 eV, 1 eV, and 10 eV (the first row), and a Maxwell velocity distribution with the same starting mean energies (the second row). Generally speaking, for a certain value of E/N,
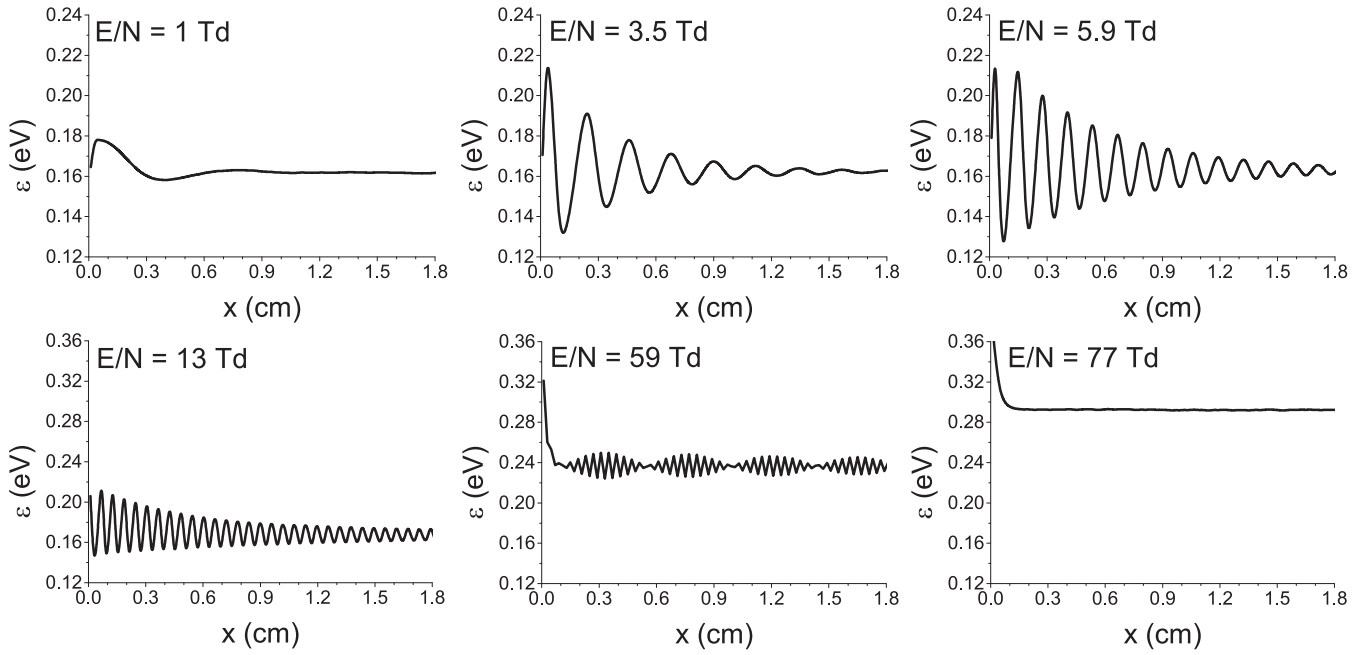
Figure 13. Spatial relaxation of the mean energy for electrons in indium vapour over a range of E/N. The calculations are for a fixed indium vapour temperature of 1260 K. x denotes the distance from the cathode.
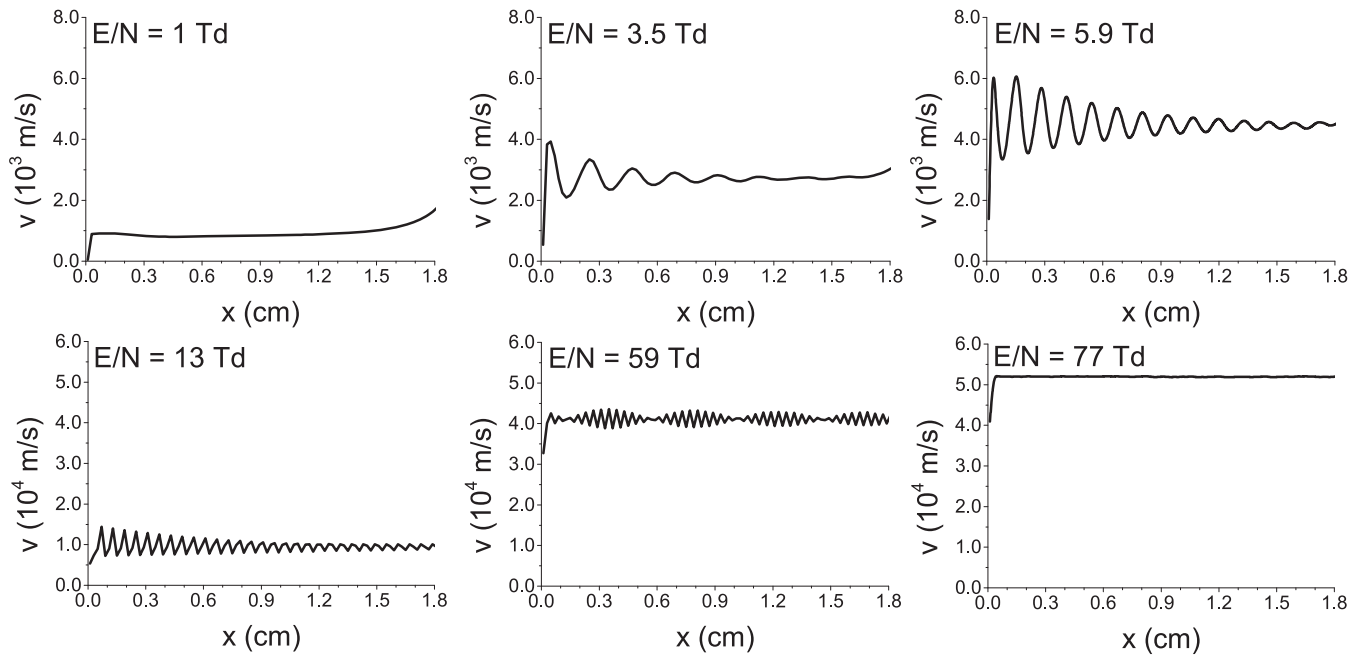

Figure 14. Spatial relaxation of the average velocity for electrons in indium vapour over a range of E/N. The calculations are for a fixed indium vapour temperature of 1260 K. x denotes the distance from the cathode.

the spatial relaxation of the mean energy or any other transport property will be different if the initial conditions for the electrons at the cathode or the disturbing source of electrons are different. On the other hand, the spatially uniform values of the transport properties are independent of the initial values. In the first row of figure 16, where the beam initial velocity distribution is used for the initial conditions, we observe that increasing the mean energy from 0.1 eV to 1 eV does not alter the spatial relaxation significantly. However, when the

initial starting mean energy is further increased to 10 eV, the relaxation is much quicker, i.e. the relaxation length is much less. In addition, we observe that the modulation amplitude and the period of oscillations are also strongly affected. When a Maxwell velocity distribution is used for the initial electrons at the cathode (second row of figure 16), we observe that increasing the starting mean energy from 0.1 eV to 1 eV dampens the oscillations. Then the relaxation proceeds much faster in comparison with the previous case, where the initial beam
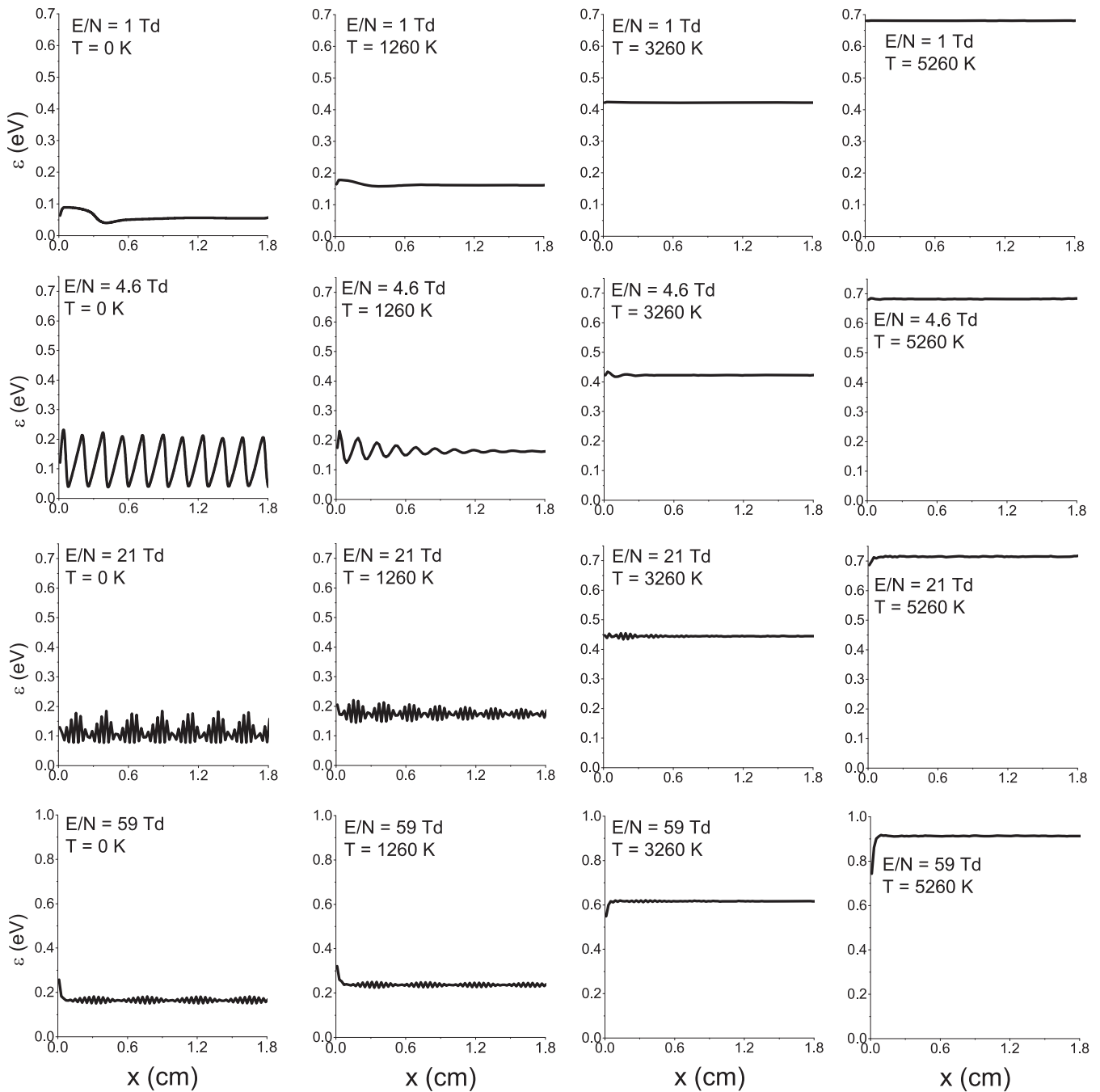
Figure 15. Spatial relaxation of the mean energy for electrons in indium vapour over a range of E/N and indium vapour temperatures T. x denotes the distance from the cathode.

velocity distribution was assumed in the calculations. Regardless of the initial conditions, if the mean electron energy is much higher than the lowest thresholds for inelastic collisions, then the elastic and inelastic collisions are essentially part of the continuous energy loss processes. As a consequence, the oscillatory feature is strongly suppressed and the relaxation towards the spatially uniform state is either monotonic or quasi-monotonic.

Comparing now, in more detail, the spatial profiles in the first and second rows of figure 16, it can be observed that the relaxation proceeds much quicker if a Maxwell initial velocity distribution is employed in the simulations. This is

clearly evident for the starting mean energy of 1 eV. This happens because, according to Maxwell's velocity distribution, the electrons can have a wider range of velocities, so the balance between energy gains from the field and losses in binary collisions with indium atoms is achieved more quickly. In addition to the relaxation length, the modulation amplitude and the period of oscillations are considerably smaller, indicating that the spatial relaxation of electrons in indium vapour may be governed by controlling the initial conditions of the electrons at the cathode.

In the following, we restrict our discussion to the spatially uniform transport properties in an idealised SST setup
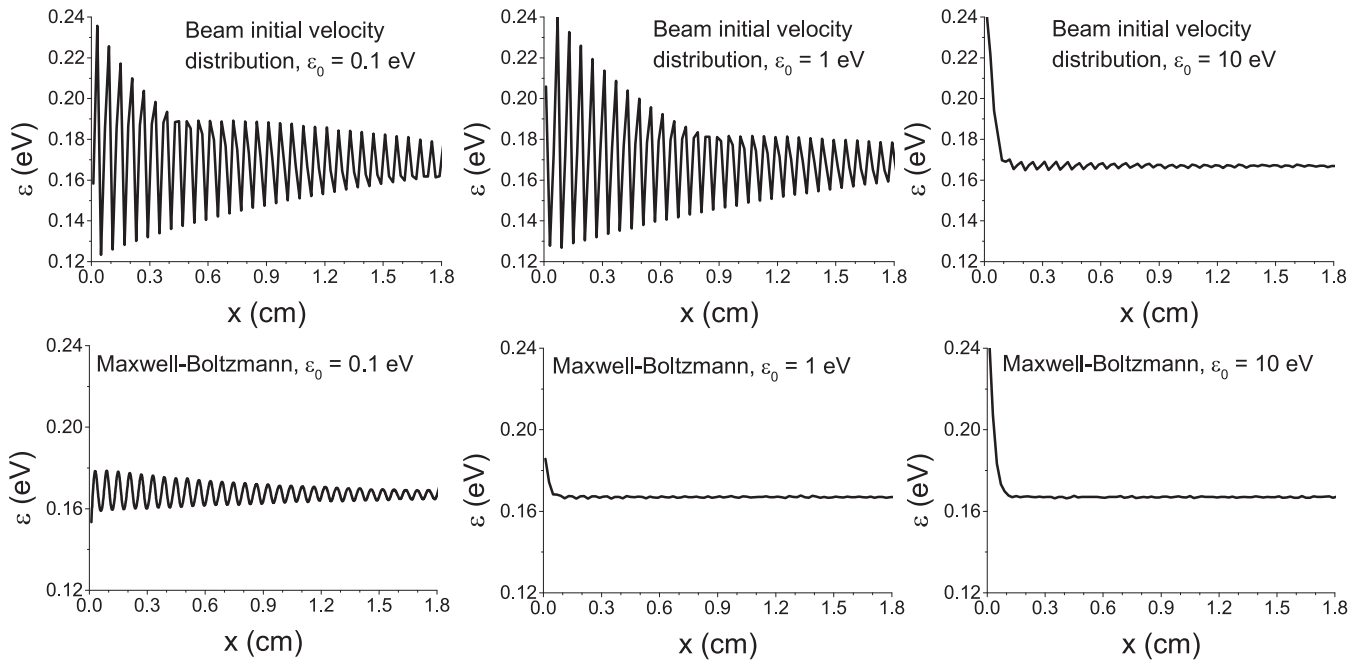
Figure 16. Spatial relaxation of the mean energy for electrons in indium vapour at $E/N = 13$ Td and an indium vapour temperature $T = 1260$ K. The calculations are for two different sets of initial conditions, including the initial beam velocity distribution (first row) and a Maxwell initial velocity distribution (second row), assuming starting mean energies of 0.1 eV, 1 eV, and 10 eV, as indicated on the graph. x again denotes the distance from the cathode.

and their comparison with the hydrodynamic transport coefficients. Using exponential growth curves for the number of electrons under SST conditions, we calculated the density-reduced ionisation coefficient. The SST ionisation coefficient is compared with that derived from our hydrodynamic calculations using the well-known expression [60]

$$\frac{1}{\alpha} = \frac{W}{2\nu_{\text{ION}}} + \sqrt{\left(\frac{W}{2\nu_{\text{ION}}}\right)^2 - \frac{D_{\text{L}}}{\nu_{\text{ION}}}}, \quad (17)$$

where ν_{ION}, W and D_{L} are the ionisation frequency, bulk drift velocity, and bulk longitudinal diffusion coefficient, respectively. This comparison is shown in figure 17. For all indium vapour temperatures and up to about 3000 Td, we observe that the two sets of results agree very well, indicating the validity of the expression (17). For higher values of E/N, however, we do observe differences between the two sets of results.

The comparison between the mean energies calculated under hydrodynamic and SST conditions is shown in figure 18. Similarly, the comparison between the bulk and flux values of the drift velocity and the SST average velocity is shown in figure 19. The calculations were performed assuming the usual indium vapour temperatures. For higher values of E/N, we observe that the mean energy and flux drift velocity are larger than the corresponding SST average velocity and SST mean energy, respectively. On the other hand, the bulk drift velocity dominates both the flux drift velocity and the SST average velocity. This can be explained using the following physical arguments: when the profile of the electron density increases exponentially, with the distance in the direction of the electric field force (see figure 12), then the diffusive flux induced by this gradient is in opposite direction to the drift

flux. As a result, the diffusive flux acts to reduce the drift flux (or the field flux), and hence the SST average velocity is less than the flux drift velocity. As far as the mean energy is concerned, it is a combination of the spatially homogeneous mean energy and the energy component induced by the diffusive processes. The spatially homogeneous mean energy represents a balance of energy accumulated by electrons moving in the electric field and the losses in binary collisions. Since the diffusive flux is in the opposite direction to the drifted flux, the electrons are forced to move against the field force, and therefore their mean energy is reduced. As a consequence, the SST mean energy is less than the corresponding hydrodynamic mean energy. It should be noted that this behaviour of the mean energy and average velocity in an idealised SST experiment does not depend on the nature of the atomic gas. This can be further generalized to molecular gases, but only for electron energies for which the ionisation contributions are larger than the losses due to electron attachment [40].

4.4. Development of an electron avalanche and its transition into a negative ionisation front

In this section we investigate the development of an electron avalanche and its transition into a negative ionisation front in indium vapour. All simulations were started with the same initial Gaussian-type distribution for the electrons and positive ions

$$n_{\text{e}}(x, 0) = \frac{100}{0.05\pi R_0^2 \frac{l}{3}\sqrt{2\pi}} \exp\left(-\frac{1}{2}\frac{(x - 0.95l)^2}{\left(0.05\frac{l}{3}\right)^2}\right), \quad (18)$$

where l is the distance between the imaginary electrodes and R_0 is the streamer radius, which is calculated to first order by
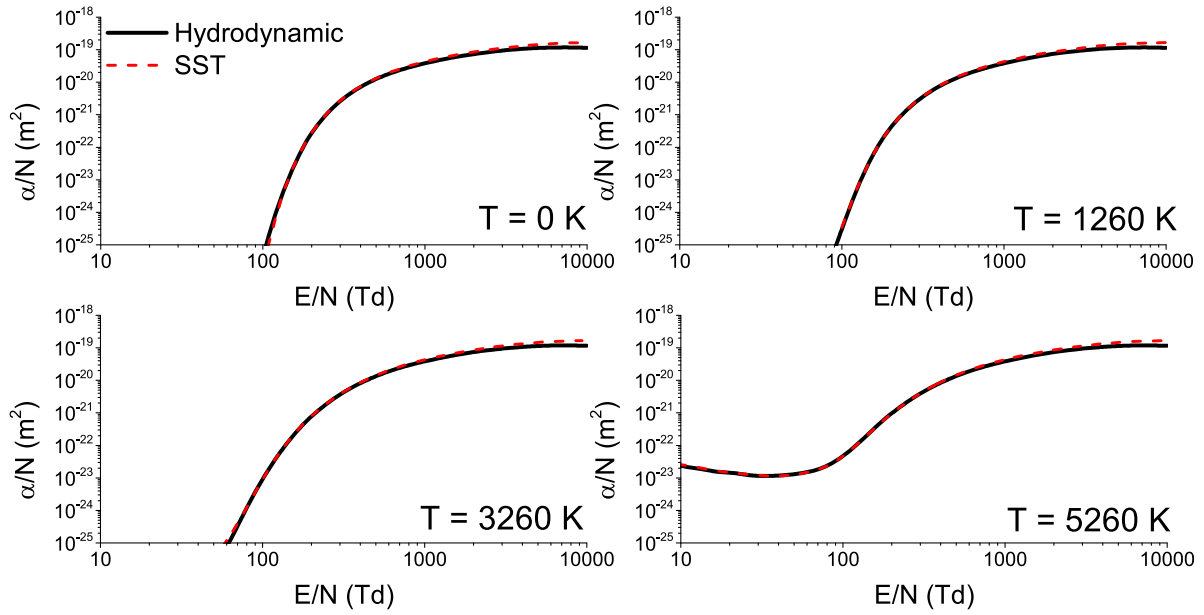
Figure 17. Comparison between the SST reduced ionisation coefficient and the reduced ionisation coefficients calculated using the hydrodynamic values of ionisation frequency, bulk drift velocity, and bulk longitudinal diffusion coefficient. Calculations are performed over a broad range of E/N and indium vapour temperatures T, as indicated on the graph.
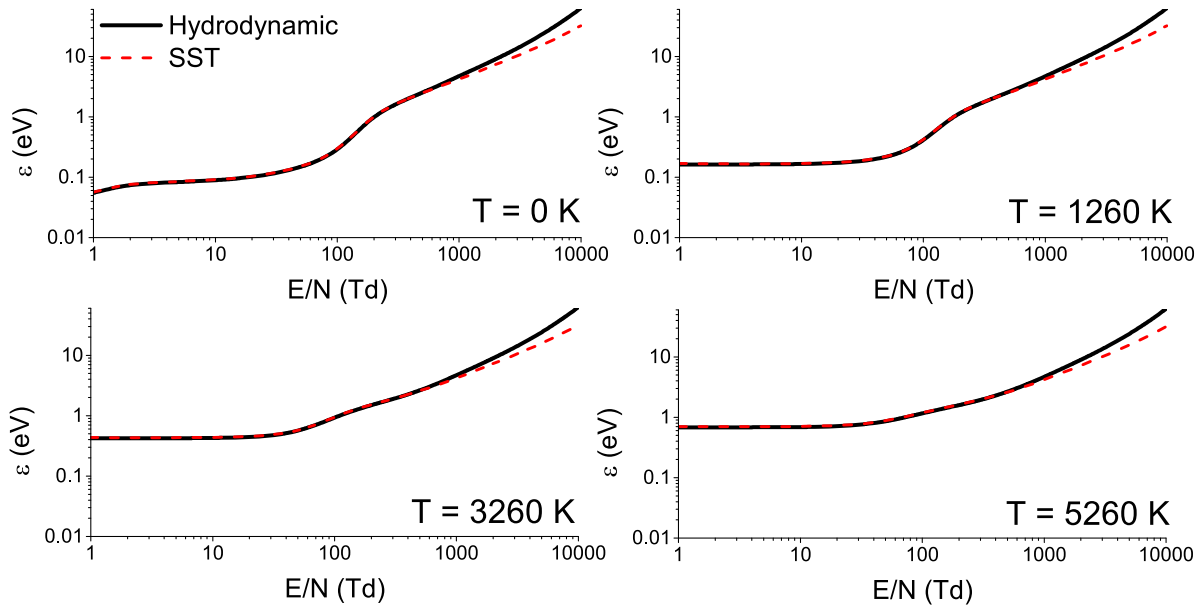

Figure 18. Comparison between the mean energies calculated under hydrodynamic and SST conditions. Calculations are performed over a broad range of E/N and indium vapour temperatures T, as indicated on the graph.

taking into account the initial electron distribution width and the spreading due to diffusion along the transverse direction. The length of the system l is an adjustable parameter, which is determined by the requirement that the streamer velocity relaxes to a stationary value. The externally applied electric field is positive in the x direction, and hence the ionisation fronts propagate to the left. Unless otherwise specified, the simulation results are presented from the 1.5D (axisymmetric) model, in which the radius of the streamer is assumed to be fixed.

Figure 20 exhibits the development of an electron avalanche and its transition into a negative ionisation front for $E/N = 270$ Td and various indium vapour temperatures, as indicated on the graph. The calculations were performed using the bulk transport coefficients as input into the system of fluid equations (13) and (14). The development of an electron avalanche, and its transition to a negative ionisation front, occurs here in the same manner as in other gases [52, 61–64]. In the early stage of development, where there are no space-charge effects, the dynamics of the electron avalanche and
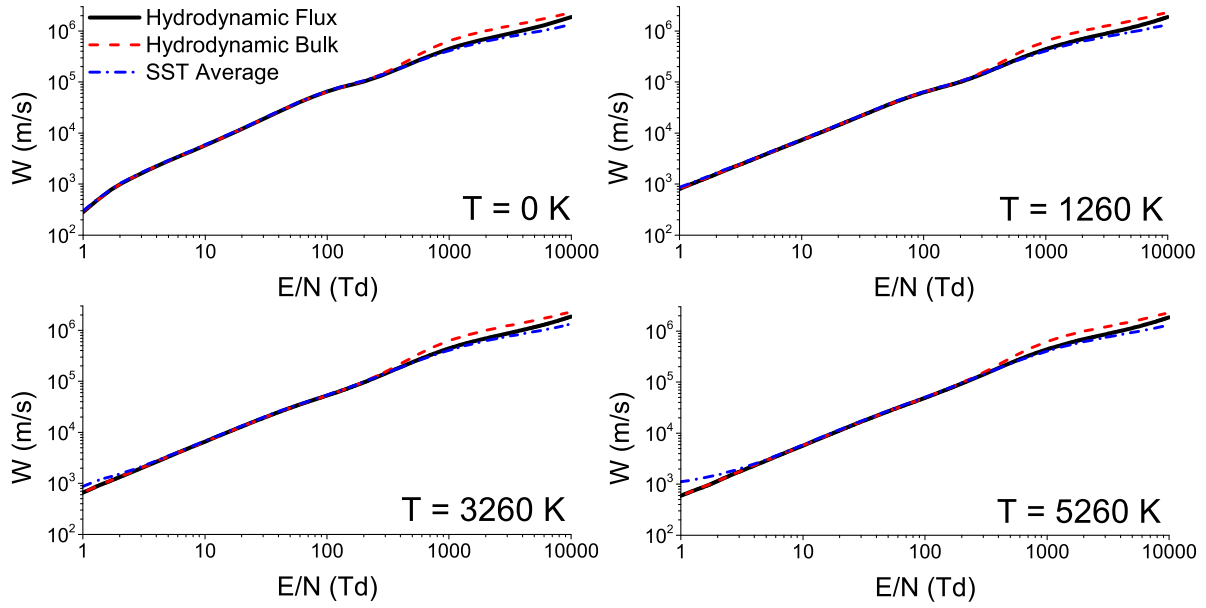
Figure 19. Comparison between the flux and bulk drift velocity, calculated under hydrodynamic conditions, and the SST average velocity. Calculations are performed over a broad range of E/N and indium vapour temperatures T, as indicated on the graph.
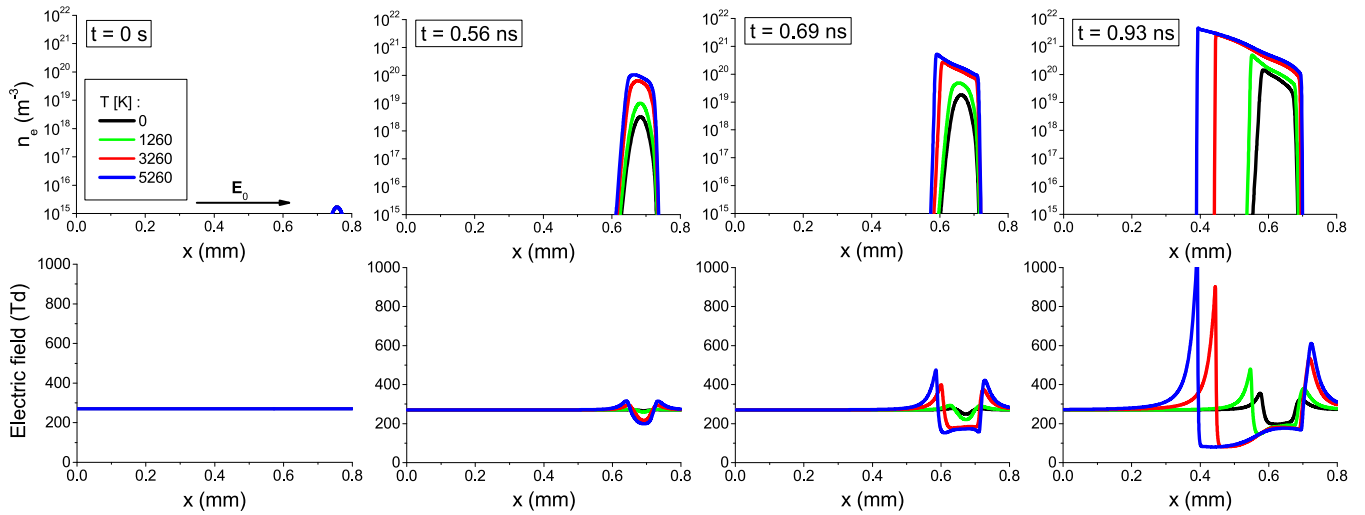
Figure 20. The formation and propagation of a negative ionisation front in indium vapour for $E/N = 270$ Td and various indium vapour temperatures. The calculations are performed using the bulk transport coefficients as input to the classical fluid model.

its spatial and temporal evolution is described by the diffusion equation. The solution of the diffusion equation in free space, and far away from the physical boundaries, is a Gaussian pulse, the peak of which drifts with the bulk drift velocity and diffuses around the centre of mass according to the values of the diffusion coefficient [65]. The electrons drift in the opposite direction to the electric field, while the positive ions are effectively motionless, since the mobility of the electrons is much higher than the mobility of positive ions on the time scales we consider in this work. As a consequence, charge separation occurs and the effects of the space charge develop, which screen the external electric field in the streamer interior. Since the simulations were performed in 1.5D, the space-charge effects do not fully screen the external electric field behind the streamer front. At the same time, at the front of the

streamer, we observe a characteristic field enhancement, which can lead to the appearance of runaway electrons. In any case, as the temperature of the indium vapour rises, the electron density and the streamer velocity increase. This can be explained by the fact that, as the temperature increases, the concentration of metastables and the ionisation coefficient are increased, which in turn accelerate the propagation of the streamer.

In order to better observe the effect of the indium vapour temperature on the spatial and temporal evolution of the electron density in the streamer channel, we show in figure 21 the formation and development of a negative streamer in 1D. The boundary conditions for the numerical solution of the fluid equations are modified: for $x = 0$ we use a homogeneous Neumann boundary condition, to ensure that the electrons that arrive at this boundary may flow out of the system, while for
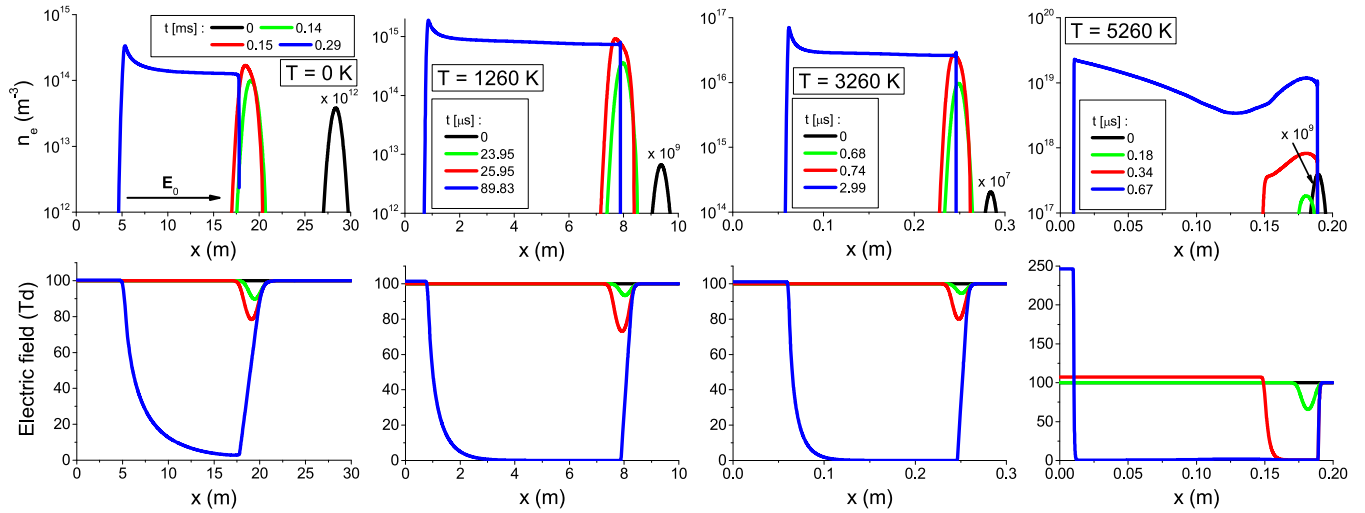
Figure 21. The formation and propagation of a negative ionisation front in indium vapour for $E/N = 100$ Td and various indium vapour temperatures. The calculations are performed using the 1D-set up and the bulk transport coefficients as input to the classical fluid model.
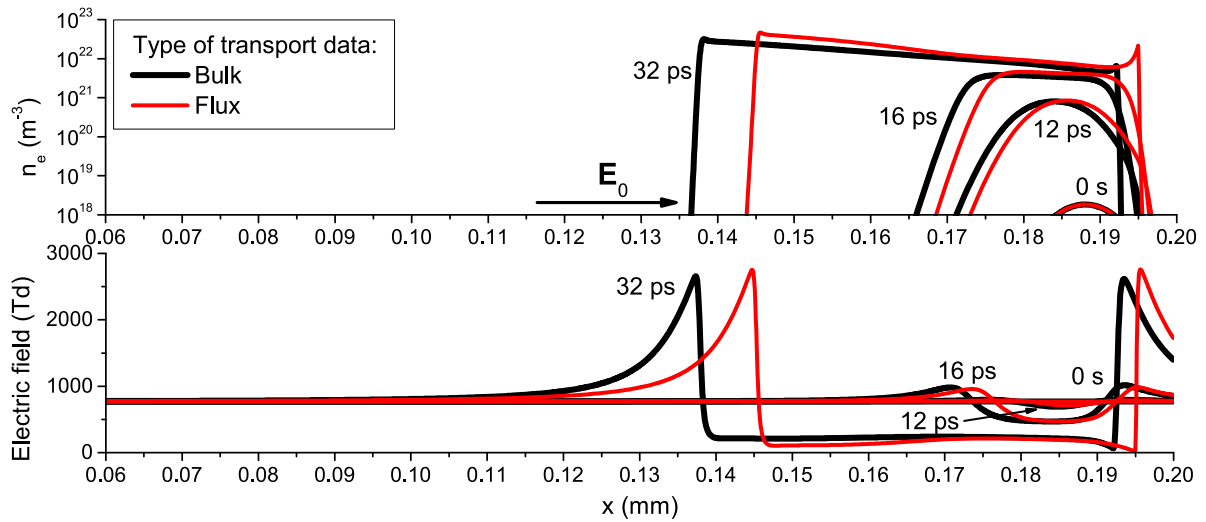
Figure 22. The formation and propagation of a negative ionisation front in indium vapour for $E/N = 770$ Td and $T = 1260$ K. The calculations are performed using the bulk and flux transport coefficients as input to the 1.5D classical fluid model.

$x = d$ we employ a homogeneous Dirichlet boundary condition in order to prevent the outflow of electrons from the system. Bulk transport coefficients were used as input data for the fluid equations. In this case we can observe in figure 21 that streamers at different indium vapour temperatures propagate on completely different time scales. When the full streamer is formed, we may observe a characteristic overshooting effect in the profile of the electron density at the streamer front. Comparing results from the 1D and 1.5D models, the electron density decreases more slowly in the streamer interior behind the front. For an indium vapour temperature $T = 5260$ K, we observe an increase in the electron density at the trailing edge of the negative streamer, where the external electric field is completely screened. This is due to the fact that electrons, even in the limit of thermal energies, where the electric field is entirely screened, may ionize indium atoms in both the ground and metastable states. Similar effects were observed

at lower temperatures, but in this case it was necessary to follow the streamers through space and time much longer. The complete screening of the electric field in the streamer channel is one of the important features distinguishing the results of our simulations in 1D and 1.5D.

Figure 22 illustrates the formation and propagation of a negative ionisation front, under the influence of an externally applied reduced electric field E_0/N of 770 Td. Calculations were performed for an indium vapour temperature of $T = 1260$ K, using the flux and the bulk transport coefficients as input into the system of fluid equations (13) and (14). Figure 22 clearly indicates that the ionisation front at a time of 32 picoseconds, obtained with the bulk drift velocity and the bulk longitudinal diffusion coefficient, is wider while its height is less than with the flux transport coefficients. Similar results were found for ionisation fronts in the 1D configuration and in other gases [52, 61, 64]. As the ionisation rate is the
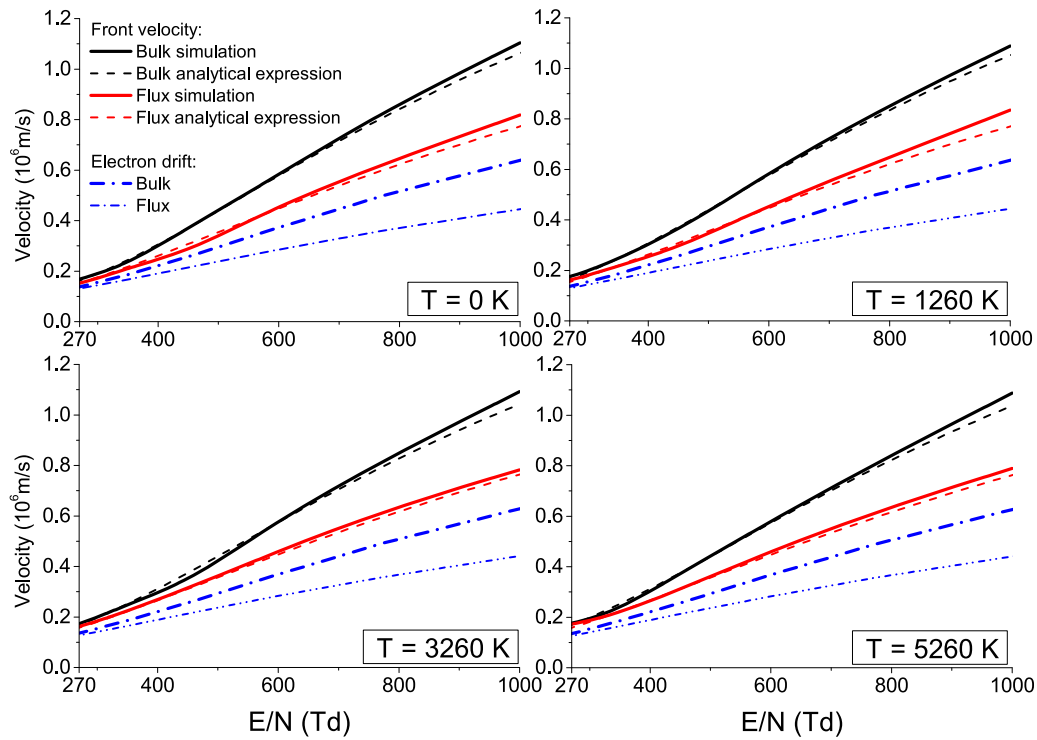
Figure 23. Velocities of planar 1D ionisation fronts as a function of the reduced electric field. The bulk and flux drift velocities of electrons are also included.

same in both cases, figure 22 can be explained by the fact that the bulk drift velocity and the longitudinal diffusion coefficient are larger than the corresponding flux data. Thus, in the early stage of evolution, the motion and diffusion of the centre of mass are faster with the bulk transport coefficients. The same trend continues after completing the transition of an electron avalanche into a negative streamer and during its propagation.

Besides the ionisation level in the streamer interior and the field enhancement at its front, the front velocity is one of the most important streamer properties. It is calculated by following the evolution of a certain level of the electron density at the ionisation front [52, 61, 64]. For ionisation fronts in indium vapour, and for the range of reduced electric fields and vapour temperatures considered in the present work, we observed that after the initial stage of acceleration, deceleration follows towards the quasi-stationary state, where the streamer velocity does not change in time. For planar ionisation fronts in 1D, the velocity of the streamer may be calculated using the following analytical expression [62, 66, 67]:

$$v = \mu(E)E + 2\sqrt{D_{\mathrm{L}}(E)\mu(E)E\alpha(E)}. \tag{19}$$

Here $\mu(E)$ is the electron mobility, E is the electric field strength, D_{L} is the longitudinal diffusion coefficient, and α is the first Townsend ionisation coefficient. Figure 23 shows a comparison between the streamer velocities we obtained in our simulations and those based on the analytic expression (19). The motivation behind using the analytical expression (19) is that, in principle, one may attempt to use swarm data to calculate the streamer velocity. The same figure shows the variation of the bulk and flux drift velocity with E/N. We observe that

the streamer velocity exceeds the bulk and flux drift velocities by more than a factor of two for the largest E/N displayed here. This is one of the common features of streamers in neutral gases [52, 61, 64] and atomic liquids [68]. The velocity of a negative planar ionisation front is determined by the combination of the electron velocity and the ionisation rate in the streamer head. In addition, the ionisation front is pushed further forward due to a strong diffusive flux, which is induced by the strong gradient in the electron density.

The front velocities we obtained in our simulations and those calculated using the analytical expression (19) agree very well. Regardless of the indium vapour temperature, the difference between the two sets of data is most pronounced for the highest E/N value. Finally, we note that the velocities obtained with the bulk data are always larger than those evaluated by the flux data.

5. Conclusions and outlook

We studied the electron transport and propagation of negative ionisation fronts in indium vapour. Among many important points, the key results originating from this work are:

(a) We utilize the available *ab initio* electron impact cross sections for elastic, inelastic, and ionisation processes in indium vapour [39]. Those calculations were performed for indium atoms in the ground state $(5s^25p)^2P_{1/2}$ and the close-by metastable state $(5s^25p)^2P_{3/2}$.

(b) Cross sections for superelastic collisions were calculated by applying the principle of microscopic reversibility and detailed balance in a thermal equilibrium. The fractional

populations of the excited metastable state $(5s^2 5p)^2 P_{3/2}$ were calculated over a range of indium vapour temperatures, and the mixtures of indium atoms in the ground state and the metastable state were made and prepared as input for our Monte Carlo simulations of electron transport.

(c) Using a Monte Carlo simulation technique, the electron swarm transport coefficients were calculated over a range of reduced electric fields E/N and indium vapour temperatures, T, under hydrodynamic conditions. We identified three distinct regimes of electron transport. In the vapour-dominated regime, the velocity distribution function was approximately thermal Maxwellian, while the electron swarm transport coefficients were distinctively dependent on the indium vapour temperature. The intermediate regime was characterized by a non-Maxwellian velocity distribution function, but the electron swarm transport coefficients were to a large extent still found to depend on the indium vapour temperature, T. For higher values of E/N, we noticed that the influence of the indium vapour temperature on the velocity distribution function and transport coefficients was minimal. Under those condition, the velocity distribution function significantly deviated from a thermal Maxwellian.

(d) The initial Monte Carlo code was extended and generalized to consider the spatial relaxation of the electrons and transport under non-hydrodynamic conditions in an idealised SST experiment, when the background gas is heated to high temperatures. It was demonstrated that the spatial relaxation of the mean energy and average velocity was controlled by the nature of the collisional energy loss process in question. It was also shown that the nature of the spatial profiles could be controlled by varying the temperature of the indium vapour, with the oscillations along the decaying profile being suppressed by increasing the indium vapour temperature. Similarly, it was observed that different initial conditions altered the spatial profiles, including the modulation amplitude, relaxation length, and the period of oscillations. The spatially uniform values of the mean energy and average velocity were compared with the corresponding hydrodynamic values. Likewise, the ionisation coefficient evaluated directly from an idealised SST experiment was compared with the value estimated using the hydrodynamic results of the ionisation rate, drift velocity, and longitudinal diffusion coefficient. That two sets of data agreed very well except for the highest E/N. The disagreement between the two sets of data for higher values of E/N was addressed using physical arguments.

(e) Employing the classical fluid model, which was implemented within the 1D and 1.5D setups, we investigated the development of an electron avalanche and its transition into a negative ionisation front. The transition from an electron avalanche into a negative streamer occurred faster with increasing indium vapour temperature. The streamer properties, including the front velocity, the field enhancement at the streamer front, the ionisation level behind the front, and the overall distribution of the electric field, depend on the indium vapour temperature and the level of presence of metastable indium atoms. This was especially pronounced at lower values of E/N, where the differences in the ionisation coefficient were large at different indium vapour temperatures. Streamers obtained in simulations with bulk transport coefficients were faster than those with flux transport coefficients, indicating that the nature of the transport coefficients in plasma modelling must be carefully considered before their direct application.

Regarding future studies, the cross sections for electron scattering in indium vapour might be gainfully applied to the modelling of electron transport in radio-frequency electric and magnetic fields. It would be interesting to consider, for example, the influence of indium metastable states on the temporal profiles of the transport coefficients, especially under conditions in which resonant absorption of energy in the oscillating radio-frequency electric and magnetic fields takes place [69]. Another logical extension of the current work in indium vapour would be to consider resonances induced by spatial non-locality, as investigated recently for electrons in argon and its mixtures with N_2 [70]. In the context of further streamer studies, it will be challenging to study the occurrence of non-local effects in the profile of the mean energy, in the streamer interior behind the propagating front, and in the branching of the streamers, by carrying out particle-in-cell/Monte Carlo simulations [71] and/or employing a high-order fluid model [52]. Likewise, another remaining step to be taken is to understand the effects of the breakdown voltages on the parameters of the equivalent circuit in high-intensity discharge lamps, where the cathode-directed streamers and the kinetics of the positive indium ions should be carefully considered. All the above applications will remain the focus of our future work.

Acknowledgments

Data availability statement

All data that support the findings of this study are included within the article (and any supplementary files).

ORCID iDs

S Dujko https://orcid.org/0000-0002-4544-9106
J Atić https://orcid.org/0000-0003-1800-8628
D Bošnjaković https://orcid.org/0000-0002-2725-5287
R D White https://orcid.org/0000-0001-5353-7440
P Stokes https://orcid.org/0000-0002-0956-5927
K R Hamilton https://orcid.org/0000-0002-8245-0122
O Zatsarinny https://orcid.org/0000-0001-8253-883X
K Bartschat https://orcid.org/0000-0001-6215-5014
D Šević https://orcid.org/0000-0002-7206-6370
B P Marinković https://orcid.org/0000-0002-6904-6360
D V Fursa https://orcid.org/0000-0002-3951-9016
I Bray https://orcid.org/0000-0001-7554-8044
F Blanco https://orcid.org/0000-0003-4332-434X
D B Jones https://orcid.org/0000-0001-7425-7157
L Campbell https://orcid.org/0000-0003-0728-554X
M J Brunger https://orcid.org/0000-0002-7743-2990

References

[1] Franck J and Hertz G 1914 *Verh. Dtsch. Phys. Ges.* **16** 457
[2] Robson R E, Li B and White R D 2000 *J. Phys. B: At. Mol. Opt. Phys.* **33** 507
[3] Sigeneger F, Winkler R and Robson R E 2003 *Contrib. Plasma Phys.* **43** 178
[4] Robson R E, White R D and Hildebrandth M 2014 *Eur. Phys. J. D* **68** 88
[5] Magyar P, Korolov I and Donko Z 2012 *Phys. Rev.* E **85** 056409
[6] Braglia G L, Diligenti M, Wilhelm J and Winkler R 1990 *Il Nuovo Cimento* D **12** 257
[7] Winkler R, Wilhelm J, Braglia G L and Diligenti M 1990 *Il Nuovo Cimento* D **12** 975
[8] Yousfi M, Zissis G, Alkaa A and Damelincourt J J 1990 *Phys. Rev.* A **42** 978
[9] England J and Elford M 1991 *Aust. J. Phys.* **44** 647
[10] McEachran R P and Elford M T 2003 *J. Phys. B: At. Mol. Opt. Phys.* **36** 427
[11] Mirić J, Simonović I, Petrović Z L, White R D and Dujko S 2017 *Eur. Phys. J. D* **71** 289
[12] Al-Amin S A J and Lucas J 1988 *J. Phys. D: Appl. Phys.* **21** 1261
[13] Rajasekaran K and Naidu M S 1991 *J. Appl. Phys.* **70** 4159
[14] Winkler R B, Wilhelm J and Winkler R 1983 *Ann. Phys.* **495** 90
[15] Winkler R B, Wilhelm J and Winkler R 1983 *Ann. Phys.* **495** 119
[16] Lister G, Lawler J, Lapatovich W and Godyak V 2004 *Rev. Mod. Phys.* **76** 541
[17] Flesch P 2006 *Light and Light Sources* (Berlin: Springer)
[18] White R D, McEachran R P, Robson R E, Elford M T and Bartschat K 2004 *J. Phys. D: Appl. Phys.* **37** 3185
[19] Born M 2001 *J. Phys. D: Appl. Phys.* **34** 909
[20] Csel M 2004 *Fundamentals of Light Sources and Lasers* (New York: Wiley)
[21] Schnick M, Füssel U, Hertel M, Rose S, Haessler M, Spille-Kohoff A and Murphy A B 2011 *Weld. World* **55** 114
[22] Yang W, Meng X, Zhou Q and Dong Z 2019 *AIP Adv.* **9** 035041
[23] Zatsarinny O and Bartschat K 2008 *Phys. Rev.* A **77** 062701
[24] Zatsarinny O, Bartschat K, Babaeva N Y and Kushner M J 2014 *Plasma Sources Sci. Technol.* **23** 035011
[25] McEachran R P, Marinković B P, García G, White R D, Stokes P W, Jones D B and Brunger M J 2020 *J. Phys. Chem. Ref. Data* **49** 013102
[26] McEachran R P, Blanco F, García G, Stokes P W, White R D and Brunger M J 2018 *J. Phys. Chem. Ref. Data* **47** 043104
[27] Hagelaar G J M and Pitchford L C 2005 *Plasma Sources Sci. Technol.* **14** 722
[28] Rabie M and Franck C M 2016 *Comput. Phys. Commun.* **203** 268
[29] McEachran R P, Blanco F, García G and Brunger M J 2018 *J. Phys. Chem. Ref. Data* **47** 33103
[30] Aldridge S 2011 The chemistry of the group 13 metals in the +3 oxidation state: simple inorganic compounds *The Group 13 Metals Aluminium, Gallium, Indium and Thallium: Chemical Patterns and Peculiarities* ed S Aldridge and A J Downs (New York: Wiley)
[31] Jones C and Stasch A 2011 The chemistry of the group 13 metals in the +1 oxidation state *The Group 13 Metals Aluminium, Gallium, Indium and Thallium: Chemical Patterns and Peculiarities* ed S Aldridge and A J Downs (New York: Wiley)
[32] Šević D, Rabasović M, Pejčev V and Marinković B P 2013 Experimental study of indium atom using electron and optical spectroscopy *Indium: Properties, Technological Applications and Health Issues* ed H G Woo and H T Choi (New York: Nova Science Publishers)
[33] Azad Malik M and O'Brien P 2011 III—V and related semiconductor materials *The Group 13 Metals Aluminium, Gallium, Indium and Thallium: Chemical Patterns and Peculiarities* ed S Aldridge and A J Downs (New York: Wiley)
[34] Nakamura S 2015 *Rev. Mod. Phys.* **87** 1139
[35] Hayashi D, Hilbig R, Körber A, Schwan S, Scholl R, Boerger M and Huppertz M 2010 *Appl. Phys. Lett.* **96** 061503
[36] Ögün C M, Truong W, Kaiser C, Kling R and Heering W 2014 *J. Phys. D: Appl. Phys.* **47** 285202
[37] Fedorov P P, Popov A I and Simoneaux R L 2017 *Russ. Chem. Rev.* **86** 240
[38] Hamilton K R *et al* 2020 *Phys. Rev.* A **102** 022801
[39] Hamilton K R *et al* 2021 *J. Phys. Chem. Ref. Data* **50** 013101
[40] Dujko S, White R D and Petrović Z L 2008 *J. Phys. D: Appl. Phys.* **41** 245205
[41] Dujko S, White R D, Raspopović Z M and Petrović Z L 2012 *Nucl. Instrum. Methods Phys. Res.* B **279** 84
[42] White R D, Robson R E, Nicoletopoulos P and Dujko S 2012 *Eur. Phys. J. D* **66** 1
[43] Czichy M, Hartmann T, Mentel J and Awakowicz P 2008 *J. Phys. D: Appl. Phys.* **41** 144027
[44] Wendt M, Peters S, Loffhagen D, Kloss A and Kettlitz M 2009 *J. Phys. D: Appl. Phys.* **42** 185208
[45] Ristivojevic Z and Petrović Z L 2012 *Plasma Sources Sci. Technol.* **21** 035001
[46] Raspopovic Z M, Sakadzic S, Bzenic S A and Petrovic Z L 1999 *IEEE Trans. Plasma Sci.* **27** 1241
[47] Dujko S, Raspopović Z M and Petrović Z L 2005 *J. Phys. D: Appl. Phys.* **38** 2952
[48] Robson R 1991 *Aust. J. Phys.* **44** 685
[49] Petrović Z L, Dujko S, Marić D, Malović G, Nikitovi Z, Šašić O, Jovanović J, Stojanović V and Radmilović-Radjenović M 2009 *J. Phys. D: Appl. Phys.* **42** 194002
[50] Mirić J, Bošnjaković D, Simonović I, Petrović Z L and Dujko S 2016 *Plasma Sources Sci. Technol.* **25** 065010
[51] Stojanovic V D and Petrovic Z L 1998 *J. Phys. D: Appl. Phys.* **31** 834
[52] Dujko S, Markosyan A H, White R D and Ebert U 2013 *J. Phys. D: Appl. Phys.* **46** 475202

[53] Agnihotri A, Hundsdorfer W and Ebert U 2016 *Japan. J. Appl. Phys.* **55** 07LD06

[54] Agnihotri A, Hundsdorfer W and Ebert U 2017 *Plasma Sources Sci. Technol.* **26** 095003

[55] Bošnjaković D, Petrović Z L and Dujko S 2016 *J. Phys. D: Appl. Phys.* **49** 405201

[56] Petrovic Z, Crompton R and Haddad G 1984 *Aust. J. Phys.* **37** 23

[57] Donkó Z, Hartmann P, Korolov I, Jeges V, Bošnjaković D and Dujko S 2019 *Plasma Sources Sci. Technol.* **28** 095007

[58] Li B, White R D and Robson R E 2002 *J. Phys. D: Appl. Phys.* **35** 2914

[59] Dyatko N A, Kochetov I V and Ochkin V N 2020 *Plasma Sources Sci. Technol.* **29** 125007

[60] Blevin H and Fletcher J 1984 *Aust. J. Phys.* **37** 593

[61] Markosyan A H, Dujko S and Ebert U 2013 *J. Phys. D: Appl. Phys.* **46** 475203

[62] Li C, Brok W J M, Ebert U and van der Mullen J J A M 2007 *J. Appl. Phys.* **101** 123305

[63] Li C, Ebert U and Hundsdorfer W 2010 *J. Comput. Phys.* **229** 200

[64] Markosyan A H, Teunissen J, Dujko S and Ebert U 2015 *Plasma Sources Sci. Technol.* **24** 065002

[65] Kumar K, Skullerud H and Robson R 1980 *Aust. J. Phys.* **33** 343

[66] Ebert U, van Saarloos W and Caroli C 1997 *Phys. Rev.* E **55** 1530

[67] Lagarkov A N and Rutkevich I M 1994 *Ionisation Waves in Electrical Breakdown of Gases* (Berlin: Springer)

[68] Simonović I, Garland N A, Bošnjaković D, Petrović Z L, White R D and Dujko S 2019 *Plasma Sources Sci. Technol.* **28** 015006

[69] Dujko S, Bošnjaković D, White R D and Petrović Z L 2015 *Plasma Sources Sci. Technol.* **24** 054006

[70] Albert A, Bošnjaković D, Dujko S and Donkó Z 2021 *J. Phys. D: Appl. Phys.* **54** 135202

[71] Nijdam S, Teunissen J and Ebert U 2020 *Plasma Sources Sci. Technol.* **29** 103001

Recommended Cross Sections for Electron–Indium Scattering _F

K. R. Hamilton, O. Zatsarinny, K. Bartschat, M. S. Rabasović, D. Šević, B. P. Marinković, S. Dujko, J. Atić, D. V. Fursa, I. Bray, R. P. McEachran, F. Blanco, G. García, P. W. Stokes, R. D. White, D. B. Jones, L. Campbell, and M. J. Brunger

COLLECTIONS

F   This paper was selected as Featured

View Online   Export Citation   CrossMark
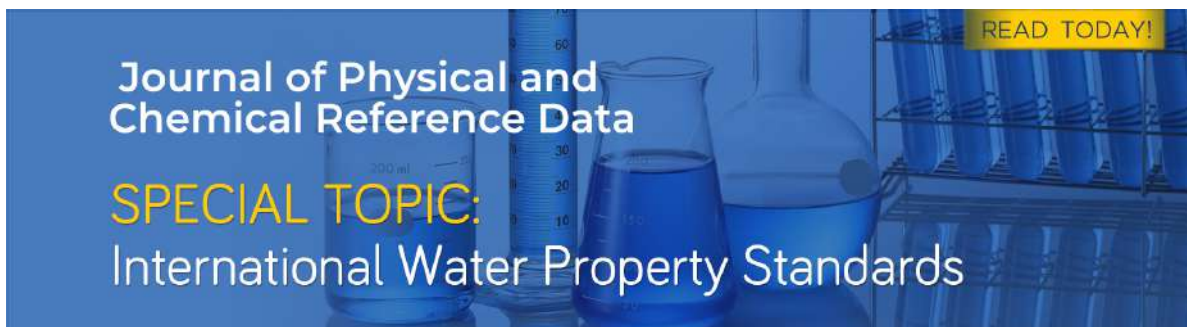
ARTICLES YOU MAY BE INTERESTED IN

Solution of Multiscale Partial Differential Equations Using Wavelets
Computers in Physics **12**, 548 (1998); https://doi.org/10.1063/1.168739

A method of flight path and chirp pattern reconstruction for multiple flying bats
Acoustics Research Letters Online **6**, 257 (2005); https://doi.org/10.1121/1.2046567

Chinese Abstracts
Chinese Journal of Chemical Physics **33**, i (2020); https://doi.org/10.1063/1674-0068/33/06/cabs

Recommended Cross Sections for Electron–Indium Scattering (F)

K. R. Hamilton,[1] (iD) O. Zatsarinny,[1] K. Bartschat,[1] M. S. Rabasović,[2] (iD) D. Šević,[2] (iD) B. P. Marinković,[2] (iD) S. Dujko,[2] (iD) J. Atić,[2] D. V. Fursa,[3] (iD) I. Bray,[3] (iD) R. P. McEachran,[4] F. Blanco,[5] (iD) G. García,[6] (iD) P. W. Stokes,[7] R. D. White,[7] (iD) D. B. Jones,[8] L. Campbell,[8] (iD) and M. J. Brunger[8,9,a)] (iD)

AFFILIATIONS

[1]Department of Physics and Astronomy, Drake University, Des Moines, Iowa 50311, USA
[2]Institute of Physics Belgrade, University of Belgrade, Pregrevica 118, 11080 Belgrade, Serbia
[3]Curtin Insititute for Computation and Department of Physics and Astronomy, Perth 6102, WA, Austraila
[4]Laser Physics Centre, RSP, Australian National University, Canberra, ACT 0200, Australia
[5]Departamento de Estructura de La Materia, Física Térmica y Electrónica e IPARCOS, Universidad Complutense de Madrid, Avenida Complutense, E-28040 Madrid, Spain
[6]Instituto de Física Fundamental, CSIC, Serrano 113-bis, E-28006 Madrid, Spain
[7]College of Science and Engineering, James Cook University, Townsville, Queensland 4810, Australia
[8]College of Science and Engineering, Flinders University, GPO Box 2100, Adelaide, SA 5001, Australia
[9]Department of Actuarial Science and Applied Statistics, Faculty of Business and Management, UCSI University, Kuala Lumpur 56000, Malaysia

a)Author to whom correspondence should be addressed: michael.brunger@flinders.edu.au

ABSTRACT

We report, over an extended energy range, recommended angle-integrated cross sections for elastic scattering, discrete inelastic scattering processes, and the total ionization cross section for electron scattering from atomic indium. In addition, from those angle-integrated cross sections, a grand total cross section is subsequently derived. To construct those recommended cross-section databases, results from original B-spline R-matrix, relativistic convergent close-coupling, and relativistic optical-potential computations are also presented here. Electron transport coefficients are subsequently calculated, using our recommended database, for reduced electric fields ranging from 0.01 Td to 10 000 Td using a multiterm solution of Boltzmann's equation. To facilitate those simulations, a recommended elastic momentum transfer cross-section set is also constructed and presented here.

Published by AIP Publishing on behalf of the National Institute of Standards and Technology. https://doi.org/10.1063/5.0035218

Key words: electron scattering cross sections; electron transport; recommended cross-section data; indium.

CONTENTS

List of Figures

1. Introduction

In our recent experimental and theoretical study on the electron-impact excitation of the $(5s^2 5p)^2 P_{1/2} \rightarrow (5s^2 6s)^2 S_{1/2}$ transition in indium (In),[1] we outlined a number of basic-science and applied rationales for why indium is a target of general interest. Of particular relevance to this work, where we attempt to compile a complete cross-section database over a wide energy range, is the need to have such a complete database in order to conduct quantitative modeling investigations for electron transport in indium under an applied electric field (e.g., Refs. 2 and 3) and for the collisional-radiative modeling of low-temperature plasmas where indium is one of the constituent species.[4] Note that the importance of having such a comprehensive database available for these types of simulations is discussed in detail in Ref. 5 and indeed is one of the prime drivers behind the establishment of the LXCat project.[6] Another important technological application of indium is its role as a tracer in two-line atomic fluorescence thermometry measurements.[7] This approach employs two diode lasers with wavelengths of 410 nm and 451 nm, in order to excite the $(5s^2 6s)^2 S_{1/2}$ resonance state of indium atoms seeded into a flame. Owing to the typically greater oscillator strengths of atoms compared to molecules, strong fluorescence signals can be obtained at lower excitation energies. A particular plus of indium atoms is that its spin–orbit coupling in the $5p$ ground state leads to an energy spacing of $\approx kT$ in standard combustion environments (2000 K–4000 K).[8]

The only previous elastic angle-integrated cross-section (ICS) results available in the literature are due to Rabasović et al.[9] In that study, experimental ICSs were determined, from extrapolation and integration of their elastic differential cross sections, for incident electron energies (E_0) between 10 eV and 100 eV. Corresponding atomic optical-potential (OP) calculations, but now for E_0 = 10 eV to 350 eV, were also reported.[9] As this previous study does not cover a comprehensive enough energy range for swarm or plasma simulation investigations and as further independent assessments of their results would be desirable, here, we report additional OP results and the results from a static-exchange plus polarization (SEP) theoretical approach, as well as the corresponding elastic cross sections from our

relativistic B-spline R-matrix (DBSR) and relativistic convergent close-coupling (RCCC-75) computations from the work of Hamilton et al.[1] With these new theoretical results, we are confident that a recommended elastic ICS database, for E_0 = 0.001 eV–10 000 eV, can now be constructed.

The situation is even worse for the case of excitation of the discrete inelastic states in indium. Aside from a set of nine angle-ICSs contained in the paper of Ögün et al.,[4] five of which were for excitation from the $(5s^2 5p)^2 P_{1/2}$ ground state and a further four of which were for excitation from the close-lying $(5s^2 5p)^2 P_{3/2}$ metastable state, as well as our results for the single $(5s^2 5p)^2 P_{1/2} \rightarrow (5s^2 6s)^2 S_{1/2}$ excitation process discussed in Ref. 1, we know of no other available results in the literature. The ICSs reported in Ref. 4 were calculated using the method of Gryziński,[10,11] which is not ab initio in its construction so that their data are unlikely to be accurate. As a consequence, we do not consider those results further here. On the other hand, we found excellent agreement between our DBSR, RCCC, and measured cross-section results for the $(5s^2 5p)^2 P_{1/2} \rightarrow (5s^2 6s)^2 S_{1/2}$ transition.[1] This gives us hope that these DBSR and RCCC computations can provide us with accurate and reliable data for a total of 42 discrete inelastic excitation processes as well as the summed ICS for these discrete excitations (which can be compared with corresponding results from our atomic OP calculations), from which an extensive recommended cross-section database can be constructed.

With regard to the total ionization cross section (TICS), however, there has been a quite significant body of earlier work already undertaken. This includes experimental results from the work of Vainshtein et al.,[12] Shimon et al.,[13] and Shul et al.,[14] as well as various types of calculations such as a semi-empirical result from the work of Lotz,[15] an empirical TICS from the work of Talukder et al.,[16] a Deutsch–Märk method result from the work of Margreiter et al.,[17] and a binary encounter Bethe (BEB) formulation TICS from the work of Kim and Stone.[18] Note that in that latter study, plane-wave-Born (PWB) calculations for some of the more important autoionizing states were also undertaken, in order to present a more physical determination of the TICS. Furthermore, note that the measurement

of Shimon et al.[13] displays an unphysical shape, possessing a local minimum in the TICS at an energy where one might expect to find a maximum cross section. As a consequence, the results from the work of Shimon et al.[13] do not figure in our further deliberations. Unfortunately, despite all this earlier work into indium's TICS, as we shall shortly see, the level of accord between those various measurements and calculations[12–18] is only marginal. Hence, in this paper, we also present TICS results from our RCCC-75, DBSR-214, and atomic OP calculations, as well as our own BEB calculation with a superior model chemistry over that used in Ref. 18 to try and clarify matters prior to constructing a recommended TICS.

The remainder of this paper is constructed as follows. In Sec. 2, we detail our theoretical approaches that were used to compute new cross sections for this investigation. Thereafter, in Sec. 3, a detailed comparison of all the available elastic ICS, discrete inelastic ICS, and TICS is provided with our recommended cross sections, which result from each of these comparisons, also being formed here. In Sec. 4, we apply our recommended electron–indium database, to study the behavior of an electron swarm, under the influence of an applied external electric field, with various transport coefficients[2,3] being derived. Finally, in Sec. 5, some conclusions from this investigation will be drawn.

2. Theory Details

In Ref. 1, an appropriate description of both our RCCC-75 and DBSR-214 calculations was given, to which we refer the interested reader. Note, however, that here we have extended our original RCCC-75 computations[1] to 7000 eV for both the elastic ICS and momentum transfer cross sections (MTCSs) and to 10 000 eV for the sum over all inelastic ICSs. In addition, as a part of this study, we re-ran our RCCC-75 calculations with a somewhat more sophisticated target description (dipole polarizability = 53.128 a_0^3 vs 40.3 a_0^3 in Ref. 1) than that employed in Ref. 1. However, at higher energies, the RCCC-75 elastic ICS and MTCS are basically identical irrespective of which target description is employed. Similarly, even though the summed discrete inelastic ICS is a little higher in magnitude, as a function of energy, with the new target description compared to that of Hamilton et al.,[1] both sets of results have the same energy dependence at higher energies. As one of the main aims of this study is to determine a recommended database for e^- + In scattering, the above observations suggest that, in terms of possibly using the RCCC-75 results to effect a higher-energy extrapolation (see later), cross sections from either target description are equally valid. Under those circumstances, we have continued to employ the RCCC-75 results from the work of Hamilton et al.[1] throughout this paper. Additional calculations using our atomic-optical approach, a SEP method, and our own application of the BEB procedure[5] are presented here, so a brief description of each of them is now given below.

2.1. OP model

We have recently described our standard OP approach in our studies of the electron–beryllium,[19] electron–magnesium,[20] electron–zinc,[21] and electron–bismuth[22] scattering systems. The generic details of this atomic OP method were given in those papers so that only the key points of this approach are summarized below.

The projectile–atom interaction is described by a local complex potential given by

$$V(r) = V_s(r) + V_{ex}(r) + V_{pol}(r) + iV_{abs}(r), \qquad (1)$$

where the real part of the potential is comprised of the following three terms. V_s is the static term derived from a Hartree–Fock calculation[23] of the atomic charge distribution. V_{ex} is an exchange term that accounts for the indistinguishability of the incident and target electrons; it is given by the semi-classical energy dependent formula derived by Riley and Truhlar.[24] Finally, V_{pol} is a polarization potential for the long–range interactions that depend on the target dipole polarizability. For this study, the polarization potential of Ref. 25, leading to results we denote as OP1, and that of Ref. 26, leading to cross sections we denote as OP2, were both applied.

The imaginary absorption potential accounts for the inelastic, both discrete and continuum, scattering events. It is based on the quasi-free model put forward by Staszewska et al.[27] but incorporates some improvements to the original formulation. These include allowing for the inclusion of screening effects, local velocity corrections, and the description of the electron indistinguishability,[28] leading to a model that provides a realistic approximation for electron–atom scattering over a broad energy range.[29]

The present atomic optical model is non-relativistic in formulation and leads to angle-integrated elastic cross sections, the sum over all discrete inelastic angle-ICSs, and the TICS. Note that as indium is only a moderately heavy atom, the differences in the calculated scattering cross sections between a relativistic and non-relativistic treatment will not be significant. As a consequence, the application of our non-relativistic OP approach is valid for this target.

2.2. SEP method

Our SEP model includes both relativistic static and polarization potentials as well as the exchange interaction. The spin–orbit interaction in indium gives rise to two "ground-state" levels, namely, $(5s^2 5p)^2 P_{1/2}$ and $(5s^2 5p)^2 P_{3/2}$ with the $j = 3/2$ state being ~0.274 eV above the $j = 1/2$ state. A linear combination of the wavefunctions corresponding to these two states was then employed in a 2-state Dirac–Fock multiconfiguration calculation[30,31] to determine the ground-state configuration of In within a frozen-core model. The static potential was then determined in the usual manner.

The dipole polarization was determined using the relativistic non-perturbative polarized-orbital method for alkali and alkali-like atoms.[26] Finally, the exchange interaction was accounted for by anti-symmetrization of the total scattering wavefunction. This approach only yields elastic scattering cross sections, and since it does not include any inelastic processes, it is expected to become less reliable as the energy of the incident electron increases.

2.3. BEB approach

Kim and Stone[18] calculated the TICS for indium using the BEB formalism.[5,32] The BEB approach is sensitive to the binding energies used in the calculation, so we have repeated the work of Kim and Stone[18] using an improved structural representation for indium based on the best available experimental data for the orbital binding energies. Those values have been assembled from the available photoionization spectra[33,34] and information regarding the convergence of spectral lines to the ionization thresholds.[35,36] These values have been combined with orbital kinetic energies for atomic indium that were derived from a single point energy calculation of indium hydride

J. Phys. Chem. Ref. Data **50**, 013101 (2021); doi: 10.1063/5.0035218

Published by AIP Publishing on behalf of the National Institute of Standards and Technology.

50, 013101-3

TABLE 1. Parameters used for the present BEB TICS calculation of atomic indium. See also supplementary material, Table S1

Orbital	B_i (eV)	U_i (eV)	N_i	η_{pqn}
$5p$	5.79	27.94	1	5
$5s$	11.16	53.70	2	5
$4d_{5/2}$	24.4	282.35	6	4
$4d_{3/2}$	25.7	282.35	4	4
$4p_{3/2}$	86.0	441.12	4	4
$4p_{1/2}$	95.4	441.12	2	4
$4s$	126.0	496.51	2	4
$3d_{5/2}$	468.5	1735.41	6	3
$3d_{3/2}$	476.4	1735.41	4	3
$3p_{3/2}$	691.8	1844.65	4	3
$3p_{1/2}$	731.3	1844.65	2	3
$3s$	854.4	1894.15	2	3

(InH, r = 9.0 Å) in Gaussian 09,[37] with the model chemistry employing density functional theory (B3LYP)[38] and a double zeta valance polarized basis set.[39] The parameters used in the present BEB calculation are summarized in Table 1.

Within the BEB formalism,[32] the TICS is obtained by summing up the contributions from each populated orbital, with the ith orbital's contribution being given by

$$Q_i(t_i) = \frac{4\pi a_0^2 N_i}{t_i + \frac{u_i + 1}{\eta_{pqn}}} \left(\frac{R}{B_i}\right)^2 \left[\frac{\ln t_i}{2}\left(1 - \frac{1}{t_i^2}\right) + 1 - \frac{1}{t_i} - \frac{\ln t_i}{t_i + 1}\right]. \quad (2)$$

In Eq. (2), the binding energy of the ionized orbital, B_i, is used to scale the incident electron-impact energy (E_0) and orbital kinetic energies (u_i): $t_i = \frac{E_0}{B_i}$ and $u_i = \frac{U_i}{B_i}$, respectively. N_i is the orbital occupation number, while R and a_0 are, respectively, the Rydberg constant and Bohr radius. A modification to the traditional BEB approach comes when dealing with heavier elements, where the scaled kinetic energy is corrected by the principal quantum number of the ionized atomic orbital (η_{pqn}) if it is greater than 2.

3. Cross Section Assessment and Recommended Data

3.1. Elastic scattering

In Fig. 1, we summarize the available experimental and theoretical elastic angle-ICSs for electron–indium scattering, including original results from computations associated with this study. It is quite clear from this figure that between 10 eV and 90 eV, the experimental data of Rabasović et al.[9] are, to within the cited error bars, in very good agreement with their optical-model SEPASo[9] computation and our OP1, SEP, and DBSR-214 calculations. Agreement with our RCCC-75 calculation is also typically fair over this energy range. This level of accord, between experiment and theory, in that energy regime is by no means unique to indium, having also been observed by us in our recent study of elastic electron scattering from bismuth.[22] Similarly, but now for energies in the range 1 eV–10 eV, we find good levels of accord between our OP1, RCCC-75, and DBSR-214 calculations. Below 1 eV, however, there is quite a significant level of discrepancy between all the available theoretical results. While all the theories predict a significant structure, which would arise due to

the temporary capture of the incident electron by the target, in the elastic ICS, the position (in the range ~0.09 eV–0.2 eV) and magnitude (~200 $\times 10^{-16}$ cm^2–700 $\times 10^{-16}$ cm^2) of that peak are seen to vary from one theory to another. Our non-relativistic OP1, OP2, and SEP calculations all show this structure arising in the ℓ = 1 (i.e., p-wave) partial wave, suggesting that the origin of this feature is consistent with a p-wave shape resonance. For our relativistic RCCC and DBSR computations, the structure is in the J = 2, parity = +1, partial wave of the total scattering system. As the $(5s^2 5p)\,^2P_{1/2}$ ground state has j = 1/2, parity = −1, this leads to the projectile waves of either j = 3/2, parity = −1, ℓ = 1 or j = 5/2, parity = −1, ℓ = 3. Normally, we would expect it, consistent with our non-relativistic results, to be in ℓ = 1, as ℓ = 3 is too large for the centrifugal barrier to support a resonance. It is interesting to note that it is known[40] that the $(5s^2 5p^2)\,^3P_{0,1,2}$ and $(5s^2 5p^2)\,^1D_2$ and $^1S_0$ states of the negative indium ion are stable, with, for example, the $^3P_0$ state having an electron affinity of 384 meV, the $^3P_1$ state having an electron affinity of 460 meV, and the $^3P_2$ state having an electron affinity of 555 meV. Under these circumstances, a low-energy electron could simply bind to the indium atom to form In$^-$, which may have consequences for electron swarm behavior[2,3] at low E/n_0 (E = applied external electric field and n_0 = background gas density number). To quantitatively specify whether the structure we observe in Fig. 1 is a resonance or simply an artifact of our computational methods, we would need to do a significantly more accurate structure calculation for both In and In$^-$ and
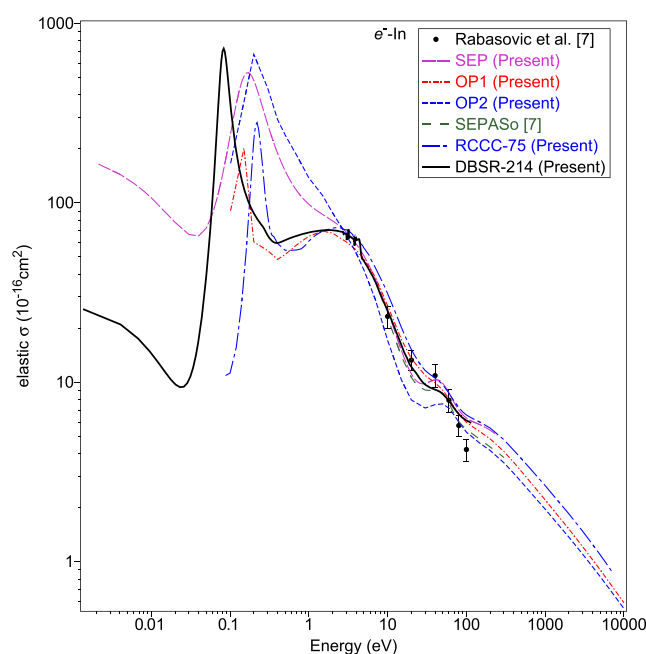

FIG. 1. Angle-integrated elastic cross sections ($\times 10^{-16}$ cm^2) for electron scattering from In. Results from the present relativistic SEP (purple dashed line); non-relativistic OP, (red dotted-dashed line) OP1 and (blue dashed line) OP2; and relativistic RCCC-75 (blue dotted-dashed line) and DBSR-214 (black solid line) computations, as well as the experimental (black circles) and SEPASo theory (green dashed line) results from the work of Rabasović et al.,[9] are plotted.

J. Phys. Chem. Ref. Data **50**, 013101 (2021); doi: 10.1063/5.0035218

Published by AIP Publishing on behalf of the National Institute of Standards and Technology.

50, 013101-4

TABLE 2. Recommended elastic ICS, MTCS, summed discrete inelastic (electronic-state) ICS, TICS, and grand total (TCS) cross sections ($\times 10^{-16}$ cm^2) for electron scattering from indium. See also supplementary material, Table S2

E_0 (eV)	Elastic ICS ($\times 10^{-16}$ cm^2)	MTCS ($\times 10^{-16}$ cm^2)	Σ discrete inelastic ($\times 10^{-16}$ cm^2)	TICS ($\times 10^{-16}$ cm^2)	TCS ($\times 10^{-16}$ cm^2)
1.361×10^{-3}	25.6	25.4			25.6
4.080×10^{-3}	21.0	20.6			21.0
4.082×10^{-3}	21.0	20.6			21.0
6.800×10^{-3}	17.5	16.9			17.5
9.520×10^{-3}	14.9	14.2			14.9
0.012 25	12.9	12.2			12.9
0.017 69	10.4	9.69			10.4
0.023 13	9.40	8.69			9.40
0.028 57	9.89	9.07			9.89
0.034 01	12.1	11.1			12.1
0.039 46	16.8	15.6			16.8
0.044 90	25.5	23.9			25.5
0.050 34	41.1	39.2			41.1
0.055 78	69.5	67.3			69.5
0.061 23	123	120			123
0.063 95	165	162			165
0.069 39	300	298			300
0.080 27	703	703			703
0.085 72	696	697			696
0.096 60	432	432			432
0.104 8	304	302			304
0.110 2	251	249			251
0.121 1	188	183			188
0.142 9	131	124			131
0.164 6	106	98.4			106
0.210 9	84.2	74.0			84.2
0.273 5	71.3	59.7	0.00		71.3
0.276 2	70.7	59.1	2.25		72.9
0.278 9	70.0	58.2	3.46		73.5
0.287 1	68.2	55.8	5.61		73.9
0.319 7	63.3	49.6	10.7		74.0
0.401 4	59.8	44.0	18.5		78.3
0.496 6	61.9	43.9	20.0		81.9
0.761 9	66.3	44.2	16.7		83.0
1.075	68.9	44.3	13.5		82.4
1.673	70.6	42.7	10.1		80.6
2.626	69.0	36.2	7.53		76.6
2.721	69.0	35.8	7.04		76.0
2.762	67.0	34.1	7.82		74.8
3.018	65.8	33.0	7.23		73.1
3.020	64.1	33.0	7.73		71.8
3.023	62.1	32.9	9.48		71.5
3.034	66.6	32.3	7.64		74.2
3.184	68.0	32.1	6.77		74.8
3.186	71.3	31.8	6.97		78.3
3.189	63.0	31.5	8.97		72.0
3.192	64.5	31.2	7.66		72.1
3.211	65.6	30.8	7.20		72.8
3.765	60.8	25.8	7.99		68.8
3.769	62.0	25.6	7.62		69.6
3.791	61.2	25.2	8.22		69.4
3.804	58.3	23.9	10.1		68.3

TABLE 2. (*Continued.*)

E_0 (eV)	Elastic ICS ($\times 10^{-16}$ cm^2)	MTCS ($\times 10^{-16}$ cm^2)	Σ discrete inelastic ($\times 10^{-16}$ cm^2)	TICS ($\times 10^{-16}$ cm^2)	TCS ($\times 10^{-16}$ cm^2)
3.810	62.0	23.5	8.70		70.7
3.823	63.2	24.8	7.95		71.2
3.908	63.1	25.3	7.43		70.6
3.913	62.4	25.4	7.92		70.3
3.921	63.6	25.5	7.40		71.0
4.327	62.9	21.2	9.91		72.8
4.531	55.2	16.5	13.4		68.6
4.612	51.9	15.5	13.6		65.5
4.776	48.8	15.3	12.2		61.0
5.786	42.6	11.7	11.3	0.00	53.9
6.00	41.4	11.3	11.2	0.310	52.9
8.71	28.5	5.60	8.95	3.46	40.9
10.0	25.0	4.40	7.99	4.96	37.9
12.4	20.0	3.46	7.14	6.68	33.8
16.2	14.7	2.56	6.65	8.38	29.7
20.0	12.2	2.02	6.39	9.24	27.8
30.0	9.71	2.98	5.81	9.78	25.3
40.0	9.11	4.49	5.37	9.29	23.8
46.4	8.84	4.36	5.08	8.87	22.8
65.0	7.51	4.07	4.35	7.87	19.7
80.0	6.66	3.13	3.93	7.21	17.8
95.0	6.22	2.53	3.60	6.66	16.5
120	5.80	2.04	3.12	5.96	14.9
150	5.42	1.81	2.68	5.36	13.5
200	4.96	1.64	2.18	4.66	11.8
300	4.22	1.41	1.61	3.79	9.62
400	3.66	1.17	1.28	3.20	8.15
600	2.97	0.865	0.923	2.59	6.49
800	2.55	0.656	0.730	2.23	5.51
1 000	2.27	0.517	0.607	1.98	4.86
2 000	1.56	0.224	0.337	1.35	3.24
3 000	1.24	0.131	0.235	1.06	2.54
4 000	1.05	0.0877	0.179	0.887	2.12
5 000	0.924	0.0637	0.144	0.771	1.84
6 000	0.826	0.0489	0.120	0.682	1.63
8 000	0.693	0.0315	0.0888	0.561	1.34
10 000	0.605	0.0221	0.0701	0.482	1.16

to perform our scattering calculations on a much finer energy grid. This is beyond the scope of this publication. Nonetheless, in spite of the above caveats, it is crucial in modeling/simulation applications to have a complete cross-section database.[5] As a consequence, given it is our most detailed relativistic *ab initio* computation, and in what follows, for energies below 1 eV, we recommend our DBSR-214 elastic ICS results. Note that at low energies, the dipole polarizability plays a very important role in the elastic scattering dynamics.[41,42] In our current work, the static dipole polarizability (α_d) of the In atom in the RCCC-75 model is 40.3 a_0^3 and in our DBSR-214 model is 61.3 a_0^3, while the experimental value is ~68.69 a_0^3.[43] We believe that these differences between theory and experiment in α_d explain, at least in part, the different peak positions and magnitudes in the elastic ICS low-energy structures and further indicate that even more detailed structure descriptions are warranted at some stage.

On the basis of the above discussion and the results shown in Fig. 1, we form our recommended elastic ICS from our DBSR-214 result from 0.001 eV to 100 eV and from a suitably scaled, to maintain continuity (scaling factor = 1.025), OP1 result from 100 eV to 10 000 eV. This recommended elastic ICS is listed in Table 2 for a selection of incident electron energies, and we estimate the uncertainty on it to be ~±20% for energies less than 3 eV and ~±15% for energies greater than 3 eV. Note that the sensitivity of our recommended cross sections to our choice of normalization energy was investigated both here and for all the later scattering processes we consider. We found that our recommended cross sections, for $E_0 \geqslant 100$ eV, were largely insensitive to our choice of normalization energy between 70 eV and 100 eV. This result gives us confidence in the robustness of our higher energy recommended cross sections. The elastic MTCS is also very important for electron transport simulations, with much of the discussion just given for the elastic ICS also
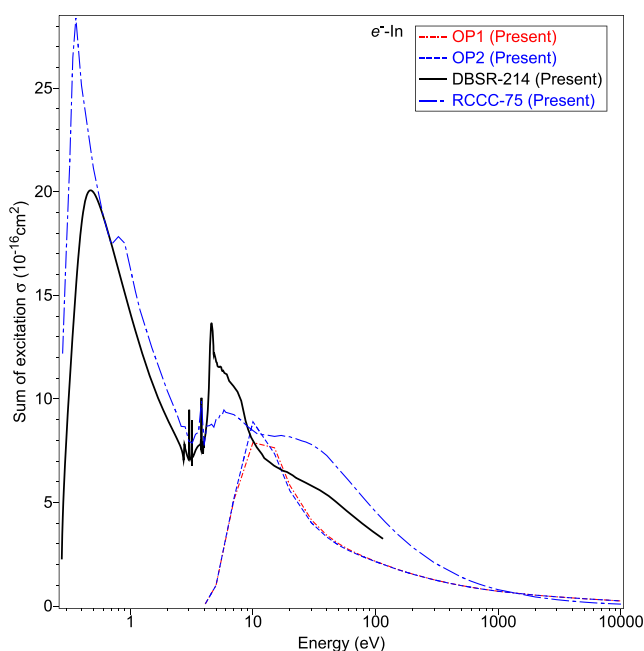
J. Phys. Chem. Ref. Data **50**, 013101 (2021); doi: 10.1063/5.0035218

Published by AIP Publishing on behalf of the National Institute of Standards and Technology.

50, 013101-6

FIG. 2. Summed discrete inelastic cross sections ($\times 10^{-16}$ cm^2) for electron-impact excitation of In. Present non-relativistic OP, (red dotted-dashed line) OP1 and (blue dashed line) OP2, and relativistic RCCC-75 (blue dotted-dashed line) and DBSR-214 (black line) computational results are plotted.
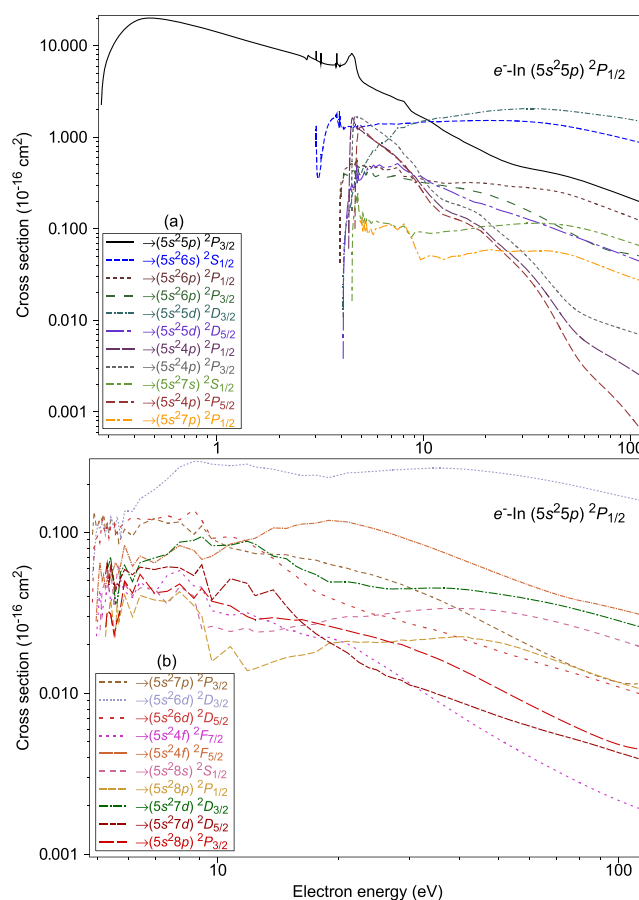

FIG. 3. Individual discrete inelastic cross sections ($\times 10^{-16}$ cm^2) for electron-impact excitation of In from the $(5s^25p)\ ^2P_{1/2}$ ground state to the higher-lying excited states as denoted in legends (a) and (b). All results are from our DBSR-214 calculation, and they represent our recommended data for each of these processes.

being applicable to it. As a consequence, we do not repeat that detail; rather, we simply note that our recommended MTCS is formed from our DBSR-214 calculation for 0.001 eV–100 eV and from our RCCC-75 result, again suitably scaled to ensure continuity (scaling factor = 0.9564) for 100 eV–7000 eV. Finally, for 7 keV–10 keV, we use our scaled OP1 result (scaling factor = 2.653) to complete our MTCS database. That recommended MTCS can also be found in Table 2, with an uncertainty on it of ~±20% for energies less than 3 eV and ~±15% for energies greater than 3 eV.

3.2. Discrete inelastic cross sections

We next consider the sum of all the discrete inelastic excited-state angle-ICSs, where only data from our OP1, OP2, RCCC-75, and DBSR-214 calculations are available. Those results are plotted in Fig. 2, where several observations are immediately apparent. First, while our OP1 and OP2 results agree well with one another, both appear to predict an incorrect threshold for the opening of inelastic excitation, and as a consequence, both predict a maximum in the summed cross section to occur at too high an incident electron energy. This is not unexpected as the OP1 and OP2 models do not account for the fine-structure splitting of the ground state. So their lowest inelastic threshold is at around 3 eV for the $(5s^26s)^2S_{1/2}$ state, while the actual value is ~0.27 eV for the $(5s^25p)^2P_{3/2}$ state. In addition, both the OP1 and OP2 results are generally in poor accord with our relativistic RCCC-75 and DBSR-214 results. In our recent work[1] on the electron-impact excitation of the $(5s^25p)^2P_{1/2} \rightarrow (5s^26s)^2S_{1/2}$ transition, we found excellent agreement between our RCCC-75, DBSR-214, and measured angle-ICSs over their common energy range (to typically

~±10%). This level of accord between them is clearly not maintained in Fig. 2, a point that is in need of further interrogation, although we note that qualitatively the RCCC-75 and DBSR-214 results remain in fair agreement. The relatively marginal quantitative accord between our RCCC-75 and DBSR-214 computations, for the summed discrete angle-integrated inelastic cross sections in Fig. 2, we believe is due to an inaccuracy of the quasi one-electron RCCC model for In, at least for some inelastic transitions that are important. One example of that is for the $(5s^25p)^2P_{1/2} \rightarrow (5s^25d)^2D_{3/2}$ transition, where the optical oscillator strength in the RCCC target-state description has a value of 0.451, which is substantially higher than those from our DBSR calculations (0.341)[1] and the corresponding NIST value (0.36).[35] The effect of this carries through in the respective RCCC-75 and DBSR-214 scattering results, where the magnitude of the RCCC $(5s^25d)^2D_{3/2}$ ICS would be anticipated to be greater than that for the DBSR-214 $(5s^25d)^2D_{3/2}$ ICS. This observation is entirely consistent, away from the influence of resonance-effects, with what we found in Fig. 2. As a consequence, for the summed discrete inelastic ICS, our recommended database is here formed from the DBSR-214 results from

J. Phys. Chem. Ref. Data **50**, 013101 (2021); doi: 10.1063/5.0035218

Published by AIP Publishing on behalf of the National Institute of Standards and Technology.

50, 013101-7

TABLE 3. Angle-ICSs (10^{-16} cm^2) at 90 incident electron energies, selected to show any structure for electron–indium scattering from the $(5s^25p)$ $^2P_{1/2}$ ground state. See also supplementary material, Table S3a

Energy (eV)	→ $(5s^25p)$ $^2P_{3/2}$	→ $(5s^26s)$ $^2S_{1/2}$	→ $(5s^26p)$ $^2P_{1/2}$	→ $(5s^26p)$ $^2P_{3/2}$	→ $(5s^25d)$ $^2D_{3/2}$	→ $(5s^25d)$ $^2D_{5/2}$	→ $(5s^24p)$ $^2P_{1/2}$	→ $(5s^24p)$ $^2P_{3/2}$	→ $(5s^27s)$ $^2S_{1/2}$	→ $(5s^24p)$ $^2P_{5/2}$	→ $(5s^27p)$ $^2P_{1/2}$
0.2743	0.00										
0.2762	2.25										
0.2789	3.46										
0.3088	9.26										
0.3524	14.5										
0.3796	17.1										
0.4476	19.9										
0.5102	19.9										
0.5714	19.2										
0.6803	17.8										
0.8027	16.2										
0.8708	15.4										
0.9796	14.3										
1.116	13.2										
1.265	12.1										
1.483	10.9										
1.673	10.1										
1.823	9.57										
2.041	8.93										
2.259	8.40										
2.653	7.44										
3.022	8.25	0.00									
3.025	8.01	1.37									
3.033	7.01	0.716									
3.041	6.93	0.506									
3.061	6.86	0.381									
3.116	6.72	0.364									
3.186	6.47	0.497									
3.189	8.32	0.657									
3.770	5.82	1.74									
3.804	8.25	1.80									
3.815	6.59	1.60									
3.908	6.07	1.37									
3.913	6.01	1.91									
3.921	5.88	1.52									
3.945	5.96	1.70	0.00								
3.946	5.93	1.71	0.0389								
3.951	6.03	1.43	0.249								
3.973	6.06	1.36	0.226								
3.982	6.07	1.33	0.296	0.00							
3.986	6.08	1.31	0.332	0.182							
4.014	6.10	1.27	0.314	0.293							
4.078	6.20	1.30	0.340	0.353	0.00						
4.081	6.21	1.30	0.342	0.356	0.00832	0.00					

TABLE 3. (*Continued.*)

Energy (eV)	→ (5s²5p) ²P₃/₂	→ (5s²6s) ²S₁/₂	→ (5s²6p) ²P₁/₂	→ (5s²6p) ²P₃/₂	→ (5s²5d) ²D₃/₂	→ (5s²5d) ²D₅/₂	→ (5s²4p) ²P₁/₂	→ (5s²4p) ²P₃/₂	→ (5s²7s) ²S₁/₂	→ (5s²4p) ²P₅/₂	→ (5s²7p) ²P₁/₂
					Cross section (10^{-16} cm²)						
4.082	6.21	1.30	0.343	0.356	0.0103	0.00348					
4.095	6.21	1.24	0.385	0.365	0.0360	0.0242					
4.150	6.31	1.25	0.444	0.396	0.0769	0.0713					
4.337	7.47	1.31	0.476	0.407	0.151	0.213	0.00				
4.340	7.50	1.31	0.477	0.408	0.153	0.215	0.0570				
4.466	8.13	1.30	0.515	0.454	0.196	0.291	1.42	0.00			
4.501	8.22	1.25	0.514	0.437	0.225	0.303	1.60	0.506	0.00		
4.503	8.22	1.24	0.514	0.433	0.227	0.303	1.61	0.546	0.0149		
4.531	8.06	1.25	0.512	0.425	0.243	0.288	1.63	0.937	0.0855		
4.643	7.31	1.32	0.516	0.422	0.339	0.290	1.42	1.71	0.172	0.00	
4.667	6.91	1.34	0.515	0.402	0.388	0.282	1.37	1.74	0.190	0.216	
4.748	5.53	1.31	0.564	0.555	0.403	0.496	1.27	1.66	0.205	0.841	
4.776	5.27	1.27	0.550	0.442	0.311	0.320	1.24	1.64	0.191	0.971	
4.818	4.92	1.33	0.475	0.421	0.401	0.359	1.24	1.64	0.217	1.11	0.00
4.830	4.83	1.33	0.474	0.444	0.402	0.376	1.24	1.64	0.197	1.14	0.130
5.020	4.15	1.31	0.467	0.387	0.417	0.357	1.17	1.60	0.116	1.29	0.130
5.075	4.04	1.31	0.490	0.421	0.451	0.376	1.15	1.58	0.148	1.26	0.0941
5.143	3.94	1.32	0.484	0.390	0.457	0.402	1.12	1.54	0.123	1.20	0.124
5.238	3.84	1.35	0.468	0.389	0.522	0.427	1.08	1.50	0.111	1.14	0.0920
5.293	3.77	1.33	0.478	0.391	0.540	0.427	1.06	1.47	0.127	1.12	0.111
5.347	3.72	1.33	0.500	0.427	0.568	0.457	1.04	1.45	0.120	1.09	0.0913
5.850	3.31	1.38	0.465	0.371	0.720	0.475	0.901	1.24	0.123	0.901	0.100
6.94	2.82	1.40	0.445	0.373	1.02	0.479	0.692	0.936	0.113	0.674	0.111
8.03	2.47	1.42	0.374	0.354	1.28	0.446	0.485	0.654	0.108	0.516	0.113
8.71	1.93	1.43	0.370	0.342	1.40	0.400	0.411	0.545	0.0809	0.388	0.0819
9.66	1.69	1.46	0.353	0.322	1.49	0.379	0.309	0.382	0.0927	0.276	0.0461
10.7	1.50	1.49	0.333	0.313	1.55	0.322	0.230	0.274	0.0893	0.194	0.0513
12.4	1.20	1.49	0.315	0.298	1.62	0.280	0.167	0.208	0.0929	0.144	0.0460
14.8	0.962	1.51	0.320	0.279	1.73	0.232	0.140	0.181	0.0951	0.125	0.0504
17.6	0.785	1.53	0.319	0.258	1.83	0.196	0.115	0.156	0.101	0.103	0.0545
18.9	0.722	1.52	0.318	0.248	1.88	0.190	0.105	0.140	0.106	0.0949	0.0573
22.4	0.597	1.52	0.307	0.220	1.97	0.165	0.0718	0.0983	0.108	0.0650	0.0580
24.9	0.541	1.52	0.295	0.202	2.01	0.153	0.0588	0.0808	0.110	0.0522	0.0569
27.3	0.502	1.51	0.289	0.186	2.03	0.144	0.0491	0.0677	0.112	0.0427	0.0568
30.1	0.475	1.50	0.286	0.169	2.05	0.133	0.0402	0.0557	0.114	0.0342	0.0572
35.8	0.440	1.45	0.274	0.140	2.05	0.117	0.0258	0.0368	0.115	0.0209	0.0576
40.4	0.416	1.41	0.265	0.121	2.02	0.106	0.0179	0.0266	0.114	0.0135	0.0575
46.4	0.388	1.35	0.250	0.102	1.97	0.0936	0.0115	0.0184	0.111	0.00769	0.0547
50.2	0.370	1.31	0.238	0.0928	1.93	0.0874	0.00904	0.0153	0.108	0.00557	0.0527
57.8	0.337	1.23	0.215	0.0786	1.86	0.0775	0.00643	0.0120	0.102	0.00339	0.0476
65.0	0.309	1.17	0.195	0.0691	1.80	0.0702	0.00529	0.0105	0.0955	0.00250	0.0431
70.0	0.292	1.13	0.183	0.0642	1.76	0.0659	0.00477	0.00987	0.0912	0.00211	0.0403
80.0	0.261	1.05	0.164	0.0576	1.70	0.0589	0.00400	0.00889	0.0834	0.00158	0.0358
90.0	0.236	0.989	0.148	0.0552	1.63	0.0532	0.00341	0.00815	0.0765	0.00119	0.0324
105	0.208	0.907	0.130	0.0519	1.54	0.0464	0.00274	0.00728	0.0682	7.83×10^{-4}	0.0286
115	0.192	0.860	0.119	0.0499	1.48	0.0428	0.00240	0.00682	0.0640	6.02×10^{-4}	0.0267

TABLE 4. Angle-ICSs (10^{-16} cm²) for electron–indium scattering from the (5s²5p) ²$P_{1/2}$ ground state. See also supplementary material, Table S3b

Energy (eV)	→ (5s²7p) ²$P_{3/2}$	→ (5p²6d) ²$D_{3/2}$	→ (5s²6d) ²$D_{5/2}$	→ (5s²4f) ²$F_{7/2}$	→ (5s²4f) ²$F_{5/2}$	→ (5p²8s) ²$S_{1/2}$	→ (5s²8p) ²$P_{1/2}$	→ (5s²7d) ²$D_{3/2}$	→ (5P²7d) ²$D_{5/2}$	→ (5s²8p) ²$P_{3/2}$
					Cross section (10^{-16} cm²)					
4.832	0.00									
4.841	0.0343	0.00								
4.848	0.0569	0.0207	0.00							
4.857	0.0921	0.0528	0.0332							
4.912	0.135	0.0709	0.0812							
4.923	0.130	0.0767	0.0831	0.00	0.00					
4.966	0.111	0.0984	0.0899	0.0212	0.0276					
5.020	0.110	0.112	0.0967	0.0298	0.0461					
5.038	0.114	0.109	0.0934	0.0345	0.0524	0.00				
5.075	0.122	0.105	0.0867	0.0440	0.0653	0.0229				
5.143	0.121	0.115	0.120	0.0308	0.0503	0.0448				
5.184	0.130	0.110	0.109	0.0364	0.0545	0.0462				
5.186	0.129	0.109	0.109	0.0365	0.0542	0.0464	0.00			
5.187	0.128	0.109	0.108	0.0365	0.0540	0.0465	4.81×10^{-4}	0.00		
5.190	0.127	0.108	0.108	0.0365	0.0534	0.0468	0.00180	0.00372	0.00	
5.193	0.126	0.108	0.107	0.0366	0.0530	0.0470	0.00281	0.00656	0.00271	0.00
5.238	0.105	0.0968	0.0987	0.0373	0.0453	0.0511	0.0218	0.0600	0.0537	0.0244
5.293	0.114	0.110	0.108	0.0467	0.0508	0.0538	0.0313	0.0592	0.0644	0.0321
5.347	0.0984	0.103	0.0924	0.0463	0.0494	0.0448	0.0321	0.0635	0.0472	0.0321
5.401	0.120	0.125	0.110	0.0369	0.0528	0.0585	0.0381	0.0704	0.0633	0.0310
5.510	0.119	0.107	0.116	0.0425	0.0612	0.0354	0.0246	0.0442	0.0491	0.0229
5.551	0.0994	0.111	0.0974	0.0458	0.0651	0.0451	0.0231	0.0361	0.0427	0.0254
5.606	0.104	0.126	0.101	0.0416	0.0622	0.0559	0.0373	0.0369	0.0481	0.0285
5.660	0.0857	0.110	0.0990	0.0424	0.0560	0.0612	0.0277	0.0439	0.0468	0.0301
5.714	0.0910	0.0951	0.108	0.0507	0.0620	0.0506	0.0310	0.0566	0.0520	0.0340
5.850	0.105	0.136	0.115	0.0430	0.0836	0.0481	0.0409	0.0627	0.0589	0.0499
6.12	0.0950	0.136	0.125	0.0394	0.0617	0.0403	0.0299	0.0494	0.0547	0.0420
6.39	0.112	0.162	0.121	0.0494	0.0715	0.0453	0.0406	0.0650	0.0609	0.0550
6.94	0.122	0.185	0.121	0.0418	0.0647	0.0450	0.0381	0.0696	0.0589	0.0421
7.48	0.114	0.216	0.127	0.0545	0.0735	0.0357	0.0372	0.0732	0.0612	0.0431
8.03	0.116	0.255	0.120	0.0580	0.0830	0.0462	0.0429	0.0871	0.0604	0.0479
8.71	0.0975	0.276	0.138	0.0466	0.0776	0.0402	0.0351	0.0894	0.0540	0.0390
9.12	0.110	0.275	0.119	0.0457	0.0681	0.0253	0.0302	0.0943	0.0631	0.0451
9.66	0.0911	0.266	0.0920	0.0327	0.0712	0.0261	0.0158	0.0828	0.0381	0.0374
10.7	0.0802	0.260	0.0943	0.0306	0.0849	0.0242	0.0196	0.0835	0.0517	0.0350
11.8	0.0761	0.266	0.0885	0.0318	0.0898	0.0255	0.0139	0.0882	0.0483	0.0300
12.4	0.0739	0.256	0.0812	0.0301	0.0921	0.0240	0.0143	0.0848	0.0405	0.0288
13.7	0.0732	0.247	0.0690	0.0275	0.107	0.0244	0.0157	0.0713	0.0440	0.0296
14.8	0.0727	0.237	0.0590	0.0248	0.106	0.0255	0.0167	0.0687	0.0348	0.0289
15.6	0.0702	0.230	0.0539	0.0243	0.111	0.0261	0.0171	0.0619	0.0300	0.0285
16.2	0.0691	0.226	0.0496	0.0234	0.113	0.0265	0.0173	0.0592	0.0276	0.0288
17.6	0.0674	0.227	0.0427	0.0223	0.114	0.0269	0.0181	0.0548	0.0235	0.0274
18.9	0.0636	0.219	0.0395	0.0223	0.119	0.0288	0.0205	0.0492	0.0209	0.0262
21.1	0.0598	0.235	0.0354	0.0203	0.116	0.0301	0.0211	0.0494	0.0178	0.0245
22.4	0.0570	0.236	0.0335	0.0186	0.112	0.0300	0.0208	0.0483	0.0157	0.0235

TABLE 4. (*Continued.*)

Energy (eV)	$\to (5s^27p)\ ^2P_{3/2}$	$\to (5p^26d)\ ^2D_{3/2}$	$\to (5s^26d)\ ^2D_{5/2}$	$\to (5s^24f)\ ^2F_{7/2}$	$\to (5s^24f)\ ^2F_{5/2}$	$\to (5p^28s)\ ^2S_{1/2}$	$\to (5s^28p)\ ^2P_{1/2}$	$\to (5s^27d)\ ^2D_{3/2}$	$\to (5P^27d)\ ^2D_{5/2}$	$\to (5s^28p)\ ^2P_{3/2}$
					Cross section (10^{-16} cm^2)					
23.8	0.0554	0.239	0.0315	0.0168	0.108	0.0302	0.0209	0.0465	0.0144	0.0228
24.9	0.0535	0.240	0.0309	0.0158	0.105	0.0307	0.0207	0.0457	0.0140	0.0221
26.3	0.0513	0.243	0.0301	0.0145	0.101	0.0313	0.0208	0.0447	0.0129	0.0212
27.3	0.0495	0.245	0.0293	0.0136	0.0975	0.0317	0.0209	0.0446	0.0125	0.0206
28.7	0.0476	0.246	0.0282	0.0126	0.0936	0.0322	0.0215	0.0448	0.0121	0.0202
30.1	0.0454	0.248	0.0271	0.0116	0.0897	0.0325	0.0213	0.0447	0.0113	0.0193
31.4	0.0434	0.249	0.0265	0.0108	0.0865	0.0329	0.0216	0.0450	0.0110	0.0184
32.8	0.0416	0.250	0.0257	0.0101	0.0833	0.0332	0.0216	0.0451	0.0106	0.0177
34.2	0.0399	0.251	0.0251	0.00943	0.0803	0.0334	0.0219	0.0452	0.0102	0.0170
35.8	0.0379	0.251	0.0243	0.00874	0.0768	0.0337	0.0222	0.0452	0.00979	0.0162
37.1	0.0363	0.251	0.0236	0.00823	0.0741	0.0337	0.0222	0.0451	0.00948	0.0156
38.8	0.0345	0.250	0.0228	0.00769	0.0711	0.0338	0.0225	0.0449	0.00913	0.0148
40.4	0.0328	0.248	0.0219	0.00720	0.0683	0.0337	0.0225	0.0445	0.00878	0.0141
42.0	0.0312	0.246	0.0212	0.00677	0.0657	0.0336	0.0224	0.0441	0.00848	0.0134
43.4	0.0300	0.245	0.0207	0.00644	0.0637	0.0336	0.0218	0.0436	0.00823	0.0129
45.0	0.0286	0.242	0.0201	0.00609	0.0615	0.0334	0.0218	0.0431	0.00796	0.0123
46.4	0.0275	0.240	0.0196	0.00584	0.0598	0.0332	0.0214	0.0426	0.00776	0.0118
48.0	0.0263	0.238	0.0190	0.00554	0.0578	0.0329	0.0212	0.0421	0.00751	0.0113
50.2	0.0248	0.235	0.0184	0.00519	0.0554	0.0325	0.0208	0.0415	0.00723	0.0107
52.1	0.0237	0.232	0.0178	0.00492	0.0535	0.0321	0.0203	0.0409	0.00700	0.0102
54.3	0.0225	0.229	0.0173	0.00464	0.0514	0.0316	0.0197	0.0402	0.00677	0.00966
55.6	0.0218	0.227	0.0170	0.00449	0.0503	0.0313	0.0194	0.0398	0.00665	0.00936
56.7	0.0213	0.225	0.0167	0.00437	0.0494	0.0311	0.0191	0.0395	0.00652	0.00913
57.8	0.0208	0.224	0.0165	0.00426	0.0485	0.0308	0.0188	0.0391	0.00645	0.00891
60.0	0.0198	0.220	0.0160	0.00404	0.0469	0.0303	0.0182	0.0385	0.00627	0.00850
65.0	0.0180	0.213	0.0151	0.00363	0.0438	0.0290	0.0170	0.0371	0.00589	0.00770
70.0	0.0165	0.206	0.0143	0.00330	0.0413	0.0278	0.0159	0.0357	0.00558	0.00703
75.0	0.0152	0.199	0.0137	0.00302	0.0393	0.0266	0.0150	0.0343	0.00533	0.00647
80.0	0.0142	0.192	0.0130	0.00279	0.0378	0.0255	0.0141	0.0329	0.00509	0.00601
85.0	0.0133	0.186	0.0125	0.00259	0.0367	0.0244	0.0134	0.0316	0.00487	0.00562
90.0	0.0126	0.180	0.0119	0.00242	0.0356	0.0234	0.0128	0.0305	0.00466	0.00529
95.0	0.0121	0.175	0.0114	0.00228	0.0345	0.0224	0.0122	0.0294	0.00447	0.00503
100	0.0117	0.170	0.0110	0.00216	0.0334	0.0215	0.0117	0.0283	0.00429	0.00482
105	0.0115	0.165	0.0106	0.00206	0.0324	0.0207	0.0113	0.0273	0.00414	0.00466
110	0.0114	0.161	0.0102	0.00197	0.0315	0.0200	0.0109	0.0264	0.00399	0.00455
115	0.0116	0.158	0.00979	0.00189	0.0306	0.0193	0.0106	0.0257	0.00384	0.00449
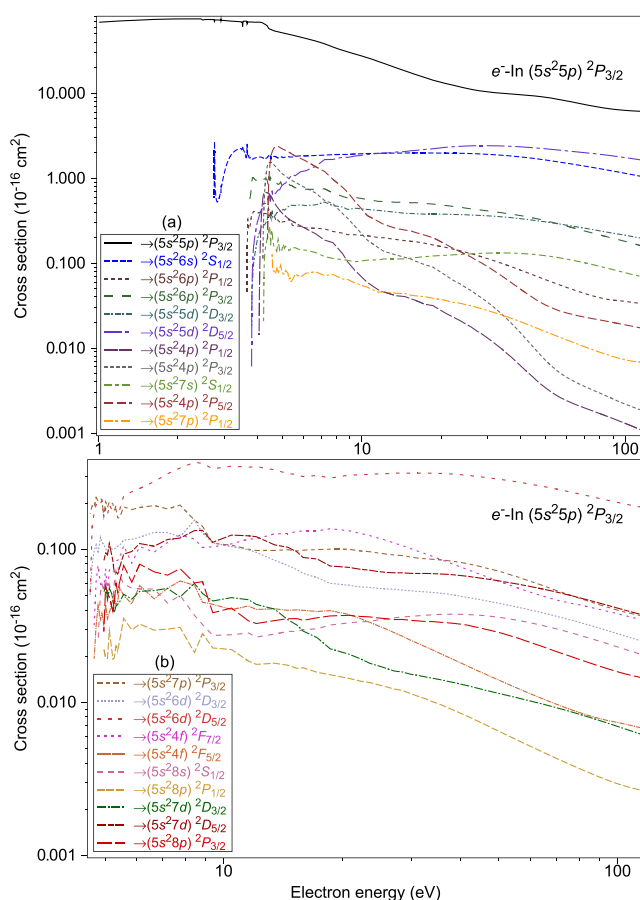
FIG. 4. Individual discrete inelastic cross sections ($\times 10^{-16}$ cm^2) for electron impact excitation of In from the $(5s^25p)\ ^2P_{3/2}$ metastable state to the higher-lying excited states as denoted in legends (a) and (b). All results are from our DBSR-214 calculation, and they represent our recommended data for each of these processes.

threshold up to 100 eV and from 100 eV up to 10 000 eV we, as in Sec. 3.1, making use of a suitably scaled RCCC-75 cross section (scaling factor = 0.7694) to facilitate the extrapolation to those higher energies and maintain continuity at 100 eV. We believe that the uncertainty estimate on this recommended ICS (again see Table 2) is ~±20%.

Given our discussion immediately above, it is no surprise that for the individual discrete inelastic transitions, from both the ground-state $(5s^25p)^2P_{1/2}$ level and the close-lying metastable $(5s^25p)^2P_{3/2}$ level, we have chosen to utilize our DBSR-214 calculations. Angle-ICSs for transitions from $(5s^25p)^2P_{1/2}$ to a higher lying level i, ICS$_i$, are plotted in Figs. 3(a) and 3(b) and listed in the corresponding Tables 3 and 4. A total of 21 discrete inelastic cross sections are presented here for the first time. Similarly, angle-ICSs from the $(5s^25p)^2P_{3/2}$ state to a higher level i are plotted in Figs. 4(a) and 4(b) and listed in the corresponding Tables 5 and 6. A further 21 discrete inelastic channels for excitation from the $(5s^25p)^2P_{3/2}$ are also presented here for the first time. Near-threshold structures are observed in most of these inelastic ICS$_i$ (see Figs. 3 and 4). These structures are not pseudo-resonances;

rather, they either originate from Feshbach resonances or are associated with the opening of higher-lying discrete electronic states (possibly Wigner cusps) as the incident electron energy is increased. Nonetheless, a more detailed study of these structures, beyond the scope of this paper, is required before any quantitative classifications can be made. We believe the errors on these ICS$_i$, on average, are ±15% for transitions originating from the ground $(5s^25p)^2P_{1/2}$ state and ~±20% for those transitions originating from the metastable $(5s^25p)$ $^2P_{3/2}$ state. Note that the $(5s^25p)^2P_{3/2}$ ICS$_i$s have been included here as we believe they will be needed in any quantitative kinetic-radiative study for a plasma in which indium is a constituent and may also be needed for our electron transport simulations in Sec. 4.

While we do not explicitly show our extrapolations for each ICS$_i$ out to 10 000 eV, such extrapolations are simple enough to undertake. If we again pick our RCCC-75 summed inelastic ICS to perform the extrapolation, and again do the normalization at 100 eV, then for all $E \geqslant 100$ eV, we find

$$\text{ICS}_i(E) = \frac{\text{ICS}_i(100\ \text{eV})}{\text{ICS}_{\text{summed}}(100\ \text{eV})} \times \text{ICS}_{\text{summed}}(E),\qquad (3)$$

where all the values for the right-hand side of Eq. (3) can be obtained from Tables 2–6 as required.

3.3. Total ionization cross section

In Fig. 5, we plot the available TICS for the scattering process $e^- + \text{In} \rightarrow \text{In}^+ + 2e^-$, including our present OP1, OP2, BEB, BEB+autoionization, RCCC-75, and DBSR-214 cross sections. It should be apparent that two experimental determinations, from Vainshtein et al.[12] and Shul et al.,[14] are available and that they disagree with one another (outside their reported uncertainties of ±18% and ±13%, respectively) in terms of their magnitudes. Vainshtein et al.[12] determined the number density of their indium beam using the quartz crystal resonator method, which Lindsay and Mangan[44] noted can lead to problematic results. Shul et al.,[14] however, employed a different approach that incorporates a fast neutral atom beam obtained by charge transfer of an energetic ion beam that is crossed by an ionizing electron beam. Unfortunately, as also noted by Lindsay and Mangan,[44] this approach does present formidable practical difficulties including being able to precisely ascertain the overlap between the electron beam and the fast neutral beam and with the possible presence of metastable species. Given the caveats in applying both those experimental procedures, we a priori have no way of choosing between them. From a theoretical perspective, we find that our RCCC-75 TICS underestimates the magnitude of all the other TICS results. This can be understood by the fact that it currently does not incorporate many of the important autoionization channels that Kim and Stone[18] noted are crucial to consider in this case. The semi-empirical calculation of Lotz[15] and the present BEB results favor the measurement of Vainshtein et al.,[12] while the present BEB+PWB autoionization, the corresponding calculation from the work of Kim and Stone,[18] and the electron impact total single ionization (EITSI) results[16] favor the experiment of Shul et al.[14] Finally, in between (but outside their stated measurement uncertainties) the experimental results, we find in Fig. 5 the present OP1, OP2, and DBSR-214 calculations and the Deutsch–Märk[17] computation. Note that, in principle, our OP1 and OP2 computations include those important autoionizing channels, while our DBSR-214 calculations incorporate most of them except for those that originate from the 4d shell.

J. Phys. Chem. Ref. Data **50**, 013101 (2021); doi: 10.1063/5.0035218   **50**, 013101-12

Published by AIP Publishing on behalf of the National Institute of Standards and Technology.

TABLE 5. Angle-ICSs (10^{-16} cm^2) for electron–indium scattering from the $(5s^25p)\ ^2P_{3/2}$ metastable state. See also supplementary material, Table S4a

Energy (eV)	$\rightarrow (5s^25p)\ ^2P_{3/2}$	$\rightarrow (5s^26s)\ ^2S_{1/2}$	$\rightarrow (5s^26p)\ ^2P_{1/2}$	$\rightarrow (5s^26p)\ ^2P_{3/2}$	$\rightarrow (5s^25d)\ ^2D_{3/2}$	$\rightarrow (5s^25d)\ ^2D_{5/2}$	$\rightarrow (5s^24p)\ ^2P_{1/2}$	$\rightarrow (5s^24p)\ ^2P_{3/2}$	$\rightarrow (5s^27s)\ ^2S_{1/2}$	$\rightarrow (5s^24p)\ ^2P_{5/2}$	$\rightarrow (5s^27p)\ ^2P_{1/2}$
					Cross section (10^{-16} cm^2)						
1.005	68.7										
1.127	70.2										
1.290	71.9										
1.399	72.8										
1.562	73.8										
1.767	74.6										
1.903	75.0										
2.079	75.2										
2.365	75.2										
2.474	73.2										
2.748	72.6	0.00									
2.753	69.3	2.71									
2.757	71.8	1.67									
2.761	72.5	1.14									
2.767	72.8	0.873									
2.787	73.1	0.597									
2.814	73.1	0.528									
2.912	74.4	0.674									
2.915	71.3	0.817									
3.154	71.0	1.79									
3.522	61.2	2.36									
3.636	70.8	1.75									
3.655	69.8	2.04									
3.660	69.2	2.54									
3.670	68.8	2.41	0.00								
3.674	69.1	1.92	0.208								
3.677	69.3	1.82	0.295								
3.685	69.4	1.79	0.329								
3.707	69.0	1.85	0.263	0.00							
3.712	68.8	1.85	0.254	0.463							
3.804	69.1	1.77	0.362	0.818	0.00						
3.807	69.1	1.77	0.368	0.838	0.0142	0.00					
3.807	69.1	1.77	0.369	0.843	0.0176	0.00596					
3.821	69.1	1.70	0.367	0.943	0.0451	0.0520					
3.875	68.8	1.70	0.406	1.01	0.0978	0.160					
4.062	68.8	1.77	0.394	0.933	0.221	0.351	0.00				
4.066	68.8	1.77	0.394	0.932	0.223	0.355	0.0143				
4.093	68.7	1.78	0.397	0.953	0.236	0.377	0.0980				
4.192	67.5	1.75	0.403	1.00	0.279	0.456	0.540	0.00			
4.202	67.2	1.75	0.403	0.999	0.285	0.461	0.580	0.106			
4.227	66.5	1.69	0.391	0.989	0.287	0.499	0.643	0.311	0.00		
4.229	66.5	1.68	0.389	0.987	0.287	0.503	0.648	0.334	0.0204		
4.256	65.7	1.68	0.385	0.978	0.283	0.503	0.678	0.577	0.107		
4.369	61.9	1.76	0.370	0.935	0.330	0.551	0.675	1.39	0.197	0.00	
4.392	60.4	1.80	0.344	0.838	0.337	0.583	0.670	1.49	0.208	0.424	

TABLE 5. (*Continued.*)

Energy (eV)	→ (5s²5p) ²P₃/₂	→ (5s²6s) ²S₁/₂	→ (5s²6p) ²P₁/₂	→ (5s²6p) ²P₃/₂	→ (5s²5d) ²D₃/₂	→ (5s²5d) ²D₅/₂	→ (5s²4p) ²P₁/₂	→ (5s²4p) ²P₃/₂	→ (5s²7s) ²S₁/₂	→ (5s²4p) ²P₅/₂	→ (5s²7p) ²P₁/₂
					Cross section (10^{-16} cm²)						
4.420	58.3	1.85	0.437	1.05	0.353	0.609	0.660	1.51	0.232	0.835	
4.474	56.9	1.74	0.389	0.946	0.359	0.540	0.635	1.54	0.246	1.49	
4.501	56.5	1.72	0.404	1.01	0.350	0.574	0.611	1.52	0.163	1.70	
4.544	55.9	1.77	0.409	0.934	0.384	0.684	0.590	1.53	0.238	1.98	0.00
4.556	55.6	1.76	0.428	0.934	0.397	0.698	0.581	1.52	0.244	2.04	0.127
4.583	55.2	1.79	0.364	0.888	0.350	0.628	0.558	1.49	0.187	2.14	0.0820
4.692	53.8	1.80	0.329	0.867	0.366	0.664	0.491	1.38	0.148	2.35	0.0746
4.746	53.4	1.76	0.343	0.873	0.394	0.695	0.466	1.32	0.138	2.38	0.0872
4.801	53.0	1.74	0.318	0.846	0.394	0.726	0.445	1.27	0.188	2.36	0.0759
4.869	52.4	1.75	0.307	0.863	0.399	0.731	0.420	1.21	0.143	2.32	0.0874
5.018	51.3	1.74	0.307	0.819	0.430	0.839	0.377	1.11	0.168	2.19	0.0754
5.236	49.8	1.78	0.317	0.843	0.462	0.979	0.337	1.01	0.149	2.06	0.0761
5.386	48.8	1.78	0.304	0.826	0.481	1.06	0.318	0.956	0.153	1.96	0.0601
5.576	47.6	1.81	0.275	0.771	0.478	1.07	0.299	0.898	0.152	1.83	0.0744
5.848	45.9	1.84	0.272	0.774	0.486	1.19	0.275	0.827	0.142	1.71	0.0689
6.66	41.3	1.85	0.258	0.740	0.486	1.38	0.222	0.670	0.133	1.37	0.0792
7.21	38.3	1.87	0.253	0.751	0.524	1.66	0.187	0.547	0.120	1.20	0.0715
7.75	35.1	1.90	0.236	0.671	0.476	1.66	0.175	0.504	0.114	0.972	0.0736
8.84	30.7	1.91	0.216	0.583	0.429	1.76	0.103	0.335	0.108	0.679	0.0641
9.39	29.1	1.93	0.216	0.595	0.444	1.82	0.0827	0.274	0.104	0.538	0.0585
10.5	26.2	1.96	0.210	0.562	0.429	1.90	0.0593	0.187	0.109	0.364	0.0522
11.6	23.6	1.96	0.200	0.534	0.418	1.96	0.0484	0.151	0.109	0.309	0.0454
12.1	22.5	1.97	0.199	0.532	0.411	1.96	0.0457	0.138	0.112	0.286	0.0463
13.5	20.0	1.98	0.190	0.521	0.398	2.04	0.0414	0.125	0.112	0.257	0.0442
15.4	17.3	1.99	0.181	0.514	0.385	2.11	0.0380	0.112	0.115	0.239	0.0419
17.3	15.4	1.99	0.172	0.506	0.378	2.18	0.0329	0.0962	0.119	0.214	0.0404
18.6	14.3	1.98	0.164	0.496	0.378	2.23	0.0316	0.0897	0.122	0.199	0.0386
20.8	13.0	1.98	0.153	0.478	0.378	2.32	0.0257	0.0718	0.124	0.167	0.0365
22.2	12.5	1.97	0.146	0.466	0.374	2.35	0.0233	0.0630	0.125	0.150	0.0345
24.6	11.5	1.96	0.135	0.446	0.372	2.39	0.0195	0.0522	0.128	0.128	0.0326
27.1	10.9	1.94	0.125	0.428	0.367	2.41	0.0162	0.0432	0.130	0.109	0.0304
29.8	10.4	1.91	0.114	0.414	0.361	2.42	0.0133	0.0352	0.131	0.0922	0.0278
32.5	10.1	1.88	0.104	0.399	0.355	2.41	0.0109	0.0283	0.132	0.0774	0.0256
35.5	9.89	1.85	0.0949	0.384	0.347	2.39	0.00867	0.0221	0.132	0.0643	0.0234
38.5	9.71	1.80	0.0866	0.370	0.339	2.36	0.00694	0.0172	0.131	0.0538	0.0214
41.8	9.53	1.76	0.0788	0.355	0.329	2.32	0.00548	0.0131	0.129	0.0450	0.0194
44.8	9.34	1.71	0.0726	0.340	0.321	2.29	0.00452	0.0103	0.127	0.0390	0.0179
49.9	8.98	1.64	0.0638	0.316	0.306	2.22	0.00339	0.00712	0.122	0.0321	0.0156
57.5	8.34	1.53	0.0542	0.283	0.286	2.13	0.00256	0.00491	0.114	0.0269	0.0131
64.7	7.77	1.45	0.0477	0.257	0.269	2.05	0.00217	0.00398	0.107	0.0244	0.0114
69.7	7.40	1.39	0.0443	0.240	0.259	2.00	0.00199	0.00356	0.101	0.0232	0.0104
79.7	6.87	1.30	0.0393	0.216	0.241	1.92	0.00170	0.00297	0.0921	0.0215	0.00899
89.7	6.51	1.22	0.0367	0.196	0.226	1.83	0.00148	0.00253	0.0841	0.0201	0.00797
99.7	6.30	1.14	0.0355	0.181	0.213	1.75	0.00130	0.00220	0.0774	0.0188	0.00729
115	6.14	1.05	0.0335	0.161	0.197	1.64	0.00109	0.00187	0.0696	0.0173	0.00685

TABLE 6. Angle-ICSs (10^{-16} cm^2) for electron–indium scattering from the $5p_{3/2}$ metastable state. See also supplementary material, Table S4b

Energy (eV)	Cross section (10^{-16} cm^2)									
	$\to (5s^27p)\ ^2P_{3/2}$	$\to (5p^26d)\ ^2D_{3/2}$	$\to (5s^26d)\ ^2D_{5/2}$	$\to (5s^24f)\ ^2F_{7/2}$	$\to (5s^24f)\ ^2F_{5/2}$	$\to (5p^28s)\ ^2S_{1/2}$	$\to (5s^28p)\ ^2P_{1/2}$	$\to (5s^27d)\ ^2D_{3/2}$	$\to (5p^27d)\ ^2D_{5/2}$	$\to (5s^28p)\ ^2P_{3/2}$
4.558	0.00									
4.567	0.0635	0.00								
4.573	0.105	0.0194	0.00							
4.583	0.170	0.0496	0.0490							
4.637	0.192	0.0800	0.142							
4.649	0.191	0.0836	0.148	0.00	0.00					
4.692	0.187	0.0968	0.172	0.0314	0.0192					
4.746	0.218	0.107	0.196	0.0616	0.0317					
4.764	0.214	0.103	0.194	0.0671	0.0354	0.00				
4.801	0.206	0.0938	0.189	0.0784	0.0430	0.0247				
4.869	0.214	0.120	0.200	0.0588	0.0346	0.0524				
4.909	0.211	0.112	0.207	0.0600	0.0381	0.0592				
4.912	0.209	0.111	0.205	0.0598	0.0379	0.0589	0.00			
4.913	0.208	0.111	0.204	0.0597	0.0377	0.0588	4.94×10^{-4}	0.00		
4.916	0.205	0.111	0.202	0.0595	0.0374	0.0584	0.00185	0.00324	0.00	
4.918	0.203	0.111	0.200	0.0593	0.0371	0.0582	0.00288	0.00571	0.00421	0.00
4.964	0.164	0.107	0.166	0.0556	0.0322	0.0531	0.0224	0.0522	0.0835	0.0290
5.018	0.204	0.101	0.184	0.0745	0.0432	0.0640	0.0194	0.0569	0.0944	0.0572
5.073	0.187	0.0935	0.167	0.0529	0.0350	0.0472	0.0193	0.0466	0.0917	0.0512
5.127	0.205	0.103	0.196	0.0729	0.0385	0.0585	0.0295	0.0555	0.109	0.0487
5.236	0.198	0.0994	0.175	0.0761	0.0472	0.0467	0.0191	0.0491	0.0837	0.0392
5.277	0.181	0.0998	0.177	0.0822	0.0496	0.0594	0.0194	0.0386	0.0702	0.0443
5.331	0.182	0.102	0.193	0.0842	0.0430	0.0736	0.0233	0.0424	0.0708	0.0599
5.386	0.160	0.104	0.186	0.0846	0.0454	0.0776	0.0220	0.0435	0.0688	0.0520
5.440	0.160	0.105	0.179	0.0863	0.0562	0.0674	0.0248	0.0449	0.0754	0.0605
5.576	0.189	0.115	0.223	0.105	0.0498	0.0592	0.0353	0.0507	0.0927	0.0783
5.848	0.181	0.116	0.237	0.0810	0.0440	0.0555	0.0296	0.0471	0.0965	0.0607
6.12	0.187	0.120	0.249	0.104	0.0578	0.0550	0.0324	0.0530	0.109	0.0798
6.66	0.193	0.129	0.276	0.0956	0.0474	0.0548	0.0295	0.0536	0.105	0.0711
7.21	0.183	0.128	0.311	0.111	0.0555	0.0444	0.0300	0.0554	0.116	0.0676
7.75	0.194	0.120	0.339	0.123	0.0619	0.0499	0.0308	0.0486	0.118	0.0746
8.43	0.155	0.155	0.369	0.117	0.0581	0.0370	0.0211	0.0597	0.132	0.0601
8.84	0.141	0.127	0.364	0.102	0.0449	0.0321	0.0281	0.0513	0.133	0.0613
9.39	0.109	0.110	0.335	0.104	0.0436	0.0273	0.0226	0.0458	0.111	0.0384
10.5	0.106	0.104	0.349	0.108	0.0403	0.0276	0.0221	0.0482	0.124	0.0412
11.6	0.0999	0.0991	0.343	0.116	0.0425	0.0283	0.0186	0.0467	0.122	0.0340
12.1	0.0981	0.0952	0.346	0.117	0.0403	0.0266	0.0177	0.0435	0.121	0.0326
13.5	0.0980	0.0847	0.330	0.126	0.0408	0.0278	0.0180	0.0406	0.107	0.0341
14.6	0.0991	0.0781	0.312	0.126	0.0398	0.0290	0.0174	0.0346	0.103	0.0351
15.4	0.0974	0.0733	0.307	0.130	0.0401	0.0290	0.0166	0.0318	0.0958	0.0351
15.9	0.0985	0.0695	0.298	0.132	0.0399	0.0298	0.0168	0.0291	0.0882	0.0343
17.3	0.0993	0.0651	0.303	0.132	0.0391	0.0302	0.0157	0.0264	0.0862	0.0356
18.6	0.0999	0.0598	0.291	0.136	0.0396	0.0319	0.0151	0.0223	0.0776	0.0366
20.8	0.0998	0.0581	0.305	0.132	0.0374	0.0330	0.0143	0.0206	0.0760	0.0369
22.2	0.0974	0.0567	0.306	0.127	0.0352	0.0335	0.0137	0.0193	0.0739	0.0363

TABLE 6. (*Continued.*)

Energy	Cross section (10^{-16} cm^2)									
	→ (5s^{2}7p) $^2P_{3/2}$		→ (5s^{2}6d) $^2D_{5/2}$		→ (5s^{2}4f) $^2F_{5/2}$		→ (5s^{2}8p) $^2P_{1/2}$		→ (5p^{2}7d) $^2D_{5/2}$	
Energy (eV)		→ (5p^{2}6d) $^2D_{3/2}$		→ (5s^{2}4f) $^2F_{7/2}$		→ (5p^{2}8s) $^2S_{1/2}$		→ (5s^{2}7d) $^2D_{3/2}$		→ (5s^{2}8p) $^2P_{3/2}$
23.5	0.0961	0.0562	0.308	0.122	0.0332	0.0337	0.0134	0.0179	0.0728	0.0361
24.6	0.0944	0.0555	0.310	0.118	0.0316	0.0344	0.0130	0.0173	0.0714	0.0355
26.0	0.0927	0.0549	0.311	0.114	0.0299	0.0349	0.0126	0.0166	0.0704	0.0351
27.1	0.0916	0.0547	0.313	0.110	0.0285	0.0355	0.0122	0.0160	0.0701	0.0347
28.4	0.0908	0.0540	0.314	0.105	0.0270	0.0360	0.0119	0.0158	0.0700	0.0347
29.8	0.0889	0.0534	0.314	0.101	0.0255	0.0363	0.0114	0.0152	0.0695	0.0343
31.2	0.0873	0.0529	0.314	0.0970	0.0242	0.0367	0.0109	0.0150	0.0694	0.0340
32.5	0.0865	0.0526	0.314	0.0933	0.0231	0.0370	0.0105	0.0146	0.0694	0.0337
33.9	0.0858	0.0521	0.314	0.0898	0.0220	0.0372	0.0101	0.0143	0.0692	0.0336
35.5	0.0852	0.0516	0.312	0.0858	0.0208	0.0375	0.00966	0.0140	0.0688	0.0333
36.9	0.0842	0.0510	0.311	0.0828	0.0199	0.0375	0.00926	0.0137	0.0685	0.0330
38.5	0.0831	0.0501	0.309	0.0793	0.0189	0.0376	0.00884	0.0134	0.0679	0.0327
40.1	0.0818	0.0492	0.306	0.0762	0.0180	0.0375	0.00843	0.0131	0.0671	0.0323
41.8	0.0803	0.0483	0.303	0.0733	0.0171	0.0373	0.00805	0.0128	0.0664	0.0318
43.1	0.0787	0.0476	0.300	0.0711	0.0165	0.0372	0.00774	0.0125	0.0655	0.0312
44.8	0.0771	0.0468	0.297	0.0685	0.0158	0.0370	0.00740	0.0122	0.0647	0.0306
46.1	0.0755	0.0461	0.294	0.0666	0.0153	0.0367	0.00714	0.0120	0.0640	0.0300
47.8	0.0739	0.0453	0.291	0.0644	0.0147	0.0364	0.00683	0.0117	0.0632	0.0294
49.9	0.0719	0.0443	0.287	0.0618	0.0139	0.0359	0.00647	0.0114	0.0621	0.0286
51.8	0.0699	0.0434	0.283	0.0597	0.0134	0.0354	0.00617	0.0112	0.0611	0.0278
54.0	0.0674	0.0425	0.278	0.0575	0.0128	0.0348	0.00587	0.0109	0.0599	0.0269
55.4	0.0662	0.0419	0.275	0.0562	0.0124	0.0344	0.00569	0.0107	0.0593	0.0264
56.5	0.0651	0.0415	0.273	0.0552	0.0122	0.0341	0.00556	0.0106	0.0588	0.0260
57.5	0.0640	0.0410	0.271	0.0543	0.0119	0.0338	0.00543	0.0105	0.0582	0.0255
59.7	0.0620	0.0402	0.267	0.0526	0.0114	0.0331	0.00519	0.0102	0.0572	0.0247
64.7	0.0578	0.0383	0.257	0.0493	0.0105	0.0317	0.00471	0.00971	0.0548	0.0230
69.7	0.0538	0.0365	0.248	0.0467	0.00973	0.0302	0.00431	0.00923	0.0526	0.0215
74.7	0.0508	0.0349	0.238	0.0447	0.00910	0.0288	0.00398	0.00879	0.0504	0.0202
79.7	0.0479	0.0333	0.230	0.0434	0.00858	0.0275	0.00370	0.00837	0.0483	0.0191
84.7	0.0455	0.0319	0.222	0.0419	0.00816	0.0263	0.00346	0.00798	0.0463	0.0181
89.7	0.0434	0.0305	0.215	0.0405	0.00783	0.0251	0.00325	0.00762	0.0445	0.0172
94.7	0.0416	0.0293	0.208	0.0391	0.00757	0.0240	0.00308	0.00728	0.0428	0.0165
99.7	0.0400	0.0281	0.202	0.0379	0.00738	0.0230	0.00294	0.00696	0.0413	0.0158
105	0.0387	0.0270	0.197	0.0367	0.00718	0.0221	0.00282	0.00668	0.0398	0.0153
110	0.0377	0.0261	0.192	0.0356	0.00698	0.0213	0.00273	0.00642	0.0386	0.0149
115	0.0368	0.0252	0.188	0.0346	0.00680	0.0205	0.00266	0.00617	0.0374	0.0145
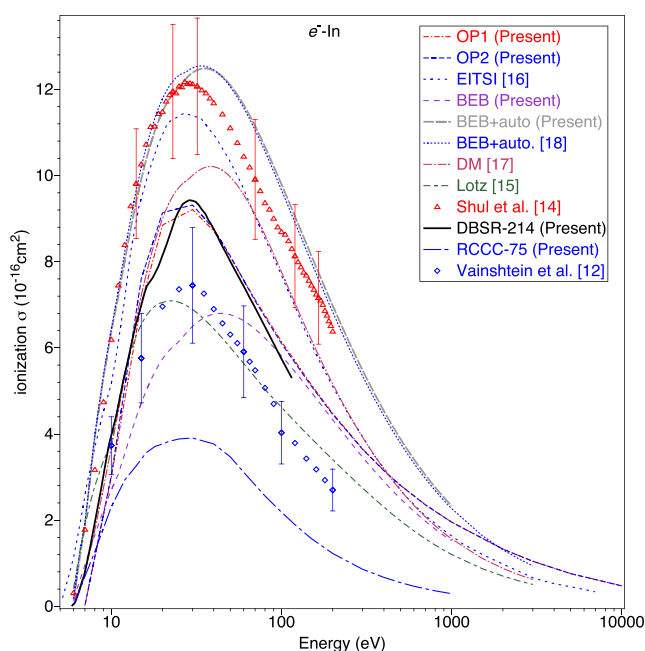
FIG. 5. TICSs ($\times 10^{-16}$ cm^2) for the process $e^- + \text{In} \rightarrow \text{In}^+ + 2e^-$. Experimental data from the work of Vainshtein et al.[12] (blue diamonds) and Shul et al.[14] (red triangles) are plotted, along with earlier theoretical results from the work of Lotz[15] (green dotted-dashed line), an EITSI calculation[16] (blue dashed line), a Deutsch–Märk computation[17] (magenta dotted-dashed line), and a BEB+PWB calculation[18] (blue dotted line). Also plotted are our current BEB result (purple dashed line), OP1 (red dotted-dashed line) and OP2 (blue dashed line) results, RCCC-75 (blue dotted-dashed line) calculation, BEB+PWB (gray dashed line) calculation, and DBSR-214 (black solid line) computation. See also the legend in the figure.

FIG. 6. Summary plot showing our recommended electron–In cross sections ($\times 10^{-16}$ cm^2) for elastic scattering, the sum over all discrete inelastic cross sections, the TICS, and the grand total cross section. See also the legend in the figure.

Given the discussion above, it appears reasonable to assert that the measurements from the work of Vainshtein et al.[12] can constitute a lower bound on the true TICS, while those from the work of Shul et al.[14] can be considered as an upper bound. In the latter case, this seems reasonable, as it is well known that PWB based calculations, without some appropriate scaling,[5] will overestimate the magnitude of the cross sections they calculate so that the BEB+PWB autoionization cross-section magnitude should also be too large. Under these circumstances, when coming to form a recommended TICS database, we will follow the approach of Itikawa (see e.g., Ref. [45]), which essentially means that for energies from threshold to 200 eV, we take an average of the available experimental data, and then from 200 eV to 10 000 eV, we use a suitably scaled (scaling factor = 1.014) OP1 result to effect the extrapolation to higher energies. Note that we have had to employ Itikawa's method (successfully) in some of our recent data compilations for electron scattering from some other atomic species.[19,20,46] The estimated uncertainty on this is ~±22%, reflecting the error carried forward in taking the average of the TICS measurements.[12,14] Interestingly, this recommended TICS, to within our error just cited, is in quite good accord with the results from our OP1, OP2, and DBSR-214 calculations. The present recommended TICS can be found in Table 2, and they are also plotted in Fig. 6 along with our recommended elastic ICS, MTCS, and sum over all discrete inelastic angle-ICSs.

3.4. TCS

The recommended TCS for $E_0 = 0.001$ eV–10 000 eV is now simply formed by, at each incident electron energy, adding up the results for the recommended elastic ICS, the recommended sum over all discrete inelastic excitation ICS, and the recommended TICS, namely, summing up the results of columns 1, 3, and 4 of Table 2. That recommended TCS can also now be found in column 5 of Table 2, as well as being plotted in Fig. 6.

4. Simulated Transport Coefficients

In what follows, we implement a well-benchmarked multi-term solution of Boltzmann's equation[2,47,48] for the calculation of electron swarm transport coefficients in gaseous In over a range of reduced electric fields E/n_0, varying from 10^{-2} Td to 10^4 Td, where 1 Td = 1 Townsend = 10^{-21} V m^2 and n_0 is the neutral number density. The two-term approximation (TTA)[47,48] tends to break down at the higher E/n_0 considered, although it remains accurate to within 20% for all transport coefficients, with the exception of some of the diffusion coefficients. Under the TTA at high E/n_0, these errors in diffusion can be as large as 51% for the flux transverse diffusion coefficient, 69% for the bulk longitudinal diffusion coefficient, and 70% for the flux longitudinal diffusion coefficient. In our calculations, we assume isotropic scattering in the excitation and ionization processes, while we have included the anisotropic nature of elastic scattering through the use of the elastic MTCSs. We consider transport through an In vapor at temperature $T = 1260$ K, which is in the vicinity of our previous crossed-beam experimental measurements.[1,9] As the corresponding thermal energy,

J. Phys. Chem. Ref. Data **50**, 013101 (2021); doi: 10.1063/5.0035218

Published by AIP Publishing on behalf of the National Institute of Standards and Technology.

50, 013101-17
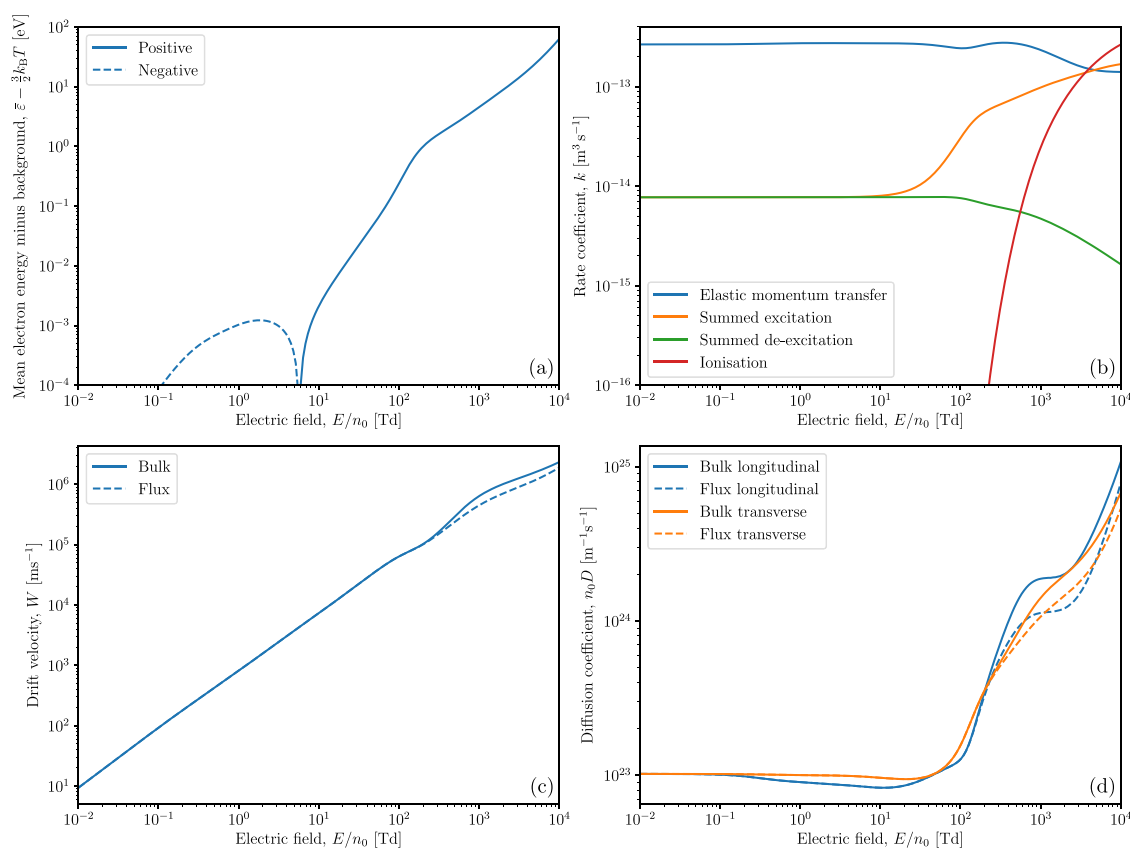
FIG. 7. Calculated mean electron energies (above the thermal background) (a), rate coefficients (b), drift velocities (c), and diffusion coefficients (d) for electrons in In vapor at temperature $T = 1260$ K (with thermal energy $\frac{3}{2}k_BT \approx 0.163$ eV) over a range of reduced electric fields. See also the legends for further details.

$\frac{3}{2}k_BT \approx 0.163$ eV, is on the order of the energy of the first $(5p)^2 P_{3/2}$ metastable state ($\sim$0.274 eV), we consider it prudent to account for de-excitation/superelastic collisions in our Boltzmann equation solution. Indeed, by applying Maxwell–Boltzmann statistics to In vapor at the aforementioned temperature, we determine that 86% of In atoms are in the ground state, with the remaining 14% almost exclusively in the first $(5p)^2 P_{3/2}$ metastable state. Note that we determine each de-excitation cross section from its corresponding excitation cross section by employing the principle of microscopic reversibility and detailed balancing.[49] We use our recommended elastic MTCS for elastic collisions with ground-state In atoms and obtain a separate elastic MTCS for In atoms in the first $(5p)^2 P_{3/2}$ metastable state by scaling our $(5p)^2 P_{3/2} \rightarrow (5p)^2 P_{3/2}$ elastic ICS by the ratio of our recommended elastic MTCS to recommended elastic ICS. Similarly, while we use our recommended TICS for ionization of In atoms in the ground state, we shift the energy threshold of our recommended TICS down to $\sim$5.786 eV − 0.274 eV = 5.512 eV for ionization of In atoms already excited to the first $(5p)^2 P_{3/2}$ metastable state. The resulting calculated mean electron energies, rate coefficients, drift velocities, and diffusion coefficients are presented in Fig. 7. Figure 7(a) shows the difference between the mean electron energy $\bar{\varepsilon}$ and the thermal energy of the In vapor, $\frac{3}{2}k_BT \approx 0.163$ eV. In the low-field regime, near 10^{-2} Td, this energy difference is very small, indicating that the electrons are in thermal equilibrium with the background In atoms. As E/n_0 increases,

the mean electron energy decreases, reaching a minimum of $\sim$1 meV below the thermal background at $\sim$1.8 Td. We attribute this cooling to be primarily due to the $(5p)^2 P_{1/2} \rightarrow (5p)^2 P_{3/2}$ transition, resulting in a greater power output from the swarm due to excitations than input from the electric field, superelastic collisions, and elastic collisions in this regime. Eventually, as E/n_0 approaches $\sim$5.7 Td, the latter heating processes dominate enough to return the swarm to thermal equilibrium with the background. Then, as E/n_0 is increased further, the mean energy increases rapidly, slowing slightly in its ascent from $\sim$200 Td onward due to the significant opening of the ionization channel. Figure 7(b) shows rate coefficients for elastic momentum transfer, summed excitation, summed de-excitation, and ionization processes. The elastic momentum transfer rate coefficient remains somewhat constant up to 1000 Td, before decreasing slightly at higher E/n_0. The summed excitation and de-excitation rate coefficients are identical close to thermal equilibrium, as is expected due to detailed balancing. These rate coefficients begin to depart visibly from 10 Td onward, with an increase in excitation events and decrease in de-excitation events. Although it should be noted that this departure starts much earlier than this as it is the slight excess of excitation events at low E/n_0 that is responsible for the $\sim$1 meV cooling of electrons below the background. The ionization rate coefficient is zero in the low-field regime, before becoming appreciable around roughly 200 Td. In the high-field regime, near 10 000 Td, ionization dominates with its rate coefficient exceeding

those for all other processes. Figure 7(c) shows the bulk and flux drift velocities of the swarm, both of which are observed to increase monotonically with E/n_0, coinciding with one another up until the nonconservative effects of ionization manifest at around 200 Td. In the nonconservative regime from ~200 Td onward, the bulk drift velocity exceeds the flux, suggesting that electrons are being preferentially created at the front of the swarm, shifting the center of mass in the direction of the applied field. Figure 7(d) shows bulk and flux diffusion coefficients in the directions longitudinal and transverse to the applied electric field. Of course, below ~200 Td, the bulk and flux diffusion coefficients coincide. Below 0.1 Td, the transverse and longitudinal diffusion coefficients are essentially equal due to the expected isotropy of the electron velocity distribution in this regime. Above 0.1 Td, both diffusion coefficients begin to decrease slightly, reaching minima at roughly 10 Td and 20 Td for the longitudinal and transverse coefficients, respectively. Past these minima, both diffusion coefficients then proceed to rise monotonically with increasing E/n_0. In the nonconservative regime above ~200 Td, the bulk diffusion coefficients exceed their flux counterparts, suggesting a preferential creation of electrons at the sides of the swarm, in addition to its front.

5. Conclusions

We have compiled a complete angle-ICS database for electron–In scattering. As a part of that process, additional theoretical computations were undertaken, with these results also being reported here. While the need for having complete and accurate cross-section databases, for modeling a variety of electron-driven phenomena,[50,51] is now well understood, recent work from the Madrid group[52–54] has reinforced that assessment.

Interesting scattering results from this investigation include the very large shape resonances in the low-energy elastic ICS and MTCS, a series of near-threshold resonances in many of the discrete inelastic scattering channels we have considered, and the lack of consistent measurements for the experimental TICS in electron–In scattering. While there is no doubt that such experiments in In are difficult to undertake, further measurements of the TICS are clearly desirable.

Finally, we have employed our recommended cross sections to study the behavior of a swarm of electrons, drifting through a background gas of In, under the influence of an applied electric field. This analysis was undertaken using a multi-term Boltzmann equation solution to determine the relevant transport coefficients. Interesting results from this study included the need to allow for superelastic processes, the breakdown of the TTA in simulating the relevant transport coefficients in some regions of E/n_0, and that there was cooling in the mean electron energy of the swarm at ~1.8 Td, which can be associated with the opening of the $(5p)^2 P_{3/2}$ metastable channel.

6. Supplementary Material

See the supplementary material for Excel tables of the present data.

Acknowledgments

7. Data Availability

The data that support the findings of this study are available from the corresponding author upon reasonable request.

8. References

[1] K. R. Hamilton, O. Zatsarinny, K. Bartschat, M. S. Rabasović, D. Šević, B. P. Marinković, S. Dujko, J. Atić, D. V. Fursa, I. Bray, R. P. McEachran, F. Blanco, G. García, P. W. Stokes, R. D. White, and M. J. Brunger, Phys. Rev. A **102**, 022801 (2020).

[2] R. D. White, D. Cocks, G. Boyle, M. Casey, N. Garland, D. Konovalov, B. Philippa, P. Stokes, J. de Urquijo, O. González-Magaña, R. P. McEachran, S. J. Buckman, M. J. Brunger, G. Garcia, S. Dujko, and Z. L. Petrovic, Plasma Sources Sci. Technol. **27**, 053001 (2018).

[3] J. de Urquijo, M. J. E. Casey, L. N. Serkovic-Loli, D. G. Cocks, G. J. Boyle, D. B. Jones, M. J. Brunger, and R. D. White, J. Chem. Phys. **151**, 054309 (2019).

[4] C. M. Ögün, W. Truong, C. Kaiser, R. Kling, and W. Heering, J. Phys. D: Appl. Phys. **47**, 285202 (2014).

[5] H. Tanaka, M. J. Brunger, L. Campbell, H. Kato, M. Hoshino, and A. R. P. Rau, Rev. Mod. Phys. **88**, 025004 (2016).

[6] L. C. Pitchford, L. L. Alves, K. Bartschat, S. F. Biagi, M.-C. Bordage, I. Bray, C. E. Brion, M. J. Brunger, L. Campbell et al., Plasma Process. Polym. **14**, 1600098 (2017).

[7] R. S. M. Chrystile, I. S. Burns, J. Hult, and C. F. Kaminski, Opt. Lett. **34**, 2492 (2009).

[8] J. Hult, I. S. Burns, and C. F. Kaminski, Proc. Combust. Inst. **30**, 1535 (2005).

[9] M. S. Rabasović, V. I. Kelemen, S. D. Tošić, D. Šević, M. M. Dovhanych, V. Pejčev, D. M. Filipović, E. Yu Remeta, and B. P. Marinković, Phys. Rev. A **77**, 062713 (2008).

[10] M. Gryziński, Phys. Rev. **138**, A336 (1965).

[11] M. Gryziński, Phys. Rev. **138**, A322 (1965).

[12] L. A. Vainshtein, D. G. Golovach, V. I. Ochkur, V. I. Rakhovskiĭ, N. M. Rumyantsev, and V. M. Shustryakov, Sov. Phys. JETP **66**, 36 (1987).

[13] L. L. Shimon, E. I. Nepiipov, and I. P. Zapesochnyi, Sov. Phys. Tech. Phys. **20**, 434 (1975).

[14] R. J. Shul, R. C. Wetzel, and R. S. Freund, Phys. Rev. A **39**, 5588 (1989).

[15] W. Lotz, Z. Phys. A **232**, 101 (1970).

[16] M. R. Talukder, S. Bose, M. A. R. Patoary, A. K. F. Haque, M. A. Uddin, A. K. Basak, and M. Kando, Eur. Phys. J. D **46**, 281 (2008).

[17] D. Margreiter, H. Deutsch, and T. D. Märk, Int. J. Mass Spectrom. Ion Proc. **139**, 127 (1994).

[18] Y.-K. Kim and P. M. Stone, Phys. Rev. A **64**, 052707 (2001).

[19] R. P. McEachran, F. Blanco, G. García, and M. J. Brunger, J. Phys. Chem. Ref. Data **47**, 033103 (2018).

[20] R. P. McEachran, F. Blanco, G. García, P. W. Stokes, R. D. White, and M. J. Brunger, J. Phys. Chem. Ref. Data **47**, 043104 (2018).

[21] B. P. Marinković, R. Panajotović, D. Šević, R. P. McEachran, G. García, F. Blanco, and M. J. Brunger, Phys. Rev. A **99**, 062702 (2019).

22 B. Predojević, D. Šević, B. P. Marinković, R. P. McEachran, F. Blanco, G. García, and M. J. Brunger, Phys. Rev. A **101**, 032704 (2020).

23 R. D. Cowan, *The Theory of Atomic Structure and Spectra* (University of California Press, 1981).

24 M. E. Riley and D. G. Truhlar, J. Chem. Phys. **63**, 2182 (1975).

25 X. Zhang, J. Sun, and Y. Liu, J. Phys. B: At., Mol. Opt. Phys. **25**, 1893 (1992).

26 R. P. McEachran, L. A. Parcell, and A. D. Stauffer, J. Phys. B: At., Mol. Opt. Phys. **28**, 2487 (1995).

27 G. Staszewska, D. W. Schwenke, D. Thirumalai, and D. G. Truhlar, Phys. Rev. A **28**, 2740 (1983).

28 F. Blanco and G. García, Phys. Rev. A **67**, 022701 (2003).

29 O. Zatsarinny, K. Bartschat, G. Garciá, F. Blanco, L. R. Hargreaves, D. B. Jones, R. Murrie, J. R. Brunton, M. J. Brunger, M. Hoshino, and S. J. Buckman, Phys. Rev. A **83**, 042702 (2011).

30 I. P. Grant, B. J. McKenzie, P. H. Norrington, D. F. Mayers, and N. C. Pyper, Comput. Phys. Commun. **21**, 207 (1980).

31 P. Jönsson, G. Gaigalas, J. Bieroń, C. F. Fischer, and I. P. Grant, Comput. Phys. Commun. **184**, 2197 (2013).

32 Y.-K. Kim and M. E. Rudd, Phys. Rev. A **50**, 3954 (1994).

33 M. Huttula, S. Heinäsmäki, E. Kukk, R. Sankari, H. Aksela, and S. Aksela, Phys. Rev. A **70**, 022714 (2004).

34 E. P. F. Lee and A. W. Potts, J. Electron Spectrosc. Relat. Phenom. **19**, 65 (1980).

35 A. Kramida, Yu. Ralchenko, J. Reader, and NIST ASD Team, *NIST Atomic Spectra Database (ver. 5.7.1)* (National Institute of Standards and Technology, Gaithersburg, MD, 2020), online available at: http://physics.nist.gov/asd; May 10 2020.

36 M. A. Baig, I. Ahmed, and J. P. Connerade, J. Phys. B: At., Mol. Opt. Phys. **21**, 35 (1988).

37 M. J. Frisch, G. W. Trucks, H. B. Schlegel, G. E. Scuseria, M. A. Robb *et al.*, Gaussian 09, Revision B.01, Gaussian, Inc., Wallingford, CT, USA, 2010.

38 C. Lee, W. Yang, and R. G. Parr, Phys. Rev. B **37**, 785 (1988).

39 C. Sosa, J. Andzelm, B. C. Elkin, E. Wimmer, K. D. Dobbs, and D. A. Dixon, J. Phys. Chem. **96**, 6630 (1992).

40 C. W. Walter, N. D. Gibson, D. J. Carman, Y.-G. Li, and D. J. Matyas, Phys. Rev. A **82**, 032507 (2010).

41 C. J. Bostock, D. V. Fursa, and I. Bray, J. Phys. B: At., Mol. Opt. Phys. **45**, 181001 (2012).

42 K. Bartschat, J. Phys. B: At., Mol. Opt. Phys. **25**, L307 (1992).

43 L. Ma, J. Indergaard, B. Zhang, I. Larkin, R. Moro, and W. A. de Heer, Phys. Rev. A **91**, 010501(R) (2015).

44 B. G. Lindsay and M. A. Mangan, in *Photon and Electron Interactions with Atoms, Molecules and Ions*, Landolt-Börnstein Vol. 17C, edited by Y. Itikawa (Springer-Verlag, Berlin, Heidelberg, 2003), Chap. 5.

45 Y. Itikawa, J. Phys. Chem. Ref. Data **45**, 033106 (2016).

46 R. P. McEachran, B. P. Marinković, G. García, R. D. White, P. W. Stokes, D. B. Jones, and M. J. Brunger, J. Phys. Chem. Ref. Data **49**, 013102 (2020).

47 G. J. Boyle, W. J. Tattersall, D. G. Cocks, R. P. McEachran, and R. D. White, Plasma Sources Sci. Technol. **26**, 024007 (2017).

48 R. D. White, R. E. Robson, B. Schmidt, and M. A. Morrison, J. Phys. D: Appl. Phys. **36**, 3125 (2003).

49 A. Hochstim, *Kinetic Processes in Gases and Plasmas* (Academic Press, New York, 1969).

50 L. Campbell and M. J. Brunger, Int. Rev. Phys. Chem. **35**, 297 (2016).

51 M. J. Brunger, Int. Rev. Phys. Chem. **36**, 333 (2017).

52 A. I. Lozano, J. C. Oller, D. B. Jones, R. F. da Costa, M. T. do N. Varella, M. H. F. Bettega, F. Ferreira da Silva, P. Limão-Vieira, M. A. P. Lima, R. D. White, M. J. Brunger, F. Blanco, A. Muñoz, and G. García, Phys. Chem. Chem. Phys. **20**, 22368 (2018).

53 A. I. Lozano, K. Krupa, F. Ferreira da Silva, P. Limão-Vieira, F. Blanco, A. Munõz, D. B. Jones, M. J. Brunger, and G. García, Eur. Phys. J. D **71**, 226 (2017).

54 F. Costa, A. Traoré-Dubuis, L. Álvarez, A. I. Lozano, X. Ren, A. Dorn, P. Limão-Vieira, F. Blanco, J. C. Oller, A. Muñoz, A. García-Abenza, J. D. Gorfinkiel, A. S. Barbosa, M. H. F. Bettega, P. Stokes, R. D. White, D. B. Jones, M. J. Brunger, and G. García, Int. J. Mol. Sci. **21**, 6947 (2020).

Electron-impact excitation of the $(5s^2 5p)\,^2P_{1/2} \to (5s^2 6s)\,^2S_{1/2}$ transition in indium: Theory and experiment

K. R. Hamilton, O. Zatsarinny, and K. Bartschat
Department of Physics and Astronomy, Drake University, Des Moines, Iowa 50311, USA

M. S. Rabasović, D. Šević, B. P. Marinković, S. Dujko, and J. Atić
Institute of Physics Belgrade, University of Belgrade, Pregrevica 118, 11080 Belgrade, Serbia

D. V. Fursa and I. Bray
Curtin Institute for Computation and Department of Physics and Astronomy, Perth, 6102 WA, Australia

R. P. McEachran
Plasma Research Laboratories, The Research School of Physics, Australian National University, Canberra, ACT 0200, Australia

F. Blanco
Departamento de Estructura de la Materia, Física Térmica y Electrónica e IPARCOS, Universidad Complutense de Madrid, Avenida Complutense, E-28040 Madrid, Spain

G. García
*Instituto de Física Fundamental, CSIC, Serrano 113-bis, E-28006 Madrid, Spain
and Centre for Medical Radiation Physics, University of Wollongong, New South Wales 2522, Australia*

P. W. Stokes and R. D. White
College of Science and Engineering, James Cook University, Townsville, Queensland 4810, Australia

M. J. Brunger[*]
*College of Science and Engineering, Flinders University, GPO Box 2100, Adelaide, SA 5001, Australia
and Department of Actuarial Science and Applied Statistics, Faculty of Business and Information Science,
UCSI University, Kuala Lumpur 56000, Malaysia*

We present angle-integrated and angle-differential cross sections for electron-impact excitation of the $(5s^2 5p)\,^2P_{1/2} \to (5s^2 6s)\,^2S_{1/2}$ transition in atomic indium. Experimental data for six incident electron energies between 10 and 100 eV are compared with predictions from semirelativistic and fully relativistic B-spline R-matrix calculations, as well as a fully relativistic convergent close-coupling model. Agreement between our measured and calculated data is, with a few exceptions, found to be typically very good. Additionally, the agreement between the present theoretical predictions is generally excellent, with the remaining small deviations being associated with the slightly different, although still very accurate, descriptions of the target structure. Agreement between the present results and an earlier relativistic distorted-wave computation [T. Das, R. Srivastava, and A. D. Stauffer, Phys. Lett. A **375**, 568 (2011)] was, however, found to be marginal, particularly at 10 and 20 eV.

I. INTRODUCTION

The soft, gray metallic element indium ($Z = 49$) belongs to the group-III elements of the Periodic Table. It is the first in a series of the $5p$ elements in the Periodic Table (which ends with xenon), with the atoms of that series being characterized by their relatively small values of the dipole polarizability ($\alpha \sim 65\,a_0^3$ for indium) [1]. Indium (In) is currently used to make transparent electrodes in liquid-crystal displays (LCDs) [2], and its spectral lines, for both its neutral and ionized (In$^+$) forms, are expected to be very important in modeling plasmas in which indium is a constituent. The latter is relevant, as indium is a possible candidate to replace mercury in low-pressure discharge lamps in lighting solutions [2,3]. Indeed, Ögün *et al.* [3] conducted some collisional-radiative modeling of an indium iodide-argon plasma to investigate that possible application. However, the excitation cross sections they

---
[*]Corresponding author: michael.brunger@flinders.edu.au

employed in that study, from the method of Gryziński [4,5], are not expected to be accurate. Hence, one of the rationales behind the present study is to make a start to provide a set of accurate cross-section data, over a wide energy range [6], for use in gas-discharge and low-temperature plasma modeling [7].

Another important application of indium is that it is particularly suitable as a tracer for two-line atomic fluorescence (TLAF) thermometry measurements [8–10]. This method works by using two diode lasers with wavelengths of 410 and 451 nm, to excite the $6s\ ^2S_{1/2}$ resonance state of indium atoms seeded into a flame. Owing to the typically greater oscillator strengths of atoms compared to molecules, strong fluorescence signals can be obtained at low excitation energies. A particular advantage of indium atoms is that its spin-orbit coupling in the $5p$ ground state leads to an energy spacing that is about equal to kT in typical combustion environments (2000–4000 K) [8].

There is currently a paucity of electron-indium scattering data, both theoretical and experimental, available in the literature. From a theoretical perspective, we know of some very low-energy spin asymmetries, for elastic scattering and excitation of the metastable $5p_{3/2}$ state, from the relativistic convergent close-coupling (RCCC) [11] and Breit-Pauli R-matrix [12] methods. Note that the current RCCC and B-spline R-matrix (BSR) and relativistic B-spline R-matrix (DBSR) calculations significantly extend those earlier investigations. An atomic optical model formulation, for elastic e-In differential cross sections (DCSs) and integral cross sections (ICSs), for electron energies between 10 and 100 eV, was reported in Rabasović *et al.* [13]. Finally, again for energies in the 10–100 eV range, a relativistic distorted-wave (RDW) computation for the $5p \rightarrow 6s$ transition, at the DCS level, is available [14]. In terms of experimental measurements, there is a comprehensive set of elastic DCSs and ICSs in Rabasović *et al.* [13], while some preliminary $5p \rightarrow 6s$ DCSs, at very forward-scattered electron angles, can be found in Rabasović *et al.* [15]. The present measurements significantly extend and supersede those earlier data [15].

Another rationale behind this work is to try and provide benchmark data for the $5p \rightarrow 6s$ transition in indium, against which results from other methods might be tested. This is of timely importance, as atomic optical-potential approaches, which are computationally cheaper than the present close-coupling approaches, have been gaining in popularity (see, e.g., [16–18]) in recent years.

The structure of the remainder of this paper is as follows. In Sec. II, we provide computational details of our BSR, DBSR, and RCCC calculations. This section also includes relevant details of their target-structure computations. Thereafter, in Sec. III, a description of our experimental methodology, including the uncertainties in making our measurements, is provided. The approaches we adopted to extrapolate our DCS data to 0° and 180°, in order to generate the corresponding ICS at that energy, are also given in this section. In Sec. IV, the present theoretical and experimental DCSs and ICSs are described and discussed, and compared to the earlier RDW results [14] where appropriate. Finally, some conclusions from the present investigation are given in Sec. V.

II. COMPUTATIONAL DETAILS

A. BSR and DBSR models

The target-structure calculations and the scattering calculations in the present work were carried out in a similar manner to previous works. Hence, we only summarize the specific aspects for the present calculation below. A comprehensive overview of the B-spline R-matrix method was given by Zatsarinny and Bartschat [19]. Below we refer to the semirelativistic models as BSR-N and to the fully relativistic models as DBSR-N, where N indicates the number of states in the close-coupling expansion.

A first general version of the BSR computer code was published by Zatsarinny [20] and is constantly being updated. A stable version with many upgrades is publicly available from github [21], and substantial efforts are underway to make it generally accessible via the AMP-Gateway [22]. The DBSR calculations are based on the work described in [23], and we are currently working to make that code available as well.

As always, the first ingredient for a collision calculation is the description of the target structure. In the present case, we used the MCHF [24], GRASP2 [25], and DBSR_HF [26] atomic structure codes to generate bound orbitals for the In$^+$ positive ion, either just for the ground state with dominant configuration $(5s^2)\ ^2S$ or also for the first two excited states with dominant configurations $(5s5p)^{3,1}P^o$, respectively. We then ran the (D)BSR code in the bound-state mode [27], which generates multiconfiguration expansions of the states for neutral In. Depending on the number of In$^+$ states, we label these models "(d)bsr_cc_01" and "(d)bsr_cc_03," respectively. All of the production collision calculations were carried out with the structure obtained with the (d)bsr_cc_03 ansatz.

While the above procedure can generate a large number of both physical and pseudostates (the individual classifications depend on whether or not the orbitals fit into the R-matrix box), an even more accurate target description can be obtained by adding a few optimized configurations as "perturbers" to the multiconfiguration expansions. Specifically, we added the $(5s5p^2)\ ^4P$, ^2D, ^2P, ^2S terms in all models and, furthermore, the $5p^3$ states in the "cc_03" model, in order to ensure that the important p^2 configuration was included properly. Although elastic scattering will be considered as part of a separate paper in the future, the latter is particularly important for that collision problem since the $5s^25p^2$ configurations lead to negative-ion bound states for the ^3P configuration, while the ^1D and ^1S configurations lead to resonance features at very low electron energies.

Table I lists the energy levels of the lowest 22 bound states of In, as obtained in the various (D)BSR structure models and compared with the recommended NIST levels [28]. As expected, the (d)bsr_cc_03 expansions provide a much better target description since they already contain the significant effect of the p^2 configuration. We ultimately adjusted the diagonal elements of the Hamiltonian matrix to reproduce the experimental excitation thresholds. This is a standard procedure that is fully described in Zatsarinny [20], to whom the interested reader is referred for more details. For a comparison with the experimental data presented in this paper, this adjustment is of essentially no consequence. However, it can affect the near-threshold predictions (within fractions of an

TABLE I. Binding energies (in eV) for the In target states included in the (D)BSR close-coupling expansions. Here, "Conf." refers to the dominant configuration.

Conf.	State	NIST [28]	bsr_cc_01	Diff.	bsr_cc_03	Diff.	dbsr_cc_01	Diff.	dbsr_cc_03	Diff.
$5s^25p$	$^2P^o_{1/2}$	−5.786	−5.187	0.599	−5.739	0.047	−4.981	0.806	−5.576	0.210
$5s^25p$	$^2P^o_{3/2}$	−5.512	−4.895	0.617	−5.437	0.075	−4.736	0.749	−5.335	0.177
$5s^26s$	$^2S_{1/2}$	−2.765	−2.546	0.219	−2.677	0.087	−2.552	0.212	−2.680	0.084
$5s^26p$	$^2P^o_{1/2}$	−1.842	−1.744	0.098	−1.820	0.022	−1.724	0.118	−1.805	0.037
$5s^26p$	$^2P^o_{3/2}$	−1.805	−1.705	0.099	−1.783	0.022	−1.692	0.112	−1.771	0.033
$5s^25d$	$^2D_{3/2}$	−1.708	−1.545	0.163	−1.701	0.007	−1.539	0.169	−1.692	0.017
$5s^25d$	$^2D_{5/2}$	−1.705	−1.544	0.162	−1.701	0.004	−1.537	0.169	−1.687	0.019
$5s5p^2$	$^4P_{5/2}$	−1.450			−1.520	−0.070			−1.607	−0.157
$5s5p^2$	$^4P_{3/2}$	−1.320			−1.409	−0.089			−1.490	−0.169
$5s^27s$	$^2S_{1/2}$	−1.286	−1.222	0.064	−1.256	0.030	−1.224	0.062	−1.259	0.026
$5s5p^2$	$^4P_{3/2}$	−1.143			−1.249	−0.106			−1.315	−0.174
$5s^27p$	$^2P^o_{1/2}$	−0.968	−0.932	0.036	−0.959	0.009	−0.925	0.043	−0.954	0.014
$5s^27p$	$^2P^o_{3/2}$	−0.954	−0.918	0.036	−0.945	0.009	−0.913	0.041	−0.942	0.013
$5s^26d$	$^2D_{3/2}$	−0.945	−0.867	0.078	−0.941	0.004	−0.863	0.081	−0.938	0.007
$5s^26d$	$^2D_{5/2}$	−0.939	−0.866	0.073	−0.939	−0.001	−0.862	0.077	−0.932	0.006
$5s^24f$	$^2F^o_{5/2}$	−0.863	−0.851	0.012	−0.863	0.001	−0.851	0.013	−0.862	0.002
$5s^24f$	$^2F^o_{3/2}$	−0.863	−0.851	0.012	−0.863	0.001	−0.851	0.013	−0.862	0.002
$5s^28s$	$^2S_{1/2}$	−0.748	−0.720	0.028	−0.734	0.014	−0.721	0.027	−0.736	0.012
$5s^28p$	$^2P^o_{1/2}$	−0.600	−0.583	0.017	−0.595	0.005	−0.580	0.021	−0.594	0.007
$5s^27d$	$^2D_{3/2}$	−0.599	−0.553	0.046	−0.596	0.004	−0.551	0.048	−0.594	0.005
$5s^27d$	$^2D_{3/2}$	−0.596	−0.553	0.044	−0.595	0.002	−0.551	0.046	−0.591	0.005
$5s^28p$	$^2P^o_{3/2}$	−0.594	−0.576	0.018	−0.589	0.005	−0.574	0.020	−0.588	0.006

eV), and hence those results need to be taken with appropriate care.

The quality of our target description can be further assessed by comparing the results for the oscillator strengths, which are very important to obtain reliable absolute values for the excitation cross sections, especially for optically allowed transitions at high incident electron energies. Table II shows the comparison of oscillator strengths between our calculated results and the recommended values from the NIST database [28].

Finally, even though this is more important for elastic scattering, we mention here that the polarizability of the ground state is obtained as $64.5\,a_0^3$, where $a_0 = 0.529 \times 10^{-10}$ m is the Bohr radius, provided the entire spectrum of discrete and pseudostates is accounted for. This agrees well with the experimental value of Ma *et al.* [29] within their stated uncertainty ($56.1 \pm 18.2\,a_0^3$) and also with the high-precision calculations of Safronova *et al.* [30]. In the (D)BSR collision models, for which we show results later, the portion of the ground-state polarizability accounted for is $26.1\,a_0^3$ (BSR-22), $56.0\,a_0^3$ (BSR-100), $61.2\,a_0^3$ (BSR-224), $29.0\,a_0^3$ (DBSR-22), $56.0\,a_0^3$ (DBSR-104), and $61.3\,a_0^3$ (DBSR-214), respectively. While missing some of the polarizability would likely be a serious defect of the models when considering elastic scattering,

experience shows that it is not so critical for the calculation of excitation processes, for which the oscillator strength of the transition is most important.

The scattering calculations were carried out with fully parallelized versions of the BSR complex [20] and the corresponding DBSR package under development. In order to check the convergence of the results with the number of states included in the close-coupling expansion, we set up several scattering models. Specifically, we show results obtained in the BSR-22, BSR-100, BSR-222, DBSR-22, DBSR-104, and DBSR-214 models. In addition to the 22 states listed in Table I, the larger models included more discrete and pseudostates to account for coupling to the discrete Rydberg spectrum as well as the ionization continuum. We chose an R-matrix radius of $80\,a_0$ with 152 B-splines of order 8 for each orbital in the BSR calculation. In DBSR, we used 186 B-splines of the order of 8 and 9 for the small and large components of the spinors. Splines of different orders are needed here for reasons of numerical stability [31]. Also, for our DBSR calculations, a finite nuclear size was modeled with a Fermi-type model for the nucleus. This required additional splines with a narrow distance between the knots at the very small radii. These models resulted in generalized eigenvalue problems with matrix dimensions up to 175 000.

TABLE II. Oscillator strengths for the $(5s^25p)\,^2P^o_{1/2} \rightarrow (5s^26s)\,^2S_{1/2}$ and $(5s^25p)\,^2P^o_{1/2} \rightarrow (5s^25d)\,^2D_{3/2}$ transitions in In obtained in the (D)BSR models. "L" and "V" indicate the results obtained with the length and velocity form of the electric dipole operator, respectively.

Lower state	Upper state	NIST [28]	bsr_cc_03 (L)	bsr_cc_03 (V)	dbsr_cc_03 (L)	dbsr_cc_03 (V)
$(5s^25p)\,^2P^o_{1/2}$	$(5s^26s)\,^2S_{1/2}$	0.14	0.120	0.118	0.135	0.129
$(5s^25p)\,^2P^o_{1/2}$	$(5s^25d)\,^2D_{3/2}$	0.36	0.320	0.326	0.349	0.341

We calculated partial waves for total electronic angular momenta up to $J_t = 24$ numerically, and then used a top-up procedure to estimate the contribution to the transition matrix elements from even higher J_t. The calculation for the external region was performed with a parallelized version of the STGF program [32].

B. RCCC model

The RCCC method was detailed in a number of publications [33,34] with application to e-In scattering presented in [11]. Hence, only a brief overview is presented here. The In atom is modeled as a quasi-one-electron atom with an active p electron above a frozen [Kr]$4d^{10}5s^2$ Dirac-Fock core. The core orbitals were obtained from the GRASP package [25]. The Dirac Hamiltonian for the active electron is diagonalized in a Dirac L-spinor basis [35] to model the spectrum of the In atom. Target symmetries up to $j^\pi = 7/2^-$ were included in the calculations. There are 26 negative-energy states (relative to the In$^+$ ionic ground state) and a large number of positive-energy states that model the coupling to the ionization channels. The total number of target states is 75, with the energy of the highest positive-energy state at about 10 eV.

We included one- and two-electron polarization potentials [36,37] to more accurately account for the effect of closed shells within the quasi-one-electron model of In, and thereby improve the accuracy of the target description and scattering calculations. The static dipole polarizability of the In$^+$ ion, $\alpha_d = 24.01\, a_0^3$, was taken from [38]. The fall-off radius of the one-electron polarization potential was optimized for each target symmetry to obtain good agreement with NIST energies [28] for the low-lying states of In. Similar to Table I for the (D)BSR models, the lowest 22 states in the RCCC model are presented in Table III. Note that states originating from $5s5p^2$ configurations are absent in the RCCC model. The target states up to the $(5s^28s)\,^2S_{1/2}$ state are well described within the RCCC model. The number and accuracy of higher-energy bound pseudostates can be easily improved by increasing the size of the underlying L-spinor basis, but proved to be unnecessary for the present study. The major difference between the number of states in the (D)BSR and RCCC models comes from the different way the square-integrable discretization is achieved with the B-splines and L-spinors, respectively.

The two-electron polarization potential does not enter the target structure calculations for the quasi-one-electron model of In, but it enters scattering calculations and effectively leads to a modified form for the oscillator strength. The fall-off radius parameter of this potential was chosen to achieve good agreement with the NIST value [28] for the $(5s^25p)\,^2P^o_{1/2} \to (5s^26s)\,^2S_{1/2}$ transition oscillator strength. The RCCC value is equal to 0.129, which is similar to the DBSR models (cf. Table II). For this choice of the polarization potential parameters, the oscillator strength value for the $(5s^25p)\,^2P^o_{1/2} \to (5s^25d)\,^2D_{3/2}$ transition is 0.451, which is substantially higher than in the DBSR and NIST values. The static dipole polarizability of the In atom in the RCCC(75) model is $40.3\, a_0^3$, which is significantly lower than the experimental value of $68.69\, a_0^3$ [29]. These are indications of the remaining imperfections of the present model. As mentioned above, however, this is

TABLE III. Binding energies (in eV) for the lowest 22 states of In included in the RCCC close-coupling expansions. Here "Conf." refers to the dominant configuration.

Conf.	State	NIST [28]	RCCC	Diff.
$5s^25p$	$^2P^o_{1/2}$	-5.786	-5.782	-0.004
$5s^25p$	$^2P^o_{3/2}$	-5.512	-5.521	0.009
$5s^26s$	$^2S_{1/2}$	-2.765	-2.754	-0.011
$5s^26p$	$^2P^o_{1/2}$	-1.842	-1.808	-0.034
$5s^26p$	$^2P^o_{3/2}$	-1.805	-1.773	-0.032
$5s^25d$	$^2D_{3/2}$	-1.708	-1.706	-0.002
$5s^25d$	$^2D_{5/2}$	-1.705	-1.702	-0.003
$5s5p^2$	$^4P_{5/2}$	-1.450		
$5s5p^2$	$^4P_{3/2}$	-1.320		
$5s^27s$	$^2S_{1/2}$	-1.286	-1.280	-0.006
$5s5p^2$	$^4P_{3/2}$	-1.143		
$5s^27p$	$^2P^o_{1/2}$	-0.968	-0.952	-0.016
$5s^27p$	$^2P^o_{3/2}$	-0.954	-0.939	-0.015
$5s^26d$	$^2D_{3/2}$	-0.945	-0.926	-0.019
$5s^26d$	$^2D_{5/2}$	-0.939	-0.924	-0.015
$5s^24f$	$^2F^o_{5/2}$	-0.863	-0.864	0.001
$5s^24f$	$^2F^o_{3/2}$	-0.863	-0.864	0.001
$5s^28s$	$^2S_{1/2}$	-0.748	-0.704	-0.044
$5s^28p$	$^2P^o_{1/2}$	-0.600	-0.506	-0.094
$5s^27d$	$^2D_{3/2}$	-0.599	-0.551	-0.048
$5s^27d$	$^2D_{3/2}$	-0.596	-0.550	-0.046
$5s^28p$	$^2P^o_{3/2}$	-0.594	-0.495	-0.099

not expected to be a serious issue for the calculation of the excitation process considered here.

In the scattering calculations, the set of target states is used to expand the total wave function of the e-In collision system and formulate a set of close-coupling Lippmann-Schwinger equations for the transition matrix. These equations are solved by standard techniques that include a partial-wave expansion and a reduction to a set of linear equations. Close-coupling calculations were conducted for partial waves up to $J_t = 20$. Account of the larger partial waves is taken with an analytical Born subtraction technique. The solution of the Lippmann-Schwinger equations enables us to determine the collision cross sections for the transition of interest. The convergence of the calculated cross sections was established by performing a number of calculations with different sizes of the underlying L-spinor basis and the inclusion of progressively more positive-energy states in the close-coupling expansion. The present calculations have been conducted with a fully parallelized MPI-OMP version of the RCCC code.

III. EXPERIMENTAL CONSIDERATIONS

In the current experiments, we utilized an electron-scattering apparatus that has already been described in some detail previously [39,40], so that only a brief description of its features and operational performance need be given here. It consists of an oven for the production of the indium beam, a monochromator for producing the incident electron beam and an analyzer, consisting of electrostatic optical elements and a single channeltron for electron detection, to energy analyze the scattered electrons. Note that the incident electron beam
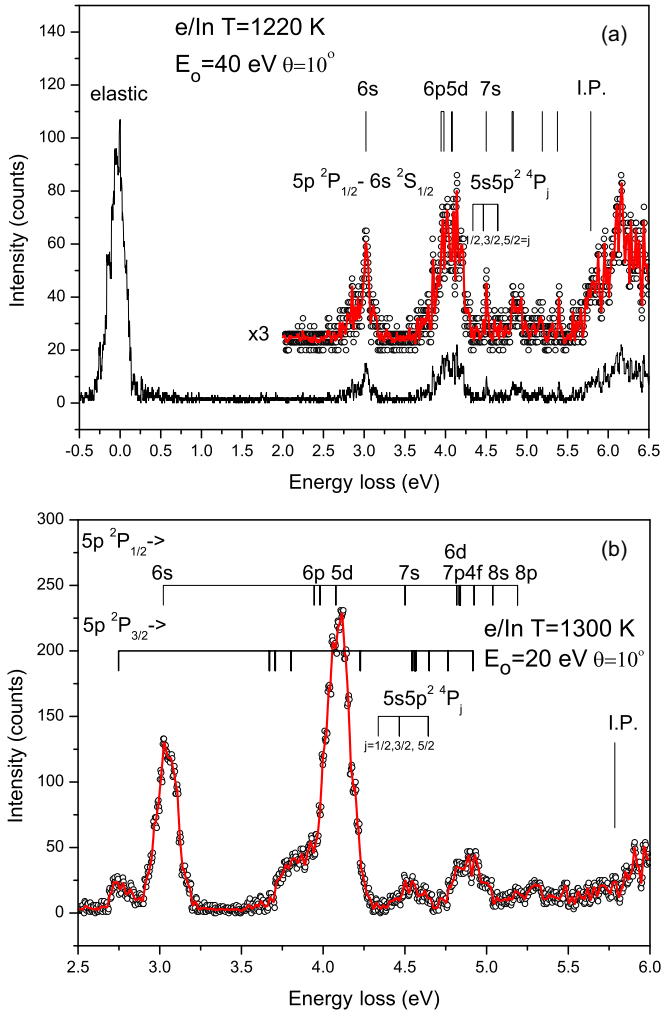
FIG. 1. Typical electron-energy-loss spectra in indium at (a) $T = 1220$ K for $E_0 = 40$ eV and $\theta_e = 10°$, (b) $T = 1300$ K for $E_0 = 20$ eV and $\theta_e = 10°$. Positions of the excited states are labeled according to the NIST labels of energy levels [28]. The ionization potential (I.P.) at 5.786 eV is also indicated. See text for further details.

was produced by thermionic emission from a tungsten hairpin filament, with further sets of electrostatic optical elements then collimating and transporting those electrons to the interaction region. The electron spectrometer was operated in three different modes: (i) an energy-loss mode where energy-loss spectra (see Fig. 1) were recorded for a given incident electron energy (E_0) and scattered electron angle (θ_e), (ii) a mode where the energy loss was set at 0 eV (i.e., on the elastic peak) and the elastic count rate at fixed θ_e is recorded as the incident electron energy is scanned for $E_0 = 1.0-4.4$ eV, and (iii) the energy loss is fixed at ∼3.022 eV [i.e., the excitation energy of the $(5s^2 6s)\,^2S_{1/2}$ state of interest] and the scattered inelastic count rate is recorded as a function of θ_e from $2°-150°$ at a fixed E_0 (either 10, 20, 40, 60, 80, or 100 eV).

The atomic indium beam was produced by a resistively heated oven filled with 99.9% purity indium granules. Two temperatures were typically employed during the present measurements, one at approximately 1220 K and the other at about 1300 K. These operational temperatures gave metal-vapor

pressures of approximately 2.1 Pa (16 mTorr) and 8.6 Pa (65 mTorr), respectively [41]. In both cases, the effusive indium beam consists of only ground-state atoms since each temperature is well below that needed to thermally populate the first $(5p)\,^2P_{3/2}$ metastable state (whose energy of 0.274 eV corresponds to a $T \sim 3180$ K). Using the electron spectrometer in mode (i) described above, two typical energy-loss spectra at $T = 1220$ and 1300 K are, respectively, given in Figs. 1(a) and 1(b). Note that, as we shall see in the next section, the inelastic $6s$ differential cross sections could vary over five orders of magnitude as θ_e changed from $2°$ to $150°$. Therefore, the lower temperature was often utilized to make measurements of the angular distributions at the more forward-scattered electron angles, thereby avoiding saturation of the scattered electron detector (channeltron), while the higher temperature was employed at the larger scattered electron angles where the excitation cross sections were very small. There are two important points to be gleaned from Fig. 1. The first is that irrespective of the operational temperature, the $(6s)\,^2S_{1/2}$ inelastic state of interest is well resolved from any of the other elastic and inelastic features. The second is that in Fig. 1(b), we can clearly also find features that originate from the excitation of the $(5p)\,^2P_{3/2}$ metastable state. These latter features can only arise if the following scenario is met: an initial electron excites the $(5p)\,^2P_{3/2}$ state from the ground $(5p)\,^2P_{1/2}$ state, and then, before that metastable atom can decay (lifetime ∼10.3 s [42]) or leave the interaction region, a subsequent incident electron scatters from it, leading to those additional observed two-step features in Fig. 1(b).

The overall energy resolution (ΔE_{res}) is ∼140 meV in this work, as determined from the full width at half maximum (FWHM) of the measured $6s$ peak in our energy-loss spectra (see Fig. 1). While allowing us to resolve the $6s$ line from all others in the relevant spectra, it did not allow us to resolve transitions to the $(6p)\,^2P_{1/2,3/2}$ states (3.945 and 3.982 eV, respectively) and to the $(5d)\,^2D_{3/2,5/2}$ states (4.078 and 4.081 eV, respectively). The next weak peak in our energy-loss spectra (again, see Fig. 1) is due to the combined excitation of the $(7s)\,^2S_{1/2}$ (4.501 eV) and the $(5s5p^2)\,^4P_{1/2,3/2,5/2}$ states (4.337, 4.467, and 4.643 eV, respectively). The existence of other higher-lying discrete inelastic states is also visible up to the ionization potential at 5.786 eV. The incident electron-energy scale was calibrated using the spectrometer in mode (ii), and looking for a Wigner-Cusp-like feature in the elastic intensity versus energy distribution at 3.022 eV. Typically, this calibration was made at $\theta_e = 20°$, and we believe it is accurate to about 100 meV.

The experimental procedure for the determination of our inelastic $6s$ DCSs initially involves calibrating the angular scale for the true $0°$ scattering angle. This is achieved, for a given E_0, by setting the energy loss to 3.022 eV (i.e., for the $6s$ peak) and then measuring the symmetry of the scattered electron intensity at small negative and positive angles about $0°$. Once calibrated, again for a given E_0 and the energy loss set at 3.022 eV, we next measured the scattered inelastic $6s$ intensity as a function of θ_e at fixed angles in the range $2°-150°$ (see Table IV). Background-intensity measurements were made at each θ_e by moving the energy loss off 3.022 eV and to a value where no peak is observed, and measuring the signal there. This background intensity is then subtracted from

TABLE IV. Differential cross sections for the excitation of the $6s\,^2S_{1/2}$ state of indium. The last row contains the angle-integrated cross sections in units of $10^{-20}\,\mathrm{m}^2$. The absolute uncertainties are indicated in parentheses.

Scattering angle (degrees)	DCS ($\times 10^{-16}\,\mathrm{cm}^2\,\mathrm{sr}^{-1}$)					
	10 eV	20 eV	40 eV	60 eV	80 eV	100 eV
2	12.5(1.6)	30.1(3.9)	45.0(6.2)	45.2(7.3)	49.9(10.6)	50.1(10.9)
4	9.2(1.2)	21.1(2.8)	24.3(3.6)	19.9(3.4)	18.3(3.4)	14.3(2.8)
6	6.10(0.83)	13.2(1.8)	11.1(1.7)	7.72(1.36)	5.17(1.01)	3.13(0.65)
8	3.73(0.52)	7.54(1.13)	4.67(0.80)	3.07(0.55)	1.44(0.28)	0.839(0.148)
10	2.32(0.35)	4.32(0.64)	2.18(0.34)	1.27(0.24)	0.555(0.099)	0.316(0.048)
20	0.266(0.041)	0.138(0.021)	0.0595(0.0103)	0.0468(0.0105)	0.0269(0.0065)	0.0090(0.0021)
30	0.0556(0.0095)	0.0527(0.0084)	0.0145(0.0035)	0.0084(0.0019)	0.0063(0.0024)	0.0040(0.0014)
40	0.0237(0.0048)	0.0173(0.0033)	0.0017(0.0009)	0.0035(0.0010)	0.0044(0.0021)	0.0026(0.0008)
50	0.0128(0.0026)	0.0026(0.0009)	0.0013(0.0008)	0.0027(0.0009)	0.0028(0.0019)	0.0022(0.0015)
60	0.0071(0.0017)	0.0024(0.0010)	0.0020(0.0009)	0.0011(0.0008)	0.0031(0.0022)	0.0025(0.0016)
70	0.0028(0.0011)	0.0012(0.0009)	0.0017(0.0009)	0.0011(0.0008)	0.0013(0.0009)	0.0025(0.0017)
80	0.0022(0.0010)	0.0032(0.0011)	0.0012(0.0008)	0.0012(0.0008)	0.0022(0.0015)	0.0019(0.0014)
90	0.0014(0.0008)	0.0015(0.0009)	0.0013(0.0009)	0.0014(0.0009)	0.0021(0.0015)	0.0040(0.0026)
100	0.00083(0.00070)	0.00072(0.00029)	0.0022(0.0010)	0.0021(0.0009)	0.00093(0.00074)	0.0041(0.0027)
110	0.0015(0.0005)	0.00043(0.00015)	0.0043(0.0012)	0.0038(0.0011)	0.0018(0.0013)	0.0043(0.0027)
120	0.0021(0.0010)	0.00107(0.00034)	0.0066(0.0017)	0.0036(0.0010)	0.0034(0.0022)	0.0045(0.0028)
130	0.0036(0.0014)	0.0039(0.0037)	0.0043(0.0014)	0.0024(0.0009)	0.00095(0.00076)	0.0046(0.0032)
140	0.0038(0.0012)	0.0023(0.0005)	0.0031(0.0011)	0.00082(0.00061)	0.0036(0.0022)	0.0041(0.0027)
150	0.0037(0.0015)	0.0054(0.0010)	0.0100(0.0022)	0.0018(0.0008)	0.0011(0.0008)	0.0054(0.0031)
ICS	0.941(0.423)	1.60(0.56)	1.53(0.54)	1.10(0.38)	0.998(0.349)	0.819(0.287)

that obtained for the 6*s* peak in order to obtain the true 6*s* signal.

This entire procedure is, at the required E_0, repeated three to five times and on different days, with the weighted mean of the relative DCSs of those measurements subsequently being determined. The resulting angular distribution is then multiplied by the effective path-length (or volume) correction factor [43,44], as previously determined, at the same E_0, by Rabasović *et al.* [45]. The absolute scale of that angular distribution is then determined, at 20, 40, 60, 80, and 100 eV, respectively, by measurement of the 6*s* inelastic to elastic intensity ratios at 10° (for each E_0) and then using the absolute values of the elastic DCS from Rabasović *et al.* [13]. We note that this method could not be employed at 10 eV, as no 10 eV and 10° elastic DCS is available in the work of Rabasović *et al.* [13]. As a consequence, the absolute scale at 10 eV is set by a generalized oscillator strength analysis [6] of its 6*s* angular distribution in a method very similar to that of the preliminary study from Rabasović *et al.* [15]. The overall uncertainty on our DCSs is determined as the square root of the sum of the squared individual error contributions: (i) statistical uncertainties determined for each E_0 and every θ_e from the weighted mean of the relative true signal intensities; (ii) estimated uncertainty contributions due to errors in the energy-scale calibration, the effective path-length correction factor, and the calibration of the true 0° scattering angle; (iii) the uncertainty in the 6*s* to elastic intensity ratios in the normalization process; and (iv) the inherited errors on the elastic DCSs from Rabasović *et al.* [13]. Values of the absolute errors in our 6*s* DCSs, at each E_0 and θ_e, can be found in Table IV. Note that in some cases (e.g., at 20 eV and $\theta_e = 130°$), relatively large and somewhat anomalous errors are

found. This is due to working in regimes where the scattered intensity is weak, and the signal-to-noise characteristics are quite marginal.

Having determined our measured inelastic 6*s* DCSs, we now need to extrapolate them to $\theta = 0°$ and 180°, perform an interpolation, and then undertake the appropriate integration in order to derive the 6*s* ICSs at each energy. Two approaches were utilized to achieve that aim. In the first, we used the angular dependence predicted by our DBSR-214 theory in order to make the extrapolation, while in the second, the fitting analysis of Allen and co-workers [46,47] provided an independent self-consistency check. In all cases, the 6*s* ICSs we obtained, from each of the aforementioned approaches, were found to be consistent with one another to within our uncertainty estimates on the ICSs. A summary of our measured ICSs and their associated errors can be found at the foot of Table IV. Note that our uncertainty estimates on the ICSs incorporate all the uncertainties on the DCS, but weighted for the $\sin\theta$ term in the integrand when calculating those ICSs, and an additional uncertainty due to the extrapolation of our DCS to 0° and 180° in order to perform the integration at each E_0.

IV. RESULTS AND DISCUSSION

In Table IV and Figs. 2(a)–2(f), we present our measured 6*s* excitation DCS for the incident electron energies (a) 10, (b) 20, (c) 40, (d) 60, (e) 80, and (f) 100 eV. Also shown in Fig. 2 are the corresponding results from our BSR-222, DBSR-22, DBSR-214, and RCCC-75 computations, as well as the results from an earlier RDW calculation [14].

There are several general observations we can make with regard to Fig. 2. First, we highlight the excellent agreement
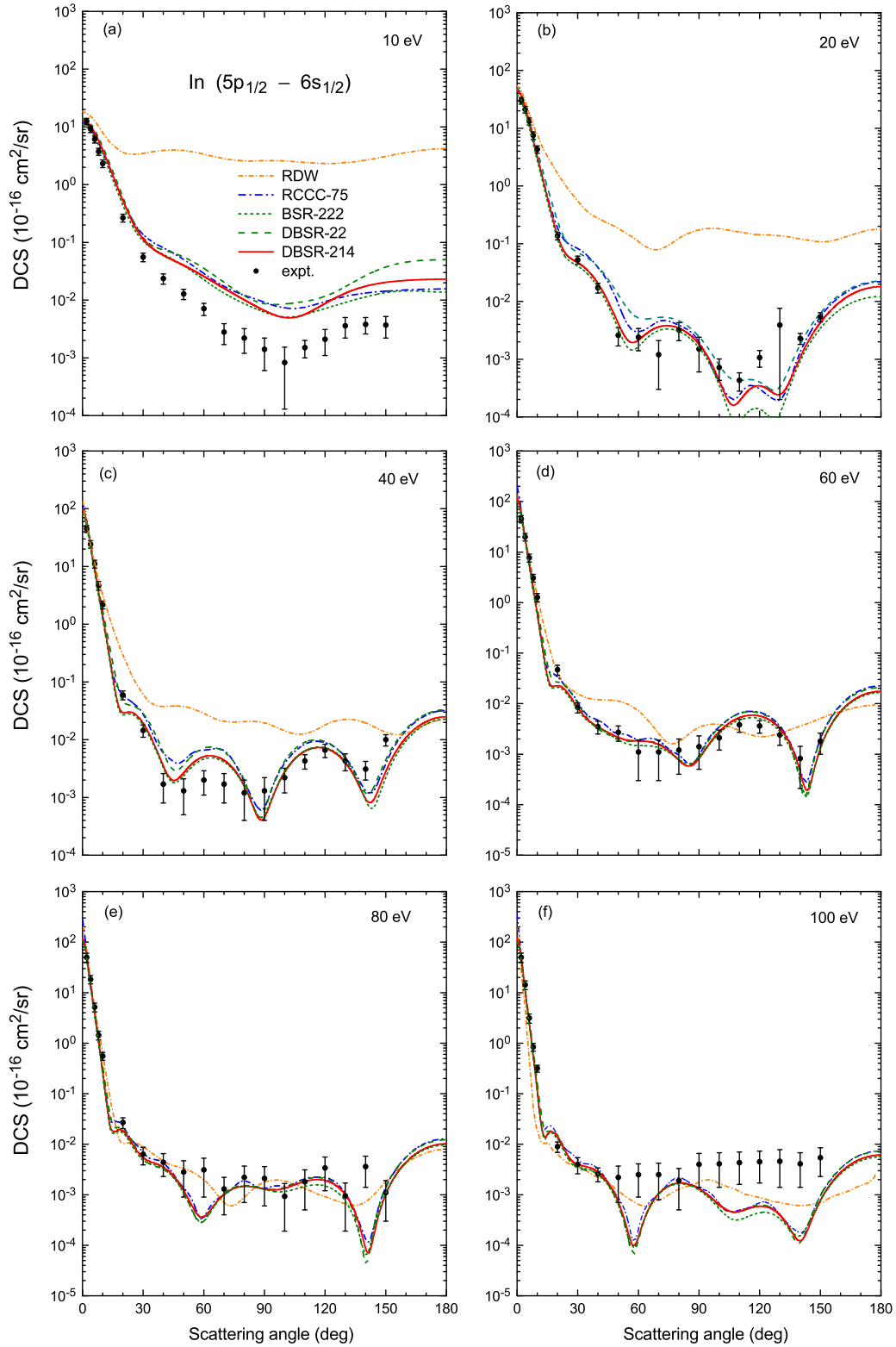
FIG. 2. Angle-differential cross section for electron-impact excitation of the $(5s^25p)\,^2P^o_{1/2} \rightarrow (5s^26s)\,^2S_{1/2}$ transition in neutral In at incident projectile energies of (a) 10, (b) 20, (c) 40, (d) 60, (e) 80, and (f) 100 eV. Predictions from the DBSR-22, BSR-222, DBSR-214, and RCCC-75 models are compared with the present experimental data. See, also, the legend in the figure.

between our DBSR-214 and RCCC-75 theories and the present experimental data, at the more forward-scattered electron angles ($\theta \leqslant 10°$) and for all the incident electron energies in the 10–100 eV range that we studied. This is no moot point;

it is precisely these very forward angles θ which make the major contribution to the integrand in calculating the ICS at each E_0. Thus, on the basis of this very good accord between measurement and calculation at those more forward-scattered
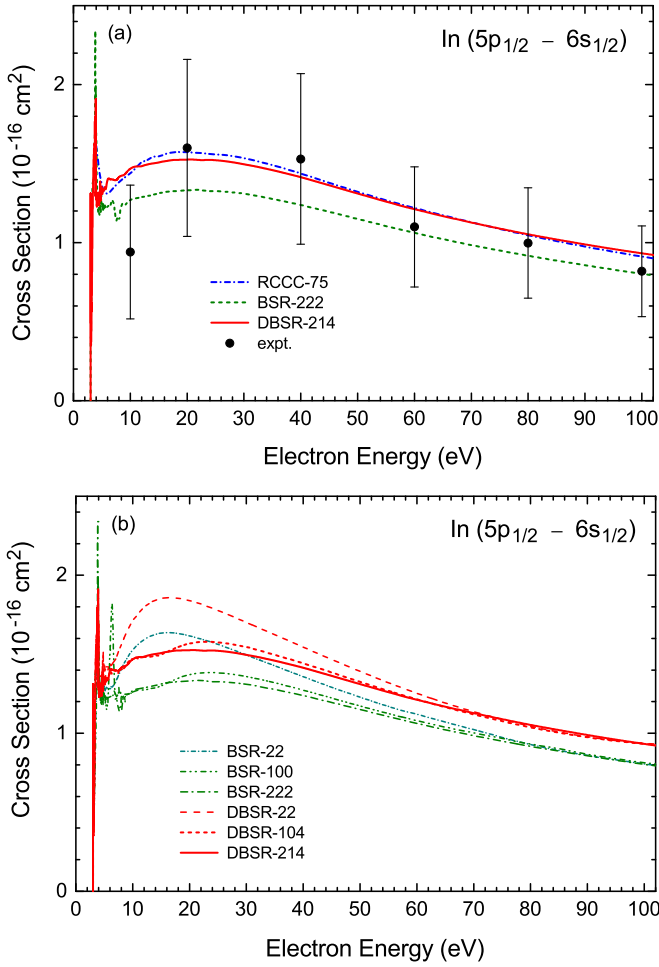
FIG. 3. Angle-integrated cross section for electron-impact excitation of the $(5s^2 5p)\,^2P^o_{1/2} \rightarrow (5s^2 6s)\,^2S_{1/2}$ transition in neutral In. We show predictions from the (b) BSR-22, BSR-100, BSR-222, DBSR-22, DBSR-104, and DBSR-214 models, as well as the (a) RCCC-75 model and a comparison with the current experimental data.

electron angles, we can also safely anticipate a good level of agreement between them at the integral cross-section level of comparison (see later and Fig. 3).

Second, we highlight the very good level of accord in Fig. 2 between our RCCC-75 and DBSR-214 calculations across all θ and at each E_0 studied. This is no moot point either, as, in attempting to construct a recommended data set for this excitation process, it is vital to have two high-level calculations in such good agreement with one another. We note that where differences in our RCCC-75 and DBSR-214 computations are observed, we believe that they are attributable to the subtle differences in the target-structure descriptions in both models.

The third general observation we make relates to the RDW results. At 10 and 20 eV, they overestimate the magnitude of the present measured and calculated DCS across the entire scattered electron angular range. This is not a new observation; the limitations of the (R)DW approach to calculating inelastic DCS at lower energies are well known. By 40 eV, however, the RDW is at least correctly predicting the magnitude and angular dependence [see Fig. 2(c)] of the very

forward-angle DCS, although it continues to overestimate the magnitude of the cross section at intermediate scattered electron energies. This forward-angle behavior of the RDW persists at 60, 80, and 100 eV, so that estimates of the RDW ICS at those energies might be expected to be physical. Furthermore, it is clear from Fig. 2 that as the energy of the incident electron increases, the RDW results become in better accord with the present measured and calculated cross sections.

The final general point that we highlight is the excellent quantitative agreement between our DBSR-214 and RCCC-75 results and the present measurements for 20, 40, 60, and 80 eV impact energies and across all the scattered electron angles (see Fig. 2). In addition, we believe that at 100 eV, the level of accord is semiquantitative in nature, with the comparison we observe in Fig. 2(f) probably highlighting just how difficult it is (experimentally) in measuring very small cross-section values at middle and backward angles.

Only at 10 eV and for $\theta > 10°$ [see Fig. 2(a)] do we find a serious discrepancy in the magnitude of the DCSs between our calculations and measurement, although the shape accord between theory and experiment remains qualitatively very good. One possible experimental explanation for this discrepancy is if, despite our best efforts, our effective path-length correction factor [45] for 10 eV was a little inaccurate. From the theoretical side, the fact that the diverse calculations are in such agreement indicates that convergence with increasing number of states in the close-coupling expansion has been reached to sufficient accuracy. However, given the smallness of the cross sections, the observed discrepancy could be due to some minor systematic inaccuracy in the calculations. Nevertheless, for practical purposes, the agreement at the forward-scattering angles is such that the integrated cross section obtained from experiment and theory would be in excellent agreement.

One of the key features from the present study is the strong oscillatory nature of the angular distributions in Fig. 2. Indeed, this behavior appears to be ubiquitous in electron-metal vapor scattering, for both the elastic and discrete inelastic channels, with a few examples supporting that assertion being bismuth [40], zinc [39], sodium [48], and magnesium [49]. The oscillatory nature of any differential cross section arises from the interference, both constructive and destructive, between the various partial waves that describe the collisional behavior. In the present case of inelastic scattering, where the orbital angular momentum of the projectile necessarily has to change from the initial state to the final state in order to conserve the parity as well as the coupled electronic angular momentum (J) of the combined target + projectile collision system, the details depend in a complex way on the interference between T-matrix elements that need to be combined with spherical harmonics in order to generate the scattering amplitudes [50] and, subsequently, the angle-differential cross section [51]. It is, therefore, generally not possible to predict either the number or the positions of the minima (maxima) in the DCS. Even though in some special circumstances and models a resemblance to elastic scattering may appear in inelastic collisions [52], and the DCS generally exhibits less structure in the angular dependence with decreasing projectile energy, drawing truly quantitative conclusions is not possible.

At the foot of Table IV and in Fig. 3(a), we present our derived $6s$ experimental excitation ICSs. Also shown in Fig. 3(a) are the results from our BSR-222, DBSR-214, and RCCC-75 computations. Our best calculations, the RCCC-75 and DBSR-214, agree extremely well with each other and, to within the uncertainties on the experimental ICSs, they also agree very well with the measured data. Our nonrelativistic BSR-222 computation also agrees with the experimental results to within the uncertainties on those measurements, with the observed differences between it and the DBSR-214 calculation being due to the different structure model used in each case. As noted in Sec. II, both the (D)BSR and RCCC calculations appear to be well converged with the number of states included in the close-coupling expansion. Indeed, if we were to take an average of the RCCC-75 and DBSR-214 ICSs, and then calculate the standard deviation of that average from the individual computations, a discrepancy of typically less than 10% is found. We therefore ascribe the uncertainty on our RCCC-75 and DBSR-214 results to be a conservative ±10%. Furthermore, that average theoretical ICS remains in very good accord, as expected, with the measured ICSs and so represents an excellent candidate for being a recommended $6s$ integral cross section for electron-indium scattering.

In Fig. 3(b), we explicitly demonstrate the convergence properties of our BSR and DBSR calculations. This is one of the procedures recommended in [53]. As we can see from this figure, away from the near-threshold energy region, the $6s$ ICS does not change significantly in going from our BSR-100 to BSR-222 calculations and, similarly, it does not change significantly in going from our DBSR-104 to DBSR-214 computations. These observations give us confidence in the convergence of our BSR-222 and DBSR-214 ICSs. In the near-threshold region, both our BSR and DBSR results, and our RCCC results, show peaklike structures in the ICS, which are mainly due to Feshbach resonances, and some more smoother structures, reminiscent of Wigner cusps, that are related to the opening of higher-lying channels as the incident electron energy is increased. The near-threshold structure seen in the (D)BSR calculation is very complex. To resolve the details and to check the stability with regard to even minor changes in the models, a very narrow energy grid would have to be used, followed by a thorough analysis of the partial-wave contributions and fitting of the T-matrix elements to multichannel resonance theory [54]. This is far beyond the scope of the present paper, where our main aim is to lay the groundwork for a set of recommended cross sections that can be used to produce reliable rate coefficients for modeling. For that purpose, the fine details of the resonance structure over a small energy range are irrelevant. Nonetheless, it does remain an interesting project for the future.

V. CONCLUSIONS

We have reported on experimental and theoretical results for electron-impact excitation of the $(5s^2 5p)\,^2 P_{1/2}^o \rightarrow$ $(5s^2 6s)\,^2 S_{1/2}$ transition in neutral indium, and in doing so we have significantly extended the available cross-section database for this scattering system. Strong interference effects, both constructive and destructive, in the partial waves describing this inelastic scattering process were clearly observed in our measured and calculated angular distributions, as was their energy dependence. Generally excellent agreement was found between our highest-level RCCC-75 and DBSR-214 calculations, at both the DCS and ICS levels of comparison; and with the main exception of 10 eV and for scattered electron angles $>10°$, there was also very good accord found between those calculations and our measured data. Given this high level of accord between our experimental and theoretical results, we believe a recommended $6s$ data set could be formed by taking an average, at any energy, between our RCCC-75 and DBSR-214 calculations with the uncertainty on that average result being about ±10%.

Structures, near threshold, in the $6s$ integral cross section were also found. These originate from either Feshbach resonances or are associated with the opening of higher-lying discrete excited electronic states (possibly Wigner cusps) as the incident electron energy is increased. However, more detailed calculations, beyond the scope of this study, are required before any attempt to classify them might be made. We note, additionally, that negative-ion resonance features in indium were also briefly mentioned in the review of Buckman and Clark [55].

[1] P. Schwerdtfeger and J. Nagle, Mol. Phys. **117**, 1200 (2019).

[2] M. S. Rabasović, B. P. Marinković, and D. Šević, Opt. Quantum Electron. **50**, 236 (2018).

[3] C. M. Ögün, W. Truong, C. Kaiser, R. Kling, and W. Heering, J. Phys. D **47**, 285202 (2014).

[4] M. Gryziński, Phys. Rev. **138**, A336 (1965).

[5] M. Gryziński, Phys. Rev. **138**, A322 (1965).

[6] H. Tanaka, M. J. Brunger, L. Campbell, H. Kato, M. Hoshino, and A. R. P. Rau, Rev. Mod. Phys. **88**, 025004 (2016).

[7] M. J. Brunger, Int. Rev. Phys. Chem. **36**, 333 (2017).

[8] J. Hult, I. S. Burns, and C. F. Kaminski, Proc. Combust. Inst. **30**, 1535 (2005).

[9] Q. N. Chan, P. R. Medwell, P. A. M. Kalt, Z. T. Alwahabi, B. B. Dally, and G. J. Nathan, Appl. Opt. **49**, 1257 (2010).

[10] R. S. M. Chrystile, I. S. Burns, J. Hult, and C. F. Kaminski, Opt. Lett. **34**, 2492 (2009).

[11] C. J. Bostock, D. V. Fursa, and I. Bray, J. Phys. B **45**, 181001 (2012).

[12] K. Bartschat, J. Phys. B **25**, L307 (1992).

[13] M. S. Rabasović, V. I. Kelemen, S. D. Tošić, D. Šević, M. M. Dovhanych, V. Pejčev, D. M. Filipović, E. Y. Remeta, and B. P. Marinković, Phys. Rev. A **77**, 062713 (2008).

[14] T. Das, R. Srivastava, and A. D. Stauffer, Phys. Lett. A **375**, 568 (2011).

[15] M. S. Rabasović, S. D. Tošić, D. Šević, V. Pejčev, D. M. Filipović, and B. P. Marinković, Nucl. Instrum. Methods B **267**, 279 (2009).

[16] R. P. McEachran, F. Blanco, G. García, and M. J. Brunger, J. Phys. Chem. Ref. Data **47**, 033103 (2018).

[17] R. P. McEachran, F. Blanco, G. García, P. W. Stokes, R. D. White, and M. J. Brunger, J. Phys. Chem. Ref. Data **47**, 043104 (2018).

[18] R. P. McEachran, B. P. Marinković, G. García, R. D. White, P. W. Stokes, D. B. Jones, and M. J. Brunger, J. Phys. Chem. Ref. Data **49**, 013102 (2020).

[19] O. Zatsarinny and K. Bartschat, J. Phys. B: At. Mol. Opt. Phys. **46**, 112001 (2013).

[20] O. Zatsarinny, Comput. Phys. Commun. **174**, 273 (2006).

[21] B-spline atomic r-matrix codes, https://github.com/zatsaroi/BSR3.

[22] Gateway for atomic and molecular physics, https://ampgateway.org.

[23] O. Zatsarinny and K. Bartschat, Phys. Rev. A **77**, 062701 (2008).

[24] C. Froese-Fischer, G. Tachiev, G. Gaigalas, and M. R. Godefroid, Comput. Phys. Commun. **176**, 559 (2007).

[25] P. Jönsson, X. He, C. F. Fischer, and I. P. Grant, Comput. Phys. Commun. **177**, 597 (2007).

[26] O. Zatsarinny and C. F. Fischer, Comput. Phys. Commun. **202**, 287 (2016).

[27] O. Zatsarinny and C. F. Fischer, Comput. Phys. Commun. **180**, 2041 (2009).

[28] A. Kramida, Yu. Ralchenko, J. Reader, and NIST ASD Team, NIST Atomic Spectra Database (ver. 5.7.1), http://physics.nist.gov/asd (National Institute of Standards and Technology, Gaithersburg, MD, 2020).

[29] L. Ma, J. Indergaard, B. Zhang, I. Larkin, R. Moro, and W. A. de Heer, Phys. Rev. A **91**, 010501(R) (2015).

[30] M. S. Safronova, U. I. Safronova, and S. G. Porsev, Phys. Rev. A **87**, 032513 (2013).

[31] C. F. Fischer and O. Zatsarinny, Comput. Phys. Commun. **180**, 879 (2009).

[32] N. R. Badnell, http://amdpp.phyd.strath.ac.uk/rmatrix.

[33] D. V. Fursa and I. Bray, Phys. Rev. Lett. **100**, 113201 (2008).

[34] C. J. Bostock, J. Phys. B: At. Mol. Opt. Phys. **44**, 083001 (2011).

[35] I. P. Grant and H. M. Quiney, Phys. Rev. A **62**, 022508 (2000).

[36] D. V. Fursa and I. Bray, J. Phys. B: At. Mol. Opt. Phys. **30**, 5895 (1997).

[37] D. V. Fursa, I. Bray, and G. Lister, J. Phys. B: At. Mol. Opt. Phys. **36**, 4255 (2003).

[38] M. S. Safronova, M. G. Kozlov, and C. W. Clark, Phys. Rev. Lett. **107**, 143006 (2011).

[39] B. P. Marinković, R. Panajotović, D. Šević, R. P. McEachran, G. García, F. Blanco, and M. J. Brunger, Phys. Rev. A **99**, 062702 (2019).

[40] B. Predojević, D. Šević, B. P. Marinković, R. P. McEachran, F. Blanco, G. García, and M. J. Brunger, Phys. Rev. A **101**, 032704 (2020).

[41] C. B. Alcock, V. P. Itkin, and M. Y. Horrigan, Canad. Met. Quart. **23**, 309 (1984).

[42] B. K. Sahoo and B. P. Das, Phys. Rev. A **84**, 012501 (2011).

[43] R. T. Brinkman and S. Trajmar, J. Phys. E **14**, 245 (1981).

[44] M. J. Brunger and S. J. Buckman, Phys. Rep. **357**, 215 (2002).

[45] M. S. Rabasović, S. D. Tošić, V. Pejčev, D. Šević, D. M. Filipović, and B. P. Marinković, Facta Univ., Ser. Phys. Chem. Technol. **6**, 119 (2008).

[46] L. J. Allen, M. J. Brunger, I. E. McCarthy, and P. J. O. Teubner, J. Phys. B **20**, 4861 (1987).

[47] M. J. Brunger, S. J. Buckman, L. J. Allen, I. E. McCarthy, and K. Ratnavelu, J. Phys. B **25**, 1823 (1992).

[48] P. J. O. Teubner, J. L. Riley, M. J. Brunger, and S. J. Buckman, J. Phys. B **19**, 3313 (1986).

[49] M. J. Brunger, J. L. Riley, R. E. Scholten, and P. J. O. Teubner, J. Phys. B **21**, 1639 (1988).

[50] K. Bartschat and N. S. Scott, Comput. Phys. Commun. **30**, 369 (1983).

[51] K. Bartschat, Comput. Phys. Commun. **30**, 383 (1983).

[52] K. Bartschat and K. Blum, J. Phys. B **15**, 2747 (1982).

[53] H. Chung, B. Braams, K. Bartschat, A. Csaszar, G. Drake, T. Kirchner, V. Kokoouline, and J. Tennyson, J. Phys. D **49**, 363002 (2016).

[54] K. Bartschat and P. G. Burke, Comput. Phys. Commun. **41**, 75 (1986).

[55] S. J. Buckman and C. W. Clark, Rev. Mod. Phys. **66**, 539 (1994).

**THE EUROPEAN
PHYSICAL JOURNAL D**

Regular Article

Electron transport in mercury vapor: cross sections, pressure and temperature dependence of transport coefficients and NDC effects[⋆]

Jasmina Mirić[1], Ilija Simonović[1], Zoran Lj. Petrović[1,2], Ronald D. White[3], and Saša Dujko[1,a]

[1] Institute of Physics, University of Belgrade, Pregrevica 118, 11080 Belgrade, Serbia
[2] Serbian Academy of Sciences and Arts, 11001 Belgrade, Serbia
[3] College of Science and Engineering, James Cook University, Townsville, QLD 4811, Australia

Abstract. In this work we propose a complete and consistent set of cross sections for electron scattering in mercury vapor. The set is validated through a series of comparisons between swarm data calculated using a multi term theory for solving the Boltzmann equation and Monte Carlo simulations, and the available experimental data. Other sets of cross sections for electron scattering in mercury vapor were also used as input in our numerical codes with the aim of testing their completeness, consistency and accuracy. The calculated swarm parameters are compared with measurements in order to assess the quality of the cross sections in providing data for plasma modeling. In particular, we discuss the dependence of transport coefficients on the pressure and temperature of mercury vapor, and the occurrence of negative differential conductivity (NDC) in the limit of lower values of E/N. We have shown that the phenomenon of NDC is induced by the presence of mercury dimers and that can be controlled by varying either pressure or temperature of mercury vapor. The effective inelastic cross section for mercury dimers is estimated for a range of pressures and temperatures. It is shown that the measured and calculated drift velocities agree very well only if the effective inelastic cross section for mercury dimers and thermal motion of mercury atoms are carefully considered and implemented in numerical calculations.

1 Introduction

The behavior of electrons in mercury vapor under the influence of electric field is of vital interest in modeling of the gas-discharge lamps [1–3], lasers [4,5] and in special applications such as ion thrusters for space propulsion [6]. Further optimization and understanding of such applications is dependent on an accurate knowledge of the cross sections for electron scattering, transport coefficients and the physical processes involved. For example, fluid models of low-pressure discharges used in fluorescent lamps often require swarm transport parameters as a function of the reduced electric field and the gas temperature [7,8]. Current models of high-pressure mercury discharges, however, usually require a knowledge of the electrical conductivity, which can be calculated from the cross sections for electron scattering in mercury vapor and electron mobility.

A number of methods have been applied to investigate the behavior of electrons in mercury vapor and have been successfully applied to a variety of problems. For scattering theorists, the problem of the scattering of electrons on mercury atoms is challenging due to importance of relativistic effects and the correlation between different subshells which require the use of either Dirac equations or modified forms of the Schrödinger equation [9,10]. The correct representation of a very large low energy resonance in both elastic and momentum transfer cross sections below the first inelastic threshold of the $^3P_0$ state at 4.66 eV and impact of $6s6p^2$ resonances on the elastic scattering and the excitation cross-section in the energy range between 4 and 7 eV are also very important issues. This makes mercury a particularly interesting target for scattering theorists. No less challenging is the problem of the transport of electrons in mercury vapor, given the difficulties that occur in both the experimental measurements, as well as in theoretical calculations based on the Boltzmann equation and Monte Carlo simulations. For example, it is very difficult to find the experimental data in the literature for drift velocity and characteristic energy of electrons in mercury vapor for high values of the reduced electric fields, because such measurements require lower vapor pressure and therefore lower temperature, which is difficult to control accurately. In the domain of the theoretical studies of electron transport in the mercury

---

vapor based on the Boltzmann equation, only recently it has been shown that nonlocal effects, resonances and striations in mercury electrical discharges have much in common with the behavior of electrons in mercury vapor in the famous Franck–Hertz experiment [11–14].

In literature, already, some cross section sets for electron scattering in mercury vapor have been reported. Raju reviewed measured and theoretically calculated electron collision cross sections for mercury vapor and recommended the values of drift velocity and reduced ionization coefficient [15,16]. Complete sets of cross section were reported by Rockwood [17], Nakamura and Lucas [18,19], Sakai et al. [20] and Suzuki et al. [21]. Winkler et al. [22,23] and Yousfi et al. [24] made significant contributions to the development of transport and collision data for electrons in mercury vapors by including the kinetics of excited states and Penning ionization in their models of fluorescent lamps. The properties of electron swarms in pure mercury vapor have also been analyzed by Garamoon and Abdelhaleem [25], Braglia et al. [26] and Liu and Raju [27] while the effects of metastable mercury and argon atoms on electron transport were subject of studies performed by the group of Prof. Tagashira [20,28,29]. The influence of thermal motion of background mercury atoms on electron transport has been analyzed by Winkler et al. [30] while the impact of a magnetic field on various transport properties in a crossed field configuration was investigated by Liu and Raju [31].

The common thread among many of these previous studies is a systematic neglect of non-hydrodynamic behavior of transport coefficients, which is reflected in their dependence upon the pressure and temperature of mercury vapor. Moreover, the effects of thermal motion of mercury atoms have also been often neglected, duality of transport coefficients (e.g., the existence of two different families of transport coefficients, the bulk and the flux) for electrons in mercury vapor has never been considered and finally many studies have been made in the framework of the two term theory for solving the Boltzmann equation, despite its limitations and concerns regarding its accuracy that have been well-documented [32,33]. Using these facts as motivational factors, in this paper, we revisit the issue surrounding computation of electron transport properties in mercury vapor as a function of electric field, pressure and temperature of mercury vapor. As a first step, we have developed a complete set of cross sections for electron scattering in mercury vapor. We apply the standard swarm procedure of deriving cross sections [33–35]. The initial set of cross sections is composed of cross sections for the individual collision processes that are collected from the literature. Using this initial set of cross sections as an input for solving Boltzmann's equation, transport coefficients are calculated and compared with the corresponding experimental data. The initial cross sections are then modified and the procedure is repeated in order to obtain better agreement with the experimental transport coefficients. The cross sections are considered satisfactory when the calculated values for drift velocity, ionization coefficient and characteristic energy match the experimental values to within a standard experimental uncertainty.

Other sets of cross sections for electron scattering in mercury vapor that are available in the literature were also incorporated into the Boltzmann equation and Monte Carlo codes with the aim of assessing their completeness and accuracy. This has been done through a series of calculations focused on comparisons between the experimentally measured and theoretically calculated transport coefficients. In particular, we consider the pressure dependence of transport coefficients due to the presence of mercury dimers. The mercury dimers are molecular species that can cause a significant change in the rate of energy lost by the electrons via rotational and vibrational excitation and hence a considerable change in the drift velocity. The formation of dimers and their effect on the measured drift has been studied by Nakamura and Lucas [18,19], Elford [36] and England and Elford [37]. It was shown that the drift velocity increases with pressure, but the occurrence of negative differential conductivity (NDC) has not been reported. A cross section for momentum transfer in elastic collisions and an effective inelastic cross section for dimers have been derived using the well-established swarm method of deriving cross sections. In order to reduce the non-uniqueness of the initially derived cross section for momentum transfer, McEachran and Elford [10] have demonstrated that cross section for the momentum transfer can be further refined by considering the additional transport data.

In the present paper we extend the previous studies by considering the occurrence of NDC in the limit of lower values of E/N. NDC is the well-known phenomenon in transport theory which is characterized by a decrease in the drift velocity for increasing the applied electric field. The conditions for the occurrence of NDC have been investigated previously. It was shown that NDC can be induced and controlled by the presence of inelastic [38,39] and non-conservative collisions [40,41], electron–electron collisions [42,43] and anisotropic scattering [44]. For liquid argon and xenon, however, there is a new type of NDC that does not require inelastic collisions or non-conservative processes, i.e. it is purely a consequence of the medium structure [45,46]. In this work we demonstrate the NDC phenomenon induced by the presence of mercury dimers. The collision frequencies and the averaged energy losses due to elastic and inelastic collisions are calculated with the aim of explaining the development of NDC. The pressure dependence of other transport properties, including the mean energy and diffusion coefficients is also investigated. Particular attention is paid to the effects of the mercury vapor temperature and how this affects the basic properties of the drift and diffusion over a range of the reduced electric fields of practical interest. This has been done through a series of calculations based on a multi term theory for solving the Boltzmann equation and Monte Carlo simulation technique in which thermal motion of background mercury atoms is rigorously accounted for.

This paper is organized as follows. In Section 2 we outline the theory used to solve the Boltzmann equation and the basic elements of our Monte Carlo method for determining transport properties of electrons in mercury vapor. In Section 3.2 we present a new collision cross section set for electron scattering in mercury vapor, which revises the

previous sets summarized by Rockwood [17], Sakai et al. [20] and Suzuki et al. [21]. Comparison between the measured and calculated swarm data is shown in Section 3.3 while the pressure dependence of transport coefficients and dimer-induced negative differential conductivity are discussed in Section 3.4. In Section 3.5 we investigate the synergism of thermal effects and the effects induced by the mercury-dimers on electron transport in mercury vapor. Finally, we summarize our conclusions in Section 4 and also provide an outlook regarding the future transport studies for electrons in mercury vapor.

2 Methods of calculation

In this work, we investigate a swarm of electrons moving through a neutral gas under the influence of a uniform electric field. The electron number density is assumed to be sufficiently low so that the following conditions apply: (i) electron–electron interactions and space-charge effects can be neglected; (ii) the motion of the electrons can be treated classically, and (iii) the background of neutral atoms remains in thermal equilibrium. Electrons gain energy from the external electric field and dissipate it by collisions to the neutral gas atoms. The collisional transfer of this energy to the neutral gas atoms occurs by elastic and different types of inelastic collisions. This is a typical non-equilibrium system and its correct mathematical description can only be obtained from kinetic theory [47].

2.1 Multi term solution of Boltzmann's equation

To calculate the transport of electrons in mercury vapor, we apply a multi term solution of the Boltzmann equation for the phase-space distribution function $f(\mathbf{r}, \mathbf{c}, t)$:

$$\frac{\partial f}{\partial t} + \mathbf{c} \cdot \frac{\partial f}{\partial \mathbf{r}} + \frac{e\mathbf{E}}{m} \cdot \frac{\partial f}{\partial \mathbf{c}} = -J(f, f_0), \quad (1)$$

where $\mathbf{r}$ and $\mathbf{c}$ denote, respectively, the position and velocity co-ordinates in phase space, while e and m are the charge and mass of electron, respectively, and $\mathbf{E}$ is the applied external field. The right-hand side of equation (1) represents the collision operator J, describing the rate of change of the phase-space distribution function due to collisions between the electrons and the neutral background mercury vapor atoms.

In the present work we employ the original Boltzmann collision operator for elastic processes [48] and its semi-classical generalization for inelastic processes [49]:

$$J_{\text{in}}(f, f_0) = \sum_{jk} \int [f(\mathbf{r}, \mathbf{c}, t) f_{0j}(\mathbf{c}_0) - f(\mathbf{r}, \mathbf{c}', t) f_{0k}(\mathbf{c}_0')] \\ \times g\sigma(jk; g, \widehat{\mathbf{g}} \cdot \widehat{\mathbf{g}}') d\widehat{\mathbf{g}} d\mathbf{c}_0, \quad (2)$$

where $\sigma(jk; g, \widehat{\mathbf{g}} \cdot \widehat{\mathbf{g}}')$ is the differential cross section for the scattering process $(j, \mathbf{c}, \mathbf{c}_0) \to (k, \mathbf{c}', \mathbf{c}_0')$. This cross section depends on the electron's incident kinetic energy and on the angle between the incident and post-collision relative velocity, $\mathbf{g}$ and $\mathbf{g}'$, respectively. For a neutral mercury vapor with temperature T and number density

N, the distribution of neutral velocities $\mathbf{c}_0$ in state j is Maxwell–Boltzmann:

$$f_0^{(j)}(\mathbf{c}_0) = \frac{N}{Z(T)} \exp\left(-\frac{\epsilon_j}{kT}\right) \omega(\alpha_0, \mathbf{c}_0), \quad (3)$$

where $Z(T)$ is the partition function, ϵ_j is the energy of a mercury atom (or mercury dimer) in quantum state j and

$$\omega(\alpha_0, \mathbf{c}_0) = \left(\frac{\alpha_0^2}{2\pi}\right)^{3/2} \exp\left(-\alpha_0^2 c_0^2\right), \quad (4)$$

with $\alpha_0^2 = m_0/kT$.

Electron ionization processes are described through the operator [51]:

$$J_I(f, f_0) = \sum_j N_{0j} c \big[\sigma_I(j; c) f(\mathbf{r}, \mathbf{c}, t) - 2 \\ \times \int c' \sigma_I(j; c') B(\mathbf{c}, \mathbf{c}'; j) f(\mathbf{r}, \mathbf{c}', t) d\mathbf{c}'\big], \quad (5)$$

where σ_I is the ionization cross section while $B(\mathbf{c}, \mathbf{c}'; j)$ is the probability for one of the two electrons after ionization having a velocity in the range $\mathbf{c}$ to $\mathbf{c} + d\mathbf{c}$, for incident electron velocity $\mathbf{c}'$, and N_{0j} is the number density of mercury atoms in the state j. In the present work we assume that all fractions are equally probable. The probability function must satisfy the following normalization conditions:

$$\int B(\mathbf{c}, \mathbf{c}'; j) d\mathbf{c} = 1, \quad (6)$$

and

$$B(\mathbf{c}, \mathbf{c}'; j) = 0, \quad \text{if} \quad \epsilon' - \epsilon < \epsilon_I(j), \quad (7)$$

where ϵ' and ϵ are the incident and post-ionization energy of the electrons while $\epsilon_I(j)$ is the ionization potential of the jth channel.

Solution of non-conservative Boltzmann's equation (1) has been extensively discussed by Robson and Ness [50,51], White et al. [52,53] and Dujko et al. [54,55]. In brief, we expand the phase-space distribution function in terms of spherical harmonics with the aim of resolving its angular dependence in velocity space. Transport coefficients of charged particle swarms are exclusively defined in the hydrodynamic regime. In the hydrodynamic regime, the space-time dependence of the phase-space distribution function is expressed by an expansion in terms of the gradient of the electron number density $n(\mathbf{r}, t)$. In order to resolve the speed-dependence of the phase-space distribution function, the expansion is made in terms of Sonine polynomials about a Maxwellian distribution function.

Thus, we solve equation (1) by making the expansions

$$f(\mathbf{r}, \mathbf{c}, t) = \omega(\alpha, c) \sum_{l=0}^{\infty} \sum_{m=-l}^{l} \sum_{\nu=0}^{\infty} \sum_{s=0}^{\infty} \sum_{\lambda=0}^{s} F(\nu lm | s\lambda)$$

$$\times N_{\nu l} \left(\frac{\alpha c}{\sqrt{2}} \right)^l S_{l+1/2}^{(\nu)} \left(\frac{\alpha^2 c^2}{2} \right) Y_m^{[l]}(\hat{\mathbf{c}}) G_m^{(s\lambda)} n(\mathbf{r}, t), \quad (8)$$

where $\omega(\alpha, c)$ is a Maxwellian distribution at a temperature T_b and $S_{l+1/2}^{(\nu)} \left(\frac{\alpha^2 c^2}{2} \right)$ are Sonine polynomials. $Y_m^{[l]}(\hat{\mathbf{c}})$ is a spherical harmonic, a function of the angles $\hat{\mathbf{c}}$ and $G_m^{(s\lambda)}$ is the irreducible gradient tensor operator [50]. The two-term approximation which forms the basis of the conventional theories for solving the Boltzmann equation, is based upon the choice of setting the upper bound on the summation in (8) to $l_{\max} = 1$. Its limitations and domains of applicability in calculating transport coefficients for electrons are thoroughly discussed in references [32,33].

Substitution of expansion (8) into equation (1) and performing the appropriate "matrix element" operations allows the Boltzmann equation to be converted into a set of matrix equations for the expansion coefficients $F(\nu lm | s\lambda)$,

$$\sum_{\nu'=0}^{\infty} \sum_{l'=0}^{\infty} \sum_{m'=-l'}^{l'} \left[M_{\nu lm, \nu'l'm'} + R\delta_{\nu'\nu}\delta_{l'l}\delta_{m'm} \right]$$

$$\times F(\nu'l'm' | s\lambda) = X_{\nu lm}(s\lambda),$$

$$\nu, l = 1, 2, \ldots, \infty; \quad m = -l, \ldots, +l, \quad (9)$$

where R is the reaction rate. Explicit expressions for the matrix of coefficients $M_{\nu lm, \nu'l'm'}$, which contains the applied electric field and matrix elements of the collision operator, and right-hand side $X_{lm\nu}(s\lambda)$, can be found elsewhere [51,54]. The expansion coefficients $F(\nu lm | s\lambda)$ are called "moments" and are related to the electron transport properties as discussed in our previous works [52–55]. These quantities are numbers that depend on the applied electric field, the neutral number density N and cross sections for electron scattering. They are required for determination of both the bulk and the flux transport coefficients. The flux drift velocity is the swarm averaged velocity, while the bulk drift velocity is the rate of change of the swarm's centre of mass. The duality of transport coefficients and its implications in plasma modeling has been recently thoroughly discussed in references [56–59].

Of particular importance for the current paper is to note that the motion of the neutrals is systematically and rigorously incorporated into all collision process operators and all spherical harmonic equations. In contrast, in conventional theories which are usually based on the two term approximation, the consideration of the thermal motion of neutrals is often limited to the isotropic matrix elements of the elastic collision operator. Errors resulting from such theories will be discussed and illustrated in Section 3.4.

2.2 Monte Carlo method

A Monte Carlo simulation technique is also used in the present work, but as an independent tool with the aim of verifying the results of Boltzmann equation analysis. We follow the space and time development of a swarm of electrons in an infinite gas under the influence of a uniform electric field. The electron trajectories between collisions are determined by solving the collisionless equation of motion of a single electron. The position and velocity of each electron are updated after the time step Δt which is determined from the mean collision time divided by a large number (usually 100) depending on the simulation conditions. These small time steps Δt are used for numerical integration of the equation for the collision probability

$$p(t) = \nu_T(\epsilon(t)) \exp\left(-\int_{t_0}^{t} \nu_T(\epsilon(t')) dt' \right), \quad (10)$$

where ν_T is the total collision frequency while t_0 is either the time of the electron entering the gas or the time of a previous collision. Equation (10) gives the probability that the electron will have a collision in the time interval $(t, t + dt)$ and its numerical solution requires the use of random numbers. The type of collision is also determined using random numbers as well as relative probabilities for individual collisional processes. The details of our Monte Carlo method and explicit formulas for both the bulk and flux transport coefficients are given in several of our previous publications [54,55,60–62].

Two important issues deserve more mentioning in this work. First, in our Monte Carlo code we have implemented the procedure for calculating the collision frequency in the case when thermal motion of the background gas cannot be neglected for a Maxwellian velocity distribution of the background gas particles. The details of the procedure can be found in the recent work of Ristivojević and Petrović [63]. This was a necessary step in this work, given the importance of thermal collisions for adequate description of electron transport in the limit of low electric fields.

Another issue in Monte Carlo simulations of electron transport in mercury vapor is the simulation speed. To achieve a good statistics of the final results and also to make sure that the relaxation of the steady-state conditions has been achieved, one needs to follow a large number of electrons. Due to numerous elastic collisions in which only a fraction of the initial electron energy is transferred to a heavy mercury atom target, the efficiency of energy transfer between the electrons and neutral mercury atoms is very low. As a consequence, the relaxation of energy is a very slow process and requires large computation time. In order to optimize the simulation speed, the simulations were usually began with a relatively low number of electrons (typically 1.5×10^3) and after relaxation to the steady state the electron swarm was scaled up in numbers at fixed time intervals. The newly created electron has the same dynamic properties as the original one until the first collision. Following the first collision the progeny and the original electrons follow different, independent trajectories. Detailed testing has shown that this technique does not affect the final results, but speeds up

the relaxation considerably. For more details the reader is referred to [54].

3 Results and discussion

3.1 Preliminaries

In the first part of this section we cover a range of reduced electric fields between 0.1 and 1000 Td. The temperature of the mercury vapor is 293 K while the pressure is set to 1 Torr. Under these conditions the impact of mercury dimers is negligible. In what follows these conditions will be designated as "no dimers". In the second part of the present work, we consider a much narrower range of the reduced electric fields: 0.1–3 Td. The temperature is set to 573 K and calculations are performed for a range of pressures. The influence of mercury dimers on the drift velocity and other transport properties is investigated over a range of conditions that are consistent with those present in the experiment of England and Elford [37]. In the last segment of this work, the transport coefficients are calculated using our new set of cross sections for electron scattering in mercury vapor over a range of E/N values and temperatures relevant to light sources which utilize mercury discharges.

The transport coefficients shown below are functions of E/N and are expressed using the unit of Townsend (1 Td = 10^{-21} Vm^2). Calculations are performed assuming that the internal states are governed by a Maxwell–Boltzmann distribution which essentially places all mercury atoms in the ground state. All scattering is assumed isotropic and hence elastic cross section is the same as the elastic momentum transfer cross section. The thermal motion of background particles is carefully considered in both Boltzmann equation analysis and in Monte Carlo simulations.

3.2 Cross sections for electron scattering in mercury vapor

In this work, we consider electron transport in mercury vapor using the cross section set developed in this study. This set of cross sections is shown in Figure 1. The cross section for momentum transfer in elastic collisions is made as follows. For lower electron energies, we use the experimentally derived cross section of England and Elford [37] while for higher energies, we use a cross section tabulated in MAGBOLTZ code [64]. As discussed by England and Elford, care must be taken in deriving of a cross section for momentum transfer from the measured drift velocities due to diffusion effects and the presence of mercury dimers [37]. Cross sections for electronic excitations for levels $^3P_0$, $^3P_1$ and $^3P_2$ are retrieved from [65] while electronic excitations to $^1S_0$ and $^1P_1$ states as well as a cross section for higher states are also taken from MAGBOLTZ code. For electron-impact ionization, we have used the cross section from [66]. Cross sections were slightly modified during the calculations to improve agreement between the calculated and measured swarm parameters. We found that we were able to achieve a good agreement between calculated and
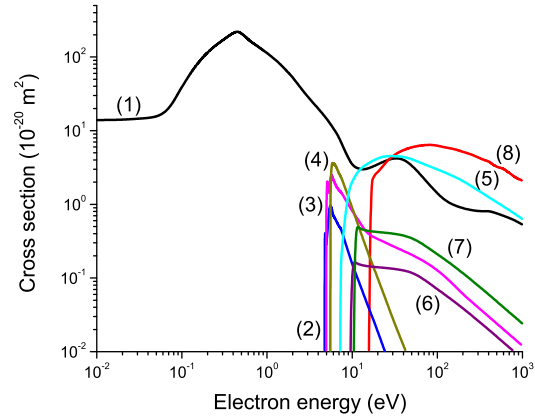
Fig. 1. Cross sections for electron scattering in Hg vapor: (1) elastic momentum transfer, (2) excitation $^3P_0$, (3) excitation $^3P_1$, (4) excitation $^3P_2$, (5) excitation $^1P_1$, (6) excitation $^1S_0$, (7) excitation to higher states and (8) ionization.

measured drift velocities for lower E/N by adjusting only the magnitude of the elastic momentum transfer cross section. For higher E/N (e.g. for higher electron energies), we have slightly modified the cross sections for electronic excitations in order to reproduce the measured ionization coefficient. This procedure is based on the experience that the calculated ionization rate is affected more by the modifications of the cross sections for electronic excitations than by the modifications of the ionization cross section [33,35].

A single effective inelastic cross section with the energy threshold of 0.04 eV is added to our cross section set, for electron scattering on mercury atoms, in order to represent the energy losses and momentum changes due to rotational and vibrational excitations of mercury dimers. It was necessary to include an effective cross section, since there are no cross sections for other channels of electron scattering on mercury dimers in the literature. There are no competing processes in the same energy range for collisions on monomers thus the contribution of the rotational–vibrational excitation will be significant. In principle, we may assume that the abundance of the dimers is sufficiently low so their overall contribution is negligible for processes that have a competing channel in scattering on monomer. In other words, we may assume that for all the other processes the cross sections are the same as for the monomer and we may apply an effective cross section for rotational and vibrational excitation of dimers and add that process to the set of cross sections for monomers. This effective cross section is derived using the experimental measurements of Elford and co-workers [36,37]. We have used the following assumptions:

– mercury dimers are always present in mercury vapor at a concentration proportional to the number density of mercury atoms;
– in order to account for the dimer number density, the amplitude of the effective cross section is scaled with their fractional abundance;
– the ideal gas law is assumed for the equation of state of mercury vapor.
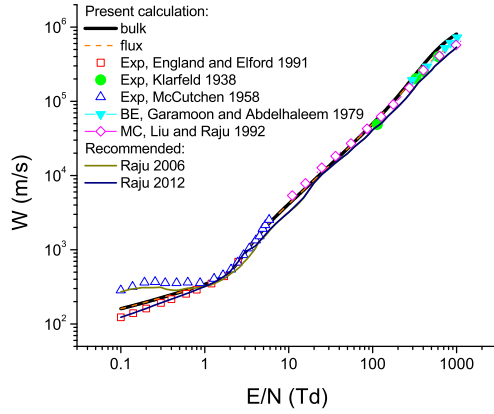
Fig. 2. Comparison of the drift velocity calculated using the present set of cross sections with the available experimental measurements of England and Elford [37], Klarfeld [67] and McCutchen [68]. Our results for the drift velocity are also compared with the available Monte Carlo calculations [27], Boltzmann equation results [25] and with the data recommended by Raju [15,16].

The effective cross section for dimers at pressure p and temperature T is given by [37]

$$\sigma\left(\epsilon\right) = 8.3\,\sigma_i\left(\epsilon\right)\Delta\left(p,T\right), \tag{11}$$

where 8.3 is a maximal value of the cross section at fractional dimer abundance of 1 ppm, $\sigma_i\left(\epsilon\right)$ is the dimer cross section used to fit the measurements of drift velocity and $\Delta\left(p,T\right)$ is the fractional abundance of dimers at pressure p and temperature T. Cross sections $\sigma_i\left(\epsilon\right)$ as a function of electron energy in units of squared angstroms are given by England and Elford [37]. Using the above assumptions and a value of 21.8×10^{-6} for fractional abundance of dimers at the pressure of 1 kPa and temperature of 573 K we have

$$\frac{\Delta\left(p,T\right)}{\Delta_1\left(p_1,T_1\right)} = \frac{n}{n_1} = \frac{p}{p_1}\frac{T_1}{T}, \tag{12}$$

and hence

$$\Delta\left(p,T\right) = 21.8 \times 10^{-6}\frac{p}{1\,\text{kPa}}\frac{573\,\text{K}}{T}. \tag{13}$$

Combining equations (11) and (13) yields the following simple expression for deriving the dimer cross section at the pressure p and temperature T

$$\sigma\left(\epsilon\right) = 180 \times 10^{-6}\,\frac{p}{1\,\text{kPa}}\frac{573\,\text{K}}{T}\,\sigma_i\left(\epsilon\right). \tag{14}$$

From equation (14) it is clear that the mercury-dimer cross section depends on the ratio p/T. If the mercury vapor temperature T is fixed and the pressure p is increased, then the mercury-dimer cross section grows and vice versa, if one keeps the pressure p fixed and increases the mercury vapor temperature T, then the mercury-dimer cross section declines. However, it should be noted that
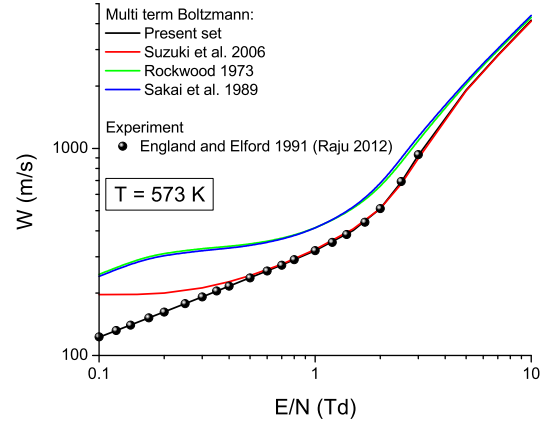
Fig. 3. Comparison of the drift velocity calculated using the present set of cross sections with those calculated using the cross sections sets developed by Rockwood [17], Sakai et al. [20] and Suzuki et al. [21]. Results are presented for the lower values of E/N and are compared with the measurements of England and Elford [37] which have been recommended by Raju [16]. The temperature of the dimer-free mercury vapor is 573 K.

the saturated mercury vapor pressure at 573 K is 33 kPa (approximately 248 Torr). This means that at the temperature of 573 K it is not possible to consider the influence of pressures higher than 33 kPa, and vice versa, it is not possible to consider the transport of electrons at a pressure of 33 kPa for the temperature less than 573 K. These conditions correspond to liquid mercury, which is certainly beyond the scope of this work.

The effective cross section which describes rotational and vibrational excitations of mercury dimers is considerable at higher pressures and lower temperatures. The corresponding superelastic cross section has been calculated using the principle of detailed balance in a thermal equilibrium.

3.3 Comparison between measured and calculated transport coefficients

In order to test the present set of cross sections for electron scattering in mercury vapor, we compare our theoretically calculated transport coefficients with various measurements and other calculations under conditions in which the influence of mercury dimers is negligible. In particular, we compare our calculations with the two sets of data recommended and published by Raju [15,16]. The transport coefficients are shown in Figures 2–6 as functions of E/N. Calculations are performed using the present set of cross sections and those developed by Rockwood [17], Sakai et al. [20] and Suzuki et al. [21]. We have applied a multi term approach for solving the Boltzmann equation assuming the pressure of 1 Torr while the temperature of mercury vapor is set to 293 K. Under these conditions the influence of mercury dimers on transport coefficients could be neglected. The convergence of transport coefficients was good and a value of $l_{\max} = 5$ was generally required for achieving an accuracy to within 1% or better.
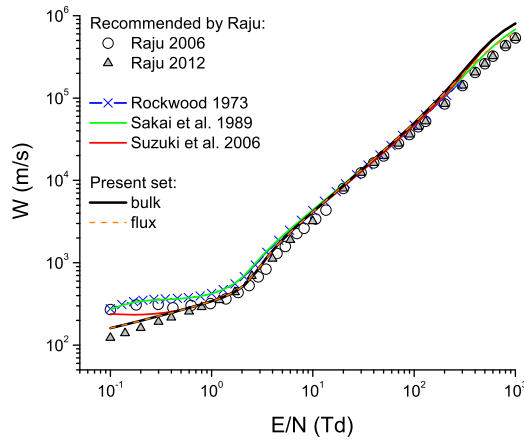
Fig. 4. Comparison of the drift velocity calculated using the present set of cross sections with those calculated using the cross sections sets developed by Rockwood [17], Sakai et al. [20] and Suzuki et al. [21]. Results are also compared with the drift velocity data recommended by Raju [15,16]. The temperature of the dimer-free mercury vapor is 293 K.
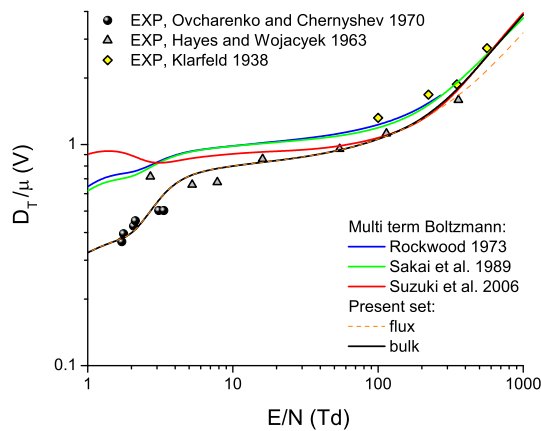
Fig. 5. Comparison of the characteristic energy, calculated using the present set of cross sections with those calculated using the cross section sets developed by Rockwood [17], Sakai et al. [20] and Suzuki et al. [21]. Results are also compared with the measurements of Ovcharenko and Chernyshev [69], Hayes and Wojacyek [70] and Klarfeld [67].

The bulk and flux drift velocities along with the experimental results of Klarfeld [67], McCutchen [68] and those recommended by Raju [15,16] are shown in Figure 2. The values of drift velocity calculated by a Monte Carlo simulation technique [27] and those obtained by solving the Boltzmann equation [25] are also plotted. For the low values of E/N we observe relatively poor agreement between our results and measurements of England and Elford [37]. This follows from the fact that our calculations have been performed assuming the mercury vapor temperature of 293 K while the experimental values of drift velocities in a dimer-free mercury vapor of England and Elford are obtained at 573 K. The Raju's 2012 recommended data are consistent with the measurements England and Elford [37]. After increasing the temperature of dimer-free mercury vapor to 573 K in our calculations, we have observed
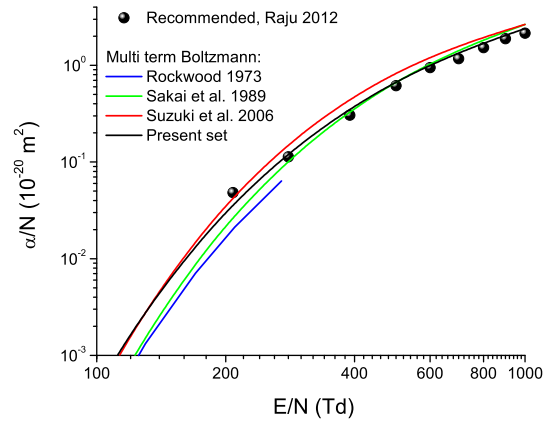
Fig. 6. Comparison of the ionization coefficient calculated using the present set of cross sections with those calculated using the cross section sets developed by Rockwood [17], Sakai et al. [20] and Suzuki et al. [21]. Results are also compared with the Raju's 2012 recommended data.

an excellent agreement between the calculated and measured drift velocities (see Fig. 3). Comparing our results and those measured by McCutchen [68], it is evident that a significant disagreement exists (see Fig. 2). The signs of NDC are clearly evident in the measurements of McCutchen [68]. This suggests that the experiment was operated under conditions in which the traces of mercury dimers were present. Indeed, the pressure of mercury vapor in his experiment was set to 350 Torr while no temperatures were given for any experimental runs. The agreement between our results and measurements of McCutchen [68] becomes much better for the higher values of E/N as the impact of mercury dimers on the drift velocity is reduced. At intermediate fields (10 Td$<$ E/N $<$100 Td), our results and Monte Carlo results of Liu and Raju [27] agree also very well. At higher E/N, above 100 Td, we see that the present calculations tend to lie a little above the experimental results of Klarfeld [67] and calculations of Garamoon and Abdelhaleem [25]. Nevertheless, the agreement is still quite reasonable. Due to the explicit contribution of ionization, the differences between the bulk and flux values of the drift velocity are of the order of 25% in the limit of the highest E/N considered in this work. Below 100 Td, however there is no appreciable difference between the two. In conclusion, from the profile of the drift velocity calculated using the present set of cross sections and temperature of 293 K for mercury vapor, there are no signs of NDC, i.e., the drift velocity is a monotonically increasing function of E/N.

In Figure 4 we show the variation of the flux and bulk drift velocities with E/N. The plots were calculated using the present set of cross sections and those developed by Rockwood [17], Sakai et al. [20] and Suzuki et al. [21]. For clarity, the flux drift velocity is shown only for the present set of cross sections. The results are also compared with the two sets of Raju's recommended data [15,16]. For the lower values of E/N, we again observe the inconsistency between our calculated data assuming the present set of cross sections and Raju's 2012 recommended data [16]. Increasing the temperature of the
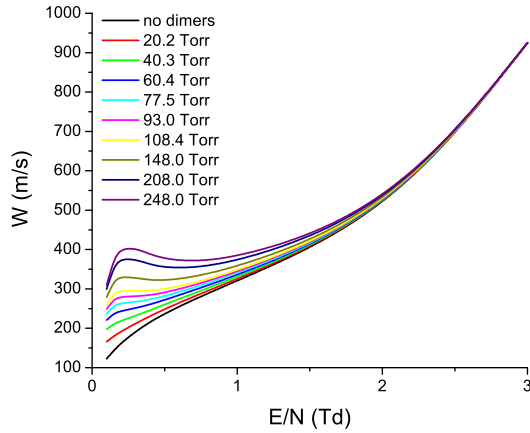
Fig. 7. Drift velocity as a function of E/N for a range of pressures. The temperature of the mercury vapor is 573 K.
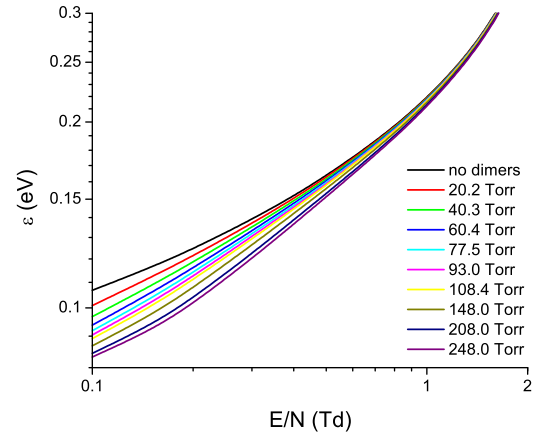
Fig. 8. Mean energy as a function of E/N for the same conditions as in Figure 7.

mercury vapor to 573 K the agreement between our calculations and Raju's 2012 recommended data is excellent (see Fig. 3). In the same region of E/N, the agreement between the calculated drift velocities assuming the cross section sets developed by Rockwood [17] and Sakai et al. [20] is very good. The agreement is not surprising, since the cross section for momentum transfer in elastic collisions developed by Rockwood [17] was also used by Sakai et al. [20]. For the intermediate values of E/N (10 Td$< E/N <$100 Td), we observe the excellent agreement between all calculated drift velocities. For the higher values of E/N, the agreement is slightly deteriorated. The calculated flux drift velocity using the present set of cross sections agrees reasonably well with the calculated bulk drift velocity assuming the set of cross sections developed by Sakai et al. [20]. On the other hand, the bulk drift velocities calculated using the present set and a set of cross sections developed by Suzuki et al. [21] agree very well. The set of cross sections developed by Rockwood [17] could not be used for calculations in the limit of higher E/N since it covers the range of electron energies only up to 30 eV. In conclusion, with the exception of the Raju's 2006 recommended data, our calculations clearly show the absence of NDC for all sets of cross sections employed in this work.

Figure 5 shows the flux and the bulk characteristic energies as a function of E/N. The characteristic energy provides a good estimate of the average energy of the electrons in the swarm. This quantity is extremely sensitive to the presence of inelastic processes and hence its comparison with experimental data indicates the quality of the energy balance of the cross section sets under consideration. Calculations using the present set of cross sections and those developed by Rockwood [17], Sakai et al. [20] and Suzuki et al. [21] are compared with the experimental results of Ovcharenko and Chernyshev [69], Hayes and Wojacyek [70] and Klarfeld [67]. For the lower values of E/N, we observe that the characteristic energy calculated from the present set of cross sections is in quite nice agreement with measurements of Ovcharenko and Chernyshev [69]. The agreement is also good with the measurements of Hayes and Wojacyek [70] for the intermediate values of

E/N while in the limit of the highest E/N considered in this work, the calculated values approach to each other and generally tend to lie a little below the experimental results of Klarfeld [67].

In Figure 6 we show the variation of the ionization coefficient with E/N. Calculations using the present set of cross sections and those published by Rockwood [17], Sakai et al. [20] and Suzuki et al. [21] are compared with the Raju's 2012 recommended data. The agreement between Raju's 2012 recommended data and those calculated assuming the present set of cross sections is very good. On the other hand, calculations assuming the set of cross sections developed by Suzuki et al. [21] are systematically higher than Raju's 2012 recommended data while calculations using the sets of cross sections developed by Rockwood [17] and Sakai et al. [20] are lower at low E/N than Raju's 2012 recommended data. We observe that calculation based on the present set of cross sections slightly deviate from the Raju's 2012 recommended data only in the limit of lower E/N. One may expect such behavior as the computer code must cope with very small values of the distribution function in the energy region where the ionization cross section is appreciable. Furthermore, the experimental measurements of the ionization coefficient in the vicinity of the ionization threshold, usually have great uncertainty.

3.4 Pressure dependence of transport coefficients and NDC effect

In this section we investigate the effects of mercury dimes on electron transport. Calculations are performed for a range of pressures while the temperature of mercury vapor is set to 573 K. The cross sections detailed in Section 3.2 and displayed in Figure 1 are used as an input into Monte Carlo simulations. In Figure 7 we show the drift velocity as a function of E/N for a range of pressures. From Figure 7 we see that the drift velocity increases with the pressure of mercury vapor for low values of E/N and becomes pressure independent for higher values of E/N. Other transport coefficients and properties show pressure
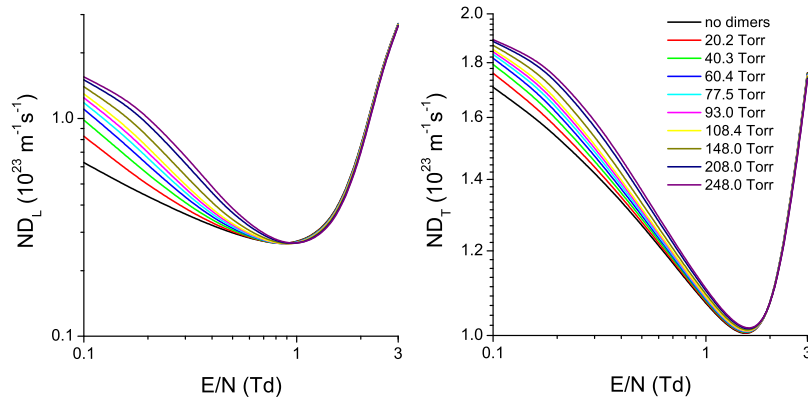
Fig. 9. Longitudinal and transverse diffusion coefficients as a function of E/N for the same conditions as in Figure 7.

dependence over the same range of E/N. As an illustrative example, in Figures 8 and 9 we show the variation of the mean energy and diffusion coefficients with E/N. While the mean energy decreases with an increasing pressure, the diffusion coefficients are increased. The pressure dependence of the drift velocity (and other transport coefficients) arises through the pressure dependence of the dimer cross section. It is well known that in elastic collisions a fraction of the initial energy m/M is transferred from the electron to the neutral particle, while for inelastic collisions a considerably larger fixed energy loss is transferred in addition, per each interaction. Assuming isotropic model of scattering, the vector of electron velocity is arbitrarily oriented after collisions, which leads to a reduction in the directed component of the velocity. In other words, elastic collisions have the effect of randomizing the direction of electron motion, while preserving their speeds. When inelastic collisions are significant, however, the energy transfer is no longer relatively small. This in turns reduces the chaotic component of the electron velocity, and inelastic collisions no longer have the effect of randomizing the direction of electron motion. This indicates that the increase in gas pressure enhances drift velocity and reduces mean energy. For higher electron energies, the cross section for mercury dimers is reduced and transport coefficients become pressure independent.

In addition to the pressure dependence of the drift velocity and other transport coefficients, we observe the presence of NDC in the profiles of drift velocity in the limit of pressures that approach to the pressure of saturated mercury vapor. A study of the NDC for model gases was performed by Petrović et al. [38] in which the conditions for elastic and inelastic cross sections required for the occurrence of NDC were discussed. Using momentum transfer theory, Robson had developed an analytical criterion for NDC in a conservative single gas [39] that was further extended in [40]. An intimate connection between NDC and inelastic collisions was recognized in these studies. It was shown that NDC arises for certain combinations of elastic and inelastic cross sections in which, on increasing the electric field, there is a rapid transition from inelastic to elastic dominated energy loss mechanism. In this transition region, for a given increase in the electric field, a greater proportion of the energy input goes into chaotic motion rather than directed motion. As a consequence, the drift velocity falls with an increasing electric field.

This is exactly what happens in mercury vapor at higher pressures. As already discussed, mercury dimers are always present in a mercury vapor at a concentration proportional to the vapor pressure. Thus, as the pressure of mercury vapor increases, the dimer cross section increases as well as the corresponding collision frequency (see Fig. 10). For pressures higher than approximately 100 Torr and in the limit of lower values of E/N, the inelastic energy loss mechanism dominates the elastic energy loss mechanism. For increasing E/N the collision frequency of inelastic collisions decreases while the collision frequency for elastic collisions rises. This favors the development of NDC even though the difference between the collision frequencies is almost five orders of magnitude! However, if one takes into account that the average energy loss in an elastic collision is between 1×10^{-7} and 1×10^{-6} eV, while the energy loss in inelastic collisions is 0.04 eV, it is clear that a relatively small ratio between collision frequencies in inelastic and elastic collisions is compensated by the substantial differences in energy losses. At pressures lower than approximately 100 Torr, the concentration of mercury dimers is low. As a consequence, the energy losses in inelastic collisions are significantly lower than those in elastic collisions over the entire range of E/N. Under these conditions, NDC does not occur in the E/N profiles of the drift velocity.

These physical arguments are illustrated in Figure 11. Figure 11 shows the ratio between the average elastic and inelastic energy losses as a function of E/N. The average inelastic energy loss Ω_{inel} is evaluated as a product of the rate coefficient for an inelastic dimer process and the corresponding threshold of 0.04 eV. It should be noted that the elastic energy loss Ω_{elas} is approximated by the product of mean energy, the collision frequency of elastic collisions and the factor $2m/M$. By doing so, we have actually reduced the contribution of elastic collisions, having in mind that the collision frequency of elastic collisions and the corresponding energy losses are greater for electrons with energies higher than the average electron energy. The accurate calculation may be very efficiently performed in Monte Carlo simulations, but we defer this to a future
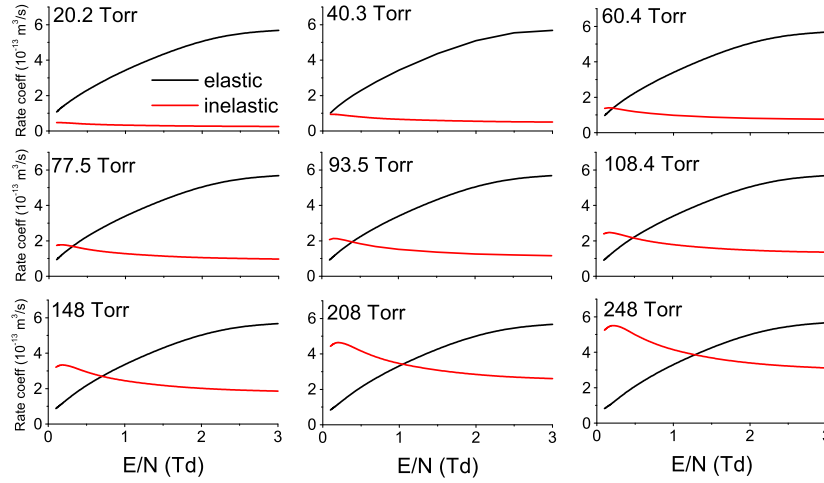
Fig. 10. Rate coefficients for elastic and inelastic collisions as a function of E/N in the presence of mercury dimers. The rate coefficient of inelastic processes which describes the presence of dimers is multiplied by the factor of 1×10^5. Calculations are performed for the same conditions as in Figure 7.
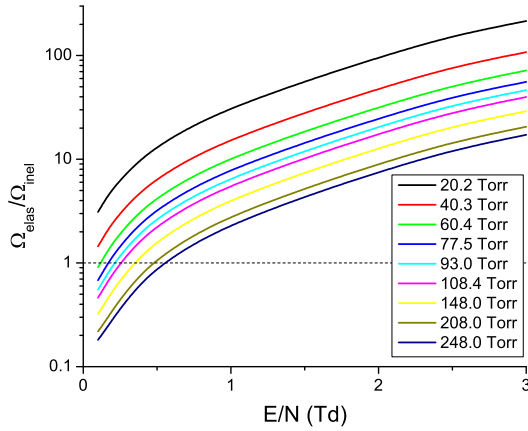
Fig. 11. Ratio between the average elastic and inelastic energy losses as a function of E/N for the same conditions as in Figure 7.

work. In any case, we observe that only for higher pressures of mercury vapor the ratio between energy losses in elastic and inelastic collisions favors the development of NDC.

Figures 12 and 13 illustrate the importance of including an accurate representation for thermal motion of the mercury atoms in our analysis of the drift velocity in the limit of lower values of E/N. Our multi term Boltzmann equation results with the rigorously incorporated effects of thermal motion of the mercury atoms are compared with our Monte Carlo results obtained under the conditions in which no thermal motion is considered. Our Monte Carlo results with the systematically incorporated effects of thermal motion of the mercury atoms are not included in this figure as they are essentially the same as those obtained through a multi term approach for solving the Boltzmann equation. Both sets of our calculated data are compared with the measurements of England and Elford [37]. Comparing experiment and our Boltzmann equation

results with the rigorously incorporated effects of thermal motion of the mercury atoms, we observe an excellent agreement between these two sets of data. In contrast, our Monte Carlo simulation results in which no thermal motion of the mercury atoms is considered, systematically overestimate the measurements in the limit of the lowest E/N. A false NDC like structure in the Monte Carlo $T = 0$ profiles of the drift velocity for all pressures of the mercury vapor is clearly evident. However, for increasing E/N the agreement between the measurements and Monte Carlo simulations in which no thermal motion is considered, becomes much better. As expected, the disagreement between the measurements and Monte Carlo simulations in which no thermal motion is considered is more pronounced for higher pressures.

3.5 Temperature dependence of transport coefficients

In this section we present results showing the variation of transport properties with E/N and mercury vapor temperature, T. Calculations are performed for two different cases: (1) the presence of mercury dimers assuming the pressure of 248 Torr, and (2) no dimers in the mercury vapor. Temperatures less than 573 K cannot be considered in the first scenario as for this pressure the mercury is in liquid form. These two scenarios for our calculations are considered with the aim of separating the thermal effects from those induced by mercury dimers.

In Figure 14 we show the variation of the mean energy with E/N for various mercury vapor temperatures, T. We observe that the mean energy is a monotonically increasing function of E/N for a fixed T. In the limit of low values of E/N the mean energy of the electrons is thermal and does not depend on E/N. This suggests that the velocity distribution function is essentially a thermal Maxwellian. For increasing T, the thermal deadlock is broken at higher E/N. For $T = 573$ K and $T = 1000$ K, we observe that the mean energy is higher in the case where
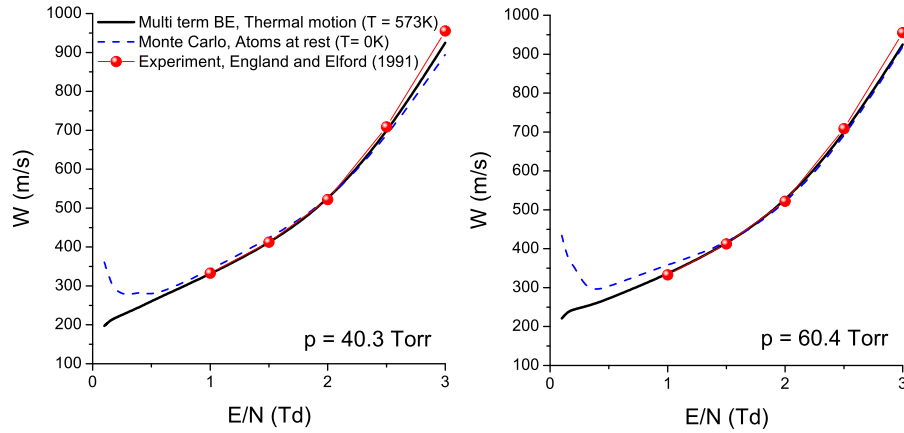
Fig. 12. Comparison between the calculated and measured values of drift velocity for pressures of 40.3 Torr (left panel) and 60.4 Torr (right panel). Monte Carlo results are obtained assuming atoms at rest ($T = 0$ K) while the gas temperature effects are considered through a multi term approach for solving the Boltzmann equation ($T = 573$ K).
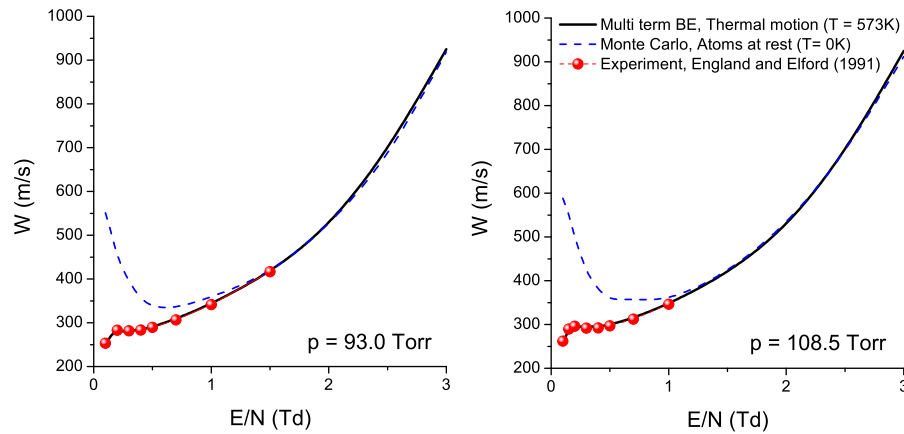
Fig. 13. Comparison between the calculated and measured values of drift velocity for pressures of 93.0 Torr (left panel) and 108.5 Torr (right panel). Calculations are performed for the same conditions as in Figure 12.
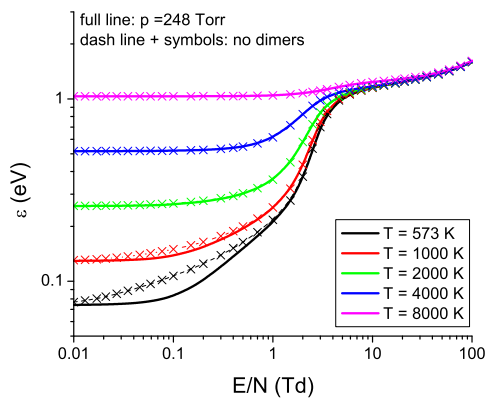
Fig. 14. Variation of the mean energy of the electron swarm as a function of E/N for various mercury vapor temperatures as indicated on the graph. The pressure of mercury vapor is 248 Torr.

no mercury dimers occur. It is clear that when the mercury dimers are present, the electrons lose more energy in inelastic collisions. For $T \geq 2000$ K the influence of mercury dimers is negligible. For low and intermediate values

of E/N the mean energy is distinctively dependent on T. In the limit of higher values of E/N the mean energies are higher than the corresponding thermal mean energies, which is a clear sign that the velocity distribution function is no longer a thermal Maxwellian. In this regime, the impact of the mercury vapor temperature T on the mean energies is minimal.

In Figures 15 and 16 we show the variation of the drift velocity with E/N for various mercury vapor temperatures, T. The drift velocity is a monotonically increasing function of E/N for all mercury vapor temperatures T, except for $T = 573$ K. At this temperature, NDC is clearly evident in the E/N-profile of drift velocity. With further increase in mercury vapor temperature, a decrease in drift velocity with increasing E/N is firstly reduced and then it is completely removed. From equation (14) it is clear that for increasing mercury vapor temperature and fixed pressure, the mercury-dimer cross section declines. As a consequence, the collision frequency of inelastic collisions whose presence is of an essential importance for the development of NDC effect, is also firstly reduced, and then severely minimized which ultimately leads to a disappearance of
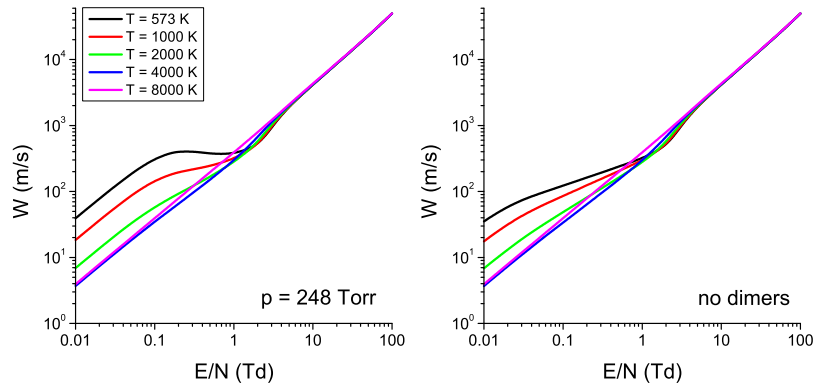
Fig. 15. Variation of the bulk drift velocity of the electron swarm as a function of E/N for the same conditions as in Figure 14.
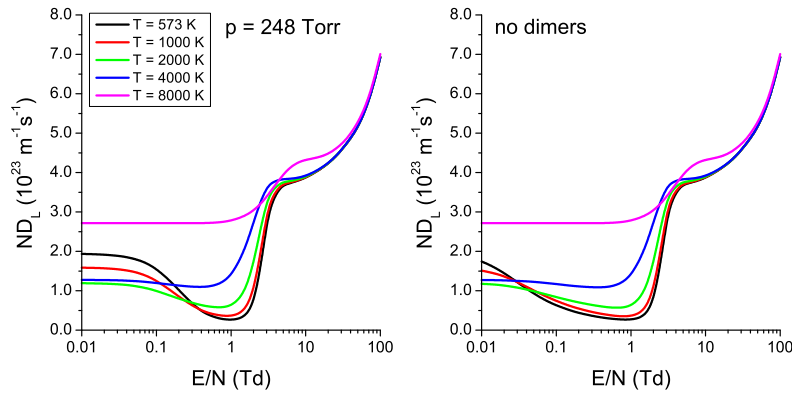
Fig. 16. Variation of the bulk longitudinal diffusion coefficient of the electron swarm as a function of E/N for the same conditions as in Figure 14.

NDC. The lesson from this is that the temperature of mercury vapor can be used to control the occurrence of NDC.

In the limit of lower E/N the drift velocity generally decreases with increasing T, though this is not the case for $T = 8000$ K. For $T = 8000$ K we see that the drift velocity is above the values calculated for $T = 4000$ K. For the temperature of 8000 K, the mean energy is high enough to exceed the peak value of the "0.4 eV" shape resonance in the cross section for elastic scattering. On the other hand, for $T = 4000$ K, the mean energy is significantly lower and corresponds to the range of energies in which the cross section for elastic collisions rises with an increasing energy of the electrons. As a consequence, the drift velocity is lower. For the intermediate values of E/N (between 1 and 10 Td, approximately) the behavior of drift velocity is very complex. In the energy region corresponding to the intermediate values of E/N, there is an overlap of the distribution function not only with a very large resonance in the elastic cross section, but also with the cross sections of inelastic processes that are now open. Finally, for higher values of E/N the drift velocity does not depend on the mercury vapor temperature and the drift of the electrons is entirely controlled by the electric field.

The variation of the diffusion coefficients with E/N for various mercury vapor temperatures, T, is shown in Figures 16 and 17. The impact of mercury dimers on both ND_L and ND_T is evident only for lower values of

E/N and lower T. At fixed T and for increasing E/N the electric field rises the energy of the electrons and the mercury-dimer cross section begins to fall. The same occurs at fixed E/N and with increasing T. Furthermore, in the limit of the lowest E/N and for a fixed E/N both ND_L and ND_T display a minimum with respect to T. In contrast to the drift velocity, the minimum occurs at $T = 2000$ K, indicating that diffusion coefficients show a remarkable sensitivity to the energy dependence of cross sections and presence of inelastic collisions. For the intermediate values of E/N, the most distinct property is the existence of a local minimum in the E/N profiles of both ND_L and ND_T. With a decreasing temperature, the minimum becomes more pronounced and is shifted towards higher E/N. The fall in both ND_L and ND_T by increasing E/N reflects the rapidly rising elastic cross section, e.g., the velocity distribution function samples the lower energy branch of the "0.4 eV" shape resonance. Comparing the behavior of diffusion coefficients at low and intermediate values of E/N, one can see that the contribution of mercury dimers is more important for lower values of E/N. In the limit of higher E/N, the impact of temperature on the behavior of diffusion coefficients is minimal. However, the longitudinal diffusion coefficient shows a more complex behavior with varying temperature.

In Figure 18 we show variation of the ratio ND_T to ND_L with E/N for various mercury vapor temperatures,
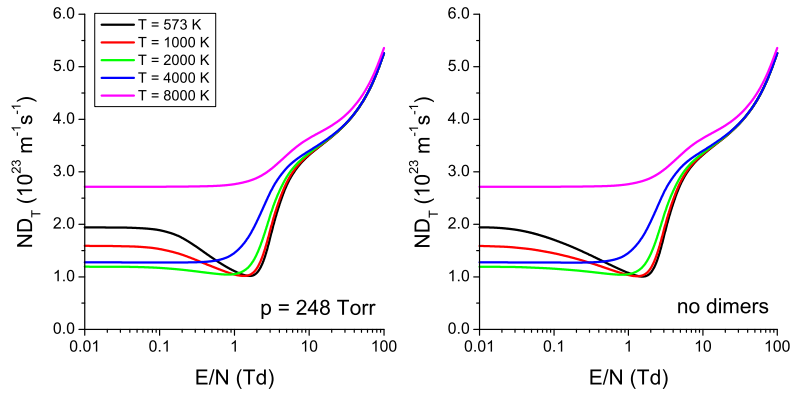
Fig. 17. Variation of the bulk transverse diffusion coefficient of the electron swarm as a function of E/N for the same conditions as in Figure 14.
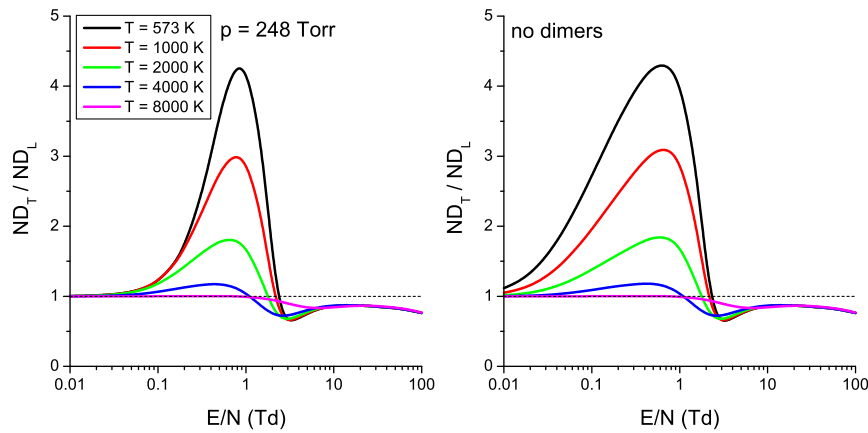
Fig. 18. Variation of the ratio of transverse to longitudinal diffusion coefficient of the electron swarm as a function of E/N for the same conditions as in Figure 14. Bulk values of diffusion coefficients are used.

T. We observe that the degree of anisotropic diffusion is significantly reduced by increasing mercury vapor temperature, T, in both scenarios considered here, i.e., in the presence of dimers and in their absence. In the limit of the lowest E/N diffusion is isotropic, i.e. $ND_L = ND_T$ since velocity distribution function is a thermal Maxwellian. At a fixed T the ratio ND_T/ND_L increases with increasing E/N, reaching a maximal value between 0.5 and 0.9 Td depending on the temperature T, and then it starts to decrease with E/N. For $T = 573$ K there is a factor higher than 4 between the longitudinal and transverse diffusion coefficients. In contrast, for $T = 8000$ K the diffusion is isotropic in a wide range of E/N, and only for $E/N > 1$ Td, the longitudinal diffusion coefficient is greater than the transverse, i.e. $ND_L > ND_T$. The reversal of the inequality is a clear sign of the rapid fall in the elastic cross section. Indeed, in this energy range the velocity distribution function samples the high energy branch of the "0.4" shape resonance of the elastic cross sections which rapidly falls with increasing electron energy.

4 Conclusion

In this paper, we have presented the results of a systematic investigation of electron transport in mercury vapor under the influence of electric field. First, we have compiled a complete set of cross sections for electron scattering in mercury vapor using the available data in the literature for individual collisional processes. In our evaluation, performed both with multi term Boltzmann and Monte Carlo codes, the initially compiled set of cross sections has been modified in order to reproduce the experimental data. The best agreement between calculated and measured drift velocities in the limit of lower electron energies was achieved by adjusting only the magnitude of the elastic momentum transfer cross section. For higher electron energies, we have only slightly modified the cross sections for electronic excitations in order to reproduce the measured ionization coefficient. We have also considered the issue of assessing the completeness, accuracy, and consistency of other cross section sets for electron scattering in mercury vapor by comparing calculated transport coefficients with those measured in various experiments. Our calculations highlight some inadequacies in these sets of cross sections and indicate possibilities for their improvements.

We have also outlined issues associated with the pressure and temperature dependences of transport coefficients. It was shown that the pressure dependence of the transport coefficients arise through the pressure dependence of the mercury-dimer cross section. In particular,

we have discussed the NDC phenomenon in the limit of lower values of the reduced electric fields. Conditions leading to NDC have been discussed and it was concluded that the phenomenon is induced by the presence of mercury dimers. Following the previous works of England and Elford [37], we have derived the mercury-dimer cross section for a range of pressures and temperatures of mercury vapor. One of the critical elements in our analysis of the drift velocity in the limit of lower values of the reduced electric fields was an accurate representation for thermal motion of the mercury atoms. Within a multi term theory for solving the Boltzmann equation used in the present work, the thermal motion of the neutral mercury atoms is systematically incorporated into all collision process operators and all spherical harmonic equations. Likewise, our Monte Carlo simulation code has been improved by implementing an efficient algorithm for calculating the collision frequency in the case when thermal motion of the background gas cannot be neglected for a Maxwellian velocity distribution of the background gas particles. Without these critical elements in a theory for solving the Boltzmann equation and Monte Carlo simulation codes, the variation of the drift velocity with the reduced electric field is unphysical in domain of lower electric fields.

Using a set of cross sections presented in this work, in the near future we plan to investigate the electron transport in crossed electric and magnetic fields. Calculations will be made with the aim of providing the data for fluid modeling of inductively coupled mercury discharges which are utilized in some types of electrodeless lamps. Similar calculations will be performed for ac electric and magnetic fields having in mind that both the electric and magnetic fields could be time-dependent. We also plan to develop complete and consistent sets of cross section for other materials, including indium, sodium and other metal vapors relevant for the lighting industry. The first steps have been made and the results are very encouraging [71].

Author contribution statement

All authors contributed equally to the paper.

References

1. G.G. Lister, J.E. Lawler, W.P. Lapatovich, V.A. Godyak, Rev. Mod. Phys. **76**, 541 (2004)
2. P. Flesch, *Light and light sources* (Springer, Berlin, 2006)
3. S. Samukawa, M. Hori, S. Rauf, K. Tachibana, P. Bruggeman, G. Kroesen, J.C. Whitehead, A.B. Murphy, A.F. Gutso, S. Starikovskaia, U. Kortshagen, J.P. Boeuf, T.J. Sommerer, M.J. Kushner, U. Czarnetzki, N. Mason, J. Phys. D: Appl. Phys. **45**, 25300 (2012)
4. G.J. Fetzer, J.J. Rocca, IEEE J. Quantum Electron. **28**, 1941 (1992)
5. C.E. Little, *Metal vapour lasers: physics, engineering and applications* (Wiley, Chichester, 1999)
6. E. Ahedo, Plasma Phys. Control. Fusion **53**, 124037 (2011)
7. G.G. Lister, J.J. Curry, J.E. Lawler, J. Phys. D: Appl. Phys. **37**, 3099 (2004)
8. W.J.M. Brok, M.F. Gendre, M. Haverlag, J.J.A.M. van der Mullen, J. Phys. D: Appl. Phys. **40**, 3931 (2007)
9. O. Zatsarinny, K. Bartschat, Phys. Rev. A **79**, 042713 (2009)
10. R.P. McEachran, M.T. Elford, J. Phys. B: At. Mol. Opt. Phys. **36**, 427 (2003)
11. R.E. Robson, R.D. White, M. Hildebrandt, Eur. Phys. J. D **68**, 188 (2014)
12. Y. Golubovskii, S. Gorchakov, D. Uhrlandt, Plasma Sources Sci. Technol. **22**, 023001 (2013)
13. F. Sigeneger, R. Winkler, R.E. Robson, Contrib. Plasma Phys. **43**, 178 (2003)
14. R.E. Robson, B. Li, R.D. White, J. Phys. B: At. Mol. Opt. Phys. **33**, 507 (2000)
15. G.G. Raju, *Gaseous electronics: theory and practice* (CRC Press Taylor & Francis, Boca Raton, 2006)
16. G.G. Raju, *Gaseous electronics: tables, atoms, and molecules* (CRC Press Taylor & Francis, Boca Raton, 2012)
17. S.D. Rockwood, Phys. Rev. A **8**, 2348 (1973)
18. Y. Nakamura, J. Lucas, J. Phys. D: Appl. Phys. **11**, 325 (1978)
19. Y. Nakamura, J. Lucas, J. Phys. D: Appl. Phys. **11**, 337 (1978)
20. Y. Sakai, S. Sawada, H. Tagashira, J. Phys. D: Appl. Phys. **22**, 276 (1989)
21. S. Suzuki, K. Kuzuma, H. Itoh, J. Plasma Fusion Res. Series **7**, 314 (2006)
22. R.B. Winkler, J. Wilhelm, R. Winkler, Ann. Phys. (Leipz.) **40**, 90 (1983)
23. R.B. Winkler, J. Wilhelm, R. Winkler, Ann. Phys. (Leipz.) **40**, 119 (1983)
24. M. Yousfi, G. Zissis, A. Alkaa, J.J. Damelincourt, Phys. Rev. A **42**, 978 (1990)
25. A.A. Garamoon, A.S. Abdelhaleem, J. Phys. D: Appl. Phys. **12**, 2181 (1979)
26. G.L. Braglia, M. Diligenti, J. Wilhelm, R. Winkler, Il Nuovo Cimento **12**, 257 (1990)
27. J. Liu, G.R. Govinda Raju, J. Phys. D: Appl. Phys. **25**, 167 (1992)
28. S. Sawada, Y. Sakai, H. Tagashira, J. Phys. D: Appl. Phys. **22**, 282 (1989)
29. Y. Sakai, S. Sawada, H. Tagashira, J. Phys. D: Appl. Phys. **24**, 283 (1991)
30. R. Winkler, J. Wilhelm, G.L. Braglia, M. Diligenti, Il Nuovo Cimento **12**, 975 (1990)
31. J. Liu, G.R. Govinda Raju, J. Phys. D: Appl. Phys. **25**, 465 (1992)
32. R.D. White, R.E. Robson, B. Schmidt, M.A. Morrison, J. Phys. D: Appl. Phys. **36**, 3125 (2003)
33. Z.Lj. Petrović, S. Dujko, D. Marić, G. Malović, Ž. Nikitović, O. Šašić, J. Jovanović, V. Stojanović, M. Radmilović-Radjenović, J. Phys. D: Appl. Phys. **42**, 194002 (2009)
34. L.G.H. Huxley, R.W. Crompton, *The drift and diffusion of electrons in gases* (Wiley, New York, 1974)
35. Z.Lj. Petrović, M. Šuvakov, Ž. Nikitović, S. Dujko, O. Šašić, J. Jovanović, G. Malović, V. Stojanović, Plasma Sources Sci. Technol. **16**, S1 (2007)

36. M.T. Elford, Aust. J. Phys. **33**, 231 (1980)
37. J.P. England, M.T. Elford, Aust. J. Phys. **44**, 647 (1991)
38. Z.Lj. Petrović, R.W. Crompton, G.N. Haddad, Aust. J. Phys. **37**, 23 (1984)
39. R.E. Robson, Aust. J. Phys. **37**, 35 (1984)
40. S.B. Vrhovac, Z.Lj. Petrović, Phys. Rev. E **53**, 4012 (1996)
41. J. Mirić, D. Bošnjaković, I. Simonović, Z.Lj. Petrović, S. Dujko, Plasma Sources Sci. Technol. **25**, 065010 (2016)
42. N.L. Aleksandrov, N.A. Dyatko, I.V. Kochetov, A.P. Napartovich, D. Lo, Phys. Rev. E **53**, 2730 (1996)
43. Z. Donko, N. Dyatko, Eur. Phys. J. D **70**, 135 (2016)
44. K. Yamamoto, N. Ikuta, J. Phys. Soc. Jpn. **68**, 2602 (1999)
45. G.J. Boyle, R.P. McEachran, D.G. Cocks, R.D. White, J. Chem. Phys. **142**, 154507 (2015)
46. G.J. Boyle, D.G. Cocks, R.P. McEachran, M.J. Brunger, S.J. Buckman, S. Dujko, R.D. White, J. Phys. D: Appl. Phys. **49**, 355201 (2016)
47. F. Taccogna, G. Dilecce, Eur. Phys. J. D **70**, 251 (2016)
48. L. Boltzmann, Wein. Ber. **66**, 275 (1872)
49. C.S. Wang-Chang, G.E. Uhlenbeck, J. DeBoer, in *Studies in statistical mechanics*, edited by J. DeBoer, G.E. Uhlenbeck (Wiley, New York, 1964), Vol. 2, p. 241
50. R.E. Robson, K.F. Ness, Phys. Rev. A **33**, 2068 (1986)
51. K.F. Ness, R.E. Robson, Phys. Rev. A **34**, 2185 (1986)
52. R.D. White, K.F. Ness, R.E. Robson, Appl. Surf. Sci. **192**, 26 (2002)
53. R.D. White, R.E. Robson, S. Dujko, P. Nicoletopoulos, B. Li, J. Phys. D: Appl. Phys. **42**, 194001 (2009)
54. S. Dujko, R.D. White, Z.Lj. Petrović, R.E. Robson, Phys. Rev. E **81**, 046403 (2010)
55. S. Dujko, R.D. White, Z.Lj. Petrović, R.E. Robson, Plasma Source Sci. Technol. **20**, 024013 (2011)
56. R.E. Robson, R.D. White, Z.Lj. Petrović, Rev. Mod. Phys. **77**, 1303 (2005)
57. S. Dujko, A.H. Markosyan, R.D. White, U. Ebert, J. Phys. D: Appl. Phys. **46**, 475202 (2013)
58. A.H. Markosyan, S. Dujko, U. Ebert, J. Phys. D: Appl. Phys. **46**, 475203 (2013)
59. D. Bošnjaković, Z.Lj. Petrović, S. Dujko, J. Phys. D: Appl. Phys. **49**, 405201 (2016)
60. Z.Lj. Petrović, Z.M. Raspopović, S. Dujko, T. Makabe, Appl. Surf. Sci. **192**, 1 (2002)
61. S. Dujko, Z.M. Raspopović, Z.Lj. Petrović, J. Phys. D: Appl. Phys. **38**, 2952 (2005)
62. S. Dujko, R.D. White, Z.Lj. Petrović, J. Phys. D: Appl. Phys. **41**, 245205 (2008)
63. Z. Ristivojević, Z.Lj. Petrović, Plasma Sources Sci. Technol. **21**, 035001 (2012)
64. http://magboltz.web.cern.ch/magboltz
65. K. Bartschat, *Third Int. Conf. on Atomic and Molecular Data and their Applications* (American Institute of Physics, New York, 2003)
66. J. Kieffer, G.H. Dunn, Rev. Mod. Phys. **38**, 1 (1966)
67. B. Klarfeld, Tech. Phys. (USSR) **5**, 913 (1938)
68. C.W. McCutchen, Phys. Rev. **112**, 1848 (1958)
69. V.A. Ovcharenko, S.M. Chernyshev, Teplofiz. Vys. Temp. **8**, 716 (1970)
70. E. Hayes, K. Wojacyek, Beitr. Plasma Phys. **3**, 74 (1963)
71. J. Mirić, Z.Lj. Petrović, R.D. White, S. Dujko, *Proc. 27th Summer School and Int. Symp. on the Physics of Ionized Gases (Belgrade)* (Institute of Physics, Belgrade, 2014), p. 126
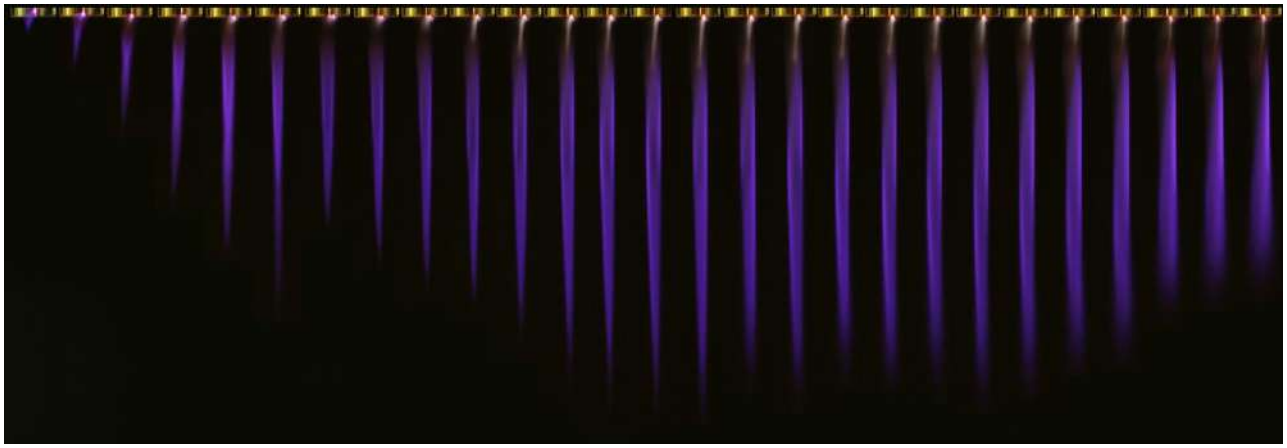
JSPP2014
COST MP1101 WS

9th EU-Japan Joint Symposium on Plasma Processing (JSPP2014) and
EU COST MP1101 Workshop on Atmospheric Plasma Processes and Sources

PROCEEDINGS

January 19th— January 23th 2014 | Bohinjska Bistrica, Slovenia (EU)

9th EU-Japan Joint Symposium on Plasma Processing (JSPP2014) and

EU COST MP1101 Workshop on Atmospheric Plasma Processes and Sources

January 19th — January 23th 2014, Bohinjska Bistrica, Slovenia

Programme and abstracts
Click on the title of a talk to see the abstract.

The 9th EU-Japan Joint Symposium on Plasma Processesing (19.-23. January 2014, Slovenia)

Sun. 19. Jan			
15.00 - 17.00	**Registration**		
17.00 - 17.30	INV	**S. Milošević** (CRO); Tailoring plasma sources and their diagnostics in various applications	slobodan@ifs.hr
17.30 - 18.00	INV	**M. Gorjanc** (SLO); Advantages and limitations of using plasma technology for modification of textiles	marija.gorjanc@ntf.uni-lj.si
18.00 - 18.30	INV	**K. Kutasi** (HUN); Layer-by-layer assembly of thin organic films on PTFE activated by air diffuse coplanar surface barrier discharge	kutasi.kinga@wigner.mta.hu
19.00 - 20.00	**Dinner**		
20.00 - 23.00	**Welcome reception**		

Mon. 20. Jan			
8.50 - 9.00	Opening	S. Hamaguchi (JPN), U. Cvelbar (SLO)	
9.00 - 9.45	Plenary	**T. Makabe** (JPN); Local distribution of gas temperature in an atmospheric- pressure microcell plasma in Ar	makabe@mkbe.elec.keio.ac.jp
9.45 - 10.30	Plenary	**M. M. Turner** (IRE); Uncertainty and error in complex plasma chemistry models	miles.turner@dcu.ie
10.30 - 11.00	**Break**		
11.00 -11.30	INV	**S. Hamaguchi** (JPN); Nano-scale damage formation during plasma etching analysed by multi-beam experiments and molecular dynamics (MD) simulations	hamaguch@ppl.eng.osaka-u.ac.jp
11.30 - 12.00	INV	**S. Dujko** (SRB); Recent results from studies of non-equilibrium electron transport in modelling of low-temperature plasmas and particle detectors	sasha@ipb.ac.rs
12.00 - 12.30	INV	**T. Murakami** (JPN); Reactive species in atmospheric pressure plasmas operated in ambient humid air	murakami@es.titech.ac.jp
12.30 - 13.00	INV	**M. Sekine** (JPN); Plasma nano-interface with organic materials for surface roughness formation	sekine@nagoya-u.jp
13.00 - 14.15	**Lunch**		
14.15 - 15.00	Plenary	**M. Shiratani** (JPN); Nanoparticle composite plasma CVD films - Fundamental and applications	siratani@ed.kyushi-u.ac.jp
15.00 - 15.30	INV	**R. Hatakeyama** (JPN); Plasma-processed control of graphene nanostructures and transport properties	hatake@ecei.tohoku.ac.jp
15.30 - 16.00	INV	**J. Kim** (JPN); Microwave plasma CVD technologies for the synthesis of nanocrystalline diamond and graphene films	jaeho.kim@aist.go.jp
16.00 – 16.30	**Break**		

Recent results from studies of non-equilibrium electron transport in modeling of low-temperature plasmas and particle detectors

S. Dujko[1], D. Bošnjaković[1], J. Mirić[1], I. Simonović[1], Z.M. Raspopović[1], R.D. White[2], A.H. Markosyan[3], U. Ebert[3] and Z.Lj. Petrović[1]

[1]Institute of Physics, University of Belgrade, Pregrevica 118, 11080 Belgrade, Serbia
[2]ARC Centre for Antimatter-Matter Studies, School of Engineering and Physical Sciences, James Cook University, Townsville 4810, Australia
[3]Centrum Wiskunde & Informatica (CWI), PO Box 94079, 1090 GB Amsterdam, The Netherlands

sasa.dujko@ipb.ac.rs

A quantitative understanding of charged particle transport processes in gases under highly non-equilibrium conditions is of interest from both fundamental and applied viewpoints, including modeling of non-equilibrium plasmas and particle detectors used in high energy physics. In this work we will highlight how the fundamental kinetic theory for solving the Boltzmann equation [1] and fluid equations [2,3] as well as Monte Carlo simulations [3], developed over many years for charged particle swarms are presently being adapted to study the various types of non-equilibrium plasma discharges and particle detectors.

Non-equilibrium plasma discharges sustained and controlled by electric and magnetic fields are widely used in materials processing [4]. Within these discharges the electric and magnetic fields can vary in space, time and orientation depending on the type of discharge. Moreover, the typical distances for electron energy and momentum relaxation are comparable to the plasma source dimensions. Consequently, the transport properties at a given point are usually no longer a function of instantaneous fields. This is the case for a variety of magnetized plasma discharges where, before the electrons become fully relaxed, it is likely that the electrons will be

reflected by the sheath or collide with the wall [5]. In this work we will illustrate various kinetic phenomena induced by the spatial and temporal non-locality of electron transport in gases. Two particular examples of most recent interest for the authors are the magnetron and ICP discharges. The magnetron discharge is used in the sputtering deposition of in films [6] where magnetic field confines energetic electrons near the cathode. These confined electrons ionize neutral gas and form high density plasma near the cathode surface while heavy ions and neutrals impinge on the solid surface ejecting material from that surface which is then deposited on the substrate. Within these discharges the angle between the electric and magnetic fields varies and thus for a detailed understanding and accurate modeling of this type of discharge, a knowledge of electron transport in gases under the influence of electric and magnetic fields at arbitrary angles is essential. In this work we will investigate the electron transport in N_2-O_2 mixtures when electric and magnetic fields are crossed at arbitrary angles for a range of pressures having in mind applications for low-pressure magnetized discharges and discharges at atmospheric pressure. Special attention is placed upon the explicit effects of three-body attachment in oxygen on both the drift and diffusion in low energy range [7]. The duality of transport coefficients arising from the explicit effects of non-conservative collisions will be discussed not only for vectorial and low-order tensorial transport coefficients but also for the high-order tensorial transport properties. The errors associated with the two-term approximation and inadequacies of Legendre polynomial expansions for solving the Boltzmann equation will be illustrated and highlighted.

In addition to magnetron discharges, we focus on the time-dependent behavior of electron transport properties in ICP discharges where electric and magnetic fields are radiofrequency. We systematically investigate the explicit effects associated with the electric and magnetic fields including field to density ratios, field frequency to density ratio, field phases and field orientations. A multitude of kinetic phenomena were observed that are generally inexplicable through the use of steady-state dc transport theory. Phenomena of significant note include the existence of transient

negative diffusivity, time-resolved negative differential conductivity and anomalous anisotropic diffusion. Most notably, we propose a new mechanism for collisional heating in inductively coupled plasmas which results from the synergism of temporal non-locality and cyclotron resonance effect. This mechanism is illustrated for discharges in pure CF_4 and pure O_2.

As an example of fluid modeling of plasmas, we will discuss the recently developed high order fluid model for streamer discharges [2,3]. Starting from the cross sections for electron scattering, it will be shown how the corresponding transport data required as input in fluid model should be calculated under conditions when the local field approximation is not applicable. The temporal and spatial evolution of electron number density and electric field in the classical first order and in the high order model are compared and the differences will be explained by physical arguments. We will illustrate the non-local effects in the profiles of the mean energy behind the streamer front and emphasize the significance of the energy flux balance equation in modeling. We consider the negative planar ionization fronts in molecular nitrogen and noble gases. Our results for various streamers properties are compared with those obtained by a PIC/Monte Carlo approach. The comparison confirms the theoretical basis and numerical integrity of our high order fluid model for streamers discharges.

In the last segment of this talk we will discuss the detector physics processes of resistive plate chambers and time-projection chambers that are often used in many high energy physics experiments [8]. For resistive plate chambers the critical elements of modeling include the primary ionization, avalanche statists and signal development. The Monte Carlo simulation procedures that implement the described processes will be presented. Time resolution and detector efficiency are calculated and compared with experimental measurements and other theoretical calculations. Among many critical elements of modeling for time-projection chambers, we have investigated the sensitivity of electron transport properties to the pressure and temperature variations in the mixtures of Ne and CO_2. In particular, we have investigated how to reduce

the transverse diffusion of electrons by calculating the electron trajectories under the influence of parallel electric and magnetic fields and for typical conditions found in these detectors.

References
 [1] S. Dujko, R.D. White, Z.Lj. Petrović and R.E. Robson "Benchmark calculations of nonconservative charged-particle swarms in dc electric and magnetic fields crossed at arbitrary angles", Phys. Rev. E 80, (2010) 046403.
[2] S. Dujko, A.H. Markosyan, R.D. White and U. Ebert, "High-order fluid model for streamer discharges: I. Derivation of model and transport data" J. Phys. D: Appl. Phys. 46 (2013) 475202.
[3] A.H. Markosyan, S. Dujko and U. Ebert "High-order fluid model for streamer discharges: II. Numerical solution and investigation of planar fronts" J. Phys. D: Appl. Phys. 46 (2013) 475202.
[4] T. Makabe and Z.Lj. Petrović " Plasma Electronics: Applications in Microelectronic Device Fabrication" (New York: Taylor and Francis 2006).
[5] H. Date, P. L. G. Ventzek, K. Kondo, H. Hasegawa, and M. Shimozuma "Spatial characteristics of electron swarm parameters in gases" J. Appl. Phys., Vol. 83. no. 8, (1988) 4024.
[6] C.H. Shon and J.K. Lee "Modeling of magnetron sputtering plasma" Appl. Surf. Sci. 192 (2002) 258.
[7] S. Dujko, U. Ebert, R.D. White and Z.Lj. Petrović, "Boltzmann equation analysis of electron transport in a N_2-O_2 streamer discharge" Jpn. J. Appl. Phys. 50 (2011) 08JC01.
[8] G. Aad et al. "The ATLAS Experiment at the CERN Large Hadron Collider" J. Inst. Vol. 3 (2008) S08003.

ICPEAC 2015

XXIX INTERNATIONAL CONFERENCE
on Photonic, Electronic and Atomic Collisions

22-28 JULY 2015 **TOLEDO** · SPAIN
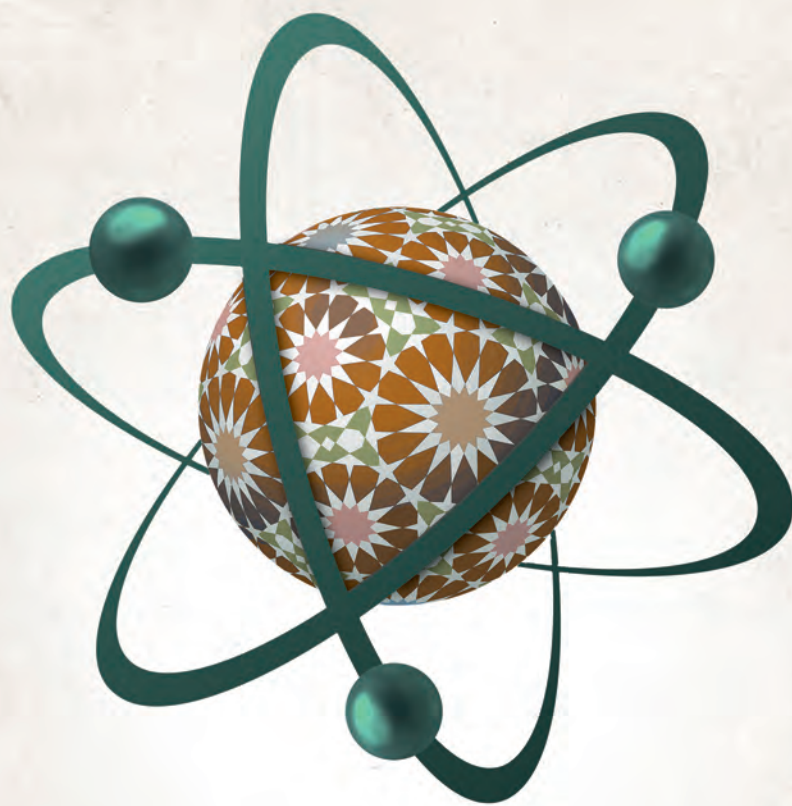
Transport processes for electrons and positrons in gases and soft-condensed matter: Basic phenomenology and applications

S. Dujko* [1], Z.Lj. Petrović*, R.D. White[†], G. Boyle[†], A. Banković*, I. Simonović*, D. Bošnjaković*, J. Mirić*, A.H. Markosyan[♥] and S. Marjanović*

* Institute of Physics, University of Belgrade, Pregrevica 118, 11080 Belgrade, Serbia
[†] College of Science, Technology & Engineering, James Cook University, Townsville 4810, Australia
[♥] Electrical Engineering and Computer Science Department, University of Michigan, Ann Arbor, MI 48109, USA

Synopsis An understanding of electron and positron transport in gases and soft-condensed matter under non-equilibrium conditions finds applications in many areas, from low-temperature plasmas, to positron emission tomography, radiation damage and particle detectors in high-energy physics. In this work we will highlight how the fundamental kinetic theory for solving the Boltzmann equation and fluid equation models are presently being adapted to study the various types of non-equilibrium plasma discharges and positron-based technologies.

The transport theory of electrons and positrons in gases and soft-condensed matter is of interest both as a problem in basic physics and for its potential for application to modern technology. For electrons, these applications range from low-temperature plasmas to particle detectors in high energy physics and to understanding radiation damage in biological matter. For positron based systems, the emission of back-to-back gamma rays resulting from annihilation of a positron and an electron is a fundamental process used as a tool in many areas, ranging from fundamental atomic and molecular physics, particle and astrophysics, to diagnostics in biological and material sciences.

In this work we explore analytical framework and numerical techniques for a multi term solution of Boltzmann's equation [1], for both electrons and positrons in gases and soft-condensed matter, and associated fluid equation models [2,3]. Together with the basic elements of our Monte Carlo method, the particular attention will be placed upon the rescaling procedures for compensation of electrons for losses under conditions when transport is greatly affected by electron attachment in strong electronegative gases.

For electrons, we will highlight recent advancements in the determination of the high-order transport coefficients in both atomic and molecular gases. Then we will discuss the elementary physical processes of electrons in the mixtures of gases used to model planetary atmospheric discharges. In particular, we will present the results of our theoretical calculations for expected heights of occurrence of sprites above lightning discharges in atmospheres of planets in our Solar system.

As an example of fluid equation models, we will discuss the recently developed high order fluid model for streamer discharges [3]. The balance equations for electron density, average electron velocity, average electron energy and average electron energy flux have been obtained as velocity moments of Boltzmann's equation and are coupled to the Poisson equation for the space charge electric field. Starting from the cross sections for electron scattering, it will be shown how the corresponding transport data required as input in fluid model should be calculated under conditions when the local field approximation is not applicable. We will illustrate the non-local effects in the profiles of the mean energy behind the streamer front and emphasize the significance of the energy flux balance equation in modeling. Numerical examples include the streamers in N_2 and noble gases.

In the last segment of this talk we will discuss the interaction of primary positrons, and their secondary electrons, with water vapor and its mixture with methane using complete sets of cross sections having bio-medical applications in mind [4]. We will also highlight recent advancements in the testing/validation of complete cross section sets for electrons in biologically relevant molecules, including water vapor and tetrahydrofuran [5].

References

[1] S. Dujko *et al* 2010 *Phys. Rev. E* **81** 056403
[2] R.D. White *et al* 2009 *J. Phys.D: Appl. Phys.* **42** 194001
[3] S. Dujko *et al* 2013 *J. Phys.D: Appl. Phys.* **46** 475202
[4] S. Marjanović *et al* 2015 Plasma Sources Sci. Technol. **24** 025016
[5] White *et al* 2014 *Eur. Phys. J. D* **68** 125

MONDAY

---

[1] E-mail: sasa.dujko@ipb.ac.rs

XIX International Symposium on Electron-Molecule Collisions and Swarms

Book of Abstracts

POSMOL 2015

17-20 July 2015, LISBOA, PORTUGAL

XVIII International Workshop on Low-Energy Positron and Positronium Physics

Book of Abstracts

POSMOL 2015

17-20 July 2015, LISBOA, PORTUGAL

XVIII International Workshop on Low-Energy Positron and Positronium Physics &
XIX International Symposium on Electron-Molecule Collisions and Swarms
17 - 20 July 2015, Lisboa, Portugal

POSMOL 2015

XVIII International Workshop on Low-Energy Positron and Positronium Physics
Lisboa, Portugal
17-21 July, 2015

XIX International Symposium on Electron-Molecule Collisions and Swarms
Lisboa, Portugal
17-21 July, 2015

ABSTRACT INDEX

Swarms as an exact representation of weakly ionized gases

Zoran Lj. Petrović[1], Saša Dujko[1], Dragana Marić[1], Danko Bošnjaković[1], Srđan Marjanović[1], Jasmina Mirić[1], Olivera Šašić[1], Snježana Dupljanin[1], Ilija Simonović[1], Ronald D. White[2]

[1]Institute of Physics University of Belgrade POB 68 11080 Zemun Serbia

[2]James Cook University of Northern Queensland, Townsville QL Australia

Zoran@ipb.ac.rs

Often swarms are regarded as idealized ensembles of charged particles that may be realized in specialized experiments to provide accurate transport coefficients, which after some analysis, yield "complete" sets of cross sections and accurate representations of non-equilibrium electron energy distribution function (EEDF) for a given *E/N*. Generally it is believed nowadays that swarms are just a tool for modeling non-equilibrium (low temperature) plasmas, as some kind of an interface through which atomic physics enters plasmas. In this review we shall show some new results that extend that picture into several directions:

- New results for the cross sections in systems where information from beam experiments and binary collision theories are insufficient such as $C_2H_2F_4$ that is commonly used as a cooling gas in modern refrigerators and air conditioners, but also it is used in particle detectors and has a potential for plasma processing applications.
- Ionized gases where swarms are exact representation of the system. Those include weakly ionized gases such as atmosphere, gas breakdown, afterglow (after the breakup of the ambipolar field), steady state Townsend regime of discharges, conduction of electricity through gases, interaction of secondary electrons produced by high energy particles with the gas or liquid background and many more. A special example will be modeling of Resistive Plate Chambers, the most frequently used gas phase detectors of elementary particles in high energy experiments.
- Swarm studies provide best insight into non-hydrodynamic (or as plasma specialists call it non-local) development of the ionized gas. It is not only that simulations are simple but also some of the accurate experiments operate in such conditions and thus allow testing of such theories. One such example are the Franck Hertz oscillations. Temporal and spatial relaxation of properties of ensembles to the final distribution belong to this group as well and are of interest for a number of positron applications and trapping in general.
- Fluid models when applied to swarms provide a good way to test the fluid models as used in more general plasmas. This has yielded the need to generalize fluid equations and extend them to a one step further while using a higher order transport coefficients.
- Finally we shall address the open issues for transport theorists and atomic and molecular collision population in the attempt to represent transport of electrons, positrons and other particles in liquids, especially in water that has a strong dipole moment. Hydrated electrons and positrons are the actually particles of interest for modeling these particles in the human tissue.

As an interface between atomic and molecular collision physics on a lower phenomenological (but deeper) level and plasmas on a higher (but less fundamental) level swarm physics has the responsibility of providing plasma physics with its intellectual basis and fundamental importance. It is how we combine the building blocks of atomic and molecular physics, transport theory and other relevant elementary processes that will define generality of the conclusions about non-equilibrium plasmas that are all different and require a special approach.

The models that we provide here are simple, yet realistic and real systems that may be described by swarm models and that may be regarded as low ionization limits of some more complex non-equilibrium plasmas.

**31ˢᵗ Summer School and
International Symposium on
the Physics of Ionized Gases**
Belgrade, Serbia,
September 5 - 9, 2022

CONTRIBUTED PAPERS

&
**ABSTRACTS of INVITED LECTURES,
TOPICAL INVITED LECTURES and PROGRESS REPORTS**

**Editors:
Dragana Ilić, Vladimir Srećković,
Bratislav Obradović and Jovan Cvetić**

**БЕОГРАД
2022**

31ˢᵗ Summer School and International Symposium on the Physics of Ionized Gases

September 5 – 9, 2022, Belgrade, Serbia

S P I G 2022

CONTRIBUTED PAPERS

&

ABSTRACTS OF INVITED LECTURES,

TOPICAL INVITED LECTURES AND

PROGRESS REPORTS

Editors

Dragana Ilić, Vladimir Srećković,
Bratislav Obradović and Jovan Cvetić

University of Belgrade –
School of Electrical
Engineering

University of Belgrade –
Faculty of Physics

Serbian Academy of
Sciences and Arts

Belgrade, 2022

SPIG 2022

SCIENTIFIC COMMITTEE

D. Ilić (Co-chair), Serbia
V. Srećković (Co-chair), Serbia

A. Antoniou, Greece
D. Borka, Serbia
J. Burgdörfer, Austria
J. Cvetić, Serbia
V. Guerra, Portugal
M. Ivković, Serbia
K. Kutasi, Hungary
I. Mančev, Serbia
D. Marić, Serbia
N. J. Mason, UK
A. Milosavljević, France
V. Milosavljević, Serbia
K. Mima, Japan
Z. Mišković, Canada
L. Nahon, France
B. Obradović, Serbia
G. Poparić, Serbia
P. Roncin, France
I. Savić, Serbia
Y. Serruys, France
N. Simonović, Serbia
M. Škorić, Japan
M. Trtica, Serbia
S. Tošić, Serbia
R. White, Australia

ADVISORY COMMITTEE

D. Belić
N. Bibić
M. S. Dimitrijević
S. Đurović
N. Konjević
M. M. Kuraica
J. Labat
G. Malović
B. P. Marinković
Z. Mijatović
M. Milosavljević
Z. Lj. Petrović
L. Č. Popović
J. Purić
B. Stanić

ORGANIZING COMMITTEE

J. Cvetić (Co-chair)
B. Obradović (Co-chair)

M. Ignjatović (Co-secretary)
L. Gavanski (Co-secretary)

N. Konjević
N. Cvetanović
T. Gajo
I. Krstić
N. Sakan

Progress Reports

Contributed Papers

FORMATION AND PROPAGATION OF STREAMERS IN CF$_3$I-SF$_6$ GAS MIXTURES

J. ATIĆ[1], D. BOŠNJAKOVIĆ[1], I. SIMONOVIĆ[1],
Z. Lj. PETROVIĆ[2] and S. DUJKO[1]

[1]*Institute of Physics Belgrade, University of Belgrade, Pregrevica 118,
11080 Belgrade, Serbia
E-mail sasa.dujko@ipb.ac.rs*

[2]*Serbian Academy of Science and Arts, Knez Mihailova 35, 11000 Belgrade, Serbia*

Abstract. The formation and propagation of streamers in CF$_3$I-SF$_6$ mixtures are studied by the classical fluid model in 1D and 1.5D configurations. We calculate the electron density, electric field, and velocity of streamers as a function of the applied reduced electric fields for various CF$_3$I-SF$_6$ mixtures. We found that the transition of an electron avalanche into a negative streamer occurs more slowly with an increasing fraction of CF$_3$I in the mixture.

1. INTRODUCTION

In high voltage technology, strong electronegative gases are used to prevent the electrical breakdown in power transmission and distribution systems. SF$_6$ is widely used in these applications because of its extraordinary dielectric characteristics (primarily, high critical electric field and low boiling point). However, SF$_6$ is a very powerful greenhouse gas with an extremely high global warming potential (22800 on a 100-year horizon) and a very long atmospheric lifetime (3200 years). Research on alternative gases is therefore one of the main activities of researchers worldwide.

The first step in this effort involves reducing the SF$_6$ concentration using gas mixtures. CF$_3$I, one of the most promising candidates for replacement of SF$_6$, is also a strong electronegative gas. Its critical electric field is higher than that of SF$_6$ and it has a very short atmospheric lifetime (shorter than 2 days), as well as negligible global warming potential (lower than the referent gas CO$_2$). However, in comparison with SF$_6$, its boiling point is not sufficiently low. Using these CF$_3$I characteristics as motivation factors, we investigated the formation and propagation of negative streamers in CF$_3$I-SF$_6$ mixtures.

2. METHODS OF CALCULATIONS

The transition from an avalanche to a streamer, and the propagation of streamers were considered by a numerical model based on fluid equations. We use the classical fluid model where the equation of continuity is combined with the drift-diffusion approximation. The resulting equation is coupled to the Poisson equation for space charge electric field calculations. The corresponding system of partial differential equations is solved numerically assuming the local field approximation (Bošnjaković et al. 2016). The calculations are carried out in the 1D and 1.5D configurations where the fixed value of the streamer radius is incorporated into the axial symmetrical model. The streamer velocities are calculated from the modeling performed in 1D and by using the analytical expression (Li et al. 2007) which requires knowledge of electron mobility, longitudinal diffusion coefficient and ionization coefficient as a function of the reduced electric field. The cross-section sets for electron scattering in CF_3I and SF_6 were developed in our laboratory (Mirić et al. 2016), and by Itoh and co-workers (Itoh et al. 1993) respectively.

3. RESULTS AND DISCUSSION
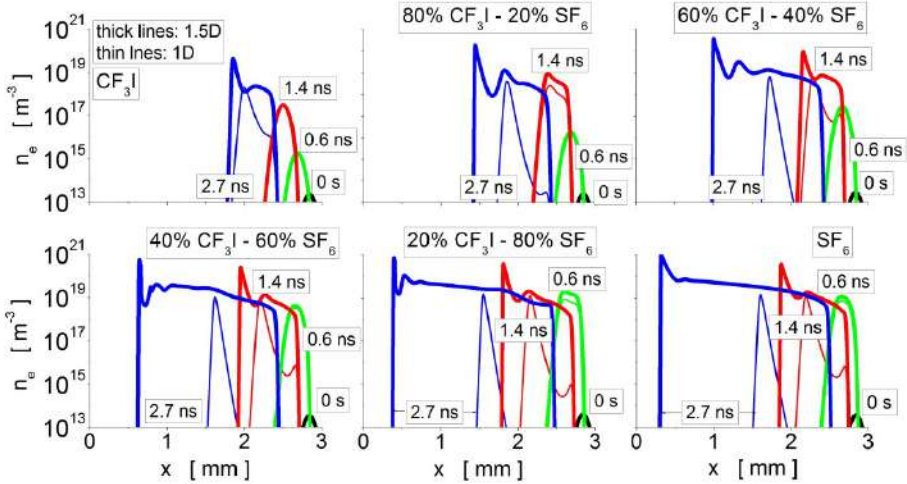
Figure 1: Electron density during streamer formation and propagation in CF_3I-SF_6 mixtures for $E_0/n_0 = 480$ Td.

Figure 1 shows the electron density during streamer formation and propagation in CF_3I-SF_6 mixtures. The results are obtained from the classical 1D and 1.5D fluid models in which the input data are electron bulk transport coefficients calculated by Monte Carlo simulations. The external electric field is 480 Td, which is larger than the critical electrical fields of the two gases. This requirement permits the development of streamers. Comparing the results in two different configurations

for the fixed mixture shows that the electron density is higher in the 1.5D model. The results in the same configuration show that the development of streamers is slower with the decrease of SF_6 in mixture. This behavior is expected based on a greater critical electric field of CF_3I (437 Td) than SF_6 (361 Td). This is one of the indicators that CF_3I is better dielectric than SF_6 because of its capacity to prevent the development of streamers at higher electric fields.
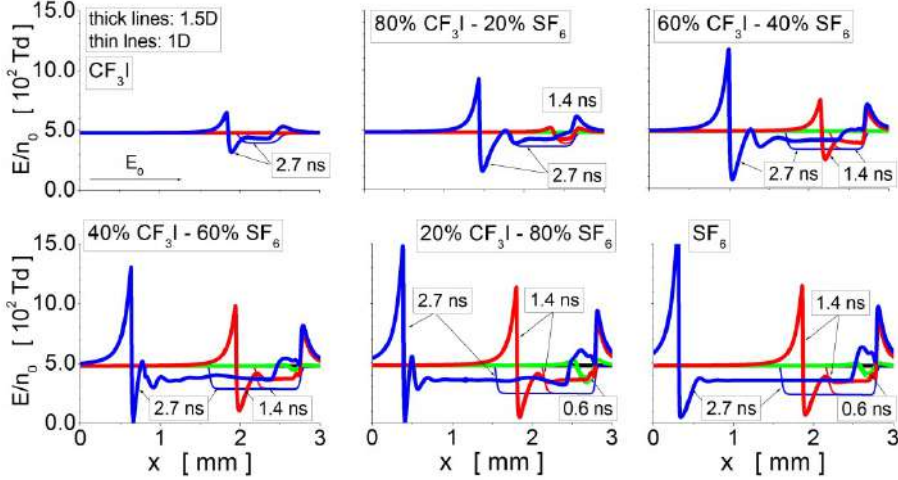
Figure 2: Electric field during streamer formation and propagation in CF_3I-SF_6 mixtures for E_0/n_0 = 480 Td. The calculation is performed using the 1.5D and 1D setups and balk transport coefficients as input to the classical fluid model.

Figure 2 shows the temporal development of the electrical field of the streamers in the CF_3I-SF_6 mixtures according to the same conditions as in Figure 1. The results of the 1.5D configuration show that the electric field in the streamer channel is equal to the critical electric field of the studied gas mixture. Field amplification in the region ahead of the streamer front starts from 40 % (pure CF_3I) up to 200 % (pure SF_6). By comparing the 1D and 1.5D configurations, we observe that the electrical field in the streamer channel descends to the lower level in the 1.5D configuration. In the 1D configuration, the electrical field in the region ahead of the streamer front is equal to the external field, independently of the gas mixture.

Figure 3 shows the streamer velocity and drift velocity of the electrons for various CF_3I-SF_6 mixtures. As the development of streamers is possible in electrical fields above the critical electrical field, the streamer velocity of gas mixtures can be calculated by the fluid model (left panel) starting from different electrical fields. The increase in streamer velocity with increasing concentration of SF_6 is a consequence of the evolution of streamers (Figures 1 and 2). Although it seems unexpected, the streamer velocity in the pure SF_6 is lower than that in the mixture 20% CF_3I - 80% SF_6 because of the behavior of the drift velocity of

electrons (right panel). The comparison of these two sets of results shows that the streamer velocity is higher than the drift velocity of electrons regardless of the gas mixture and the electric field. This follows from the fact that the streamer velocity is a combination of the electron drift velocity, the velocity induced by the strong diffusive flux at the streamer front and the creation of the electrons by electron-impact ionization. A comparison of the streamer velocities computed from the fluid model (left panel) and the analytical expression (middle panel) shows that these two sets of results differ from each other. This figure clearly illustrates the limits of the analytical formula that is often used for calculating streamer velocity.
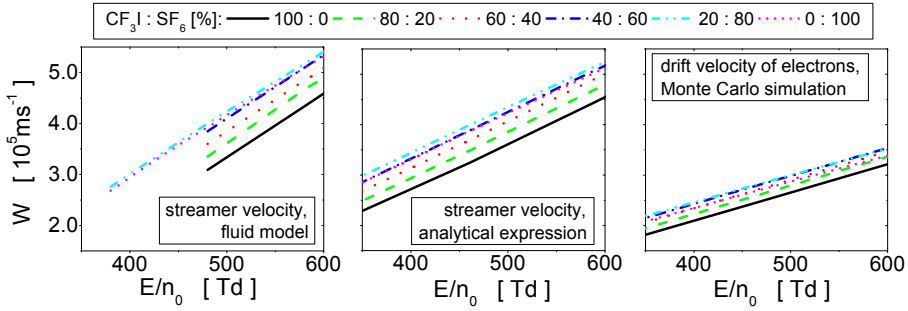
Figure 3: Streamer velocity calculated by the fluid model (left panel) and analytical expression (middle panel) and the drift velocity of electrons (right panel). Results in the CF_3I-SF_6 mixtures are given as a function of the reduced electric field.

Acknowledgment

References

Bošnjaković, D., Petrović, Z.Lj., Dujko, S.: 2016, *J. Phys. D: Appl. Phys*. **49**, 405201.

Li, C., Brok, W.J.M., Ebert, U., van der Mullen, J.J.A.M.J.: 2007, *Appl. Phys*. **101**, 123305.

Mirić, J., Bošnjaković, D., Simonović, I., Petrović Z.Lj., Dujko, S.: 2016, *Plasma Source Sci. Technol*. **25**, 065010.

Itoh, H., Matsumura, T., Satoh, K., Date, H., Nakano, Y., Tagashira, H.: 1993, *J. Phys. D: Appl. Phys*. **26**, 1975.

Electron transport coefficients and negative streamer dynamics in CF_3I-SF_6 mixtures

Saša Dujko
Institute of Physics
University of Belgrade
Belgrade, Serbia
sasa.dujko@ipb.ac.rs

Jasmina Atić
Institute of Physics
University of Belgrade
Belgrade, Serbia
jasmina.atic@ipb.ac.rs

Danko Bošnjaković
Institute of Physics
University of Belgrade
Belgrade, Serbia
dbosnjak@ipb.ac.rs

Zoran Lj. Petrović
Institute of Physics
University of Belgrade and Serbian
Academy of Sciences and Arts
Belgrade, Serbia
zoran@ipb.ac.rs

Jaime de Urquijo
Instituto de Ciencias Físicas,
Universidad Nacional Autónoma de
México
Cuernavaca, Morelos, Mexico
mistenisrojos@gmail.com

Abstract—A multi term theory for solving the Boltzmann equation and a Monte Carlo simulation technique are used to calculate electron transport coefficients in the mixtures of CF_3I and SF_6 as a function of the applied electric field. The calculated transport coefficients are then used as an input in the fluid equation based models to investigate the transition from an electron avalanche into a streamer and streamer propagation. Electron transport coefficients are also calculated in radio-frequency electric and magnetic fields crossed at arbitrary phases and angles. A multitude of kinetic phenomena induced by the synergism of the magnetic field and electron attachment is observed and discussed using physical arguments.

Keywords—Boltzmann equation, Monte Carlo, transport coefficients, streamers, electron attachment, ionization

I. INTRODUCTION

Studies of electron transport processes in strongly attaching gases in electric and magnetic fields have many important applications. These applications range from the modelling of magnetically-assisted low-pressure collision dominated plasma discharges to the modelling of gaseous particle detectors in high-energy physics and to the development of a new generation of gaseous dielectrics in high-voltage technology. In the present work, we are investigating the electron transport and the streamer propagation in the mixtures of strongly attaching gases trifluoroiodomethane (CF_3I) and sulfur hexafluoride (SF_6). In high-voltage technology, strongly attaching gases and their mixtures with other appropriate gases such as N_2 and/or CO_2 are used with the aim of controlling and preventing the electrical breakdown in electric power systems. The most important gaseous dielectric in high voltage technology nowadays is SF_6. SF_6 is a strongly attaching gas, with a high dielectric strength, and a breakdown voltage nearly three times higher than that of air at atmospheric pressure. However, in electrical discharges, SF_6 creates highly toxic and corrosive compounds such as S_2F_{10} and SOF_2. In addition, SF_6 has an extremely high global warming potential (23900 times higher than that of CO_2) and an extremely long atmospheric lifetime (3200 years) [1]. These facts have moved physicists and engineers into finding possible substitutes of SF_6. One of the most promising candidates is CF_3I. CF_3I is also a strongly attaching gas, but with much higher dielectric strength than SF_6. The global warming potential of CF_3I is much less than that of SF_6 (approximately 0.4 times that of CO_2), and its lifetime in the atmosphere is very short (1.8 days). Using these facts as motivational factors, we have undertaken a program to understand electron interactions with CF_3I as well as the basic properties of electron transport and streamer propagation in pure CF_3I and its mixtures with SF_6.

In the present investigations, we have calculated electron transport coefficients in various mixtures of CF_3I and SF_6 subjected to an external static electric field. Our results are based on a numerical multi term solution of the Boltzmann equation [2,3], which is solved for values of E/N ranging from approximately 50 to 10 000 Td (1 Td = 10^{-21} Vm^2). For the lower values of E/N, due to poor convergence of transport coefficients we have applied the Monte Carlo method. The Monte Carlo code has been recently optimized and specified to consider the transport processes of electrons in strongly attaching gases [4]. The poor convergence of transport coefficients is a consequence of predominant removal of the lower energy electrons due to a strong electron attachment, which in turn shifts the bulk of the distribution function towards a higher energy. Under these conditions, the moment method for solving the Boltzmann equation used in the present work usually fails, as it requires a prohibitive number of basis functions for resolving the energy dependence of the distribution function.

Calculations have also been performed in the case of alternating current (ac) electric and magnetic fields. We investigate the way in which the transport coefficients and other swarm properties are influenced by the field frequency, electric and magnetic field strengths, and the phase difference between the fields under conditions in which the electron transport is greatly affected by electron attachment. The time-dependent behavior of electron swarms in varying configurations of electric and magnetic fields is particularly important for the modeling of magnetically controlled/assisted radio-frequency plasma discharges [3]. In addition, the time-dependent studies are useful for a future development of sensors for detection of electromagnetic waves induced in gas-insulated high-voltage switchgear (GIS) by partial discharges.

Finally, the calculated transport coefficients in a direct current (dc) electric field are used as an input in the fluid-equation based models with the aim of investigating the transition from an electron avalanche into a streamer and

streamer propagation. Among many important points, in the present work we discuss how streamer properties, including the electron density, electric field and streamer velocity are affected by introducing CF$_3$I into SF$_6$.

II. Theoretical Method

The behavior of electron swarms in neutral gases under the influence of electric and magnetic fields is described by the phase-space distribution function $f(\boldsymbol{r}, \boldsymbol{c}, t)$, representing the solution of the Boltzmann equation

$$\frac{\partial f}{\partial t} + \boldsymbol{c} \cdot \frac{\partial f}{\partial \boldsymbol{r}} + \frac{e}{m}(\boldsymbol{E} + \boldsymbol{c} \times \boldsymbol{B}) \cdot \frac{\partial f}{\partial \boldsymbol{c}} = -J(f, f_0), \quad (1)$$

where $\boldsymbol{r}$, and $\boldsymbol{c}$ denote the position and velocity coordinates respectively, while e and m are the charge and the mass of the swarm particle and t is the time. The right-hand side $J(f,f_0)$ denotes the linear electron-neutral molecule collision operator, accounting for elastic, inelastic and non-conservative collisions. The electric and magnetic fields are assumed to be spatially-homogeneous and in the general case time-dependent.

The methods and techniques for solving the Boltzmann equation are by now standard and the reader is referred to our previous works [3,4]. Nevertheless, we highlight some important steps of our methodology for solving the Boltzmann equation:

1) No assumptions on symmetries in velocity space are made, and the directional dependence of $f(\boldsymbol{r},\boldsymbol{c},t)$ in velocity space is represented in terms of a spherical harmonic expansion:

$$f(\boldsymbol{r}, \boldsymbol{c}, t) = \sum_{l=0}^{\infty} \sum_{m=-l}^{l} f(\boldsymbol{r}, \boldsymbol{c}, t) Y_m^{[l]}(\hat{\boldsymbol{c}}), \quad (2)$$

where $Y_m^{[l]}(\hat{\boldsymbol{c}})$ are spherical harmonics, and $\hat{\boldsymbol{c}}$ represents the angles of $\boldsymbol{c}$. In contrast to the frequently used two-term approximation which forms the basis of the classical theory of electron transport in gases, our method is a truly multi-term approach. The differences between the two-term approximation and our multi-term approach for solving the Boltzmann equation will be illustrated for electron transport in CF$_3$I in the next section.

2) Under hydrodynamic conditions (far away from the boundaries, sources and sinks of electrons) a sufficient representation of the space dependence is an expansion of $f(\boldsymbol{r},\boldsymbol{c},t)$ in terms of the powers of the density gradient operator:

$$f(\boldsymbol{r}, \boldsymbol{c}, t) = \sum_{k=0}^{\infty} f^{(k)}(\boldsymbol{c}, t) \odot (-\nabla)^k n(\boldsymbol{r}, t), \quad (3)$$

where $f^{(k)}(\boldsymbol{c}, t)$ are time-dependent tensors of rank k while $\odot$ denotes a k-fold scalar product.

3) The energy dependence of $f(\boldsymbol{r},\boldsymbol{c},t)$ is represented by an expansion about a variety of Maxwellians at an arbitrary temperature in terms of Sonine polynomials.

The combination of spherical harmonics and Sonine polynomials yields the well-known Burnett functions. Using the appropriate orthogonality relations of the Burnett functions, the Boltzmann equation is converted into a hierarchy of doubly and infinite coupled inhomogeneous matrix equations for the time-dependent moments. The finite truncation of the Burnett functions, permits a solution of this hierarchy by direct numerical inversion. These equations are solved numerically and both families of

transport coefficients, the bulk and the flux, including other transport properties, are expressed in terms of moments of the distribution function [2,3].

In addition to Boltzmann's equation, in the present work we apply a Monte Carlo simulation technique. Our standard MC code has been recently extended to consider the spatially inhomogeneous electron swarms in strongly attaching gases by implementing the rescaling procedures [4]. The so-called discrete and continuous rescaling procedures are developed and benchmarked in the aim of simulating electron transport under conditions of extensive losses of seed electrons due to a strong electron attachment. In this work, Monte Carlo method is employed as a tool to confirm the numerical accuracy and integrity of a multi-term theory for solving the Boltzmann equation. However, whenever the convergence of transport coefficients was poor in the Boltzmann equation analysis, then MC results are in turn included in the plots.

Transition from an avalanche into a streamer, and propagation of streamers have been considered by the fluid equation based models. We employ the so-called classical fluid model in which the equation of continuity is combined with the drift-diffusion approximation. The resulting equation is coupled with the Poisson equation for the space charge electric field calculations. The resulting system of partial differential equations is solved numerically assuming the local field approximation [5,6].

III. Results and Discussion

A. Cross sections and inputs

The development of the complete cross-section set of electron scattering in CF$_3$I has been detailed in recent studies [4,7], and is based largely on the original set proposed by Kimura and Nakamura [8]. The accuracy and the completeness of the initial set developed by Kimura and Nakamura was improved by applying the standard swarm procedure using the measurements of transport coefficients in the mixtures of CF$_3$I with Ar and CO$_2$ under the pulsed-Townsend (PT) conditions. Cross sections for electron scattering in SF$_6$ are taken from Itoh et al. [9]. In the present investigation, we consider the density-reduced electric field range from 1 to 10^4 Td. The background gas mixture temperature is fixed at 293 K. In the domain time-dependent studies, we cover a range of magnetic field amplitudes between 0 and 10^4 Hx (1 Hx = 10^{-27} Tm^{-3}).
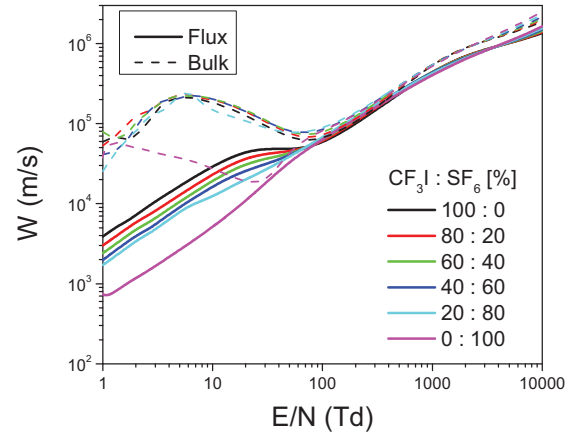
Fig. 1. Variation of the flux and bulk drift velocities with E/N for various CF$_3$I-SF$_6$ mixtures.

B. Transport coefficients in the mixtures of CF₃I and SF₆

In Fig. 1 we show the variation of the flux and bulk drift velocities with E/N for various CF$_3$I-SF$_6$ mixtures. We observe that over the entire range of E/N the flux drift velocity is a monotonically increasing function of E/N, while the bulk drift velocity in pure CF$_3$I and SF$_6$, as well as in their mixtures, exhibits a pronounced negative differential conductivity (NDC). NDC is characterized by a decrease in the bulk drift velocity despite an increase in the magnitude of the applied electric field. In the case of strongly attaching gases such as CF$_3$I and SF$_6$, NDC is induced by the combined effects of attachment heating and inelastic cooling of the swarm. In addition, due to attachment heating and explicit effects of ionization, the bulk drift velocity dominates the flux component over the entire range of E/N considered in this work.

In Fig. 2 we show the variation of the ionization and attachment rate coefficients with E/N for various mixtures. As expected, the ionization rate coefficient is a monotonically increasing function of E/N and becomes significant at the higher values of E/N when sufficient electrons have enough energy, to cause ionization. We observe that the ionization rate is less sensitive with respect to the composition of the gas mixture at higher values of E/N. The behavior of the attachment rate coefficient is more complex, but generally it tends to decrease with increasing E/N.
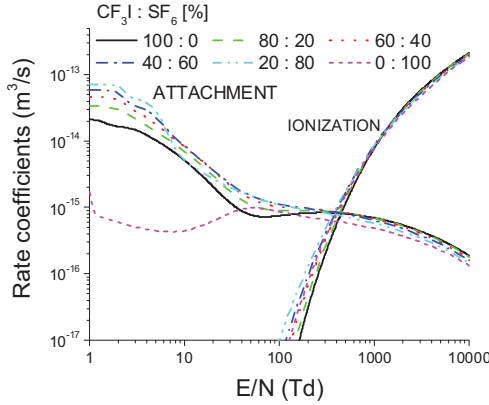
Fig. 2. Variation of the attachment and ionization rate coefficients with E/N for various CF$_3$I-SF$_6$ mixtures.
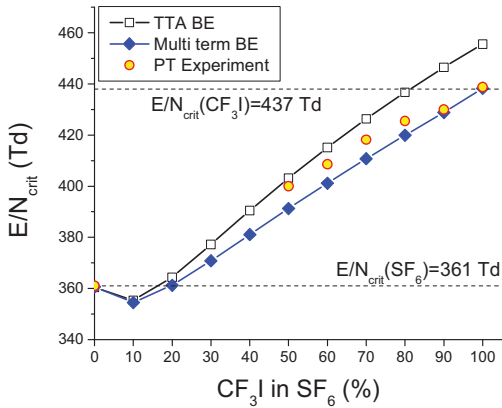
Fig. 3. Variation of the critical field strength as a function of the CF$_3$I content in the CF$_3$I-SF$_6$ mixture. Results obtained by the two-term approximation (TTA) and multi-term approach for solving the Boltzmann equation are compared with the measurements under the PT conditions.
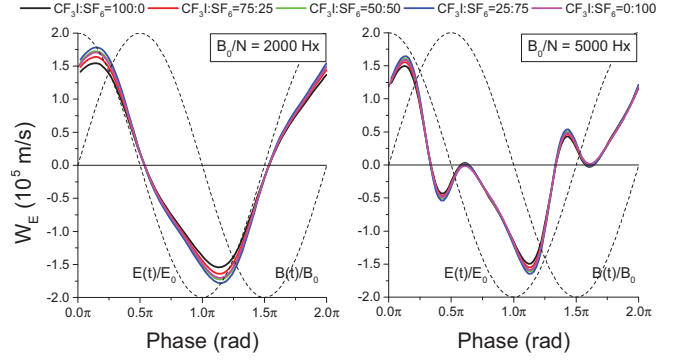
Fig. 4. Temporal profiles of the flux drift velocity for various CF$_3$I-SF$_6$ mixtures. The electric field amplitude is 350 Td and the field frequency is 1000 MHz.

In Fig. 3 we show the variation of the critical electric field (or limited electric field) as a function of the per cent content of CF$_3$I in the mixture. The critical electric field is a value of E/N for which rate coefficients of electron attachment and ionization are equal. This property is of great importance not only in studies of low-current dc discharges and streamers, but may also be useful for studies of some rf discharges. The results obtained by solving the Boltzmann equation are compared with the measurements under the PT conditions. Our multi term results and measurements agree very well for the pure gases. We observe that the TTA significantly overestimates the measurements and multi-term results for pure CF$_3$I.

C. Transport coefficients in radio-frequency electric and magnetic fields

In Fig. 4 we show the temporal profiles of the longitudinal flux drift velocity for various CF$_3$I-SF$_6$ mixtures. Calculations are performed in a crossed field configuration while the phase difference between the electric and magnetic fields is set to π/2 rad. The magnetic field amplitudes are 2000 Hx (left panel) and 5000 Hx (right panel). We observe that the profiles are asymmetric and phase-delay of the W_E curves relative to the electric field is clearly evident due to temporal non-locality [4]. The maximum values of W_E are dependent on the gas composition. The time-averaged power absorbed by the swarm (or plasma or any active medium) is given by:

$$\langle p_{abs} \rangle = \frac{1}{T} \int_0^T -e N_0 \boldsymbol{W}(t) \cdot \boldsymbol{E}(t) dt \,, \qquad (4)$$

where N_0 is the number of electrons in the swarm, T=2π/ω is the period, $\boldsymbol{W}$ is the time-dependent average velocity and $\boldsymbol{E}$ is the time-dependent electric field. From Eq. (4), it is clear that the phase difference between the drift velocity and electric field controls the power absorption: (i) when the drift velocity $\boldsymbol{W}$ and electric field $\boldsymbol{E}$ have the same sign, the instantaneous power is positive, and (ii) when the drift velocity $\boldsymbol{W}$ and electric field $\boldsymbol{E}$ have the opposite sign, then the instantaneous power is negative. This suggests that when the power is positive the electric field pumps the energy into the system while when the power is negative the energy is transferred from an active medium to the external circuit.

In Fig. 5 we show the variation of the cycle-averaged power as a function of the magnetic field amplitude for various CF$_3$I-SF$_6$ mixtures. We observe that the absorbed power depends on the gas composition. One of the most striking phenomena is the presence of periodic structures in

the profile of the absorbed power. Comparing CF_3I and SF_6, these structures are more pronounced for CF_3I. For dc electric and magnetic fields the absorbed power is always a monotonically decreasing function of the applied magnetic field, while in this case we may observe a multitude of peaks in the B_0/N-profiles of this property. This is a clear sign of the resonant absorption of energy from the rf electric and magnetic fields. We see that these effects are more pronounced for the lower values of B_0/N, where on the average the electrons only complete partial orbits between collisions.

D. Transition from an electron avalanche into a negative streamer its propagation in the CF_3I-SF_6 mixtures

In Figs. 6 (a) and (b) we show the temporal evolution of the electric field and electron density, respectively for various CF_3I-SF_6 mixtures. Calculations are performed in a 1-dimensional setup. The initial Gaussian grows due to the ionization and then charge separation occurs due to the drift of positive ions in the opposite direction. As a consequence, the initial homogeneous electric field is disturbed and the field in the ionized region becomes more and more screened. Due to space charge effects the electric field drops off to the level in which ionization stops and only attachment occurs. As a consequence, the electron density in the streamer channel is significantly reduced. By mixing CF_3I with SF_6, the streamers become slower and the screening of the externally applied electric field is less pronounced.
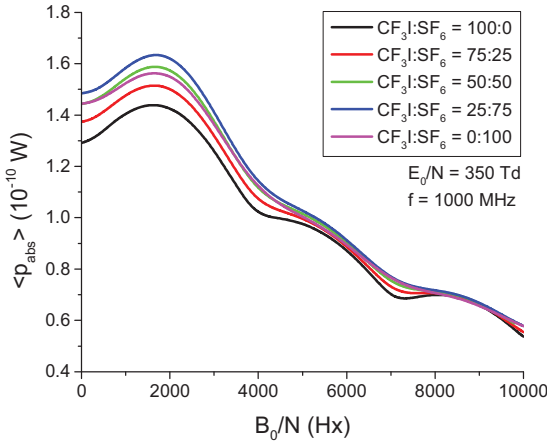
Fig. 5. Variation of the cycle-averaged power of electrons for various CF3I-SF6 mixtures. The electric field amplitude is 350 Td and the field frequency is 1000 MHz.
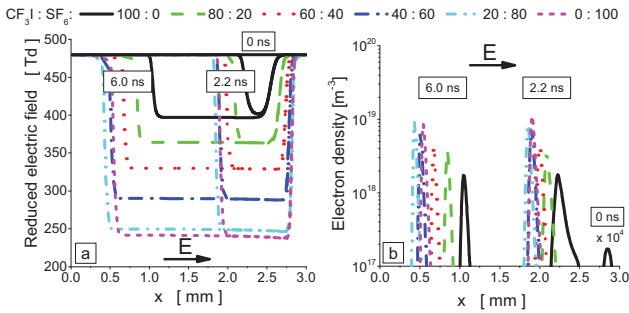
Fig. 6. Temporal evolution of the electric field (a) and electron density (b) in a planar front in various CF_3I-SF_6 mixtures. The externally applied electric field is 480 Td and streamers move from the right to the left.

IV. Conclusion

In this paper, we have used a multi term theory for solving the Boltzmann equation and a Monte Carlo simulation technique to investigate electron transport in the mixtures of CF_3I and SF_6. From the point of view of a possible application of CF_3I and its mixtures with SF_6 as gaseous dielectrics, we have calculated the drift velocity, rate coefficients for electron attachment and ionization and critical electric field. The previous studies [10] are extended by considering the duality of transport coefficients, e.g. the existence of two different families of transport coefficients, the bulk and the flux. Comparing the bulk and flux drift velocities, it is found that the bulk component shows a very strong NDC and behaves in a qualitatively different fashion. Calculations in dc electric fields are augmented by those in rf electric and magnetic fields. We have paid a particular attention to the power absorption of the swarm. Due to a complex interplay of the effects induced by temporal non-locality, magnetic field and cyclotron resonance, we have observed a multitude of peaks in the B_0/N profiles of the absorbed power. Finally, using the classical fluid model we have simulated the transition from an electron avalanche into a negative streamer. It is shown that streamers in the mixtures with a higher content of CF_3I are slower, the electron density is reduced and the electric field in the streamer interior is enhanced. Thus, by mixing CF_3I with SF_6, the insulation characteristics of the mixtures are considerably improved.

References

[1] J. de Urquijo, "Is CF_3I a good gaseous dielectric? A comparative swarm study of CF_3I and SF_6," J. Phys. Conf. Series, vol. 86, 012008, 2007.

[2] S. Dujko, R.D. White, Z.Lj. Petrović and R.E. Robson, "Benchmark calculations of nonconservative charged-particle swarms in dc electric and magnetic fields crossed at arbitrary angles," Phys. Rev. E. vol. 81, 046403, 2010.

[3] S. Dujko, R.D. White, Z.Lj. Petrović and R.E. Robson, "A multi-term solution of the non-conservative Boltzmann equation for the analysis of temporal and spatial non-local effects in charged-particle swarms in electric and magnetic fields," Plasma Sources Sci. Technol. vol. 20, 024013, 2011.

[4] J. Mirić, D. Bošnjaković, I. Simonović, Z.Lj. Petrović, "Electron swarm properties under the influence of a very strong attachment in SF_6 and CF_3I obtained by Monte Carlo rescaling procedures," Plasma Sources Sci. Technol. vol. 25, 065010, 2016.

[5] C. Li, W.J.M.Brok, U.Ebert nd J.J.A. van der Mullen,R. Nicole, "Deviations from the local field approximation in negative streamer heads," J. Appl. Phys. vol. 101, 123305,2007.

[6] D. Bošnjaković, Z.Lj. Petrović and S. Dujko, "Fluid modeling of resistive plate chambers: impact of transport data on development of streamers and induced signals," J. Phys. D: Appl. Phys. vol. 49, 405201,2016.

[7] J. Atić et al. "Scattering cross sections and electron transport in CF_3I," unpublished.

[8] M. Kimura and Y. Nakamura, "Electron swarm parameters in CF_3I and a set of electron collision cross sections for the CF_3I molecule," J. Phys. D: Appl. Phys. vol. 43, 145202, 2010.

[9] H. Itoh ,T. Matsumura, K. Satoh K, H. Date, Y. Nakano and H. Tagashira, "Electron transport coefficients in SF_6," J. Phys. D: Appl. Phys. vl. 26, 1975, 1993.

[10] J. de Urquijo, A. Mitrani, G.R. Vargaz E. Baurto, "Limited field strength and electron swarm coefficients of the CF_3I-SF gas mixtures," J. Phys. D: Appl. Phys. vol. 44, 342001, 2011.

Proceedings of the
22nd International Conference on
Gas Discharges and Their Applications

Novi Sad - Serbia
September, 2-7, 2018

Volume 1

Proceedings of the 22nd International Conference on
Gas Discharges and Their Applications

Vol. 1

Serbian Academy of
Sciences and Arts

PROCEEDINGS OF
THE XXII$^{\text{ND}}$ INTERNATIONAL
CONFERENCE ON GAS DISCHARGES
AND THEIR APPLICATIONS

- VOLUME 1 -

2$^{\text{nd}}$ - 7$^{\text{th}}$ September 2018

Novi Sad, SERBIA

Serbian Academy of Sciences and Arts

&

Institute of Physics, University of Belgrade

Editors: Prof. Zoran Lj. Petrović

Dr. Nevena Puač

Dr. Saša Dujko

Dr. Nikola Škoro

EXECUTIVE MANAGMENT COMMITTEE

Dr. J.E. Jones, Chair
Prof. G.R. Jones
Prof. J.W. Spencer
Prof. K Hidaka
Dr. A.B. Murphy
Prof. D. Hong
Dr. P. Robin-Jouan

INTERNATIONAL SCIENTIFIC COMMITTEE

Dr. J.-M. Bauchire, France
Prof. Yann Cressault, France
Prof. C.M. Franck, Switzerland
Prof. K. Hidaka, Japan
Prof. G.R. Jones, UK
Dr. A.B. Murphy, Australia
Prof. G.J. Pietsch, Germany
Prof. Ph. Robin-Jouan, France
Prof. Kohki Satoh, Japan
Prof. J.W. Spencer, UK
Dr. T. Teich, Switzerland
Prof. J. -Y. Trepanier, Canada
Prof. Y. Wu, China
Dr. J. L. Walsh, UK

Dr. J.-P. Borra, France
Prof. M. Farzaneh, Canada
Prof. A. Haddad, UK
Prof. D. Hong, France
Dr. J.E. Jones, UK
Prof. Z. Lj. Petrović, Serbia
Prof. V. Rakov, USA
Prof. A. Robledo-Martinez, Mexico
Dr. M. Seeger, Switzerland
Dr. S. Stangherlin, Switzerland
Dr. Igor Timoshkin, UK
Prof. K.-D. Weltmann, Germany
Dr. J. D. Yan, UK

LOCAL ORGANIZING COMMITTEE

Prof. Zoran Lj. Petrović, Chair
Dr. Saša Dujko, Co-Chair

Dr. Nevena Puač, Co-Chair
Dr. Nikola Škoro, Secretary

Dr. Danko Bošnjaković
Dr. Dragana Marić
Kosta Spasić
Marija Puač
Nenad Selaković
Ilija Simonović

Prof. Bratislav Obradović
Dr. Gordana Malović
Jelena Sivoš
Dejan Maletić
Jasmina Atić
Vladan Simić

Panacomp Wonderland Travel

K. Test Techniques and Diagnostics

L. Fundamental Processes and Cross-Sections

ELECTRON TRANSPORT IN STRONGLY ATTACHING GASES IN RADIO-FREQUENCY ELECTRIC AND MAGNETIC FIELDS

J. ATIĆ[1]*, D. BOŠNJAKOVIĆ[1], Z.LJ. PETROVIĆ[1,2], J. DE URQUIJO[3],
R.D. WHITE[4] AND S. DUJKO[1]

[1] Institute of Physics, University of Belgrade, Pregrevica 118, 11080, Belgrade, Serbia
[2] Serbian Academy of Sciences and Arts, Knez Mihailova 35, 11001, Belgrade, Serbia
[3] Instituto de Ciencias Fisicas, Universidad Nacional Autonoma de Mexico, PO Box 48-3, 62251,Cuernavaca, Mor., Mexico
[4] College of Science and Engineering, James Cook University, Townsville 4810, Australia
*jasminapz@ipb.ac.rs

ABSTRACT

A multi term theory for solving the Boltzmann equation and a Monte Carlo simulation technique are used to investigate electron transport in strongly attaching gases, including SF_6, CF_3I and their mixtures in radio-frequency (rf) electric and magnetic fields. We investigate the way in which the transport coefficients and other swarm properties are influenced by the field frequency, electric and magnetic field strengths, and the phase difference between the fields under conditions in which the electron transport is greatly affected by electron attachment. A multitude of kinetic phenomena induced by the synergism of the magnetic field and electron attachment has been observed and discussed using physical arguments. In particular, we investigate the power absorption of electrons in rf electric and magnetic fields. The existence of periodic structures in the absorbed power versus amplitude of the applied rf magnetic field has been explained by considering the effects of resonant absorption of energy in association with the temporal non-locality of electron transport.

1. INTRODUCTION

Studies of electron transport processes in strongly attaching gases in combined electric and magnetic fields have many important applications. These applications range from the modelling of magnetically-assisted low pressure collision dominated plasma discharges [1] to the modelling of gaseous particle detectors in high-energy physics and to the development of insulating dielectrics in high-voltage technology. The majority of these investigations, including the experimental measurements and theoretical calculations of transport coefficients concern the magnetic field free case in which the effects of a magnetic field are systematically neglected or, eventually, are described in terms of the scaled transport coefficients [2]. One aspect that strikes a reader surveying the literature on electron transport in electric and magnetic fields is that only in a limited number of cases the effects of a magnetic field are fully incorporated and studied. In swarm experiments, the electric and magnetic fields as well as the properties of the background gas can be very efficiently controlled, enabling one to perform accurate measurements of transport coefficients. Transport coefficients can be then unfolded to yield information about cross sections for electron scattering, required as input in kinetic/particle models of plasma discharges [3]. Fluid models of such discharges usually require transport coefficients as a function of the reduced electric and magnetic fields and/or collision frequencies for elastic, inelastic and non-conservative collisions, usually as a function of the mean electron energy.

For the more general case of alternating current (ac) electric and magnetic fields, however, there has been comparatively much less investigation [3,4]. The reason is twofold: firststly, there are no swarm experiments in ac electric and magnetic fields and secondly, the presence of an ac magnetic field introduces unavoidable mathematical complexity in theories for solving the Boltzmann equation. In the domain of Monte

Carlo simulations, one of the most challenging issues is how to optimize the computer code by increasing its efficiency under conditions in which a magnetic field controls the behavior of the swarm. The physical content is even more complicated when it comes to the studies of electron transport in strongly attaching gases. Under conditions of predominant removal of the lower energy electrons due to strong electron attachment, the bulk of the distribution function is often shifted towards a higher energy which in turn results in the high energy tail falling off much slower than a Maxwellian. The moment method for solving the Boltzmann equation under these circumstances usually fails as it requires a prohibitive number of basis functions for resolving the energy dependence of the distribution function. Along similar lines, electron attachment imposes many difficulties in Monte Carlo simulations due to extensive losses of seed electrons. Recently, we have developed the rescaling procedures for Monte Carlo simulations of electron transport in strongly attaching gases. Calculations have been performed for electron swarms in pure SF_6 and pure CF_3I assuming the magnetic field free case [5].

In this work, we extend the previous studies by considering electron transport in strongly attaching gases under the influence of rf electric and magnetic fields. We focus on the time-dependent behavior of electron transport properties with the aim of understanding the electron kinetics in magnetically-assisted low pressure plasma discharges. In addition, this research is focused on a possible implementation of obtaining results for a future development of sensors for detection of electromagnetic waves induced in gas-insulated high-voltage switchgear (GIS) by partial discharges.

2. THEORETICAL METHOD

The behavior of charged particle swarms in neutral gases under the influence of rf electric and magnetic fields is described by the phase-space distribution function $f(\mathbf{r}, \mathbf{c}, t)$ representing the solution of the Boltzmann equation

$$\frac{\partial f}{\partial t} + \mathbf{c} \cdot \frac{\partial f}{\partial \mathbf{r}} + \frac{q}{m} \left[\mathbf{E} + \mathbf{c} \times \mathbf{B} \right] \cdot \frac{\partial f}{\partial \mathbf{c}} = -J(f, f_0), \quad (1)$$

where $\mathbf{r}$, and $\mathbf{c}$ denote the position and velocity co-ordinates respectively, while q and m are the

charge and mass of the swarm particle and t is the time. The right-hand side $J(f, f_0)$ denotes the linear charged particle-neutral molecule collision operator, accounting for elastic, inelastic, and non-conservative collisions. The electric and magnetic fields are assumed to be spatially homogeneous and time-dependent.

In the present approach equation (1) is solved by decomposing $f(\mathbf{r}, \mathbf{c}, t)$ in terms of spherical harmonics in velocity space [2,4]:

$$f(\mathbf{r}, \mathbf{c}, t) = \sum_{l=0}^{\infty} \sum_{m=-l}^{l} f_m^{(l)}(\mathbf{r}, c, t) Y_m^{[l]}(\hat{c}), \quad (2)$$

where $Y_m^{[l]}(\hat{c})$ are spherical harmonics and $\hat{c}$ denotes the angles of $\mathbf{c}$. Under hydrodynamic conditions a sufficient representation of the space dependence is an expansion in terms of the powers of the density gradient operator:

$$f_m^{(l)}(r, c, t) = \sum_{s=0}^{\infty} \sum_{\lambda=0}^{s} \sum_{\mu=-\lambda}^{\lambda} f(lm \mid s\lambda\mu; c, t) G_\mu^{(s\lambda)} n(r, t), \quad (3)$$

where $G_\mu^{(s\lambda)}$ is the irreducible gradient tensor operator. The speed dependence is treated as follows:

$$f(lm \mid s\lambda\mu; c, t) = \omega(\alpha, c) \sum_{\nu=0}^{\infty} F(\nu lm \mid s\lambda\mu, \alpha, t) R_{\nu l}(\alpha c), \quad (4)$$

where $\alpha^2(t) = m / kT_b(t)$ and $\omega(\alpha(t), c)$ is a Maxwellian,

$$R_{\nu l}(\alpha(t)c) = N_{\nu l} \left[\frac{\alpha c}{\sqrt{2}} \right]^l S_{l+\frac{1}{2}}^{(\nu)} \left(\alpha^2(t) c^2 / 2 \right) \quad (5)$$

$$N_{\nu l}^2 = \frac{2\pi^{3/2} \nu!}{\Gamma(\nu + l + 3/2)}, \quad (6)$$

and $S_{l+\frac{1}{2}}^{(\nu)}$ is a Sonine polynomial. Using the above decompositions of f and implicit finite difference evaluation of time derivatives, the Boltzmann equation is transformed into a hierarchy of doubly infinite coupled inhomogeneous matrix equations for the time-dependent moments. The finite truncation of both the Sonine polynomial and spherical harmonic expansions, permit the solution of this hierarchy by direct numerical inversion. Having obtained the moments, the transport coefficients and other transport properties can be explicitly calculated [5,7].

In addition to Boltzmann's equation, in the present work we apply a Monte Carlo simulation technique. Our standard MC code has been

recently extended to consider the spatially inhomogeneous electron swarms in strongly attaching gases by implementing the rescaling procedures. The so-called discrete and continuous rescaling procedures are developed and benchmarked with the aim of simulating electron transport under conditions of extensive losses of seed electrons due to a strong electron attachment. In this work, a Monte Carlo method is employed as a tool to confirm the numerical accuracy and integrity of a multi-term theory for solving the Boltzmann equation. However, if the convergence of transport coefficients was poor in the Boltzmann equation analysis, then only MC results are presented and discussed.

In the present work we pay particular attention to the power absorption of electrons in rf electric and magnetic fields. The time-averaged power absorbed by the swarm (or plasma or any active medium) is given by [6]:

$$\langle p_{abs} \rangle = \frac{1}{T} \int_0^T -eN\mathbf{W}(t)\mathbf{E}(t)dt , \qquad (7)$$

where N is the number of electrons in the swarm, $T=2\pi/\omega$ is the period, $\mathbf{W}$ is the time-dependent average velocity and $\mathbf{E}$ is the time-dependent electric field. From Eq. (7) it is clear that the phase difference between the drift velocity and electric field controls the power absorption: (i) when the drift velocity $\mathbf{W}$ and electric field $\mathbf{E}$ have the same sign, the instantaneous power is positive, and (ii) when the drift velocity $\mathbf{W}$ and electric field $\mathbf{E}$ have the opposite sign, the instantaneous power is negative. This suggests that when the power is positive the electric field pumps energy into the system while a negative power means that energy is transferred from an active medium into the external circuit.

3. RESULTS AND DISCUSSION

In the present work we consider electron transport in SF_6, CF_3I and their mixtures. Electric and magnetic fields are in the crossed orientation and $\pi/2$ out of phase (the electric field is a cosine while the magnetic field is a sine function of time). The amplitude of the density normalized electric field is set to 350 Td ($1Td=1\times10^{-21}$ Vm^2) and we consider the density normalized magnetic field range: 0 - 10000 Hx, where $1Hx=1\times10^{-27}$ Tm^3.

For electron scattering in SF_6, we use a set of cross sections developed by Itoh and co-workers [7]. For the CF_3I cross sections we use the set developed in our laboratory. This set consists of the elastic momentum transfer cross section, cross sections for vibrational and electronic excitations as well as cross sections for electron attachment and ionization. We have used the measured data under pulsed Townsend conditions for pure CF_3I and its mixtures with Ar and CO_2 in a standard swarm procedure with the aim of improving the completeness and accuracy of a set of cross sections.
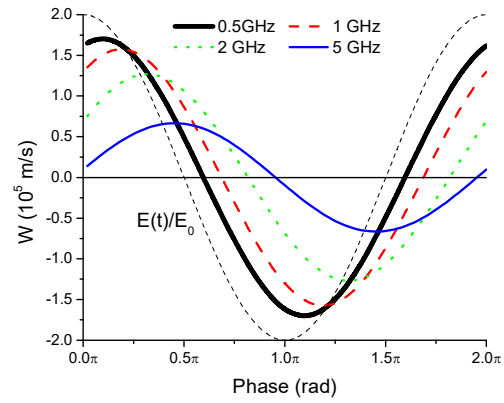
Fig. 1 Temporal profiles of the drift velocity for electrons in CF₃I as a function of the field frequency.

In Fig. 1 we show temporal profiles of the flux drift velocity as a function of the field frequency for electrons in pure CF_3I. Due to temporal non-locality, the phase delay of W with respect to the applied electric field increases with increasing frequency.
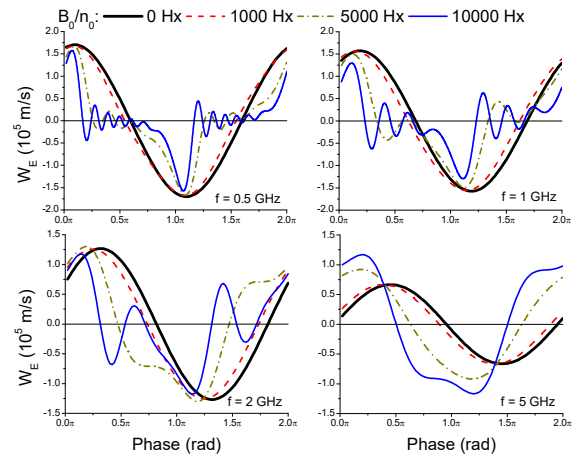
Fig. 2 Temporal profiles of the drift velocity for electrons in CF₃I as a function of the magnetic field amplitude for various applied frequencies.

The amplitude modulation is reduced with increasing frequency and there are no signs of

the time-resolved negative differential conductivity (NDC). Thus, the absorbed power is a decreasing function of the field frequency. It should be noted, however, that the time-resolved NDC is observed in the profile of the bulk drift velocity due to explicit effects of electron attachment.

In Fig. 2 we show temporal profiles of the flux longitudinal drift velocity W_E as a function of the magnetic field amplitude B_0/n_0 and for various field frequencies as indicated on the graph. For increasing B_0/n_0 and for a fixed field frequency, we observe the presence of additional oscillatory-type behavior in the W_E profiles. The phase delay of W_E with respect to the applied electric field decreases with increasing B_0/n_0. The amplitude modulation is enhanced with increasing B_0/n_0 and a field frequency of 5 GHz. Thus, one may expect a more complex and less intuitive behavior of the absorbed power when both the electric and magnetic fields are present.
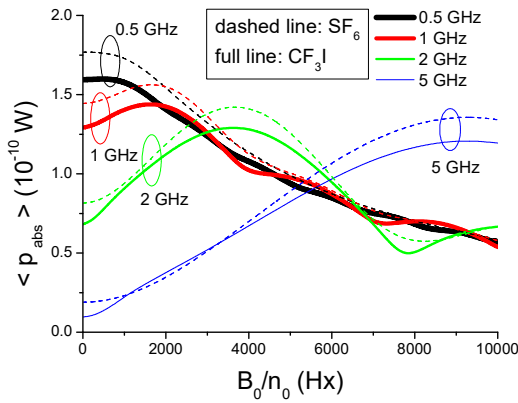
Fig. 3 Variation of the cycled-averaged power for electrons in SF$_6$ and CF$_3$I with the magnetic field amplitude for various field frequencies.

In Fig. 3 we show the variation of the cycle-averaged power as a function of the magnetic field amplitude for electrons in SF$_6$ and CF$_3$I. Perhaps the most striking phenomenon is the presence of periodic structures in the profile of the absorbed power. For 0.5 GHz, the absorbed power is a monotonically decreasing function of B_0/n_0, while for higher frequencies the resonant-type behavior is clearly evident. For dc electric and magnetic fields the absorbed power is always a monotonically decreasing function of the applied magnetic field, while in this case we may observe a multitude of peaks in the B_0/n_0-profiles of this property. This is a clear sign of the resonant absorption of energy from the rf electric and magnetic fields. We see that for

increasing field frequency, the periodic structures become wider, and extremes occur at higher values of B_0/n_0.

Comparing SF$_6$ and CF$_3$I we see that the absorbed power is higher for electrons in SF$_6$ than in CF$_3$I except between approximately 1000 and 3500 Hx and field frequency of 5 GHz. On the other hand, we found that the positions of the extremes are approximately the same for pure SF$_6$, CF$_3$I and their mixtures. Our calculations have revealed that the positions of these extremes are defined exclusively by the ratio between the mean cyclotron frequency and the field frequency.

4. CONCLUSION

In this work we have investigated the power absorption of electrons in strongly attaching gases in rf electric and magnetic fields. Due to complex interplay of the effects induced by temporal non-locality, magnetic field and cyclotron resonance, we have observed a multitude of peaks in the B_0/n_0 profiles of the absorbed power.

REFERENCES

[1] T. Makabe and Z.Lj. Petrović, *Plasma Electronics: Applications in Microelectronic Device Fabrication*, 2nd edn, CRC New York, 2015.

[2] S. Dujko, R.D. White, Z.Lj. Petrović and R.E. Robson, Plasma Sources Sci. Technol., **20**, 024013, 2011.

[3] Z. Lj. Petrović et al., J. Phys. D: Appl. Phys., **42**, 19002, 2009.

[4] R.D. White, R.E. Robson, S. Dujko, P. Nicoletopoulos and B. Li, J. Phys. D: Appl. Phys., **42**, 19002, 2009.

[5] J. Mirić, D. Bošnjaković, I. Simonović, Z.Lj. Petrović and S. Dujko, Plasma Sources Sci. Technol., **25**, 065010, 2016.

[6] S. Dujko, D. Bošnjaković, R.D. White, and Z.Lj. Petrović, Plasma Sources Sci. Technol., **24**, 054006, 2015.

[7] H. Itoh, T. Matsumara, K. Satoh, H. Date, Y. Nakano and H. Tagashira, J. Phys. D: Appl. Phys., **26**, 199, 1975.

29th Summer School and International Symposium on the Physics of Ionized Gases

Aug. 28 - Sep. 1, 2018, Belgrade, Serbia

CONTRIBUTED PAPERS

&

ABSTRACTS OF INVITED LECTURES, TOPICAL INVITED LECTURES, PROGRESS REPORTS AND WORKSHOP LECTURES

Editors:
Goran Poparić, Bratislav Obradović,
Duško Borka and Milan Rajković

Vinča Institute of
Nuclear Sciences

Serbian Academy
of Sciences and Arts

29th Summer School and International Symposium on the Physics of Ionized Gases

S P I G 2018

CONTRIBUTED PAPERS

&

ABSTRACTS OF INVITED LECTURES,
TOPICAL INVITED LECTURES, PROGRESS REPORTS
AND WORKSHOP LECTURES

Editors

Goran Poparić, Bratislav Obradović,
Duško Borka and Milan Rajković

Vinča Institute of
Nuclear Sciences

Serbian Academy
of Sciences and Arts

Belgrade, 2018

CONTRIBUTED PAPERS & ABSTRACTS OF INVITED LECTURES, TOPICAL INVITED LECTURES, PROGRESS REPORTS AND WORKSHOP LECTURES

of the 29th Summer School and International Symposium on the Physics of Ionized Gases

August 28 – September 1, 2018, Belgrade, Serbia

ACKNOWLEDGEMENT

SPIG 2018

SCIENTIFIC COMMITTEE

G. Poparić (Co-chair), Serbia
B. Obradović (Co-chair), Serbia
D. Borka, Serbia
S. Buckman, Australia
J. Burgdörfer, Austria
J. Cvetić, Serbia
E. Danezis, Greece
Z. Donko, Hungary
V. Guerra, Portugal
D. Ilić, Serbia
M. Ivković, Serbia
I. Mančev, Serbia
D. Marić, Serbia
N. J. Mason, UK
A. Milosavljević, France
K. Mima, Japan
Z. Mišković, Canada
L. Nahon, France
P. Roncin, France
I. Savić, Serbia
Y. Serruys, France
N. Simonović, Serbia
M. Škorić, Japan
M. Trtica, Serbia

ADVISORY COMMITTEE

D. Belić
N. Bibić
M. S. Dimitrijević
S. Đurović
N. Konjević
M. Kuraica
J. Labat
G. Malović
B. P. Marinković
Z. Mijatović
M. Milosavljević
Z. Lj. Petrović
L. Č. Popović
J. Purić
B. Stanić

ORGANIZING COMMITTEE

D. Borka (Co-chair)
M. Rajković (Co-chair)

V. Borka Jovanović (Co-secretary)
N. Potkonjak (Co-secretary)

N. Konjević
N. Cvetanović
A. Hreljac
B. Grozdanić
J. Aleksić
M. Nešić
S. Živković
J. Ciganović

Section 2. PARTICLE AND LASER BEAM INTERACTIONS WITH SOLIDS

Invited Lecture

Topical Invited Lectures

ELECTRON TRANSPORT AND STREAMER PROPAGATION IN CF$_3$I-SF$_6$ GAS MIXTURES

J. Atić, D. Bošnjaković, Z. Lj. Petrović and S. Dujko

Institute of Physics, University of Belgrade,
Pregrevica 118, 11080 Belgrade, Serbia

Abstract. A Monte Carlo simulation technique has been used to calculate electron transport coefficients in the mixtures of trifluoromethyl iodide (CF$_3$I) and sulfur hexafluoride (SF$_6$). The calculated transport coefficients are then used as an input into the fluid equation based models with the aim of investigating the transition from an avalanche into a streamer and streamer propagation. It was found that CF$_3$I and its mixture with SF$_6$ and N$_2$ have the good insulation properties to be regarded as viable gaseous dielectrics.

1. INTRODUCTION

In this work we investigate electron transport and streamer propagation in the mixtures of strong electronegative gases CF$_3$I and SF$_6$ as well as in the mixtures of CF$_3$I and N$_2$. In high voltage technology, strong electronegative gases and their mixtures with other appropriate gases such as N$_2$ and/or CO$_2$, are used with the aim of controlling and preventing the electrical breakdown in electric power systems. The most important gaseous dielectric in high voltage technology is SF$_6$. SF$_6$ is a strongly electronegative gas, with a high dielectric strength, and a breakdown voltage nearly three times higher than that of air at atmospheric pressure. However, in electrical discharges, SF$_6$ creates highly toxic and corrosive compounds such as S$_2$F$_{10}$ and SOF$_2$. In addition, SF$_6$ has extremely high global warming potential (23900 times higher than CO$_2$) and extremely long atmospheric lifetime (3200 years) [1]. These facts have moved scientists and engineers into finding possible substitutes of SF$_6$. One of the most promising candidates is CF$_3$I. CF$_3$I is also a strongly electronegative gas, but with much higher dielectric strength than SF$_6$. The global warming potential of CF$_3$I is much less than that of SF$_6$, and its lifetime in the atmosphere is very short. Using these facts as motivational factors, we have undertaken a program to understand electron interactions with CF$_3$I as well as the basic properties of streamer propagation in pure CF$_3$I and its mixtures with SF$_6$ and N$_2$.

In the present work, we discuss the variation of transport coefficients with the applied electric field. Calculations are performed for electrons in the CF$_3$I-SF$_6$ and CF$_3$I-N$_2$ mixtures. Values of mean energy, drift velocity, diffusion tensor, and rate coefficients are reported here. Among many important points, we

discuss the occurrence of kinetic phenomena such as negative differential conductivity, induced by the explicit effects of electron attachment. Transport coefficients for electrons are then used as an input into the fluid equation based models with the aim of investigating the transition from an avalanche into a streamer and streamer propagation. Two fundamental issues have been discussed: (i) how to use two different families of transport coefficients, the flux and the bulk in the modeling of streamers, and (ii) how streamer properties, including the electron density, electric field and streamer velocity are affected by introducing CF_3I into SF_6 and N_2 into CF_3I.

2. METHODS OF CALCULATION

In our Monte Carlo simulations, we follow a large number of electrons (typically 10^6-10^7) moving in an infinite gas under the influence of electric field. The electrons gain the energy from the electric field and dissipate this energy through binary collisions with background neutral molecules. The motion of a single electron is followed until collision with the background molecule of a neutral gas occurs. The equation for the collision probability is solved numerically by using the appropriate set of random numbers. The type of collision determines the scattering parameters after collision, including the electron speed and direction of motion. Due to extensive vanishing of the seed electrons in strongly electronegative gases, we have employed the rescaling procedures in our Monte Carlo simulation code with the aim of compensating the number of electrons in simulations without disturbing the distribution function [2]. Transport coefficients are determined after relaxation to steady state using formulae given in our previous publications [3].

Transition from an avalanche into a streamer, and propagation of streamers have been considered by the fluid equation based models. We employ the so-called classical fluid model in which the equation of continuity is combined with the drift-diffusion approximation. The resulting equation is coupled with the Poisson equation for the space charge electric field calculations. The resulting system of partial differential equations is solved numerically assuming the local field approximation [3].

3. RESULTS AND DISCUSSION

In this section, we firstly show our results for transport coefficients of electrons in the CF_3I-SF_6 mixtures. We consider the reduced electric field range: 1-10000 Td (1Td = 1×10^{-21} Vm^2) while the temperature of the background gas is 293 K. Cross sections for electron scattering in SF_6 are taken from Itoh *et al.* [4] while for electron interactions with CF_3I, we use a set of cross sections developed in our laboratory [2]. Our set of cross sections provides an excellent agreement between calculated and measured transport coefficients under the Pulsed-Townsend conditions in pure CF_3I and a fairly good agreement for the mixtures of CF_3I with Ar and CO_2.
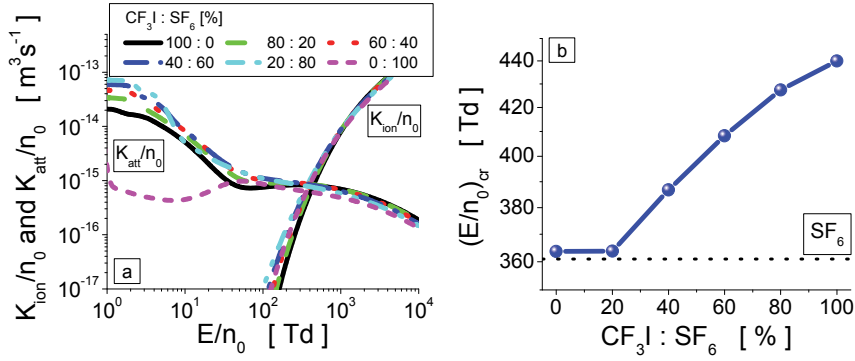
Figure 1. (a) Variation of the ionization and attachment rate coefficients with E/n_0, and (b) critical electric field in the CF_3I-SF_6 mixtures.

Figure 1 (a) shows the variation of ionization and attachment rate coefficients with E/n_0 in the CF_3I-SF_6 mixtures. As expected, the ionization rate coefficient is a monotonically increasing function of E/n_0 and becomes significant at the higher values of E/n_0 when sufficient electrons have enough energy to undergo ionization. The behavior of the attachment rate coefficient is more complex, but generally it tends to be decreased with an increasing E/n_0. When the attachment and ionization rates are equal, the E/n_0 corresponds to the so-called critical electric field. The critical electric field is shown in Figure 1 (b) for various CF_3I-SF_6 mixtures. We see that by introducing CF_3I into SF_6 the critical electric field is increased. It should be noted that in our simulations the transition from an avalanche into a streamer occurs in electric fields higher than the critical electric field.
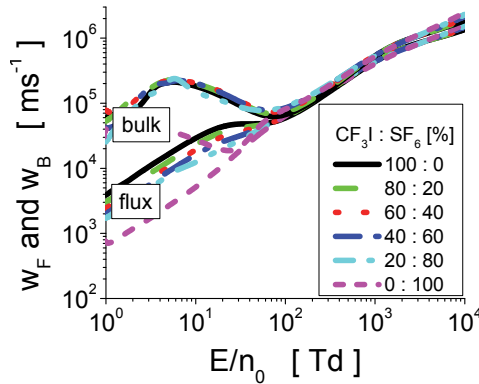
Figure 2. Variation of the flux and bulk drift velocities in various CF_3I-SF_6 mixtures.

Figure 2 shows the variation of the flux and bulk drift velocities with E/n_0 for various CF_3I-SF_6 mixtures. We observe that over the entire range of E/n_0 the flux drift velocity is a monotonically increasing function of E/n_0 while the bulk drift velocity in pure CF_3I and in pure SF_6, as well as in the mixtures shows

a strong negative differential conductivity (NDC). The phenomenon is induced by the explicit effects of electron attachment. Due to attachment heating and explicit effects of ionization the bulk drift velocity is greater than the flux drift velocity over the entire range of E/n_0 considered in this work.
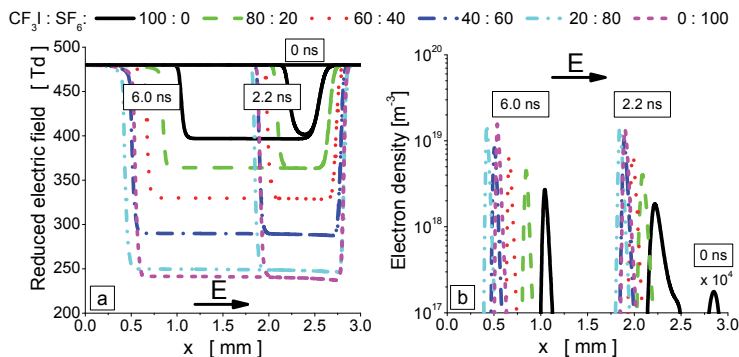
Figure 3. Temporal evolution of the electric field (a) and electron density (b) in a planar front in various CF_3I-SF_6 mixtures. The externally applied electric field is 480 Td and streamers move from the right to the left.

In Figures 3 (a) and 3 (b) we show the temporal evolution of the electric field and electron density, respectively for various CF_3I-SF_6 mixtures. Calculations are performed in a 1-dimensional setup. The initial Gaussian grows due to the ionization and then charge separation occurs due to the drift of positive ions in the opposite direction. As a consequence, the initial homogeneous electric field is disturbed and the field in the ionized region becomes more and more screened. Due to space charge effects the electric field drops off to the level in which the ionization stops and only attachment occurs. As a consequence, the electron density in the streamer channel is significantly reduced. By introducing CF_3I into SF_6, the streamers become slower and the screening of the externally applied electric field is less pronounced.

Acknowledgements

REFERENCES

[1]   J. de Urquijo, J. Phys: Conf. Ser. 86, 012008 (2007).
[2]   J. Mirić, D. Bošnjaković, I. Simonović, Z. Lj. Petrović and S. Dujko. Plasma Source Sci. Technol. 25, 065010 (2016).
[3]   D. Bošnjaković, Z. Lj. Petrović and S. Dujko, J. Phys. D: Appl. Phys. 49, 405201 (2016).
[4]   H. Itoh, T. Matsumura, K. Satoh, H. Date, Y. Nakano and H. Tagashira, J. Phys. D: Appl. Phys. 26, 1975 (1993).

Overview of the procedure to obtain cross section data from the transport coefficients

Zoran Lj. Petrović[(*)1,2], Dragana Marić[2], Saša Dujko[2], Gordana Malović[2], Jasmina Atić[2], Ilija Simonović[2], Olivera Šašić[3]

[1] Serbian Academy of Sciences and Arts, 11000 Belgrade Serbia
[2] Institute of Physics University of Belgrade 11080 Zemun, Belgrade Serbia
[3] Faculty of Transport and Traffic Engineering, University of Belgrade, 11000 Belgrade, Serbia
[(*)] zoran@ipb.ac.rs

With an increased interest for specific applications, it is perhaps the right time to revise and update the standard procedure to obtain the cross sections from the measured transport coefficients- the so called swarm procedure. The idea for this presentation is threefold: to repeat and update the well-known procedures associated with the swarm procedure, to present some successes and failures as well as the recent examples of the swarm derived cross section sets for electrons and ions (but also for fast neutrals and positrons) and finally to indicate the issues that may still affect the results both in the interpretation of experimental data and the foundations of the transport theory.

The swarm technique to establish scattering cross section sets from the swarm data has been used for many years. Only with the development of numerical techniques to solve Boltzmann equation has it become very reliable, useful and reproducible technique [1,2,3,4]. The physical basis for using the swarm derived cross sections and the consequently measured or calculated transport coefficients stems from the application of the moments of the Boltzmann equation as the foundation for modelling of the non-equilibrium low-temperature collisional plasmas [4,5].

The swarm derived sets of cross sections provide the following to the plasma models:

- Satisfied balances of number, momentum and energy;
- Representation of the non-equilibrium nature of the discharge based on the local equilibrium between the energy gained from the field and lost in collisions (mainly inelastic);
- Completeness of the cross section set (this will be addressed later);
- Representation of the spatial and temporal relaxation (non-local transport) of the properties of the ensemble and
- Swarm data and rates of processes required to describe the spatial development and temporal development of the plasma and to interpret experiments.

The swarm derived sets are often used indirectly through calculated transport data and rates as a function of either E/N or mean electron energy $< \varepsilon >$ or directly in kinetic schemes (PIC-particle in cell simulation techniques, Monte Carlo plasma models or non-local kinetic sections of the hybrid models). On the other hand, the transport data are used to describe swarm experiments and extract swarm data from the measured quantities [6,7]. Consequently the transport theory and the swarm data have to be presented coherently and with internal consistency which is often not the case. The most important inconsistency is the nature of transport coefficients when non-conservative processes (for electrons attachment and ionization, for ions reactive collisions and for positrons positronium (Ps) formation and annihilation) are present and affect the numbers of particles in a significant way. The most frequent manner in which this multiple nature of transport coefficients is explained is through bulk and flux transport data [4,8]. Versions of both exist for all transport coefficients but most notable is the difference in drift velocities. While it has been mentioned that it is some theoreticians' whimsy of little consequence to most users, it is important to understand that in most experiments bulk properties are being measured while most basic (especially two term) Boltzmann codes provide the flux properties. As differences between the two types of drift velocities may be between several percent and 30% for electrons (under normal conditions) the resulting difference in the cross sections may be quite large. When rates of non-conservative processes are high the difference between the two types of transport coefficients may be even an order of magnitude (as observed for positrons and ions with large reactive collisions and for electrons in gases with excessive thermal attachment [9]).

If carried out properly the swarm procedure leads to cross sections of exceptional accuracy. Still the most accurately determined cross section for electrons is the momentum transfer cross section for

electrons in helium that has been determined independently from both drift velocities and characteristic energies (eD_T/μ) and confirmed later by very accurate theories with an uncertainty of less than 0.5% [10]. It is a common experience that in order to improve the quality of the cross sections, one needs to make very accurate measurements of the well defined transport coefficients.

Usually drift velocities convert to momentum transfer and characteristic energy to overall inelastic losses. Those two sets of experimental data are the foundation of the classical swarm technique. Unfortunately, those are only two independent sets of data. As a result, when number of collisional processes exceeds two, then a non-uniqueness problem may arise. According to this, a contribution of one process may be completely or partly reassigned to another process without a loss of the quality of the fit of the experimental transport coefficients. Quite often swarm practitioners provide only effective inelastic cross sections. While such sets provide a good fit and electron energy distribution function (EEDF) they do not have enough detail to model rates and contributions of specific channels especially for spectroscopy. Another problem is the lack of resolution due to the fact that the effect of sharp features in the cross sections (which are quite frequent) are washed out over a wider energy range due to the width of the distribution function under swarm conditions. Thus, while swarm cross section provides overall contributions to the balances, those may be broadened and may lack salient features of a resonance. Finally, the sensitivity of the measured data to specific channels while projected over a wide range of energies has a limited significance due to the limits set out by the range of mean energies in the original measurements of transport coefficients. One should be aware of the range of the sensitivity, (sometimes tabulations extend up to ten times the limit of reasonable sensitivity based on the transport data).

On the other hand, swarm technique has an advantage of not needing arbitrary callibration techniques to provide absolute values (with, as stated before, all balances taken care of). The first and most natural strategy to improve the quality of the swarm derived sets is to use as much input from other sources as possible. It is best to employ binary collision experiments, but also one has to be aware that a single scaling of numerous channels may not be appropriate. A more coherent first guess would be to use theoretical calculations but, again one may run into problems with some processes while not having issues with the remaining processes. A typical example of this is the so called 'hydrogen problem' [11] where the swarm derived cross sections for momentum transfer and rotational excitation for parahydrogen [3] are in excellent agreement with the theory while there is a discrepancy for vibrational excitation that goes beyond the experimental uncertainties.

The second strategy would be to extend the range of the available experimental data. While longitudinal diffusion does not add much independent information to that provided by the drift velocity excitation rates for numerous inelastic processes do and it has been the strategy employed by Art Phelps in numerous cases [12].

The third strategy is to employ mixtures as a way to provide independent sets of data or data covering an extended range of energies. The basic technique would be to add a very small amount of attaching gas to a non-attaching buffer gas (typically either nitrogen to cover lower energies or argon to cover higher energies) [13]. Under such conditions one may use unperturbed EEDFs for pure nitrogen and argon and thus derive almost directly the attachment cross section (even automated procedures have been developed). Mixture techniques have also been used to reduce the mean energy in rare gases such as argon without having to go to high pressures where multiple collisions may take place [14]. Another example was to use helium hydrogen mixtures to provide independent data to test the vibrational excitation of hydrogen (from drift velocities only) [15]. In general, mixture technique has been applied in a wide range of gases and it allowed the use of better defined transport coefficients over a wider energy range than available in the pure gas [16].

A special case of swarm analysis had to be devised in order to cover moderate energies (tens of eV) as usually swarm experiments do not function well beyond 2-3 eV. At such mean energies one may

measure ionization rates and not other transport data. Petrović et al [4,17] have been promoting a technique to use fits to ionization rates by setting the vibrational and electronic excitation to the best available data from the combination of the swarm and binary collision techniques. Then, assuming that the ionization cross section has been measured accurately, as it almost always is, one would fit the ionization rates by modifying the least known excitation process which is normally dissociation to the ground state. Elastic scattering at those energies is of lesser importance, so extrapolation based on measurements and calculations is sufficiently accurate. Low energy cross sections should be set to fit accurately the drift velocities and characteristic energies.

Extending the energy range even further would require fitting non-hydrodynamic steady state Townsend (SST) discharges at high and very high *E/N*. Under those conditions one may run into a situation where fast neutrals produce most of the excitation, so fitting the spatial emission profiles may yield fast neutral cross sections [18,19].

Term 'kinetic phenomena' has been coined to describe behaviour of transport coefficients under conditions where we may affect the EEDF and thus the behaviour of the ensemble [4]. Such phenomena cannot be described easily based on the cross sections or individual processes, full kinetic treatment is required. There may be two groups of such phenomena, those that occur under fully hydrodynamic conditions such as anisotropic diffusion, negative differential conductivity (NDC) and more. Some of those such as NDC have been used to determine the dominant inelastic cross section in mixtures where the main buffer gas has a Ramsauer Townsend minimum. On the other hand, even measurements of experimental observables under conditions where hydrodynamic expansion is not applicable (non-local) if modelled by a full kinetic technique could provide excellent cross section data (especially at higher energies). Those include Holst Oosterhuis effects (related to Franck Hertz experiment, but observed through optical emission), runaway phenomena and temporal relaxations.

Recently, databases have been developed to disseminate the swarm derived cross sections the most successful being the LxCat [20]. The problem with this was usually that most sets that were provided overlapped a lot and their basis originated from the sets of Phelps or Crompton, so it was difficult to understand the differences. Practice to provide more detailed information on the cross section sets has been introduced and users are warned to seek the original sources rather than use the 'black box approach' but that is yet to become a common practice. In addition, some guidance on the range of sensitivity defined by the original set of transport data is lacking (even in the original sources).

Additional issues include that of benchmarking of the numerical techniques to solve the Boltzmann equation or perform Monte Carlo Simulations (MCS) [21]. Those are not often performed by the new codes and a set of benchmarks needs to be devised for the plasma models as well. In its limit plasma models should satisfy all swarm benchmarks before one starts thinking about the space charge effects. The use of two term theory (TTT) is quite common and it provides a reasonably good data in most cases especially for the drift velocity. Another important aspect is that once you have used TTT to obtain the cross sections subsequent use of TTT will provide good transport data as the basis of modelling but one should be aware of that. Still it is better to have the full accuracy [22] available for the MCS and particle in Cell Monte Carlo collision (PIC MCC) codes.

New avenues that may be used to provide more information on cross sections are to use ExB field measurements of the drift velocities, in particular angle of effective drift $tan(\alpha)=W_{ExB}/W_E$, that may provide more sensitivity than the use of D_T/μ [23] and the application of the higher order transport coefficients that are yet to be measured accurately but there is a solid theoretical foundation [24].

Finally a word of warning has been issued regarding the highly non-conservative processes. Most codes assume that particles are not lost and continue to provide EEDF as if the ensemble is fully populated. In reality, the depletion will occur at some energies and the mean energy would be strongly affected [9]. Thus, one has to make a full kinetic modelling of the transport.

When it comes to the ions the data have been usually provided in terms of interaction potentials but the need to model plasmas has prompted the use of cross sections to describe the transport of ions [25]. Ion transport shows all the same effects as electron except that due to similar masses, the energy exchange in elastic processes is significant. TTT is thus never valid for ions, even if ions undergo only elastic collisions with neutral molecules. Furthermore, ions may show very strong non-conservative effects. Finally, it is worth noting that a similar work on cross section data and associated transport data has been initiated for positrons [26,27].

References

[1] A.V. Phelps *Rev. Mod. Phys.* **40** (1968) 399

[2] R. W. Crompton Advances *In Atomic, Molecular, and Optical Physics Elsevier*, **33** (1994) 97-148

[3] R. W. Crompton, D. K. Gibson and A. I. McIntosh *Aust. J. Phys.* **22** (1969) 715.

[4] Z Lj Petrović, S Dujko, D Marić, G Malović, Ž Nikitović, O Šašić, J Jovanović, V Stojanović and M Radmilović-Radenović, *J. Phys. D: Appl. Phys*. **42** (2009) 194002.

[5] D. Bošnjaković, Z. Lj Petrović and S. Dujko *J. Phys. D: Appl. Phys.* **49** (2016) 405201

[6] H Tagashira, Y Sakai and S Sakamoto *J. Phys. D: Appl. Phys.* **10** (1977) 1051

[7] L. G. H. Huxley and R. W. Crompton "The drift and diffusion of electrons in gases" Wiley Interscience New York (1974)

[8] R. E. Robson *Aust. J. Phys.* **44** (1991) 685

[9] J Mirić, D Bošnjaković, I Simonović, Z Lj Petrović and S Dujko, *Plasma Sources Sci. Technol*. **25** (2016) 065010

[10] R. K. Nesbet *Phys. Rev*. A **20** (1979) 58

[11] M.A. Morrison, R.W. Crompton, B. C. Saha and Z.Lj. Petrović, *Aust. J. Phys*. **40** (1987) 239.

[12] K. Tachibana A.V. Phelps *J.Chem. Phys*. **71** (1979) 3544

[13] S.R. Hunter, L.G. Christophorou, D.L. McCorkle, I sauers, H.W. Ellis, D.R. James *J. Phys. D* **16** (1983) 573

[14] Z.Lj. Petrović, T.F. O'Malley and R.W. Crompton, *J.Phys. B* **28** (1995) 3309

[15] Z.Lj. Petrović and R.W. Crompton, *Aust. J. Phys*. **40** (1987) 347

[16] G.N. Haddad R.W. Crompton, Aust J. Phys 33 (1980) 975

[17] Olivera Šašić, Snježana Dupljanin, Jaime de Urquijo and Zoran Lj Petrović, *J. Phys. D: Appl. Phys.* **46** (2013) 325201

[18] Z.Lj. Petrović and A.V. Phelps, *Phys. Rev. E* **80** (2009) 016408

[19] V.D.Stojanović, B.M. Jelenković and Z.Lj.Petrović, *J.Appl.Phys.* **81** (1997) 1601

[20] L C Pitchford, L L Alves, K Bartschat, S F Biagi, M C Bordage, A V Phelps, C M Ferreira, G J M Hagelaar, W L Morgan, S Pancheshnyi, V Puech, A Stauffer and O Zatsarinny, *J. Phys. D: Appl. Phys.* **46** (2013) 334001

[21] Z.M. Raspopović S. Sakadžić S. Bzenić and Z.Lj. Petrović, *IEEE Trans. Plasma Sci.* **27** (1999) 1241-1248

[22] R.D. White R.E. Robson B. Schmidt and M.A Morrison, J. Phys. D: Appl. Phys. 36 3125 (2003)

[23] B. Schmidt, J. Phys. B 24 (1991) 4809

[24] Z Lj Petrović, I Simonović, S Marjanović, D Bošnjaković, D Marić, G Malović and S Dujko *Plasma Phys. Control. Fusion* **59** (2017) 014026

[25] Z.Lj. Petrović, Z.M. Raspopović, V.D. Stojanović, J.V. Jovanović, G. Malović, T. Makabe, J. de Urquijo, *Applied Surface Science* **253** (2007) 6619–6640

[26] M Charlton, *J. Phys. Conference Series,* **162** (2009) 012003

[27] A Banković, S Dujko, R D White, J P Marler, S J Buckman, S Marjanović, G Malović, G Garcıa and Z Lj Petrović, *New Journal of Physics* **14** (2012) 035003

28th Summer School and International Symposium on the Physics of Ionized Gases

Aug. 29 - Sep. 2, 2016, Belgrade, Serbia

CONTRIBUTED PAPERS

&

ABSTRACTS OF INVITED LECTURES, TOPICAL INVITED LECTURES, PROGRESS REPORTS AND WORKSHOP LECTURES

Editors:
Dragana Marić, Aleksandar Milosavljević,
Bratislav Obradović and Goran Poparić

University of Belgrade,
Faculty of Physics

Serbian Academy
of Sciences and Arts

CONTRIBUTED PAPERS & ABSTRACTS OF INVITED LECTURES, TOPICAL INVITED LECTURES, PROGRESS REPORTS AND WORKSHOP LECTURES

of the 28th Summer School and International Symposium on the Physics of Ionized Gases

August 29 – September 2, 2016, Belgrade, Serbia

MONTE CARLO SIMULATIONS OF ELECTRON TRANSPORT IN CF$_3$I AND SF$_6$ GASES

J. Mirić, D. Bošnjaković, I. Simonović, Z. Lj. Petrović and S. Dujko

Institute of Physics, University of Belgrade,
Pregrevica 118, 11080 Belgrade, Serbia

Abstract. Electron transport coefficients in CF$_3$I and SF$_6$ gases are calculated using Monte Carlo simulations for a wide range of reduced electric field strengths. In order to compensate for the loss of electrons in simulation due to strong attachment, three different rescaling techniques are considered and applied. Among many observed phenomena, in case of SF$_6$ we highlight the reduction of mean electron energy with increasing electric field. In addition, we observe that for both gases bulk drift velocities exhibit negative differential conductivity which is not present in the flux drift velocity.

1. INTRODUCTION

Electron attachment in strongly electronegative gases, such as CF$_3$I and SF$_6$, has many industrial applications. For example, in high-voltage circuit breakers, it is the most significant process for the prevention of electric breakdown [1]. Electronegative gases are also used for plasma etching and cleaning in semiconductor fabrication [2].

On the other hand, electron attachment imposes practical difficulties in experiments for measurement of transport coefficients [1,3]. Considerable difficulties also appear in Monte Carlo simulations of electron transport in strongly electronegative gases at low electric fields where electron attachment is the dominant process. Due to this process, the number of electrons in a simulation can reach extremely low values leading to poor statistics or complete loss of electrons in the simulation [4,5]. In order to compensate for this loss of electrons, some sort of rescaling techniques must be used.

In this work, we discuss the existing rescaling techniques for Monte Carlo simulations of electron transport in strongly electronegative gases. Furthermore, we introduce our modified rescaling procedure and demonstrate how these techniques affect the calculated transport data for CF$_3$I and SF$_6$ gases.

2. RESCALING TECHNIQUES

The following rescaling techniques, applicable for Monte Carlo simulations, can be found in the literature:

1. Duplication of electrons randomly chosen from the remaining swarm at certain discrete time steps [6];
2. Duplication of the entire electron swarm (one or more times) at certain time steps [5] or at certain distance steps [7];
3. Introduction of an additional fictitious ionization [4] or attachment process [8] with a constant collision frequency.

An unaltered electron distribution function and its evolution are a common objective for all these techniques. In this work, the first technique will be referred to as discrete rescaling, the second as swarm duplication and the third as continuous rescaling. However, we introduce a modification to the third procedure where the fictitious ionization process is dynamically adjusted during the simulation in such way that the fictitious ionization rate is chosen to be equal to the attachment rate. Therefore, it is not necessary to define a fictitious ionization rate in advance and as a benefit, the number of electrons is kept nearly constant during the simulation.

3. RESULTS

In this section, we present the transport data for CF_3I and SF_6 gases, calculated using our Monte Carlo code [6,9] with three different rescaling techniques. The cross section set for electron scattering in SF_6 is taken from Itoh *et al.* [10]. In case of CF_3I, we use our modified cross section set [11] which is based on cross sections of Kimura and Nakamura [12]. This modification of the CF_3I set was necessary in order to provide a better agreement between the calculated data and the reference data measured in a pulsed Townsend experiment for pure CF_3I and its mixtures with Ar and CO_2.

Figure 1(a) shows the variation of mean electron energy with E/n_0 in CF_3I. Calculations are performed assuming the three rescaling techniques. Excellent agreement between the cases of discrete rescaling and swarm duplication can be understood, having in mind that these two techniques are essentially the same. The only difference between the two is the fact that in case of discrete rescaling, the probability for duplication of an electron is determined by the ratio of current number and desired number of electrons, while in case of swarm duplication technique, this probability is set to unity i.e. the duplication is performed for all electrons. Continuous rescaling is also in a good agreement with the other two techniques.

In case of mean electron energy for the SF_6 gas, Figure 1(b) shows excellent agreement between the three rescaling techniques. Furthermore, one anomalous behavior is observed — a decrease of mean energy with increasing electric field. This phenomenon is associated with mutual influence of attachment heating and inelastic cooling. Since it is observed only in case of SF_6,
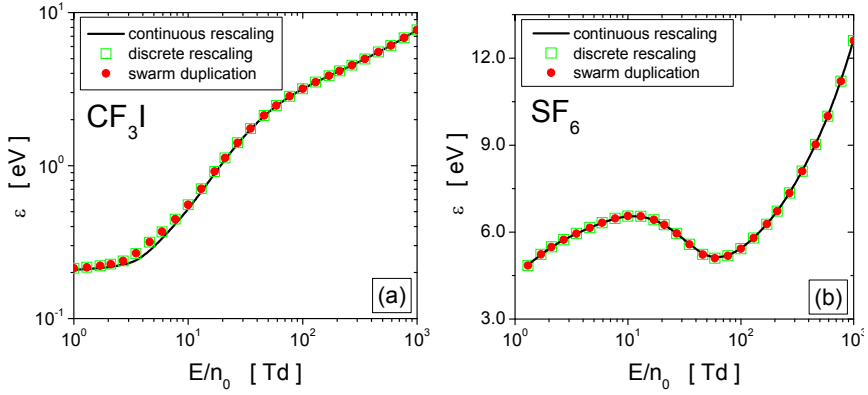
Figure 1. Mean electron energy in (a) CF_3I and (b) SF_6 gases as a function of reduced electric field. The profiles are calculated using three different rescaling techniques.

it is evident that the specific cross sections for electron scattering are essentially responsible for the occurrence of this phenomenon.

Figure 2 shows flux and bulk drift velocities in (a) CF_3I and (b) SF_6 gases, obtained with three rescaling techniques. For electrons in CF_3I, the drift velocities calculated using discrete rescaling and swarm duplication are again in excellent agreement while continuous rescaling at low electric fields gives slightly lower values than the other two techniques. For drift velocities in the SF_6 gas, all three rescaling techniques are in good agreement over the entire range of reduced electric fields considered in this work. We can conclude that the nature of the cross sections for electron scattering in CF_3I and SF_6 and their energy dependence are responsible for the differences between the results obtained using different rescaling techniques.

Two interesting phenomena are also observed in Figure 2. First, for
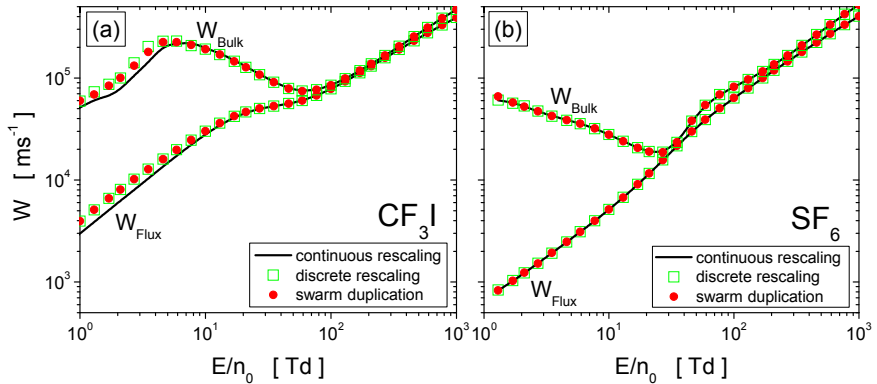
Figure 2. Variation of the drift velocity with E/n_0 for electrons in (a) CF_3I and (b) SF_6 gases. The profiles are calculated using three different rescaling techniques.

both gases the bulk drift velocity is higher than the flux drift velocity. In low energy range, this is a consequence of strong attachment heating (the consumption of slow electrons due to attachment) while in higher energy range the explicit effect of ionization is responsible. As a result, new electrons are preferentially created at the front of the swarm and/or slow electrons are consumed at the back of the swarm resulting in a forward shift of centre of mass of the swarm which is observed as an increase of bulk drift velocity over the flux drift velocity. The other phenomenon is a very strong NDC effect (negative differential conductivity) which is noticed for both gases, but only in case of bulk component drift velocity. This behavior appears to be common for all strongly electronegative gases since it is induced by explicit effects of electron attachment.

Acknowledgements

REFERENCES

[1] L. G. Christophorou and J. K. Olthoff, *Fundamental electron interactions with plasma processing gases*, (Springer, New York, 2004).
[2] T. Makabe and Z. Lj. Petrović, *Plasma Electronics: Applications in Microelectronic Device Fabrication*, (CRC Press, New York, 2014).
[3] Z. Lj. Petrović *et al.*, J. Phys. D: Appl. Phys. 42, 194002 (2009).
[4] M. Yousfi, A. Hennad and A. Alkaa, Phys. Rev. E 49, 3264 (1994).
[5] A. M. Nolan, M. J. Brennan, K. F. Ness and A. B. Wedding, J. Phys. D 30, 2865 (1997).
[6] Z. M. Raspopović, S. Sakadžić, S. Bzenić and Z. Lj. Petrović*,* IEEE Trans. Plasma Sci. 27, 1241 (1999).
[7] N. A. Dyatko and A. P. Napartovich, J. Phys. D 32, 3169 (1999).
[8] Y. M. Li, L. C. Pitchford and T. J. Moratz, Appl. Phys. Lett. 54, 1403 (1989).
[9] S. Dujko, R. D. White and Z. Lj. Petrović, J. Phys. D: Appl. Phys. 41, 245205 (2008).
[10] H. Itoh, T. Matsumura, K. Satoh, H. Dane, Y. Nakano and H. Tagashira, J. Phys. D 26, 1975 (1993).
[11] J. Mirić, O. Šašić, S. Dujko and Z. Lj. Petrović, Proc. 27th Summer School and International Symposium on the Physics of Ionized Gases (Belgrade) 2014, p. 122.
[12] M. Kimura and Y. Nakamura, J. Phys. D 43, 145202 (2010).

28th Summer School and International Symposium on the Physics of Ionized Gases

Aug. 29 - Sep. 2, 2016, Belgrade, Serbia

CONTRIBUTED PAPERS

&

ABSTRACTS OF INVITED LECTURES, TOPICAL INVITED LECTURES, PROGRESS REPORTS AND WORKSHOP LECTURES

Editors:

Dragana Marić, Aleksandar Milosavljević,
Bratislav Obradović and Goran Poparić

University of Belgrade,
Faculty of Physics

Serbian Academy
of Sciences and Arts

CONTRIBUTED PAPERS & ABSTRACTS OF INVITED LECTURES, TOPICAL INVITED LECTURES, PROGRESS REPORTS AND WORKSHOP LECTURES

of the 28th Summer School and International Symposium on the Physics of Ionized Gases

August 29 – September 2, 2016, Belgrade, Serbia

ELECTRON TRANSPORT IN MERCURY VAPOR: DIMER INDUCED NDC AND ANALYSIS OF TRANSPORT PHENOMENA IN ELECTRIC AND MAGNETIC FIELDS

J. Mirić, I. Simonović, D. Bošnjaković, Z. Lj. Petrović and S. Dujko

Institute of Physics, University of Belgrade,
Pregrevica 118, 11080 Belgrade, Serbia

Abstract. Transport coefficients for electron swarms in mercury vapor in the presence of electric and magnetic fields are calculated and analyzed using a multi term theory for solving the Boltzmann equation and Monte Carlo simulation technique. Particular attention is paid to the occurrence of negative differential conductivity (NDC) at higher gas pressures and temperatures. It is shown that the correct representation of the presence of mercury dimers and superelastic collisions plays a key role in the analysis of NDC. When both the electric and magnetic fields are present, another phenomenon arises: for certain values of electric and magnetic field, we find regions where swarm mean energy increases with increasing magnetic field for a fixed electric field. Spatially-resolved electron transport properties are calculated using a Monte Carlo simulation technique in order to understand these phenomena.

1. INTRODUCTION

In this work we discuss the transport of electrons in mercury vapor and its mixtures with argon under conditions relevant for metal vapor lamps. Current models of such lamps require knowledge of transport coefficients as a function of electric field strengths, gas pressures and temperatures. Recently developed inductively coupled plasma light sources require the knowledge of transport coefficients when both the electric and magnetic fields are present and crossed at arbitrary angles [1]. These transport coefficients can be either measured in swarm experiments or calculated from transport theory. To date, no experiments exist that can measure all the required transport coefficients, including rate coefficients, drift velocities, and diffusion coefficients for electrons in gases in the presence of electric and magnetic fields.

In the present work we solve the Boltzmann equation for electron swarms undergoing ionization in mercury vapor and its mixtures with argon in the presence of electric and magnetic fields crossed at arbitrary angles. For the *E*-only case we discuss the occurrence of negative differential conductivity (NDC) for

higher gas pressures and temperatures in the limit of lower electric fields. NDC is a phenomenon where the drift velocity decreases with increasing electric field. For electrons in mercury vapor this behavior of the drift velocity is attributed to the presence of mercury dimers.

In the second part of this work we investigate the electron transport in varying configurations of electric and magnetic fields. In particular, we discuss the following phenomenon: for certain values of electric and magnetic fields, we find regions where swarm mean energy increases with increasing magnetic field for a fixed electric field. The phenomenon is discussed using spatially-resolved transport data calculated in Monte Carlo simulations.

2. CROSS SECTIONS AND SIMULATION TECHNIQUES

The cross section for momentum transfer in elastic collisions is made as follows. For lower electron energies, we use a cross section from [2] while for higher energies, we use a cross section tabulated in MAGBOLTZ code [3]. Cross sections for electronic excitations for levels $^3P_0$, $^3P_1$ and $^3P_2$ are retrieved from [4] while electronic excitations to $^1S_0$ and $^1P_1$ states as well as a cross section for higher states are also taken from MAGBOLTZ code. For electron-impact ionization, we have used a cross section from [5]. The effective cross section which describes vibration and electronic excitations of mercury dimers is derived using the experimental measurements of Elford [6]. Cross sections were slightly modified during the calculations to improve agreement between the calculated swarm parameters and the experimental values [6].

Electron transport coefficients are calculated from the multi term solution of Boltzmann's equation. A Monte Carlo simulation technique is used to verify the Boltzmann equation results and also for the calculations of spatially-resolved transport data.

3. RESULTS AND DISCUSSIONS

In Figure 1 (a) we show the variation of the drift velocity with E/n_0 for a range of gas pressures, as indicated on the graph. Calculations are performed in a wide range of pressures, from 20.2 to 108.4 Torr. The temperature of the background gas is 573K. The same range of pressures and temperatures was considered by Elford in his experiments [6]. We extend his measurements by considering the drift of electrons for six additional gas pressures. For E/n_0 less than approximately 2.5 Td the pressure dependence of the drift velocity is clearly evident. For higher E/n_0, however, the drift velocity does not depend on the pressure. For pressures higher than approximately 200 Torr, we see that the drift velocity exhibits a region of NDC, i.e. over a range of E/n_0 values the drift velocity decreases as the driving field is increased. The conditions for the occurrence of NDC have been investigated previously [7]. For electrons in mercury vapor, NDC arises for certain combinations of elastic cross sections of dimer-free mercury vapor and inelastic cross sections of mercury dimers in

which, on increasing the electric field, there is a rapid transition in the dominant energy loss mechanism from inelastic to elastic. For pressures lower than 200 Torr the elastic cross section of dimer-free mercury vapor dominates the effective inelastic cross section of mercury dimers. Thus, the conditions for the occurrence of NDC are not set. For higher pressures, the phenomenon is promoted by either or both of (i) a rapidly increasing cross section for elastic collisions and (ii) a rapidly decreasing inelastic cross section. It is clear that the presence of dimmers plays a key role in the development of NDC in mercury vapor.

        In Figure 1 (b) we show a comparison between our calculations and experimental measurements of the drift velocity for a range of pressures. Our Monte Carlo results (figure 1 (b)) agree very well with those measured in the Bradbury-Nielsen time-of-flight experiment [6]. The agreement is achieved only after careful implementation of superelastic collisions in our calculations. Cross sections for superelastic collisions are calculated directly in our code from the principle of detailed balance.
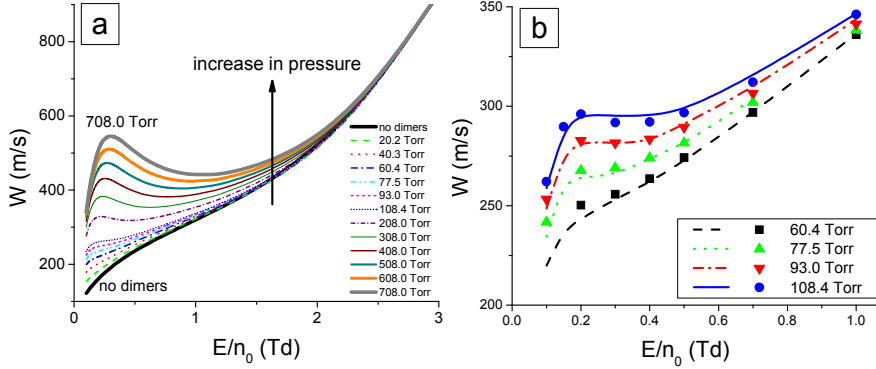
Figure 1. Variation of the drift velocity with E/n_0 for a range of pressures (a) and comparison between our Monte Carlo results and experimental measurements. Calculations are performed for electrons in mercury vapor. The temperature of the background gas is 573K.

        In the last segment of this work we discuss the impact of a magnetic field on the electron transport in mercury vapor. The pressure and temperature of the mercury vapor are set to 1 Torr and 293K, respectively. As an example of our study, in figure 2 we show the variation of the mean energy with E/n_0 for a range of the reduced magnetic fields B/n_0, in a crossed field configuration. In the limit of the lowest E/n_0 the electrons are essentially in the quasi-thermal equilibrium with the mercury vapor, independent of the strength of the applied magnetic field. In this regime, the longitudinal and transverse drift velocity components are dependent on both E/n_0 and B/n_0 while the diagonal diffusion tensor elements along the **E** and **E**×**B** directions are dependent on B/n_0 only. The diffusion coefficient along the magnetic field direction is reduced to its thermal value as magnetic field only affects the diffusion in this direction indirectly, through the magnetic field's action to cool the swarm. Certainly one of the most striking

properties observed in the profiles of transport coefficients is an increase in the swarm mean energy with increasing magnetic field for a fixed electric field. The phenomenon is evident in the range E/n_0=5-200 Td for B/n_0 considered in this work. This behavior is contrary to previous experiences in swarm physics as one would expect the mean swarm energy to decrease with increasing B/n_0 for a fixed E/n_0. The phenomenon could be associated with the interplay between magnetic field cooling and inelastic/ionization cooling, although the role of the cross sections in both phenomena is of course vital. The electron energy distribution function and spatially-resolved mean energy, rate coefficients and other properties are calculated using a Monte Carlo simulation technique in order to explain this phenomenon.
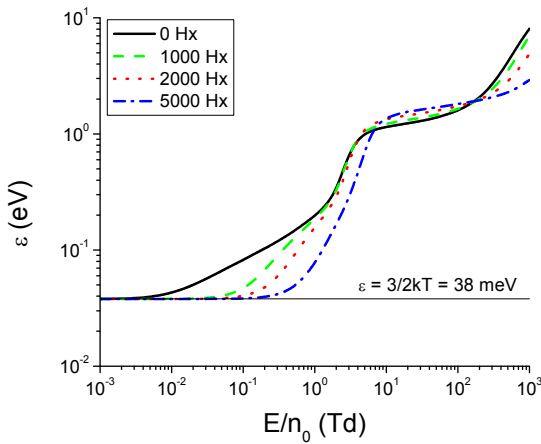
Figure 2. Variation of the mean energy with E/n_0 for a range of B/n_0. Calculations are performed for electrons in mercury vapor.

Acknowledgements

REFERENCES

[1] G.G. Lister, J.E. Lawler, W.P. Lapatovich and V.A. Godyak, Rev. Mod. Phys. 76, 541 (2004)
[2] J. P. England and M. T. Elford, Aust. J. Phys. 44, 647 (1991)
[3] http://magboltz.web.cern.ch/magboltz
[4] K. Bartschat, 3rd Int. Conf. on Atomic and Molecular Data and their Applications (New York: American Institute of Physics), 2003
[5] L. J. Kieffer and G. H. Dunn, *Rev.* Mod. Phys. 38, 1 (1966)
[6] M. T. Elford, Aust. J. Phys. 33, 231 (1980)
[7] S.B. Vrhovac and Z.Lj. Petrovič, Phys. Rev. E 53, 4012 (1996)

27th Summer School and International Symposium on the Physics of Ionized Gases

August 26-29, 2014, Belgrade, Serbia

CONTRIBUTED PAPERS

&

ABSTRACTS OF INVITED LECTURES, TOPICAL INVITED LECTURES, PROGRESS REPORTS AND WORKSHOP LECTURES

Editors:
Dragana Marić
Aleksandar R. Milosavljević
Zoran Mijatović

Institute of Physics, Belgrade
University of Belgrade

Serbian Academy
of Sciences and Arts

www.spig2014.ipb.ac.rs

CONTRIBUTED PAPERS & ABSTRACTS OF INVITED LECTURES, TOPICAL INVITED LECTURES, PROGRESS REPORTS AND WORKSHOP LECTURES
of the 27th Summer School and International Symposium on the Physics of Ionized Gases

August 26 – 29, 2014, Belgrade, Serbia

Section 2. PARTICLE AND LASER BEAM INTERACTION WITH SOLIDS

Invited Lectures

SCATTERING CROSS SECTIONS AND TRANSPORT COEFFICIENTS FOR ELECTRONS IN CF$_3$I

J. Mirić[1], O. Šašić[1,2], S. Dujko[1] and Z.Lj. Petrović[1]

[1]*Institute of Physics, University of Belgrade, Pregrevica 118, 11080 Belgrade, Serbia*
[2]*Faculty of Transport and Traffic Engineering, University of Belgrade, Vojvode Stepe 305, 11000, Belgrade, Serbia*

Abstract. Scattering cross sections for electrons in CF$_3$I are discussed using the swarm method. Electron drift velocity, effective ionization coefficient and diffusion coefficients are calculated using a Monte Carlo simulation technique and from solution of the non-conservative Boltzmann equation. Calculated data for pure CF$_3$I and its mixtures with rare gases, N$_2$ and SF$_6$ are compared with those measured experimentally under both the time-of-flight and pulsed-Townsend conditions. Among many important phenomena observed in electron transport we note the existence of negative differential conductivity in the profile of the bulk drift velocity with no signs of the same phenomenon in the profile of flux drift velocity.

1. INTRODUCTION

Trifluoroiodomethane (CF$_3$I) is a processing gas employed for plasma etching of various materials. Due to its short atmospheric lifetime (1.8 days), low GWP (0.4 times than of CO$_2$) and high critical electric field (437 Td) CF$_3$I shows a promise for application as an alternative refrigerant to commonly used fluorocarbons such as CF$_4$ [1], and as a potential high voltage insulator, both on its own and mixed with N$_2$ and CO$_2$ in high-voltage insulation technology [2]. In spite of these important applications of CF$_3$I, still there is a lack of reliable sets of cross sections for electron scattering and associated electron transport coefficients.

In this work we discuss the existing sets of cross sections for electron scattering in CF$_3$I. Using the swarm method, our initial set of cross sections is constructed from other available sets, and data for individual scattering channels. Calculated transport data are then compared with those measured in experiments and if the agreement is not enough, then cross sections are modified. This process is repeated until some preset agreement between theoretically calculated and experimentally measured data is achieved. Increasing the accuracy of the set of

cross sections, the electron transport is investigated using the multi term approach for solving the Boltzmann equation where particular emphasis was placed upon the explicit effects of non-conservative collisions on the drift and diffusion.

2. CROSS SECTIONS FOR ELECTRON SCATTERING IN CF$_3$I

The initial set of cross sections in this work was developed by Kimura and Nakamura [3], and is presented by solid curves in Figure 1. Due to disagreement between experimentally measured swarm data and those obtained in theoretical calculations, we have concluded that there are some internal inconsistencies in the set proposed by Kimura and Nakamura. Similar conclusions have been recently found by Kawaguchi *et al.* [4].
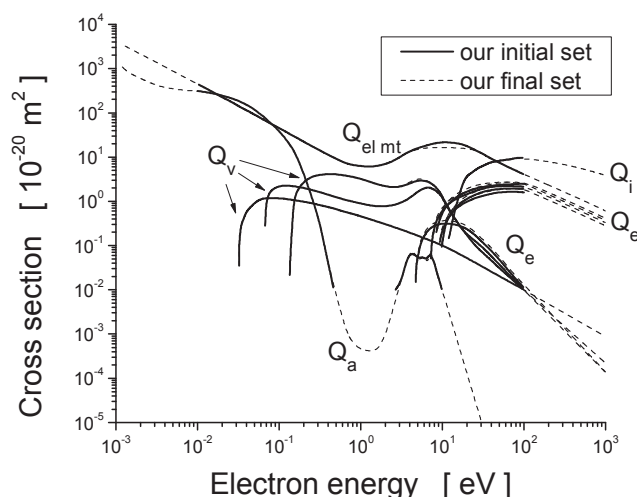
Figure 1. Cross sections for electron scattering in CF$_3$I from Kimura and Nakamura (solid curves) [3] and from our work (broken curves).

In this work the cross sections were extended in energy up to 1000 eV so that calculated data may cover the region between a few Td and few thousands of Td. This is of great importance having in mind the high critical field of CF$_3$I. The logarithmic extrapolation was used for electronic excitation with the lowest threshold and for all vibrational excitations as well as for the electron attachment. The Born-Bethe approximation was used to extrapolate the cross sections for momentum transfer in elastic collisions and for the cross sections for electronic excitation. The cross section for ionization was modified as follows: in the energy range up to 45 eV we have used the cross section from [3] while for higher energies than 45 eV we have included the theoretically calculated cross section developed by Anthony *et al.* [5]. Using the data

suggested by Christophorou [6], the cross section for attachment between 0.5 and 3 eV was reconstructed.

Cross section for momentum transfer in elastic collisions in the energy region between 4 and 20 eV was modified together with the cross section for vibrational excitation with the highest threshold in order to fit the drift velocity from experimental measurements of Kimura and Nakamura [3]. The ionization coefficient was fitted through the modification of cross sections for electronic excitations having in mind the large uncertainties associated with the magnitudes of these cross sections. Our final set of cross sections for electron scattering in CF_3I is shown in Figure 1. This set of cross sections provides much better agreement between theoretically calculated and experimentally measured swarm transport data as discussed below.

3. TRANSPORT COEFFICIENTS FOR ELECTRONS IN CF_3I

In Figure 2 we compare our results for the electron drift velocity with experimental data obtained under the time-of-flight [3] and pulsed-Townsend conditions [2]. The calculated values of W are initially lower than those measured in experiments. After modification of cross sections the calculated values of W are in a good agreement with experimental measurements obtained under the time-of-flight conditions. Our flux drift velocity is calculated by the two-term approximation (TTA) for solving the Boltzmann equation and using a Monte Carlo simulation technique.
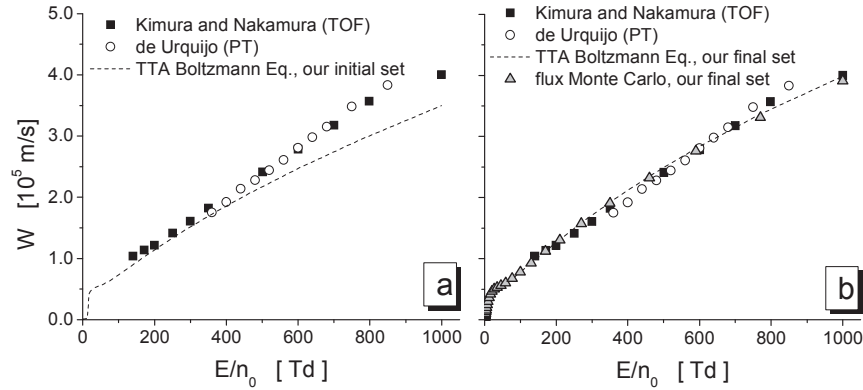
Figure 2. Variation of the drift velocity with E/n_0 for electrons in CF_3I. Our TTA results are compared with those obtained in experiments for (a) our initial set of cross sections and (b) our final set of cross sections.

Figure 3 shows the calculated values of effective ionization coefficient $(\alpha-\eta)/n_0$ using the initial set of cross sections (a) and our final set of cross sections (b). Values of $(\alpha-\eta)/n_0$ measured by Kimura and Nakamura [3] and de

Urquijo *et al.* [2] are also plotted. In Figure 3 (a), calculated values of $(\alpha\text{-}\eta)/n_0$ are higher than the measured data for higher E/n_0. Calculated values using our final set of cross sections agree well with the measured data in a wide range of E/n_0 except for E/n_0 less than approximately 200 Td where the effects of attachment are dominant.
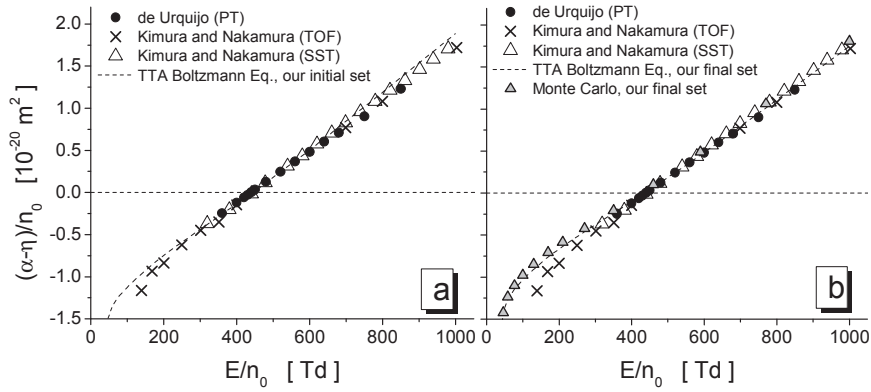
Figure 3. Variation of the effective ionization coefficient with E/n_0 for electrons in CF$_3$I. Our TTA results are compared with those obtained in experiments for (a) our initial set of cross sections and (b) our final set of cross sections.

Other transport properties including diagonal elements of the diffusion tensor, mean energy and rate coefficients are also calculated using a Monte Carlo simulation technique and from multi term solutions of the Boltzmann equation. Bulk values of the drift velocity and diffusion coefficients are evaluated and explicit effects of the electron attachment and/or ionization are examined.

Acknowledgements

REFERENCES

[1] Y.T. Duan, L. Shi, L.Q. Sun, M.S. Zhu and L.Z. Han, Int. J. Thermophys. 21, 393 (2000).

[2] J. de Urquijo, A. M. Juarez, E. Basurto and J. L. Hernandez-Avila, J. Phys. D 40, 2205 (2007).

[3] M. Kimura and Y. Nakamura, J. Phys. D: Appl. Phys. 43, (2010).

[4] S. Kawaguchi, K. Satoh and H. Itoh, Eur. Phys. J. D 68, 100 (2014).

[5] B. K. Antony, K. N. Joshipura and N. J. Mason, J. Phys. B: At. Mol. Opt. Phys 38, 189 (2005).

[6] L. G. Christophorou and J. K. Olthoff, J. Phys. Chem. Ref. Data 29, 553 (2000).

27th Summer School and International Symposium on the Physics of Ionized Gases

CONTRIBUTED PAPERS

&

ABSTRACTS OF INVITED LECTURES, TOPICAL INVITED LECTURES, PROGRESS REPORTS AND WORKSHOP LECTURES

Editors:
Dragana Marić
Aleksandar R. Milosavljević
Zoran Mijatović

Institute of Physics, Belgrade
University of Belgrade

Serbian Academy
of Sciences and Arts

www.spig2014.ipb.ac.rs

CONTRIBUTED PAPERS & ABSTRACTS OF INVITED LECTURES, TOPICAL INVITED LECTURES, PROGRESS REPORTS AND WORKSHOP LECTURES
of the 27th Summer School and International Symposium on the Physics of Ionized Gases

August 26 – 29, 2014, Belgrade, Serbia

Section 2. PARTICLE AND LASER BEAM INTERACTION WITH SOLIDS

Invited Lectures

ELECTRON TRANSPORT IN NOBLE-GAS METAL-VAPOR MIXTURES

J. Mirić[1], Z.Lj. Petrović[1], R.D. White[2] and S. Dujko[1]

[1]*Institute of Physics, University of Belgrade,*
Pregrevica 118, 11080 Belgrade, Serbia
[2]*ARC Centre for Antimatter-Matter studies, James Cook University,*
School of Electrical Engineering and Physical Sciences, 4810 Townsville,
Australia

Abstract. Electron transport coefficients required for the modeling of light sources are calculated from the multi term solution of the non-conservative Boltzmann equation. Calculations are performed over a range of E/n_0 values (ratio of the electric field, E, to the neutral number density n_0), gas temperatures and metal vapor concentrations relevant to lamp discharges. Values and general trends of mean energy, drift velocity, diffusion tensor and rate coefficients are presented in this work.

1. INTRODUCTION

The progress and further improvements of light sources based on low or high pressure electrical gas discharges require the most accurate modeling of charged particle transport processes in noble-gas-metal-vapor mixtures [1]. In particular, modern high intensity discharge lamps are usually filled with noble gas at high pressure (0.1 to 12 bar) and metallic salts. Noble gas provides light during the initial warm-up phase of the operation while metallic salts take over light emission after they have evaporated [2]. Our work has been motivated, in part, by recent suggestions that highly accurate data for transport coefficients required as input in fluid models of lamp discharges may significantly improve the existing models. Current models of such lamps require knowledge of the plasma electrical conductivity, which can be calculated from the cross sections for electron scattering in noble-gas-metal-vapor mixtures and mobility coefficients presented in this work.

In this work we investigate electron transport in mixtures of noble gases (He, Ne, Ar, Kr and Xe) and metal vapors (Na, K, Cs, Mg and Hg)

under swarm conditions using a multi term theory for solving the Boltzmann equation [3]. In section 2, we give a brief discussion of the theoretical multi term solution of the Boltzmann equation under non-conservative conditions while in section 3 we present a few examples of our systematic study of electron transport in noble-gas-metal-vapor mixtures.

2.THEORETICAL METHODS

Electron transport coefficients are determined by solving the non-conservative Boltzmann's equation under the hydrodynamic conditions for electrons drifting and diffusing through the noble-gas-metal-vapor mixtures under the influence of spatially homogeneous electric field. In brief, the solution of Boltzmann's equation is found be expanding the distribution function as sums of products with the directional dependence of c contained in spherical harmonics $Y_l^{(m)}(\hat{c})$ (where c is the electron velocity), the spatial distribution contained in $G_\mu^{(s\lambda)}$, the s-th application of the spatial gradient operator operating on $n(r,t)$, and the speed distribution contained in an expansion discussed below [3]. Thus, we have

$$f(\boldsymbol{r},\boldsymbol{c},t) = \sum_{l=0}^{\infty} \sum_{m=-l}^{l} \sum_{s=0}^{\infty} \sum_{\lambda=0}^{s} \sum_{\mu=-\lambda}^{\lambda} f(lm|s\lambda\mu) Y_l^{(m)}(\hat{c}) G_\mu^{(s\lambda)} n(\boldsymbol{r},t). \quad (1)$$

The coefficients $f(lm|s\lambda\mu)$ are functions of the speed c and are obtained by the expansion

$$f(lm|s\lambda\mu) = \omega(T_b,c) \sum_{\nu=0}^{\infty} F(\nu lm|s\lambda\mu) R_{\nu l}(T_b,c), \quad (2)$$

where $\omega(T_b,c)$ is a Maxwellian distribution at a temperature T_b. T_b is not equal to the neutral gas temperature and serves as an adjustable parameter to optimize the convergence. $R_{\nu l}$ are related to a Sonnine polynomial of order (ν,l) while the coefficients $F(\nu lm|s\lambda\mu)$ are the so-called moments that are relatively simply related to transport coefficients. The classical two term approximation (TTA) for solving the Boltzmann equation covers only the range in l of 0 and 1, which is not sufficient for good accuracy in noble-gas metal-vapors. Using the above decomposition of f (1), the Boltzmann equation is converted to a hierarchy of doubly infinite set of coupled algebraic equations for the moments. The resulting coefficient matrix is sparse and direct numerical inversion procedure is used to calculate the moments.

3.RESULTS AND DISCUSSIONS

The transport coefficients shown below are functions of E/n_0 and are expressed using the unit townsend (1 Td= 10^{-21}Vm^{-1}). In this work

we will cover a range of E/n_0 up to 1000 Td. The temperature of Hg vapor is varied between 0 and 8000 K. The internal states are assumed to be governed by a Maxwell-Boltzmann distribution which essentially places all metal-vapor atoms in the ground state for the temperatures considered. The effects of dimmers are not included. Cross sections for electron scattering in Na, K and Cs are taken from [4] while for Hg and Mg are taken from the Lxcat database [5].

In figure 1 (a) we show the variation of the mean energy with E/n_0 and gas temperature T, for electrons in Hg vapor. For lower E/n_0 the mean energy is different for different gas temperatures and only for $T = 8000$ K the electrons are in thermal equilibrium with the Hg vapor. This means that the electron velocity distribution is approximately thermal-Maxwellian. For increasing E/n_0 the effects of the gas temperature are less pronounced; the electron velocity distribution is non-equilibrium and non-Maxwellian though transport properties are still dependent on T. In the limit of higher E/n_0, the electron swarm is far from thermal-equilibrium and the influence of the Hg vapor temperature can be neglected.
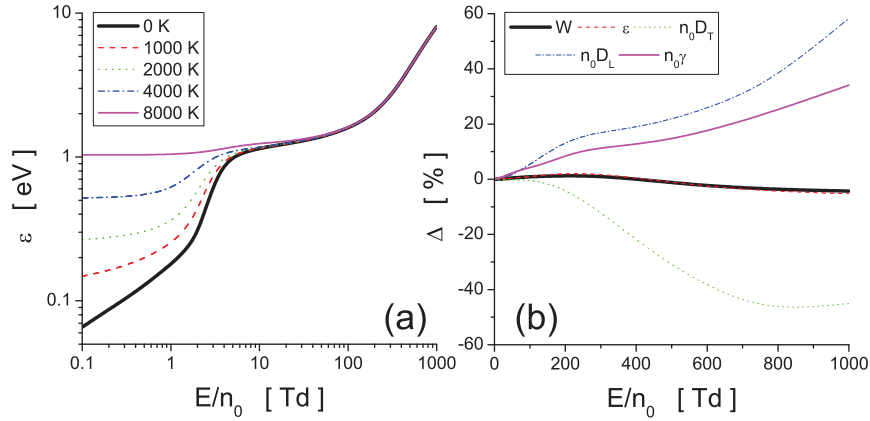
Figure 1. (a) Variation of the mean energy with E/n_0 and gas temperature T for electrons in Hg vapor. (b) Percentage difference between the two term and multi term results for various transport properties. The gas temperature is set to 293 K.

In figure 1 (b) we illustrate the errors associated with the TTA for solving the Boltzmann equation for electrons in Hg vapor. We observe that increasing E/n_0 deteriorates the accuracy of the TTA. For the chosen set of conditions, the mean energy and drift velocity have the errors of the order of 5% while the errors of the diffusion coefficients are much higher and are of the order of 50 %.

Figure 2 (a) shows the variation of the mean energy and drift ve-

locity with E/n_0 for electrons in various metal-vapors. For lower E/n_0, we observe that the electrons are in thermal-equilibrium only with the K-vapor. The properties of the cross sections are reflected in the profiles of the mean energies. When elastic collisions are dominant, the mean energy grows very fast. Much slower rise of the mean energy is a consequence of the large energy loss of the electrons as the inelastic channels become important. Except for very low E/n_0 the mean energy in Hg vapor dominates the mean energies of electrons in other vapors.

From figure 2 (b) we see that for $E/n_0 \geq 6$ Td the drift velocity in Hg vapor dominates the drift velocities of electrons in other vapors. This suggests that plasma electrical conductivity will be the highest for Hg vapor.
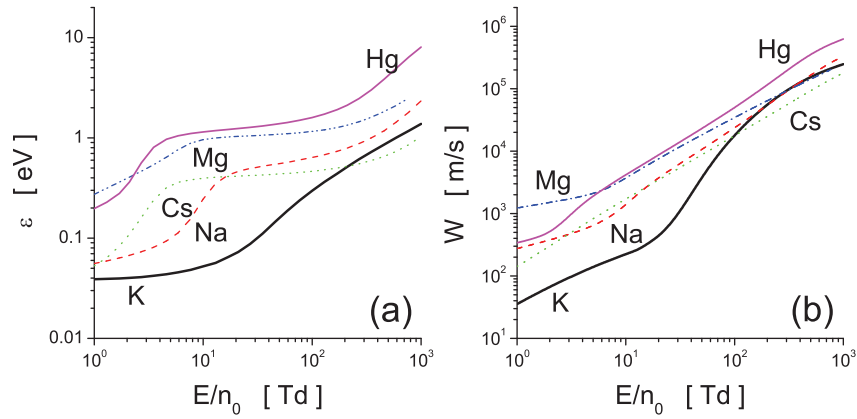
Figure 2. Variation of the mean energy (a) and drift velocity (b) with E/n_0 for electrons in metal-vapors. The gas temperature is $T = 298$ K.

REFERENCES

[1]   G.G. Lister, J.E. Lawler, W.P. Lapatovich and V.A. Godyak, Rev. Mod. Phys. 76 541 (2004)

[2]   A. Sobota, F. Manders, E.M. van Veldhuizen, J. van Dijk, and M. Haverlag, IEEE Trans. Plasma Sci. 38, 2289 (2010).

[3]   S. Dujko, R.D. White, Z.Lj. Petrović and R.E. Robson, Phys. Rev. E 81, 046403 (2010).

[4]   Al-Amin S A J, Lucas J, J. Phys. D: Appl. Phys. 21, 1261 (1988).

[5]   http://fr.lxcat.net/home/
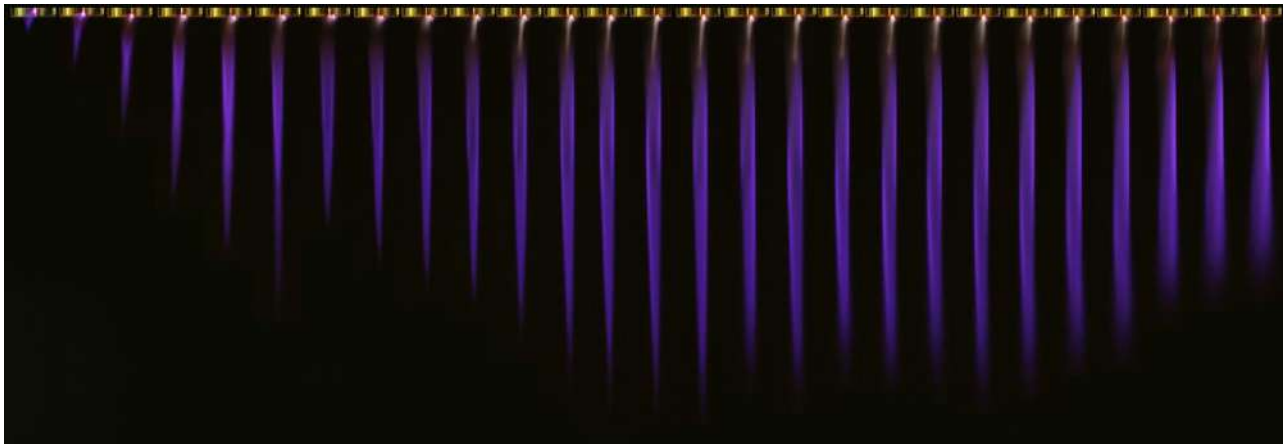
JSPP2014
COST MP1101 WS

9th EU-Japan Joint Symposium on Plasma Processing (JSPP2014) and
EU COST MP1101 Workshop on Atmospheric Plasma Processes and Sources

PROCEEDINGS

January 19th— January 23th 2014 | Bohinjska Bistrica, Slovenia (EU)

9th EU-Japan Joint Symposium on Plasma Processing (JSPP2014) and

EU COST MP1101 Workshop on Atmospheric Plasma Processes and Sources

January 19th — January 23th 2014, Bohinjska Bistrica, Slovenia

Poster session

P-01	*Simulation of Resistive Plate Chambers using Monte Carlo technique*	**D. Bošnjaković, Z.Lj. Petrović and S. Dujko**
P-02	*High order fluid model for negative planar streamer fronts in rare gases*	**S. Dujko, A. Markosyan and U. Ebert**
P-03	*Self-arrangement of phospholipids under plasma conditions*	**Kristina Eleršič, Uroš Cvelbar, Miran Mozetič**
P-04	*Effects of cold atmospheric pressure plasma on primary human fibroblasts*	**J. Filipović, A. Valenta-Šobot, Andreja Leskovac, D. Maletić, N. Puač, G. Malović, S. Lazović, Z. Lj. Petrović, G. Joksić**
P-05	*Plasma induced DNA damage: comparison with the effects of ionizing radiation*	**J. Filipović, A. Leskovac, S. Petrović, A. Valenta-Šobot, D. Maletić, N. Puač, G. Malović, S. Lazović, Z.Lj. Petrović, G. Joksić**
P-06	*Repair kinetics of DNA double strand breaks in human primary fibroblasts induced by a plasma needle*	**D. Maletić, J. Filipović, A. Leskovac, N. Puač, G. Malović, S.Lazović, G. Joksić, Z. Lj. Petrović**
P-07	*Scattering cross sections and transport data for electrons in CF_3I*	**J. Mirić, S. Dujko and Z.Lj. Petrović**
P-08	*Oxygen plasma selective etching for the enhanced electrical insulation properties of polyphenol composites*	**H. Puliyalil, M. Mozetič, U. Cvelbar**

Scattering cross sections and transport data for electrons in CF$_3$I

J. Mirić, S. Dujko and Z.Lj. Petrović

Institute of Physics, University of Belgrade, Pregrevica 118, 11080 Belgrade, Serbia

jasmina.miric@ipb.ac.rs

The trifluoroiodomethane (CF$_3$I) is a halofluorocarbon gas employed in the plasma etching of various materials. It also shows promise as a gaseous dielectric in the application of high-voltage power equipment. This is an environmentally friendly gas due to the following characteristics. First, C-I bond in this molecule is weak so can easily be broken by ultraviolet light which leads to a very short atmospheric lifetime (1.8 days). GWP (global warming potential) of CF$_3$I is ultra low (0.4 times that of CO$_2$) [1]. Second, this molecule has higher critical electric field (437 Td) [2] than SF$_6$ and hence it meets the basic requirements for application to environmentally-benign power equipment. Despite the need for reliable swarm and cross section data, there have only been a few swarm measurements of transport data covering relatively narrow *E/N* range [2] and only one set of cross sections for electron scattering [3]. This work represents an attempt to overcome such lack of reliable collisional and transport data for CF$_3$I.

Cross sections for electron scattering are critical input data in modeling of plasma discharges. The compilation of the cross-sections from different sources, without their renormalization to fit the swarm parameters, is usually not sufficient. Starting from the existing set of cross sections for electrons in CF$_3$I [3], we have employed a standard swarm procedure for the analysis of measured drift velocities and effective ionization coefficient.

1

In [3] the momentum transfer is composed of theoretical values up to 0.5 eV by Christophorou [4] while in the energy range between 1.5 and 60 eV the numerical integration of the differential cross sections of Kitajima [5] was performed. For higher energies the momentum transfer cross section is found as a sum of individual cross sections for momentum transfer of constituent atoms [6, 7]. The attachment cross section suggested by Christophorou [4] was included and six vibrational modes of CF_3I by Shimanouchi [8] were grouped into three. The total ionization cross section is given as a sum of experimentally determined partial ionization cross sections [9]. Finally, in the same set of cross sections there are five cross sections for electronic excitations (and possibly neutral dissociation) whose magnitudes were decided by considering the relative loss peak height of Kitajima [5]. Using a two-term Boltzmann code, the calculated transport coefficients (drift velocity under the time-of-flight conditions and rate coefficients for ionization and attachment obtained under the steady-state Townsend conditions) were compared with the corresponding experimental data and in figure 1(a) we show the final set of cross sections developed by Kimura and Nakamura [3]. This is the initial set of cross sections used in this work.
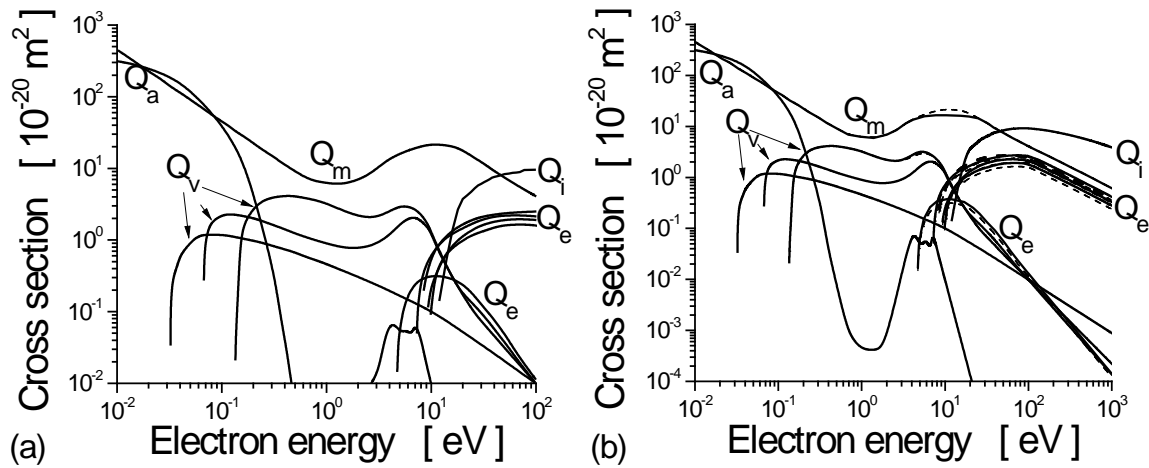
Figure 1. Cross section sets for electron scattering of CF_3I: (a) from Kimura and Nakamura's work [3], (b) from this work (solid curves - our final and dashed curves - our initial set of cross sections).

The first step in our work was calculation of transport data based on the cross sections developed in [3]. Calculations of transport coefficients were performed by Bolsig+ [10] and our Monte Carlo simulation code and the results for the drift velocity and rate coefficients for attachment and ionization were compared with the available experimental measurements. The disagreement between these two sets of data was an indication of some internal inconsistencies within the set of cross sections developed by Kimura and Nakamura [3].
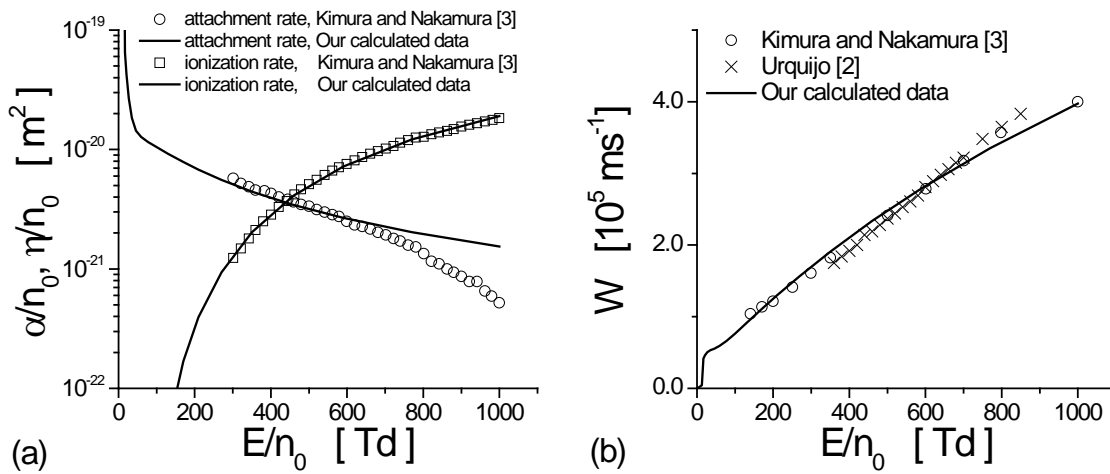
Figure 2. Comparison of our calculated and experimentally measured transport coefficients presented [2,3]: (a) ionization and attachment rates, and (b) drift velocity.

In this work the cross-sections were extended in energy up to 1000 eV so that calculated data may cover the region between a few Td and few thousands of Td. This is of great importance having in mind the high critical field of CF_3I. The logarithmic extrapolation was used for electronic excitation with the lowest threshold and for all vibrational excitations as well as for the electron attachment. The Born-Bethe approximation was used to extrapolate the cross sections for momentum transfer in elastic collisions and for the cross sections for electronic excitation. The cross section for ionization was modified as follows: in the energy range up to 45 eV we have used the cross section from [3] while for higher energies than 45 eV we have included the theoretically calculated cross section developed by Anthony [11]. Using the data suggested by Christophorou

[4], the cross section for attachment between 0.5 and 3 eV was reconstructed.

Cross section for momentum transfer in elastic collisions in the energy region between 4 and 20 eV was modified together with the cross section for vibrational excitation with the highest threshold in order to fit the drift velocity from experimental measurements of Kimura and Nakamura [3]. The ionization coefficient was fitted through the modification of cross sections for electronic excitations having in mind the large uncertainties associated with the magnitudes of these cross sections. Our cross sections for electron scattering in CF_3I are shown in figure 1(b). This set of cross sections provides much better agreement between theoretically calculated and experimentally measured swarm transport data as shown in figure 2.

In this work the cross section set for electron-CF_3I collisions was developed on the basis of the cross sections developed by Kimura and Nakamura [3]. Further improvements of the present set will be made by considering the transport data in the mixtures of CF_3I with Ar, Xe and N_2.

References

[1] G. Acerboni, J. A. Beukes, N. R. Jensen, J. Hjorth, G. Myhre, C. J. Nielsen, J. K. Sundet "Atmospheric degradation and global warming potentials of three perfluoroalkens", Atmos. Environ. Vol.35, Issue 24 (2001)

[2] J. de Urquijo "Is CF3I a good gaseous dielectric? A comparative swarm study of CF_3I and SF_6", J. Phys. Conf. Ser. Vol.86, Issue 1 (2007)

[3] M. Kimura, Y. Nakamura "Electron swarm parameters in CF_3I and a set of electron collision cross sections for CF_3I molecule", J. Phys. D: Appl. Phys. Vol.43, Issue 14 (2010)

[4] L. G. Christophorou, J. K. Olthoff "Electron interactions with CF_3I", J. Phys. Chem. Ref. Data, Vol.29, (2000)

[5] M. Kitajima, M. Okamoto, K. Sunohara, H. Tanaka, H. Cho, S. Samukawa, S. Eden, N. J. Mason "Low-energy electron impact elastic and inelastic scattering fron CF_3I", J. Phys. B: At. Mol. Opt. Phys. Vol.35, Issue 15 (2002)

[6] M. Fink, J. Ingram "Theoretical electron scattering amplitudes and spin polarizations", At. Data Vol.4, (1972)

[7] M. E. Riley, C. J. MacCallum, F. Biggs "Theoretical electron-atom elastic scattering cross sections: selected elements, 1 keV to 256 keV", At. Data Nucl. Data Tables Vol.15, Issue 5 (1975)

[8] T. Shimanouchi "Tables of molecular vibrational frequencies, part 8", J. Phys. Chem. Ref. Data Vol.3, (1974)

[9] C. Q. Jiao, B. Ganguly, C. A. DeJoseph Jr., A. Garscadden "Comparations of electron impact ionization and ion chemistries of CF_3Br and CF_3I", Int. J. Mass Spectrom. Vol.208, Issue 1-3 (2001)

[10] G.J.M. Hagelaar and L.C. Pitchford, "Solving the Boltzmann equation to obtain

electron transport coefficients and rate coefficients for fluid models", Plasma Sources Sci. Technol. 14, 722 (2005)

[11] B. K. Antony, K. N. Joshipura, N. J. Mason "Total and ionization cross sections of electron scattering by fluorocarbons", J. Phys. B: At. Mol. Opt. Phys Vol.38, Issue 3 (2005)

74th Annual Gaseous Electronics Conference Virtual: GEC Platform

Time Zone: Central Daylight Time, USA

Monday, October 4, 2021 8:00 AM - 8:30 AM

Session AM11 : Welcome Remarks Virtual GEC platform

8:00AM AM11.00001: Welcome Remarks — Welcome Remarks

Monday, October 4, 2021 8:30 AM - 5:30 PM

Session BM21 : Workshop I: Plasma Diagnostics Virtual GEC platform - Ryan Gott, NASA Kennedy

8:30AM BM21.00001: Principles and some progress in floating probe method (FPM) for process plasma diagnostics and monitoring [Invited]   CHINWOOK CHUNG (Presenter), Hanyang Univ, HYUNDONG EO, MOO-YOUNG LEE, HO WON LEE, Hanyang University — Floating probe method (FPM) applicable to process plasma has recently been developed. Recent progress and variant methods based on these FPM are introduced. A method of measuring plasma wirelessly by modifying the FPM has been developed, and plasma densities and electron temperatures were measured considering the deposition of the probe surface. This technique will be applicable to process plasma diagnosis and monitoring.

9:15AM BM21.00002: Pushing the boundaries of established plasma diagnostics[*] [Invited]   PETER BRUGGEMAN (Presenter), University of Minnesota — While low temperature atmospheric pressure plasma diagnostics have been extensively studied in the last decades, there remains a strong need for improved diagnostics to increase our understanding of the underlying plasma processes particularly of emerging applications. The interpretation of plasma diagnostics poses often challenges due the distinctive non-equilibrium properties of atmospheric pressure plasmas in combination with their high collisional nature. This is further enhanced by spatial gradients down to micrometer length scale, transient behavior down to nanosecond timescales and challenging operation conditions required for some applications.

 The presentation will summarize the state of the art of well-established diagnostics for atmospheric pressure plasmas including Thomson scattering, laser induced fluorescence, broad band absorption spectroscopy and mass spectrometry. We will highlight some examples that illustrate the capability to advance these diagnostics by enabling a more convenient implementation approach, a broader detection range of species and the investigation of more challenging plasma conditions.

10:00AM BM21.00003: Coffee Break — Coffee Break

GT61.00027: Relationship between photon energy and current induced by photo-excited desolvation of hydrated electrons in atmospheric-pressure dc glow discharge[*] YOSHINOBU INAGAKI (Presenter), KOICHI SASAKI, Hokkaido University — Hydrated electrons are generated by plasma-liquid interaction. However, there have been limited reports on the detection of hydrated electrons in liquids interacting with plasmas. The difficulty is caused by the fact that hydrated electrons generated by the plasma irradiation are localized in a narrow region with a thickness of several nanometers below the plasma-liquid interface. To overcome the difficulty, we have developed a method to detect hydrated electrons in the interfacial region. Hydrated electrons in the interfacial region are converted to free electrons when they are irradiated with laser beam having a photon energy exceeding the desolvation energy. Free electrons produced by the desolvation are ejected into the gas phase.

In a previous work, we used an atmospheric-pressure helium dc glow discharge with a liquid electrode, and observed the pulsed increase in the discharge current when the liquid electrode was irradiated with a Nd:YAG laser pulse. In this experiment, we used a dye laser to examine the relationship between the increase in the discharge current and the photon energy. In addition, we estimated the depth profile of hydrated electron density with the help of a numerical simulation on the collisional transport process of free electrons in water.

GT61.00028: Effects of Physiological Saline Solution Treated by Ar Dielectric Barrier Discharge on Proliferation of Jurkat Cell[*] EIJI OYAMA (Presenter), AKHIRO SHIRAI, Tokushima University, TADAHIKO NAKAGAWA, The University of Shimane, MASAHIRO SOGABE, TOSHIYA OKAHISA, KENJI TERANISHI, Tokushima University — Recently, applications of discharge plasma to medical fields have been actively studied by many research groups [1]. The authors have conducted fundamental study aiming to apply the discharge plasma to a therapy for autoimmune disease [2]. The present study investigated the effect of the physiological saline solution treated by argon dielectric barrier discharge (DBD) on Jurkat cells. The plasma-treated saline (PTS) solution was prepared by exposing physiological saline solution to the DBD generated by feeding 1-L/min argon for 15 minutes. Jurkat (RCB0806) cells were exposed to the PTS for 30 minutes and then incubated for 30 hours. The number of viable and non-viable cells were evaluated at the several time points of incubation using Trypan blue staining method. In the case of Jurkat cells unexposed to any solutions and plasma, the viable cell number was increased favorably during the 30-hours incubation while the non-viable cells were maintained almost constant in small numbers. These results also led to the favorable increase of the total cell number. In contrast, in the case of Jurkat cells exposed to the PTS, the number of viable and non-viable cells were respectively decreased and increased with incubation time, resulted in the slight decrease in the total cell number. From these results, it was found that the PTS inhibits the cellular proliferation of Jurkat cells and promotes the cell death. We are now conducting apoptosis detections by a flow cytometry to investigate further the cell death of Jurkat cells.

GT61.00029: Electron transport and negative streamers in indium vapor[*] SASA DUJKO (Presenter), JASMINA ATIĆ, DANKO BOŠNJAKOVIĆ, Institute of Physics Belgrade, University of Belgrade, Serbia, RONALD WHITE, PETER STOKES, College of Science and Engineering, James Cook University, Australia, LAURENCE CAMPBELL, MICHAEL BRUNGER, College of Science and Engineering, Flinders University, Australia — We investigate the transport of electrons and propagation of negative ionization fronts in indium vapor. Electron swarm transport coefficients are calculated using a numerical multi term solution of Boltzmann's equation and a Monte Carlo simulation technique over a range of the reduced electric fields and the indium vapor temperatures. As many indium atoms are in the first $(5s^2 5p)$ $^2P_{3/2}$ metastable state at vapor temperatures of a few thousands of Kelvin, the presence of thermal motion of the host gas atoms and superelastic collisions are carefully considered and implemented in our codes. We observed a significant sensitivity of the spatial relaxation of the electrons under non-hydrodynamic conditions in the steady-state Townsend experiment, with respect to the indium vapor temperature and the initial conditions used to release electrons from the cathode. In order to simulate the inception and propagation of negative ionization fronts in indium vapor, we here apply the classical fluid model, which is based on the drift-diffusion approximation, the local field approximation and Poisson's equation. This model is implemented numerically in 1D and 1.5D configurations without photoionization. Among many important points, we found tthat he transition from an avalanche into a negative ionization front occurs faster with increasing indium vapor temperature, due to enhanced ionization and more efficient production of electrons at higher vapor temperatures.

XX International Workshop on
Low-Energy Positron and Positronium Physics

XXI International Symposium on
Electron-Molecule Collisions and Swarms

V Workshop on Non-Equilibrium Processes

18-21 July 2019, Belgrade, Serbia

POSMOL 2019

BOOK OF ABSTRACTS

XX Међународна радионица о физици
ниско енергијских позитрона и позитронијума

XXI Међународни симпозијум о
електрон-молекулским сударима и ројевима

V Радионица о неравнотежним процесима

XX International Workshop on Low-Energy Positron and Positronium Physics

XXI International Symposium on Electron-Molecule Collisions and Swarms

V Workshop on Non-Equilibrium Processes

POSMOL 2019

BOOK OF ABSTRACTS

Editors

David Cassidy, Michael J. Brunger,
Zoran Lj. Petrović, Saša Dujko, Bratislav P. Marinković,
Dragana Marić and Sanja Tošić

BOOK OF ABSTRACTS of the

XX International Workshop on Low-Energy Positron and Positronium Physics

XXI International Symposium on Electron-Molecule Collisions and Swarms

V Workshop on Non-Equilibrium Processes

18-21 July 2019, Belgrade, Serbia

ACKNOWLEDGEMENT

POSMOL 2019

POSITRON INTERNATIONAL ADVISORY COMMITTEE

David Cassidy
(University College London), *Chair*
Gustavo García
(Consejo Superior de Investigaciones Científicas)
Michael Bromley
(University of Queensland)
Márcio Varella
(Universidade de São Paulo)
Masanori Tachikawa
(Yokohama City University)
Roberto Brusa
(Università di Trento)
James Danielson
(University of California, San Diego)
László Liszkay
(University of Paris, Saclay)

ELECTRON INTERNATIONAL ADVISORY COMMITTEE

Michael J. Brunger
(Flinders University), *Chair*
Ilya I. Fabrikant
(University of Nebraska, Lincoln)
Roman Čurík
(J. Heyrovský Institute of Physical Chemistry)
Roma da Costa
(Universidade Federal do Espirito Santo)
Paulo Limão-Vieira
(Universidade Nova de Lisboa)
Dragana Marić
(Institute of Physics Belgrade)
Sylwia Ptasińska
(University of Notre Dame)
Petra Swiderek
(University of Bremen)
Hajime Tanuma
(Tokyo Metropolitan University)
 Ronald D. White
(James Cook University)

LOCAL ORGANIZING COMMITTEE

Zoran Lj. Petrović (Serbian Academy of Sciences and Arts, Institute of Physics Belgrade) *Chair*
Bratislav Marinković (Institute of Physics Belgrade) *Co-Chair*
Saša Dujko (Institute of Physics Belgrade) *Co-Chair*
Sanja Tošić (Institute of Physics Belgrade) *Secretary*
Dragana Marić (Institute of Physics Belgrade) *Conference Manager*
Gordana Malović (Institute of Physics Belgrade)
Danko Bošnjaković (Institute of Physics Belgrade)
Andrej Bunjac (Institute of Physics Belgrade)
Jelena Sivoš (Institute of Physics Belgrade)
Marija Puač (Institute of Physics Belgrade)
Ilija Simonović (Institute of Physics Belgrade)
Vladan Simić (Institute of Physics Belgrade)
Nenad Selaković (Institute of Physics Belgrade)
Dejan Maletić (Institute of Physics Belgrade)
Kosta Spasić (Institute of Physics Belgrade)
Olivera Jovanović (Institute of Physics Belgrade)
Anđelija Petrović (Institute of Physics Belgrade)
Goran Poparić (Faculty of Physics, Belgrade)
Biljana Grozdanić (Serbian Academy of Sciences and Arts)
Aleksandra Hreljac (Serbian Academy of Sciences and Arts)

INVITED TALKS Workshop on Non-Equilibrium Processes

Cross Sections for Scattering of Electrons on Tetrafluoropropene HFO1234ze Obtained from the Swarm Data

Zoran Lj. Petrović[1,2], Jasmina Atić[1], Dragana Marić[1], Saša Dujko[1], Gordana Malović[1],
Jaime de Urquijo[3], Martin Ise[4], Thomas Hammer[4]

[1]Institute of Physics Belgrade, University of Belgrade, Pregrevica 118, 11080 Zemun, Serbia
[2]Serbian Academy of Sciences and Arts, Knez Mihajlova 35, 11000 Belgrade, Serbia
[3]Instituto de Ciencias Físicas, Universidad Nacional Autónoma de México, 62251, Cuernavaca, Mor., Mexico
[4]Siemens AG, Corporate Technology, CT REE ENS, Erlangen, 91058, Germany
zoran@ipb.ac.rs

Tetrafluoropropene (HFO1234ze, $C_3H_2F_4$) is a newly synthesized hydrofluoroolefine gas that due to its favorable properties has been considered for application as a gaseous dielectric and as a coolant. The transport data have been measured by de Urquijo and coworkers and by Franck and coworkers [1]. In both cases pulsed Townsend experiments were used and in both cases, preliminary data for fitting were drift velocities and effective ionisation coefficients (combination of ionization and attachment). We have tried to fit both sets of data for the pure gas and its mixtures with argon and nitrogen as measured by de Urquijo and coworkers. A two-term code has been used for numerous iterations and in the final stage Monte Carlo code [2] has been applied to obtain accurate and well defined transport coefficients.
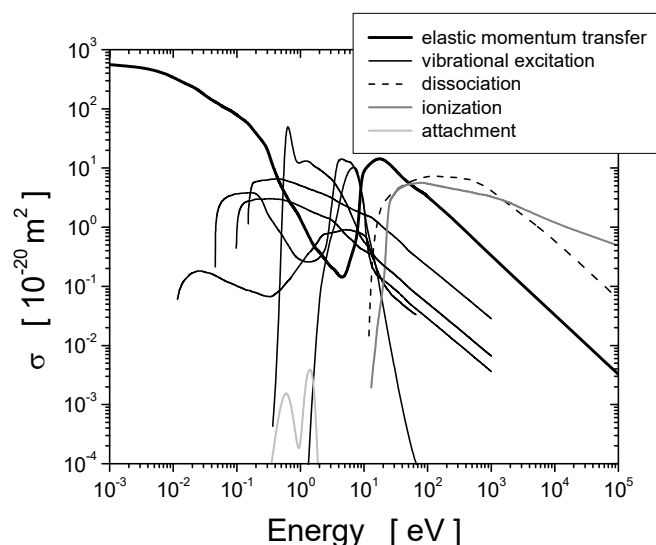
Figure 1. The cross sections for electron scattering on HFO1234ze, including vibrational excitation, one attachment process, dissociative excitation and ionization.

Starting from an initial set of cross sections taken from a similar gas (in this case octafluoropropane [3]) the set of cross sections shown in Figure 1 was achieved. Due to lack of information on the energy losses in the moderate energy range, the inelastic cross sections should be regarded as effective (i.e., each one may represent more than one process, or may bear a contribution from processes other than one effective cross section).

The critical reduced electric field of HFO1234ze is substantially lower than that of SF_6 because of low attachment cross sections. Thus, because of its boiling point of -19°C pressurized gas mixtures with buffer gases such as N_2 or CO_2 may be considered for dielectric application [4].

References
[1]   A. Chachereau, M. Rabie and C.M. Franck, *Plasma Sources Sci. Technol.* **25** (2016) 045005.
[2]   Z. Lj. Petrović, Z. M. Raspopović, S. Dujko and T. Makabe, *Appl. Surf. Sci.*, **192** (2002) 1.
[3]   MAGBOLTZ 2, Ver. 10.0.4, http://magboltz.web.cern.ch/magboltz/.
[4]   M. Koch and C. M. Franck, *IEEE Trans. Dielectr. Electr. Insul.* **22** (2015) 3260.

TWENTIETH INTERNATIONAL SUMMER SCHOOL ON VACUUM, ELECTRON AND ION TECHNOLOGIES

VEIT 2017

25 - 29 September 2017
SOZOPOL, BULGARIA

PROGRAM

ABSTRACTS

Editors: M. Dimitrova, M. Damyanova and Ch. Ghelev

VEIT '17

TWENTIETH INTERNATIONAL SUMMER SCHOOL
ON VACUUM, ELECTRON AND ION TECHNOLOGIES
25 – 29 September 2017, Sozopol, Bulgaria

PR–12

TRANSPORT OF CHARGED PARTICLE SWARMS AS A BASIS FOR PLASMA MODELS

Z.Lj. Petrović[1,2], T. Makabe[2,3], G. Malović[1], J. Mirić[1], S. Dujko[1]

[1]Institute of Physics, University of Belgrade, Zemun, Serbia
[2]Serbian Academy of Sciences and Arts, Belgrade, Serbia
[3]Keio University, Tokyo Japan

Non-equilibrium, collision-dominated discharges represent a combination of the two quite different phenomenological foundations. The first is the collisions and transport of particles (most importantly electrons). In the zero space charge limit, this phenomenology is represented by the physics of swarms and by transport equations. The second foundation is a hierarchy of space charge associated effects from the field shielding all the way to the strong Coulomb coupling. These effects are negligible in the swarm realm and dominate in the region of high degree of ionization to such a degree that the identity of collisional targets becomes unimportant. The collisions and transport enter the physics of non-equilibrium plasmas through transport equations of different forms, most importantly through Boltzmann equation and transport coefficients, through fluid equations and also in kinetic models representation of collisions proceeds through swarm normalized cross section data sets. These sets have to have completeness in representation of momentum, energy and number balances rather than details in the shape. If such a condition is met, then one may expect the energy distribution functions (EDF) to be predicted accurately. A powerful alternative to the Boltzmann equation would be to employ a Monte Carlo simulation (MCS) which suffers no limitations in accuracy for swarm conditions. Most importantly, MCS allows implementation of measured numerical boundary processes in a direct, easily interpreted way, rather than by mathematical boundary conditions. Swarm models are an accurate representation of a wide range of ionized gases, for example corona discharges, Townsend discharge, gaseous dielectrics and a wide range of particle detectors.

The theoretical foundation of non-equilibrium plasmas in fluid or hybrid models is another way of representing the flow of charged particles that is driven by external or local fields and by collisions. These equations allow us to produce spatial distributions of charges and calculate the effective local fields mostly representing space charge effects such as shielding and double layers. A direct effect of Coulomb interaction on electron EDF has to be introduced directly in the kinetic equations and it is one of the open issues in modeling. Non-hydrodynamic transport in strong fields due to sheaths leads to strongly non-local effects that cannot be easily calculated by the fluid models. Some corrections may be provided through the relaxation continuum model or by using higher-order transport in fluid equations based on higher-order transport coefficients. In such circumstances, however, kinetic models are the best option, again with the swarm derived cross sections.

POSMOL 2017

XIX International Workshop on
Low-Energy Positron and Positronium Physics

XX International Symposium on
Electron-Molecule Collisions and Swarms

BOOK OF ABSTRACTS

22-24 July 2017

Amaroo on Mandalay Resort, Magnetic Island
Queensland, Australia

posmol2017.edu.au
@posmol2017

Hydrodynamic and non-hydrodynamic studies of electron transport in mercury vapour

J. Mirić[1], I. Simonović[1], D. Bošnjaković[1], Z.Lj. Petrović[1], R.D. White[2] and S. Dujko[1]

[1]Institute of Physics, University of Belgrade, Pregrevica 118, 11080 Belgrade, Serbia
[1]College of Science and Engineering, James Cook University, Townsville, QLD 4811, Australia

sasa.dujko@ipb.ac.rs

The behaviour of electrons in mercury vapour under the influence of varying configuration of electric and magnetic fields is of vital interest in modelling of gas-discharge lamps [1]. Fluid models of low-pressure discharges used in fluorescent lamps usually require swarm parameters as a function of the reduced electric field and the gas temperature [2]. Current models of inductively coupled mercury discharges which are utilized in some types of electrodeless lamps [3] require knowledge of electron transport parameters in the presence of both the electric and magnetic fields. Modelling of electron transport processes in these applications demands an accurate and complete set of cross sections for electron-mercury atom interactions in the gas phase.

In this work we present a complete and consistent set of cross sections for electron scattering in mercury vapour. The set is validated through a series of comparisons between swarm data calculated using a multi term solution of Boltzmann's equation and Monte Carlo simulations, and the available experimental data. For magnetic field free case, we discuss the dependence of transport coefficients on the pressure and temperature of mercury vapour, and the occurrence of negative differential conductivity (NDC) in the limit of lower values of the reduced electric fields. The phenomenon of NDC is induced by the presence of mercury dimers. Mercury dimers are molecular species that can cause a significant change in the rate of energy loss by the electrons via rotational and vibrational excitations. This in turn may significantly affect the drift velocity and the overall balance of the momentum in the system. Following the previous studies of England and Elford [4], we have estimated the effective inelastic cross section for mercury dimers for a range of pressures and temperatures. Calculations of electron transport properties have been performed and two important conclusions emerged: (1) the occurrence of NDC can be controlled by varying either pressure or temperature of mercury vapor, and (2) the measured and calculated drift velocities agree very well only if the mercury-dimer cross section and thermal motion of mercury atoms are carefully considered and implemented in numerical calculations.

In the second part of this work we investigate the influence of the electric and magnetic field strengths on the transport coefficients over ranges consistent with the operation of inductively coupled mercury discharges. Values of mean energy drift velocity, diffusion tensor, and ionization rate are reported in this work. An unexpected phenomenon arises: for certain values of electric and magnetic field, we find regions where mean energy of electrons increases with increasing magnetic field for a fixed electric field. In addition, we demonstrate the Maxwellization of high-energy electrons and magnetic cooling effects associated with an increasing magnetic field.

References
[1] G.G. Lister, J.E. Lawler, W.P. Lapatovich and V.A. Godyak, Rev. Mod. Phys. **76** (2004) 541
[2] Brok et al, J. Phys. D: Appl. Phys. **40** (2007) 3931
[3] Y. Liu, G. Zissis and Y. Chen, Plasma Source Sci. Technol. **22** (2013) 035002
[4] J.P. England and M.T. Elford, Aust. J. Phys. **44** (1991) 647

BULLETIN

69th Annual Gaseous Electronics Conference

October 10–14, 2016
Bochum, Germany
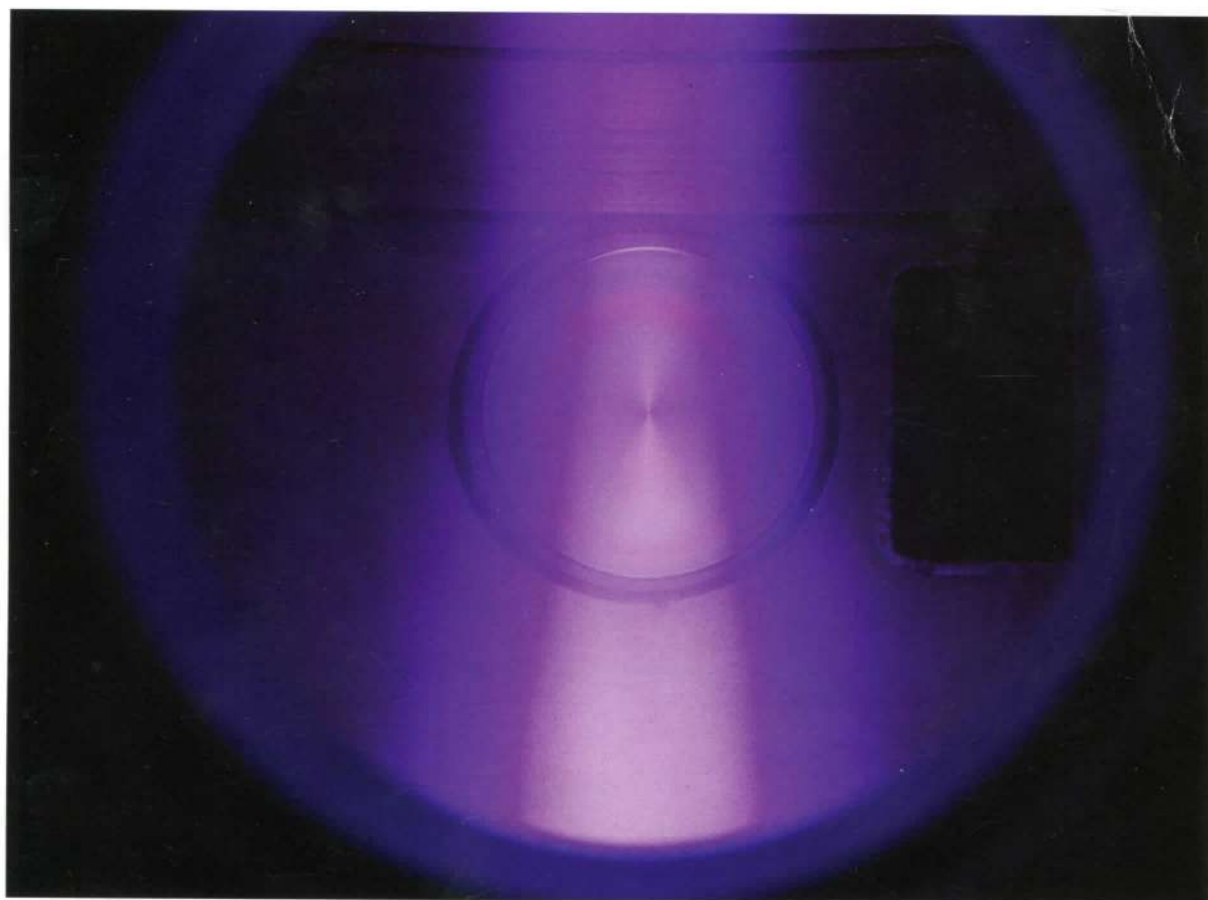
APS
physics

APS COUNCIL OF REPRESENTATIVES 2016

President
Homer A. Neal*, *University of Michigan*

President-Elect
Laura H. Greene*, *Florida State University*

Vice President
Roger W. Falcone*, *University of California, Berkeley/LLBL*

Past President
Samuel H. Aronson*, *Brookhaven National Laboratory (retired)*

Chief Executive Officer
Kate P. Kirby*, *Harvard Smithsonian (retired)*

Speaker of the Council
Nan Phinney*, *Stanford University*

Treasurer
James Hollenhorst*, *Agilent Technologies*

Corporate Secretary
Ken Cole

General Councillors
Marcelo Gleiser, Nadya Mason,
Bonnie Flemming, Gail McLaughlin*

Division, Forum and Section Councillors
Miriam Forman (*Astrophysics*); Timothy Gay* (*Atomic, Molecular & Optical*); Jose Onuchic (*Biological*); Amy Mullin* (*Chemical*); John Bradley Marston (*Condensed Matter Physics*); Giulia Galli (*Computational*); Ann Karagozian (*Fluid Dynamics*); Gay Stewart* (*Forum on Education*); Julia Gonski (*Forum on Graduate Student Affairs*); Dan Kleppner* (*Forum on History of Physics*); John Rumble (*Forum on Industrial and Applied Physics*); Young-Kee Kim* (*Forum on International Physics*); Pushpa Bhat (*Forum on Physics and Society*); Nicholas Bigelow* (*Laser Science*); James Chelikowsky (*Materials*); Wick Haxton* (*Nuclear*); P. Michael Tuts (*Particles & Fields*); Thomas Roser (*Physics of Beams*); Cary Forest (*Plasma*); Mark Ediger (*Polymer*); Nan Phinney* (*California Section*); Carlos Wexler (*Prairie Section*)

International Councilors
Marcia Barbosa, Eliezer Rabinovici, Johanna Stachel, Kiyoshi Ueda

Chair, Nominating Committee
Paul Chaikin

Chair, Panel on Public Affairs
Julia Phillips

Editor in Chief
Pierre Meystre*

Staff Representatives
Mark Doyle, *Chief Information Officer*; Amy Flatten, *Director of International Affairs*; Ted Hodapp, *Director of Project Development and Senior Advisor to the Department of Education and Diversity*; Trish Lettieri, *Director of Membership*; Irene Lukoff, *Director of Development*; Michael Lubell, *Director, Public Affairs*; Dan Kulp, *Editorial Director*; Christine Giaccone, *Director, Journal Operations*; Terri Olsen, *Director of Meetings*; Monica Plisch, *Director of Education and Diversity*; Matthew Salter, *Publisher*; Michael Stephens, *Controller and Assistant Treasurer*; James W. Taylor, *Deputy Executive Officer and Chief Operating Officer*

*** Members of the APS Board of Directors**

coefficients for low and moderate reduced electric fields E/N (N-gas density) accounting for non-conservative processes.

MW6 35 Third order transport coefficients for electrons and positrons in gases

SASA DUJKO, ILIJA SIMONOVIC, *Institute of Physics, University of Belgrade, Serbia* RONALD WHITE, *College of Science, Technology & Engineering, James Cook University, Australia* ZORAN PETROVIC, *Institute of Physics, University of Belgrade, Serbia* Third order transport coefficients (the skewness tensor) of the electron and positron swarms, in atomic and molecular gases, are investigated. The knowledge of the skewness tensor is necessary for the conversion of the hydrodynamic transport coefficients to the arrival time and steady-state Townsend transport data as well as for the determination of the deviations of the spatial density profiles from an ideal Gaussian. In this work, we investigate the structure and symmetries along individual elements of the skewness tensor by the group projector method. Individual components of the skewness tensor are calculated using a Monte Carlo simulation technique and multi term theory for solving the Boltzmann equation. Results obtained by these two methods are in excellent agreement. We extend previous studies by considering the sensitivity of the skewness components to explicit and implicit effects of non-conservative collisions, post-ionization energy partitioning, and inelastic collisions. The errors of the two term approximation for solving the Boltzmann equation are highlighted. We also investigate the influence of a magnetic field on the skewness tensor in varying configurations of electric and magnetic fields. Among many interesting points, we have observed a strong correlation between the skewness and diffusion.

MW6 36 Transport properties of electrons and transition of an electron avalanche into a streamer in atomic liquids

SASA DUJKO, ILIJA SIMONOVIC, *Institute of Physics, University of Belgrade, Serbia* GREGORY BOYLE, RONALD WHITE, *College of Science, Technology & Engineering, James Cook University, Australia* DANKO BOSNJAKOVIC, ZORAN PETROVIC, *Institute of Physics, University of Belgrade, Serbia* A Monte Carlo simulation technique is developed and used to calculate transport coefficients of electron swarms in non-polar atomic liquids. We employ the two model processes in which only momentum and energy are exchanged, respectively, to account for structure dependent coherent elastic scattering at low energies. The validity of the code is confirmed by comparison with results of previous authors. We apply two scenarios for higher energy cross sections. In the first scenario excitations in the liquid phase are approximated by excitations in the gas phase. In the second scenario excitations are completely neglected. Ionization threshold is reduced to values which are suggested in the literature, in both scenarios. Transport coefficients in these two scenarios, as well as transport coefficients for gas and liquid phases are compared. Special attention has been given to the structure induced negative differential conductivity (NDC), which has been observed both in this work, and in previous publications. Spatially-resolved electron transport properties are calculated in order to understand this phenomenon. The important aspect of this work is modeling of the transition of an electron avalanche into a streamer. Calculations are performed using 1D and 1.5D fluid models. Streamer properties in scenarios with and without excitations are compared.

MW6 37 Monte Carlo simulations of electron transport in strongly attaching gases

ZORAN PETROVIC, JASMINA MIRIC, ILIJA SIMONOVIC, DANKO BOSNJAKOVIC, SASA DUJKO, *Institute of Physics, University of Belgrade, Serbia* Extensive loss of electrons in strongly attaching gases imposes significant difficulties in Monte Carlo simulations at low electric field strengths. In order to compensate for such losses, some kind of rescaling procedures must be used. In this work, we discuss two rescaling procedures for Monte Carlo simulations of electron transport in strongly attaching gases: (1) discrete rescaling, and (2) continuous rescaling. The discrete rescaling procedure is based on duplication of electrons randomly chosen from the remaining swarm at certain discrete time steps. The continuous rescaling procedure employs a dynamically defined fictitious ionization process with the constant collision frequency chosen to be equal to the attachment collision frequency. These procedures should not in any way modify the distribution function. Monte Carlo calculations of transport coefficients for electrons in SF_6 and CF_3I are performed in a wide range of electric field strengths. However, special emphasis is placed upon the analysis of transport phenomena in the limit of lower electric fields where the transport properties are strongly affected by electron attachment. Two important phenomena arise: (1) the reduction of the mean energy with increasing E/N for electrons in SF6, and (2) the occurrence of negative differential conductivity in the bulk drift velocity of electrons in both SF_6 and CF_3I.

MW6 38 Electron transport in mercury vapor: magnetic field effects, dimer induced NDC and multi-term analysis

ZORAN PETROVIC, JASMINA MIRIC, ILIJA SIMONOVIC, SASA DUJKO, *Institute of Physics, University of Belgrade, Serbia* A multi term theory for solving the Boltzmann equation and Monte Carlo simulation technique are used to investigate electron transport in varying configurations of electric and magnetic fields in mercury vapor. Using different sets of cross sections for electron scattering in mercury as an input in our Boltzmann and Monte Carlo codes, we have calculated data for electron transport as a function of reduced electric and magnetic fields. A multitude of kinetic phenomena in electron transport has been observed and discussed using physical arguments. In particular, we discuss two important phenomena: (1) for certain values of electric and magnetic field, we find regions where swarm mean energy increases with increasing magnetic field for a fixed electric field, and (2) the occurrence of negative differential conductivity (NDC) for higher pressures and temperatures. In particular, NDC is induced by the presence of mercury dimers. The measured drift velocities agree very well with our Monte Carlo results only if the superelastic collisions are included in our calculations. Spatially-resolved electron transport properties are calculated using a Monte Carlo simulation technique in order to understand these phenomena.

MW6 39 Dependence of ion drift velocity and diffusion coefficient in parent gas on its temperature*

SERGEY MAIOROV, *Joint Institute for High Temperatures of RAS, Moscow* RUSUDAN GOLYATINA, *A.M. Prokhorov General Physics Institute of RAS, Moscow* The results of Monte Carlo calculations of the ion drift characteristics are presented: ions of noble gases and Ti, Fe, Co, Cs, Rb, W and mercury ions in case of constant and uniform electric field are considered. The dependences of the ion mobility on the field strength and gas temperature are analyzed. The parameters of the drift velocity approximation by the Frost formula for gas temperatures of 4.2, 77, 300, 1000, and 2000 K are presented. A universal drift velocity approximation depending on the reduced electric field strength and gas temperature is obtained. In the case of strong electric fields or low gas temperatures, the deviation of the ion distribution function from the Maxwellian one (including the shifted Maxwellian one) can be very significant. The average
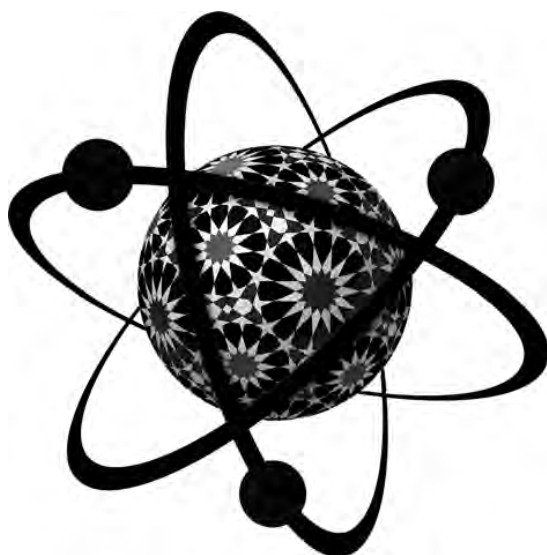
ICPEAC 2015

XXIX INTERNATIONAL CONFERENCE
on Photonic, Electronic and Atomic Collisions

22-28 JULY 2015 **TOLEDO** · SPAIN
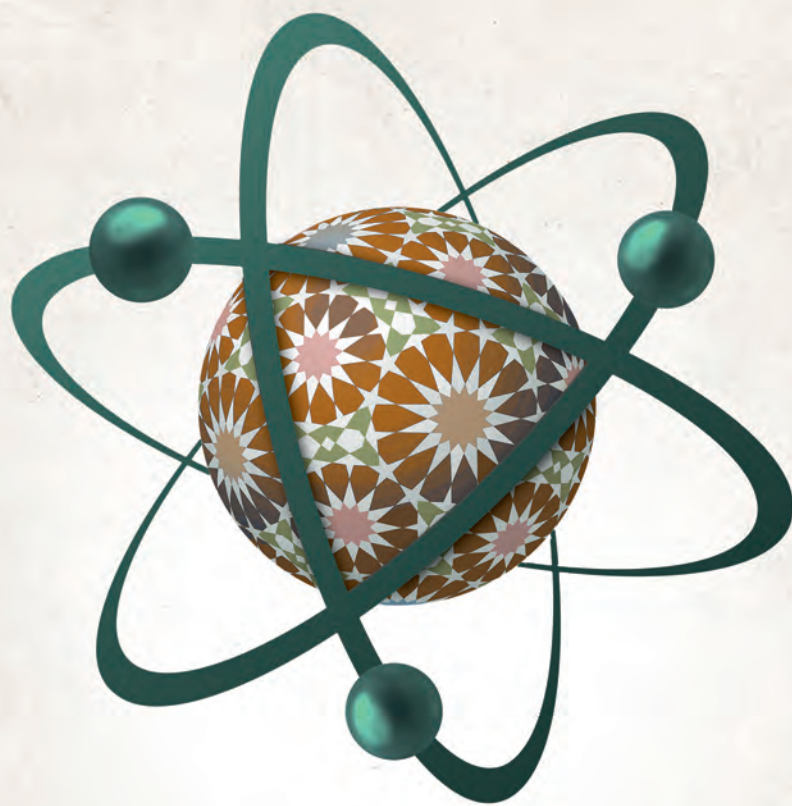
ICPEAC 2015

XXIX INTERNATIONAL CONFERENCE
on Photonic, Electronic and Atomic Collisions

22-28 JULY 2015 TOLEDO · SPAIN

CONFERENCE PROGRAM

Edited By:

Fernando Martín, Gustavo García, Luis Méndez,
Luca Argenti, Alicia Palacios

XXIX ICPEAC Local Organizing Committee

Chair: Fernando Martín (UAM)

Co-Chairs: Gustavo García (CSIC)
                  Luis Méndez (UAM)

Secretaries: Luis Bañares (UCM)
                  Luis Roso (CLP)

Members: Manuel Alcamí (UAM)
                  Luca Argenti (UAM)
                  Enrique Conejero (US)
                  Inés Corral (UAM)
                  Gerardo Delgado (CSIC)
                  Cristina Díaz (UAM)
                  Sergio Díaz-Tendero (UAM)
                  Luis F. Errea (UAM)
                  Clara Illescas (UAM)
                  Otilia Mó (UAM)
                  Alicia Palacios (UAM)
                  Luis Plaja (US)
                  Rita Prosmiti (UAM)
                  Ismanuel Rabadán (UAM)
                  Paula Rivière (UAM)
                  Manuel Yáñez (UAM)

CLP	Centro de Láseres Pulsados, Salamanca
CSIC	Consejo Superior de Investigaciones Científicas, Madrid
UAM	Universidad Autónoma de Madrid
UCM	Universidad Complutense de Madrid
US	Universidad de Salamanca

6. Lepton - Molecule / Small Cluster

FR-089 **Integral electron impact ionization cross section of molecules through Coulomb crystallization of the product ions**

Lukasz Klosowski, Mariusz Piwinski, Michael Drewsen

FR-090 **The cryogenic storage ring CSR for collision experiments with state-controlled and phase-space cooled molecular ion beams**

Arno Becker, Klaus Blaum, Christian Breitenfeldt, Florian Fellenberger, Sebastian George, Jürgen Göck, Manfred Grieser, Florian Grussie, Robert Von Hahn, Philipp Herwig, Jonas Karthein, Claude Krantz, Holger Kreckel, Sunil Kumar, Michael Lange, Svenja Lohmann, Christian Meyer, Preeti M Mishra, Oldřich Novotný, Aodh O'connor, Roland Repnow, Stefan E Schippers, Claus D Schröter, Kaija Spruck, Dirk Schwalm, Lutz Schweikard, Xavier Urbain, Stephen Vogel, Andreas Wolf

FR-091 **Analytical and molecular dynamical investigations of the influence of molecular vibrations upon the (e,2e) electron momentum distributions of furan**

Filippo Morini, Michael S. Deleuze, Noboru Watanabe, Masahiko Takahashi

FR-092 **Scattering of near-zero-energy positronium by H_2**

Junyi Zhang, Y. Qian, Y.-J. Yang, Z.-C. Yan, U. Schwingenschlög

FR-093 **Use of heavy-Rydberg ion-pair states to probe dissociative electron attachment**

Michael Kelley, Sitti Buathong, Barry Dunning

FR-094 **Dissociative electron attachment to molecular chlorine**

Krishnendu Gope, Vaibhav S Prabhudesai, Nigel Mason, Erumathadathil Krishnakumar

FR-096 **Streamer studies in gases for Resistive Plate Chambers**

Danko Bošnjaković, Zoran Lj. Petrović, Sasa Dujko

FR-097 **Transport coefficients and scattering cross sections for electrons in CF_3I**

Jasmina Mirić, Danko Bošnjaković, Zoran Lj. Petrović, Sasa Dujko

FR-098 **Cluster-Electron Interaction for Poly-Anion Production**

Franklin Martinez, Steffi Bandelow, Gerrit Marx, Lutz Schweikhard, Albert Vass

FR-099 **Isotope effect in dissociative electron attachment to H_2 at 4 eV**

Juraj Fedor, Jaroslav Kočišek, Radmila Janečková

FR-100 **Spontaneous decay of small copper cluster anions Cu_N^-, N = 3 ... 6**

Mark Hugo Stockett, Magdalena Kaminska, Rodrigo F. Nascimento, Emma K. Anderson, Michael Gatchell, Klavs Hansen, Henning Zettergren, Henning T Schmidt, Henrik Cederquist

FR-101 **Resonant and non-resonant electron-molecule collisions in molecular plasmas**

Roberto Celiberto, Kasturi L. Baluja, Vincenzo Laporta, Ratko K. Janev

FR-102 **Development of a method to measure molecular frame EELS cross sections**

Noboru Watanabe, So Yamada, Tsukasa Hirayama, Atsushi Seki, Daisuke Suzuki, Masahiko Takahashi

FR-103 **Hydrogen and Deuterium Continuum Radiation ($a^3\Sigma_g^+ \to b^3\Sigma_u^+$) Induced by Electron Impact**

Anita Ribar, Marián Danko, Juraj Országh, Štefan Matejčík

FR-104 **Detection of N_2 Metastable Molecules using a solid N_2 Matrix Detector**

Wladek Kedzierski, Cyrus Cerkauskas, William McConkey

FR-105 **Electron induced dissociative excitation of C_2H_2**

Juraj Országh, Marián Danko, Anita Ribar, Štefan Matejčík

FR-106 **Electron-ion collisional approach in the study of Rydberg and doubly-excited electronic states of H_2 and HeH^+**

Mourad Telmini, Soumaya Bezzaouia, Houaida Oueslati, Fatma Argoubi, Islem Bouhali, Christian Jungen

FR-107 **Electronic excitation to low-lying states of GeF_4 molecule by electron impact: A comparative study with CF_4 and SiF_4 molecules**

Shohei Ohtomi, Midori Matsui, Yu Mochizuki, Atsushi Suga, Hidetoshi Kato, Masamitsu Hoshino, Denis Duflot, Paulo Limão-Vieira, Hiroshi Tanaka

Transport coefficients and scattering cross sections for electrons in CF$_3$I

J. Mirić [1], **D. Bošnjaković, Z. Lj. Petrović and S. Dujko** [2]

Institute of Physics, University of Belgrade, Pregrevica 118, 11080 Belgrade, Serbia

Synopsis Scattering cross sections for electrons in CF$_3$I are developed using the swarm method. Drift velocity, effective ionization coefficient and diffusion coefficients are calculated using a Monte Carlo simulation technique and from solution of the non-conservative Boltzmann equation. Transport coefficients are also calculated in radio-frequency (rf) electric and magnetic fields and a multitude of phenomena induced by temporal non-locality is observed. We systematically study the origin and mechanisms for such phenomena and physical implications which arise from their explicit inclusion into plasma models.

Tetrafluoroiodomethane (CF$_3$I) is a processing gas employed for plasma etching of various materials. Due to its short atmospheric lifetime (1.8 days), low GWP (0.4 times than of CO$_2$) and high critical electric field ($(E/n_0)_{crit} = 437$ Td; 1 Td $= 10^{-21}$ Vm^2), CF$_3$I could be used as a high voltage insulator instead of SF$_6$ (atmospheric lifetime = 3200 years, GWP = 22800, $(E/n_0)_{crit} = 361$ Td), both on its own and mixed with N$_2$ and CO$_2$.

Transport coefficients for electrons in pure CF$_3$I and its mixture with Ar, Xe, N$_2$ and SF$_6$ are calculated for a set of cross-sections which was based on the work of Kimura and Nakamura [1] but which was modified to improve agreement between the calculated swarm parameters and the experimental values. As an illustrative example, in figure 1 we show the variation of the drift velocity with the reduced electric field E/n_0 before (a) and after the modification (b) of cross sections. After modification of cross sections the calculated values of drift velocity agree much better with those measured in experiments [2].

As CF$_3$I has a huge cross section for dissociative attachment, special attention is paid upon the implementation of procedure for compensation of electrons for losses due to strong electron attachment in our Monte Carlo code. In this presentation, we will discuss the following two procedures: (1) addition of new electrons by uniform scaling of the electron swarm at time instants when number of electrons reaches a certain threshold; and (2) introduction of a fictitious ionization channel/process with constant collision frequency (chosen to be approximately equal to the attachment rate).

The next issue is the electron transport in time-varying electric and magnetic fields. Calculations are performed for the radio-frequency fields having in mind applications in plasma processing technology. Among many important phenomena, we have observed the periodic structures in the absorbed power versus amplitude of the applied rf magnetic field curve which have a physical origin similar to the oscillatory phenomena observed for collisionless electron motion.
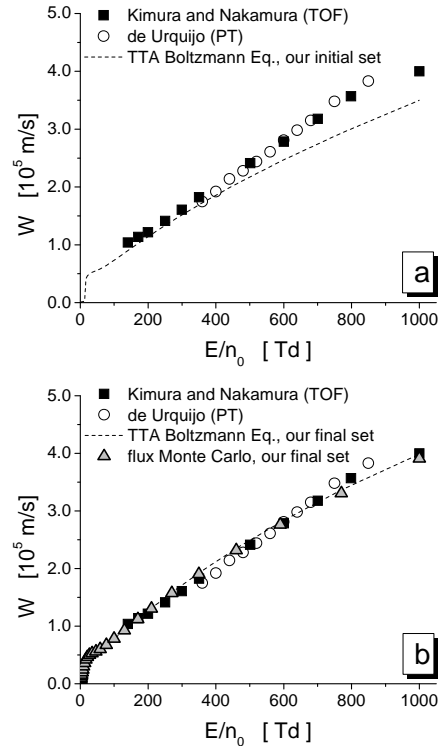
Figure 1. Drift velocity for electrons in CF$_3$I calculated from (a) our initial set and (b) our final set of cross sections. Results are compared with experimental data.

References

[1] M. Kimura and Y. Nakamura 2010 *J. Phys. D: Appl. Phys.* **43** 145202

[2] J. de Urquijo 2007 *J. Phys. Conf. Ser.* **86** 012008

[1] E-mail: jasmina.miric@ipb.ac.rs

[2] E-mail: sasha@ipb.ac.rs

XIX International Symposium on Electron-Molecule Collisions and Swarms

Book of Abstracts

POSMOL 2015

17-20 July 2015, LISBOA, PORTUGAL

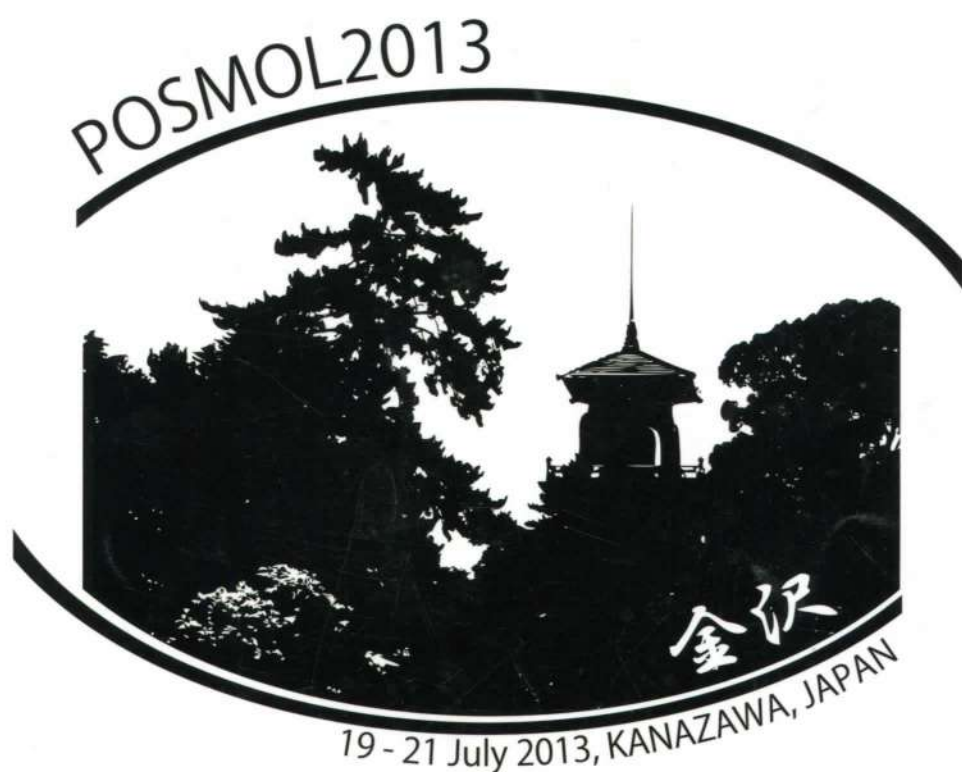XVIII International Workshop on Low-Energy Positron and Positronium Physics &
XIX International Symposium on Electron-Molecule Collisions and Swarms
17 - 20 July 2015, Lisboa, Portugal

POSMOL 2015

XIX International Symposium on Electron-Molecule Collisions and Swarms
Lisboa, Portugal
17-21 July, 2015

Edited by:
Paulo Limão-Vieira
Filipe Ferreira da Silva
Guilherme Meneses
Emanuele Lange
Tiago Cunha

Rescaling procedures for Monte Carlo simulations of electron transport in strong electronegative gases

D. Bošnjaković, J. Mirić, Z.Lj. Petrović and S. Dujko

Institute of Physics, University of Belgrade, Pregrevica 118, 11080 Belgrade, Serbia

dbosnjak@ipb.ac.rs

Electron attachment often imposes practical difficulties in Monte Carlo (MC) simulations of electron transport in strong electronegative gases at low electric field strengths. If the attachment rate is too high, the entire electron swarm can be consumed before steady state is achieved. In such extreme cases the transport data cannot be calculated. An obvious solution would be to use a very large number of initial electrons. However, in order to obtain the results with reasonable statistical accuracy, this would usually require computing resources which are beyond practical limits.

In order to address this issue in an optimal fashion, two distinctive procedures for electron compensation were proposed. The first one, which we refer to as *discrete rescaling*, is based on duplication of electrons randomly chosen from the remaining swarm at certain discrete time instants [1]. The other one we refer to as *continuous rescaling* introduces a fictitious ionization process with constant collision frequency chosen to be roughly equal to the attachment rate [2]. Both of these procedures were devised with the aim not to alter the electron distribution function and its evolution. However, it can be shown theoretically that only continuous rescaling meets this requirement [2].

In this work, we investigate the effects of MC rescaling procedures on the electron transport in CF_3I and SF_6 gases. Additionally, we propose a new implementation of continuous rescaling procedure which does not require the fictitious ionization rate to be defined *a priori*. Transport data is calculated using our electron impact cross sections for CF_3I [3] and a cross section set for SF_6 developed by Itoh et al. (1993). The results show that in case of CF_3I the transport parameters obtained using these two rescaling procedures can differ as much as 30% for the flux drift velocity or the attachment rate. Figure 1 shows the calculated flux drift velocity for CF_3I over a range of reduced electric field strengths. The results calculated using two term approximation for solving Boltzmann equation (BE TTA), are also shown for comparison.
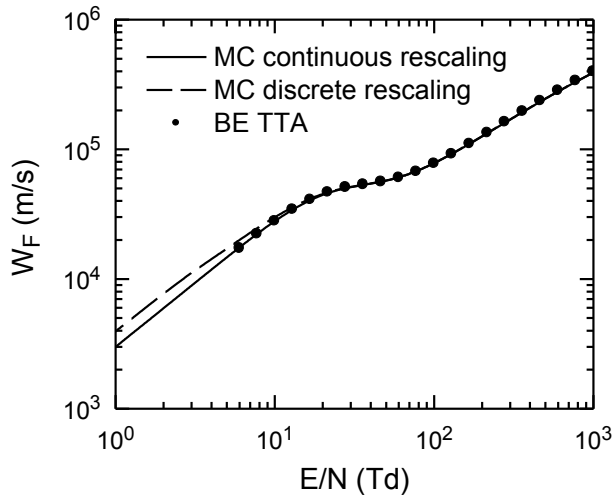
Figure 1. Flux drift velocity for CF_3I calculated over a range of reduced electric field strengths using two different MC rescaling procedures. Values obtained using two term approximation for solving Boltzmann equation are also shown (BE TTA).

References
[1] A.M. Nolan, M.J. Brennan, K.F. Ness and A.B. Wedding, *J. Phys. D: Appl. Phys.*, **30**, (1997), 2865.
[2] Y.M. Li, L.C. Pitchford and T.J. Moratz, *Appl. Phys. Lett.*, **54**, (1989), 1403.
[3] J. Mirić et al. (2015) unpublished.

ICOPS 2015
Abstract Book

The 42nd IEEE
International
Conference
On Plasma Science
24-28 May 2015
Belek, Antalya, Turkey

SCATTERING CROSS SECTIONS AND ELECTRON TRANSPORT COEFFICIENTS FOR ELECTRONS IN CF$_3$I

J. Mirić[1], D. Bošnjaković[1], O. Šašić[2], J. de Urquijo[3], S. Dujko[1] and Z.Lj. Petrović[1]

[1]*Institute of Physics, University of Belgrade, Pregrevica 118, 11080 Belgrade, Serbia*

[2]*Faculty of Transport and Traffic Engineering, University of Belgrade, Vojvode Stepe 305, 11000*

[3]*Instituto de Ciencias Fısicas, Universidad Nacional Autonoma de Mexico, PO Box 48-3, 62251 Cuernavaca, Mor., Mexico*

Electron transport coefficients and rate coefficients in pure CF$_3$I and its mixtures with Ar, Xe, N$_2$ and SF$_6$ have been calculated for a set of cross-sections which was based on the work of Kimura and Nakamura [1] but which was modified to improve agreement between the calculated swarm parameters and the experimental values. Electron drift velocity, effective ionization coefficient and diffusion coefficients are calculated using a Monte Carlo simulation technique and from solution of the non-conservative Boltzmann equation [2]. Calculated data for pure CF$_3$I and its mixtures with Ar, Xe, N$_2$ and SF$_6$ are compared with those measured under both time-of-flight (TOF) and pulsed-Townsend (PT) conditions. We note the existence of negative differential conductivity (NDC) in the profile of the bulk drift velocity with no signs of the same phenomenon in the profile of flux drift velocity. We systematically study the origin and mechanisms for such phenomena as well as the possible physical implications which arise from their explicit inclusion into plasma models. Spatially-resolved electron transport properties are calculated using a Monte Carlo simulation technique in order to understand these phenomena. Special attention is paid upon the implementation of procedure for compensation of electrons for losses due to strong electron attachment in our Monte Carlo code.

The Monte Carlo method is used to analyze the behavior of electron transport coefficients in radio-frequency electric field in pure CF$_3$I. Among many interesting kinetic phenomena, we observe the time-resolved NDC and anomalous anisotropic behavior of the longitudinal diffusion coefficient. We explore the validity of the quasi-static approximation for lower field frequencies and effective field approximation for higher frequency for electrons in CF$_3$I.

1. M. Kimura and Y. Nakamura, J. Phys. D: Appl. Phys. 43 (2010) 145202.
2. S. Dujko, R.D. White, Z.Lj. Petrović and R.E. Robson, Phys. Rev. E (2010) 81 046403.

XVIII International Symposium on Electron-Molecule Collisions and Swarms

Programme and Book of Abstracts

POSMOL2013

金沢

19 - 21 July 2013, KANAZAWA, JAPAN

POSMOL 2013

XVII International Workshop on Low-Energy Positron and Positronium Physics

Programme and Book of Abstracts

POSMOL2013

19 - 21 July 2013, KANAZAWA, JAPAN

XVII International Workshop on Low-Energy Positron and Positronium Physics &
XVIII International Symposium on Electron-Molecule Collisions and Swarms
19 - 21 July 2013, Kanazawa, Japan

POSMOL 2013

Abstracts of Plenary Talks

Abstracts of Progress Reports (ems)

Non-conservative electron transport in gases and its application in modelling of non-equilibrium plasmas and particle detectors

S. Dujko[1,2], D. Bošnjaković[1], J. Mirić[1], Z.Lj. Petrović[2], R.D. White[3], A.H. Markoyan[2] and U. Ebert[2]

[1]Institute of Physics, University of Belgrade, Pregrevica 118, Zemun 11080, Serbia

[2]Centrum Wiskunde & Informatica, (CWI), P.O. Box 94079, 1090 GB Amsterdam, The Netherlands

[3]ARC Centre for antimatter-Matter Studies, School of Engineering and Physical Sciences, James Cook University, Townsville 4810, Australia

sasa.dujko@ipb.ac.rs, S.Dujko@cwi.nl

The advancements in modern day technology associated with non-equilibrium plasma discharges depend critically on accurate modeling of the underlying collision and transport processes of charged particles in gases. To meet these challenges, we have undertaken a program to understand the kinetic behavior of charged particles under the combined action of electric and magnetic fields in neutral gases. A multi term theory for solving the Boltzmann equation has been developed and used to calculate transport coefficients of charged-particle swarms in neutral gases [1,2].

In the first part of this talk I will focus on non-equilibrium magnetized plasma discharges where the electric and magnetic fields can vary in space, time and orientation depending on the type of discharge and where attention must be paid to the correct treatment of temporal and spatial non-locality within the discharge. I will highlight the duality of transport coefficients arising from the explicit effects of non-conservative collisions particularly for electrons in rare gas metal-vapor mixtures, having in mind applications in lighting industry. As an example of fluid modeling of plasmas, I will discuss the recently developed high order fluid model for streamer discharges [3,4]. Starting from the cross sections for electron scattering, it will be shown how the corresponding transport data required as input in fluid model should be calculated under conditions when the local field approximation is not applicable. The temporal evolution of electron number density and electric field in the classical first order and in the high order model are compared and the differences will be explained by physical arguments.

In the second part of this talk I will discuss the detector physics processes of resistive plate chambers that are often used in many high energy physics experiments. Critical elements of modeling include the primary ionization, avalanche statists and signal development. The Monte Carlo simulation procedures that implement the described processes will be presented. Time resolution and detector efficiency are calculated and compared with experimental measurements and other theoretical calculations.

References

[1]   S. Dujko, R.D. White, Z.Lj. Petrović and R.E. Robson, Phys. Rev. E **81** 046403 (2010)
[2]   R.D. White, R.E. Robson, S. Dujko, P. Nicoletopoulos and B. Li, J. Phys. D: Appl. Phys. **42** 194001 (2009)
[3]   S. Dujko, A. Markosyan, R.D. White and U. Ebert, under revision for J.Phys.D.
[4]   A. Markosyan, S. Dujko and U. Ebert, under revision for J.Phys.D.

EMS

XVIII International Symposium on Electron-Molecule Collisions and Swarms

Programme and Book of Abstracts

POSMOL2013

金沢

19 - 21 July 2013, KANAZAWA, JAPAN

POSMOL 2013

XVII International Workshop on Low-Energy Positron and Positronium Physics

Programme and Book of Abstracts

POSMOL2013

金沢

19 - 21 July 2013, KANAZAWA, JAPAN

XVII International Workshop on Low-Energy Positron and Positronium Physics &
XVIII International Symposium on Electron-Molecule Collisions and Swarms
19 - 21 July 2013, Kanazawa, Japan

POSMOL 2013

Abstracts of Posters (ems)

E-06

Transport coefficients for electrons in rare-gas metal-vapor mixtures

J. Mirić[1], Z.Lj. Petrović[1], R.D. White[3] and S. Dujko[1,2]

[1]Institute of physics, University of Belgrade, Pregrevica 118, 11080 Zemun, Serbia

[2]Centrum Wiskunde & Informatica (CWI), P.O. Box 94079, 1090 GB Amsterdam, The Netherlands

[3]ARC Centre for Antimatter-Matter studies, James Cook University, School of Electrical Engineering and Physical Sciences, 4810 Townsville, Australia

sasa.dujko@ipb.ac.rs, S.Dujko@cwi.nl

The progress and further improvements of light sources based on low pressure electrical gas discharges require the most accurate modeling of charged particle transport processes in rare-gas-metal-vapor mixtures [1]. In this work we investigate electron transport in mixtures of rare gases (argon and neon) and metal vapors (sodium, potassium, cesium, magnesium and mercury) under swarm conditions using a multi term theory for solving the Boltzmann equation [2]. Calculations are performed over a range of E/N values, gas temperatures and metal vapor concentrations relevant to lamp discharges. Values and general trends of mean energy, drift velocity, diffusion tensor and rate coefficients are presented in this work.

Our work has been motivated, in part, by recent suggestions that highly accurate data for transport coefficients required as input in fluid models of lamp discharges may significantly improve the existing models. Current models of such lamps require knowledge of the plasma electrical conductivity, which can be calculated from the cross sections for electron scattering in rare-gas-metal-vapor mixtures and mobility coefficients presented in this work. In addition, we discuss the duality of transport coefficients arising from the explicit effects of ionization and correct implementation of transport data in fluid models of such discharges. Special attention is paid to the determination of transport data under steady-state Townsend conditions and their relations to transport coefficients obtained under hydrodynamic conditions [3]. The effects of metastable atoms and presence of dimmers in metal vapors on the swarm parameters are also discussed. Therefore, in this work we revisit and distill the most essential aspects of the definition and calculation of transport coefficients, giving numerical results for a range of transport data in rare-gas metal-vapor mixtures required as input in fluid models of lamp discharges.

References
[1]   G.G. Lister, J.E. Lawler, W.P. Lapatovich and V.A. Godyak, *Rev. Mod. Phys.* **76** 541 (2004)
[2]   S. Dujko, R.D. White R D, Z.Lj. Petrović and R.E. Robson, Phys. Rev. E **81** 046403 (2010)
[3]   S. Dujko, R.D. White and Z.Lj. Petrović, J. Phys. D:Appl. Phys. **41** 245205 (2008)